

# Spark Ignition: Experimental and Numerical Investigation With Application to Aviation Safety

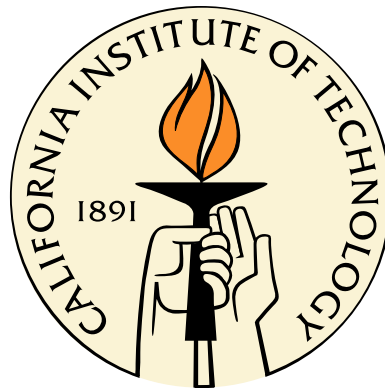
Thesis by

Sally P. M. Bane

In Partial Fulfillment of the Requirements

for the Degree of

Doctor of Philosophy



California Institute of Technology

Pasadena, California

2010

(Defended May 26, 2010)



# Acknowledgments

I first and foremost want to thank my advisor and mentor, Professor Joseph Shepherd. When I first joined his group, I did not know a screwdriver from a hammer, much less a single thing about combustion. Through his guidance and patience, I was able to grow as a scientist and experimentalist beyond what I thought possible. Professor Shepherd was always available to provide help and guidance, but also knew when to step back and let me teach myself. Out of the countless pieces of advice he has given me over the past five years, the one that has stood out the most in my mind was to “have the confidence to take control and ownership of my lab and project.” He gave me this stern directive early on in my research, and years later I am grateful to have developed such confidence and knowledge. I have been extremely lucky to have had Professor Shepherd as my mentor and cannot thank him enough.

I would also like to thank the members of my thesis committee, Professors Guillaume Blanquart, Beverley McKeon, and Guruswami Ravichandran. Because they so kindly agreed to serve on my committee at the last minute, I will be finished in time to walk at Commencement. I am also grateful to Professor Ravichandran and Professor Dale Pullin, who served on my candidacy committee, for their continual guidance and support over the years and as I plan my future.

Over the years I have worked extensively with colleagues at Boeing in Seattle, Washington on the applications of my research to aircraft safety. I would like to acknowledge especially Eddie Kwon, a physicist at Boeing, with whom I spent many long stretches in the lab performing experiments and meeting deadlines. We had a lot of fun trying out wacky experiments on the fly and throwing around scientific ideas, and he became not only a valued colleague but a good friend as well.

I have been lucky to work with the absolute best research group around, the Explosion Dynamics Lab. Not only did we get to “blow stuff up” but we also had a lot of fun doing it. I particularly want to acknowledge former group members Jim Karnesky and Shannon Kao. Jim was the older student in the lab when I joined, and if he had not been there I never would have figured anything out! He was incredibly patient with me, teaching me the ins and outs of working in an experimental lab, and has been a good friend since. Shannon was always my sounding board and was and continues to be a wonderfully supportive friend. In the current group, I must thank Phil Boettcher and Jason Damazo. They have been not only invaluable collaborators in the lab but also really great friends, as evidenced by their willingness to read and edit my very long thesis. We had a lot of fun together and I’ll definitely miss working with them every day. I also must acknowledge Alexandra Katsas, without whom, nothing in our group would get done. I greatly appreciate all her help and her bright smile over the past few years! And thanks to the T5 folks Nick Parziale and Joe Jewell for always giving me a good laugh.

Finally, I want to acknowledge and thank my family. While my parents and two brothers have been all the way on the other side of the country, they have done so much to show me unwavering love and support. They always tell me that they are proud of me no matter what, and knowing that gives me peace and confidence moving forward in my life. I also want to thank my amazing husband, Thomas. He has stood by side from the first day I came to Caltech, and I have never once doubted his support or love. He has the patience of a saint, and the kindest heart.

This work was supported by a National Science Foundation fellowship and by the Boeing Company through a Strategic Research and Development Relationship Agreement CT-BA-GTA-1.

# Abstract

Determining the risk of accidental ignition of flammable mixtures is a topic of tremendous importance in industry and aviation safety. The concept of minimum ignition energy (MIE) has traditionally formed the basis for studying ignition hazards of fuels. However, in recent years, particularly in the aviation safety industry, the viewpoint has changed to one where ignition is statistical in nature. Approaching ignition as statistical rather than a threshold phenomenon appears to be more consistent with the inherent variability in the engineering test data.

Ignition tests were performed in lean hydrogen-based aviation test mixtures and in two hexane-air mixtures using low-energy capacitive spark ignition systems. Tests were carried out using both short, fixed sparks (1 to 2 mm) and variable length sparks up to 10 mm. The results were analyzed using statistical tools to obtain probability distributions for ignition versus spark energy and spark energy density (energy per unit spark length). Results show that a single threshold MIE value does not exist, and that the energy per unit length may be a more appropriate parameter for quantifying the risk of ignition than only the energy. The probability of ignition versus spark charge was also investigated, and the statistical results for the spark charge and spark energy density were compared. It was found that the test results were less variable with respect to the spark charge than the energy density. However, variability was still present due to phenomena such as plasma instabilities and cathode effects that are caused by the electrodynamics.

Work was also done to develop a two-dimensional numerical model of spark ignition that accurately simulates all physical scales of the fluid mechanics and chemistry. In this work a two-dimensional model of spark discharge in air and spark ignition was

developed using the non-reactive and reactive Navier-Stokes equations. One-step chemistry models were used to allow for highly resolved simulations, and methods for calculating effective one-step parameters were developed using constant pressure explosion theory. The one-step model was tuned to accurately simulate the flame speed, temperature, and straining behavior using one-dimensional flame computations. The simulations were performed with three different electrode geometries to investigate the effect of the geometry on the fluid mechanics of the evolving spark kernel and on flame formation. The computational results were compared with high-speed schlieren visualization of spark and ignition kernels. It was found that the electrode geometry had a significant effect on the fluid motion following spark discharge and hence influences the ignition process.

# Contents

<b>Acknowledgments</b>	<b>iii</b>
<b>Abstract</b>	<b>v</b>
<b>Contents</b>	<b>vii</b>
<b>List of Figures</b>	<b>xii</b>
<b>List of Tables</b>	<b>xxii</b>
<b>1 Introduction</b>	<b>1</b>
1.1 Motivation . . . . .	1
1.2 Spark Ignition of Flames . . . . .	4
1.2.1 Spark Breakdown and Flame Formation . . . . .	4
1.2.2 Flame Structure . . . . .	6
1.3 Minimum Ignition Energy . . . . .	10
1.3.1 Analytical Models . . . . .	11
1.3.2 Ignition as a Statistical Phenomenon . . . . .	13
1.3.3 Probability and Historical Spark Ignition Measurements . . . . .	15
1.4 Spark Ignition Modeling and Experimental Investigations . . . . .	16
1.5 Goals of the Investigation . . . . .	17
1.6 Thesis Outline . . . . .	18
<b>2 Experimental Setup</b>	<b>20</b>

2.1	Combustion Vessel . . . . .	20
2.2	Diagnostics . . . . .	21
2.2.1	Pressure and Temperature Measurement . . . . .	21
2.2.2	Schlieren Visualization . . . . .	22
2.3	Low-Energy Capacitive Spark Ignition Systems . . . . .	23
2.3.1	Short, Fixed-Length Spark Ignition System . . . . .	25
2.3.2	Variable-Length Spark Ignition System . . . . .	28
2.4	Spark Energy and Charge . . . . .	32
2.5	Experimental Procedure . . . . .	36
<b>3</b>	<b>Results &amp; Analysis: Short, Fixed-Length Spark Ignition Tests</b>	<b>38</b>
3.1	Flammable Test Mixtures . . . . .	38
3.2	Schlieren Visualization and Pressure Measurement . . . . .	40
3.2.1	5% Hydrogen Mixture . . . . .	40
3.2.2	6% Hydrogen Mixture . . . . .	41
3.2.3	7% Hydrogen Mixture . . . . .	42
3.2.4	Effect of Turbulence . . . . .	42
3.2.5	Implications . . . . .	44
3.3	Statistical Analysis . . . . .	47
3.3.1	Choosing Stimulus Levels: Bruceton Technique and Langlie Method . . . . .	47
3.3.2	Logistic Regression Method . . . . .	48
3.4	Probability of Ignition Versus Spark Energy . . . . .	52
3.4.1	Results for Hydrogen Test Mixtures . . . . .	53
3.4.2	Comparison to Historical MIE Data . . . . .	56
3.4.3	Comparison with Analytical Ignition Energy . . . . .	58
<b>4</b>	<b>Results &amp; Analysis: Variable-Length Spark Ignition Tests</b>	<b>63</b>
4.1	Capacitance Measurement . . . . .	64
4.2	Flammable Test Mixtures . . . . .	64
4.3	Probability Versus Spark Energy Density . . . . .	65

4.3.1	Comparison With Analytical Model . . . . .	71
4.4	Probability Versus Spark Charge . . . . .	74
4.5	Ignition Variability . . . . .	78
<b>5</b>	<b>Numerical Modeling: Spark Discharge in Non-Reactive Gas</b>	<b>87</b>
5.1	Electrode Geometries and Spark Duration . . . . .	88
5.2	Numerical Simulation . . . . .	89
5.2.1	Model Description . . . . .	89
5.2.2	Initial and Boundary Conditions . . . . .	92
5.2.3	Numerical Solution . . . . .	95
5.3	Schlieren Visualization . . . . .	95
5.4	Results: Spark Discharge in Air . . . . .	96
<b>6</b>	<b>One-Step Chemistry Models for Flame and Ignition Simulation</b>	<b>105</b>
6.1	Model Parameters . . . . .	106
6.2	Constant Pressure Explosion Method . . . . .	107
6.2.1	Estimating Effective Reaction Order . . . . .	107
6.2.2	Estimating Effective Activation Energy . . . . .	111
6.3	Constant Pressure Explosion Method with Constant Volume Initial Conditions . . . . .	114
6.4	Constant Volume Explosion Method . . . . .	118
6.5	Development of One-Step Models for Flame Simulation . . . . .	121
6.5.1	1D Flat Flame with One-Step Chemistry . . . . .	121
6.5.2	Implementation of a One-Step Model in the 1D Flame Code . . . . .	125
6.6	Two-Species One-Step Model for Hydrogen-Air Systems . . . . .	127
6.6.1	First-Order Reaction . . . . .	128
6.6.2	Second-Order Reaction . . . . .	133
6.7	Multi-Species One-Step Model: Flame Strain and Extinction . . . . .	139
6.7.1	Strained Flame Calculations . . . . .	139
6.7.2	Two-Species One-Step Model . . . . .	141

6.7.3	Four-Species One-Step Model with Realistic Transport Properties . . . . .	143
<b>7</b>	<b>Numerical Modeling: Spark Ignition</b>	<b>147</b>
7.1	Implementing One-Step Models in AMROC . . . . .	147
7.2	Numerical Model . . . . .	147
7.3	Spark Ignition in Hydrogen . . . . .	151
7.4	Summary of Simulation Results . . . . .	152
<b>8</b>	<b>Conclusion</b>	<b>157</b>
8.1	Summary . . . . .	157
8.2	Future Work . . . . .	162
	<b>Bibliography</b>	<b>164</b>
<b>A</b>	<b>Historical MIE Data and Probability</b>	<b>176</b>
A.1	Introduction . . . . .	176
A.2	Claims and the Historical Record . . . . .	176
A.3	Comparison of Historical and Modern Data . . . . .	180
A.3.1	Probability = 0.01 (1 <sup>st</sup> Percentile) . . . . .	184
A.3.2	Probability = 0.50 (50 <sup>th</sup> Percentile) . . . . .	186
A.3.3	Probability = 0.99 (99 <sup>th</sup> Percentile) . . . . .	187
A.4	Summary . . . . .	188
<b>B</b>	<b>Spark Ignition Test Checklist</b>	<b>190</b>
<b>C</b>	<b>Test Matrix: Spark Ignition Tests in 3 to 13% Hydrogen, Oxygen, Argon Mixtures</b>	<b>193</b>
<b>D</b>	<b>Short, Fixed-Length Spark Ignition Tests: Spark Energies</b>	<b>196</b>
D.1	5% Hydrogen Test Mixture . . . . .	196
D.2	6% Hydrogen Test Mixture . . . . .	199
D.3	7% Hydrogen Test Mixture . . . . .	202

<b>E</b>	<b>Variable-Length Spark Ignition Tests: Spark Energy Densities</b>	<b>205</b>
E.1	6% Hydrogen, 12% Oxygen, 82% Argon Test Mixture . . . . .	205
E.2	Stoichiometric Hexane-Air Test Mixture . . . . .	209
E.3	Rich ( $\phi = 1.72$ ) Hexane-Air Test Mixture . . . . .	211
<b>F</b>	<b>MATLAB Scripts for Performing Statistical Analysis on Ignition</b>	
	Test Data	<b>215</b>
<b>G</b>	<b>Statistical Analysis Results</b>	<b>223</b>
G.1	Short, Fixed-Length Spark Tests: Probability Versus Energy . . . . .	223
G.2	Variable-Length Spark Tests: Probability Versus Energy Density . . . . .	224
G.3	Probability Versus Charge . . . . .	227
<b>H</b>	<b>Constant Pressure Explosion Method MATLAB Code</b>	<b>229</b>
<b>I</b>	<b>Effective Reaction Orders and Activation Energies for Hydrogen-Air</b>	
	Systems	<b>235</b>
<b>J</b>	<b>Sensitivity of Effective Activation Energy to Flamespeed</b>	<b>239</b>
<b>K</b>	<b>Python 1D Adiabatic Flame Code</b>	<b>242</b>
<b>L</b>	<b>One-Step Model Parameters for Hydrogen-Air Systems</b>	<b>246</b>
<b>M</b>	<b>Cantera Python Code <i>STFLAME1.py</i> for Simulating a Flat Flame</b>	
	in a Strained Flow Field	<b>249</b>
<b>N</b>	<b>Second-Order One-Step Model Cantera Input (.cti) File</b>	<b>254</b>
<b>O</b>	<b>Four-Species One-Step Model Cantera Input (.cti) File</b>	<b>257</b>

# List of Figures

1.1	(a) Schlieren image of a deflagration wave propagating in a 10% hydrogen, 11.37% oxygen, 78.63% argon mixture in a closed vessel and (b) the pressure trace from the deflagration. The peak pressure in the vessel is 551 kPa. . . . .	2
1.2	(a) Schlieren image of a detonation wave propagating in a $2\text{H}_2 + \text{O}_2 + 17 \text{ Ar}$ mixture with $p_0 = 20 \text{ kPa}$ (Akbar, 1997) and (b) the pressure trace from a detonation in stoichiometric ethylene-oxygen with $p_0 = 50 \text{ kPa}$ . The peak pressure after the detonation is 1.78 MPa (1780 kPa). . . . .	2
1.3	Schematics of the spark breakdown process. (a) A circuit is connected to two conductors a distance apart and the voltage difference across the gap is increased; (b) the breakdown voltage is reached, causing the gap to ionize through the “electron avalanche”; (c) a high-temperature, high-pressure, electrically conductive plasma channel forms across the gap. . . . .	5
1.4	Schematics of the flame formation process. (a) A blast wave is emitted due to the high temperature, high pressure spark channel; (b) the hot gas kernel expands rapidly following the blast wave and fluid is entrained along the electrodes; (c) chemical reactions produce heat inside the gas kernel and diffusion of heat and species occurs at the boundary; (d) if the proper conditions exist, a self-sustaining flame forms after approximately 10 to 100 $\mu\text{s}$ . . . . .	7
1.5	A schematic showing the profiles of temperature and species across a flame front in a flame-fixed frame . . . . .	9

2.1	A schematic of the constant volume combustion vessel used for the spark ignition testing . . . . .	21
2.2	Large field-of-view (a) and small field-of-view (b) schlieren systems used for spark and flame visualization . . . . .	24
2.3	Timing diagram illustrating the triggering of the oscilloscope and the opening of the high-voltage relay after the spark discharge . . . . .	27
2.4	Schematic of the short, fixed-length, low-energy spark ignition system .	28
2.5	Photograph of the short, fixed-length, low-energy spark ignition system	29
2.6	(a) Front and (b) back views of the spark gap fixture . . . . .	29
2.7	The short, low-energy spark ignition system mounted on the combustion vessel . . . . .	30
2.8	Schematic of the isolated conductor phenomenon in aircraft fuel tanks	31
2.9	Schematic of the variable-length spark ignition system . . . . .	32
2.10	Front (a) and back (b) views of the spark gap fixture . . . . .	33
2.11	(a) Current waveform from an example spark and (b) spark charge versus time obtained by numerically integrating the current waveform . . . . .	36
3.1	Schlieren images from high-speed visualization of ignition in the 5% hydrogen test mixture recommended by the ARP standards ( <a href="#">International, 2005</a> ) . . . . .	41
3.2	Pressure versus time during combustion of the three hydrogen test mixtures . . . . .	41
3.3	Schlieren images from high-speed visualization of ignition in the 6% hydrogen test mixture . . . . .	42
3.4	Schlieren images from high-speed visualization of ignition in the 7% hydrogen test mixture . . . . .	43
3.5	Normalized pressure traces for ignition in the 6% hydrogen mixture with little initial gas motion (solid line) and with a higher degree of initial motion (dashed line) . . . . .	44

3.6	Schlieren images of combustion in the 6% hydrogen mixture with (a) little initial gas motion and (b) with a higher degree of initial gas motion induced by a fan mixer . . . . .	45
3.7	Normalized peak pressure versus hydrogen concentration near the lower flammability limit . . . . .	46
3.8	Jet A spark ignition data (Lee and Shepherd, 1999) shown as (a) a plot of 25 tests versus spark energy and (b) as tabulated results in binary form	51
3.9	Logistic probability distribution and 95% confidence envelope for the Jet A spark ignition data . . . . .	52
3.10	Results for ignition of the 5% ARP-recommended test mixture: (a) ignition test data points with data overlap region and (b) probability distribution and 95% confidence intervals . . . . .	54
3.11	Data points and resulting probability distribution and 95% confidence intervals for the 6% hydrogen test mixture . . . . .	55
3.12	Data points and resulting probability distribution and 95% confidence intervals for the 7% hydrogen test mixture . . . . .	56
3.13	Probability distributions of ignition versus spark energy for the three hydrogen test mixtures . . . . .	57
3.14	Illustration of the percentiles used to calculate the relative width of the probability distribution . . . . .	58
4.1	Probability distribution of ignition versus spark energy density (energy per unit spark length) for the 6% H <sub>2</sub> mixture. The 50th percentile ignition energy density for the fixed-length spark tests, obtained by dividing the energy by 1.5 mm, is indicated by the dashed line. . . . .	66
4.2	Schlieren images from two spark tests in the 6% test mixture; (a) a spark with a higher energy where no ignition occurs and (b) a spark with lower energy but larger energy density so ignition does occur . . . . .	67
4.3	Probability distributions for ignition versus spark energy for the 6% H <sub>2</sub> test mixture with the 50th percentiles indicated by the red lines . . . . .	68

4.4	Data points and probability distributions for ignition versus spark energy density for the rich hexane-air ( $\phi = 1.72$ ) test mixture . . . . .	69
4.5	Data points and probability distributions for ignition versus spark energy density for the stoichiometric hexane-air ( $\phi = 1$ ) test mixture . . . . .	69
4.6	Comparison of the probability distributions for the 6% hydrogen mixtures and two hexane-air mixtures . . . . .	71
4.7	Approximate minimum spark charge (a) and spark energy (b) required for ignition versus spark gap length for the 6% H <sub>2</sub> test mixture and the two hexane-air test mixtures . . . . .	77
4.8	Statistical analysis of the ignition test results for the 6% H <sub>2</sub> -12% O <sub>2</sub> -82% Ar mixture. (a) Probability of ignition versus spark energy density; (b) probability of ignition versus spark charge; (c) probability versus normalized energy density and normalized charge shown on the same axis . . . . .	79
4.9	Statistical analysis of the ignition test results for the rich ( $\phi=1.72$ ) hexane-air mixture. (a) Probability of ignition versus spark energy density; (b) probability of ignition versus spark charge; (c) probability versus normalized energy density and normalized charge shown on the same axis . . . . .	80
4.10	Statistical analysis of the ignition test results for the stoichiometric ( $\phi=1$ ) hexane-air mixture. (a) Probability of ignition versus spark energy density; (b) probability of ignition versus spark charge; (c) probability versus normalized energy density and normalized charge shown on the same axis . . . . .	81
4.11	Comparison of the probability distributions for ignition versus normalized energy and charge for the short, fixed spark tests in the three hydrogen-based test mixtures. (a) 5% H <sub>2</sub> ; (b) 6% H <sub>2</sub> ; (c) 7% H <sub>2</sub> . . . . .	82
4.12	Comparison of the probability distributions for ignition versus spark charge for the short and variable-length spark ignition tests . . . . .	83
4.13	Schlieren images from high-speed video of localized ignition in the 6% hydrogen test mixture . . . . .	84

4.14	Schlieren images from high-speed video of localized ignition in the rich ( $\phi = 1.72$ ) hexane-air mixture . . . . .	85
4.15	Magnified schlieren images of a spark channel in the 6% hydrogen mixtures with multiple plasma instabilities and flame kernels . . . . .	85
4.16	Three consecutive sparks in air with the same gap length, breakdown voltage, energy, and charge . . . . .	86
5.1	Three electrode configurations used in the experiments and numerical simulations: (a) wire electrode; (b) conical electrode; and (c) flanged electrode . . . . .	90
5.2	Fits of the temperature dependence of (a) the thermal conductivity and (b) the viscosity to Cantera calculations . . . . .	92
5.3	Computational domain and boundary conditions for the numerical simulation . . . . .	94
5.4	Initial pressure field for the spark discharge and ignition simulations . . . . .	94
5.5	Spark discharge in air using wire electrodes: (a) images from high-speed schlieren visualization and (b) density fields from the simulation. The simulation region corresponds to the quadrant outlined in white on the upper left schlieren image . . . . .	98
5.6	Simulated pressure field and velocity vectors showing the cylindrical and spherical portions of the blast wave at time $t = 0.5 \mu s$ . . . . .	99
5.7	Simulation results (vorticity and velocity vectors) showing the vortex pair generated near the tip of the cylindrical electrode at time $t = 10 \mu s$ . . . . .	99
5.8	Simulation results of the temperature showing the hot gas trapped by the vortex . . . . .	100
5.9	Spark discharge in air using conical electrodes: (a) images from high-speed schlieren visualization and (b) density fields from the simulation. The simulation region corresponds to the quadrant outlined in white on the upper left schlieren image. . . . .	101

5.10	Spark discharge in air using flanged electrodes: (a) images from high-speed schlieren visualization and (b) density fields from the simulation. The simulation region corresponds to the quadrant outlined in white on the upper left schlieren image. . . . .	103
5.11	Simulation results (vorticity field) showing the vortex pair generated at the surface of the flanged electrode at time $t = 10 \mu s$ . . . . .	104
6.1	Effective reaction orders for H <sub>2</sub> -air mixtures calculated using the constant pressure explosion method (Equation 6.18) using 5 different density intervals . . . . .	112
6.2	Effective reaction orders for H <sub>2</sub> -air mixtures calculated using the constant pressure explosion method (Equation 6.18) with $\rho' = 0.10\rho_0$ . . .	112
6.3	(a) Effective activation energies and (b) corresponding Zeldovich numbers calculated using the constant pressure explosion method (Equation 6.23) with reaction orders obtained from the constant pressure explosion method (Equation 6.18) . . . . .	115
6.4	(a) Effective activation energies and (b) corresponding Zeldovich numbers calculated using the constant pressure explosion method with reaction order dependence (Equation 6.23) and using the constant pressure explosion method with constant volume initial conditions (Equation 6.28)	117
6.5	(a) Effective activation energies and (b) corresponding Zeldovich numbers calculated using the three different methods: the constant pressure explosion method with reaction order dependence (Equation 6.23), the constant pressure explosion method with constant volume initial conditions (Equation 6.28), and the constant volume explosion method (Equation 6.34) . . . . .	120

6.6	Problem domain for 1D flat flame calculation, with an example temperature profile shown. The flame is discretized into $N$ grid points (at varying intervals), and the flame equations are solved for $T$ , $u$ , and $Y_i$ at each grid point. The temperature is fixed at one interior grid point as part of the solution algorithm. . . . .	122
6.7	Profiles of the velocity and density (a) and temperature (b) through the flame generated using both the one-step model and full chemistry for stoichiometric hydrogen-air . . . . .	128
6.8	(a) Laminar flame speeds and (b) flame temperatures calculated using first-order one-step models and the Li et al. mechanism (Li et al., 2004) for hydrogen-air compositions . . . . .	130
6.9	Flame speed response to small changes in initial (a) temperature and (b) pressure and flame temperature response to initial (c) temperature and (d) pressure calculated using first-order one-step models and detailed chemistry (Li et al., 2004) for 30% hydrogen-air . . . . .	131
6.10	Flame speed response to large changes in initial (a) temperature and (b) pressure and flame temperature response to initial (c) temperature and (d) pressure calculated using first-order one-step models and detailed chemistry (Li et al., 2004) for 30% hydrogen-air . . . . .	134
6.11	(a) Laminar flame speeds and (b) flame temperatures calculated using second-order one-step models and the Li et al. mechanism (Li et al., 2004) for hydrogen-air compositions . . . . .	135
6.12	Flame speed response to small changes in initial (a) temperature and (b) pressure and flame temperature response to initial (c) temperature and (d) pressure calculated using second-order one-step models and detailed chemistry (Li et al., 2004) for 30% hydrogen-air . . . . .	136
6.13	Flame speed response to large changes in initial (a) temperature and (b) pressure and flame temperature response to initial (c) temperature and (d) pressure calculated using second-order one-step models and detailed chemistry (Li et al., 2004) for 30% hydrogen-air . . . . .	137

6.14	Flame speed response to changes in initial pressure calculated using detailed chemistry (Li et al., 2004), a first-order one-step model, and a second-order one-step model for 30% hydrogen-air. Also shown (red dashed line) is the predicted one-step model flame speed with effective reaction order $n = 1.8$ obtained from the constant pressure explosion model (Equation 6.18). . . . .	139
6.15	Schematic of axisymmetric stagnation point flow used to study flame strain in the Cantera script <i>STFLAME1.py</i> . . . . .	140
6.16	(a) Flow velocity and (b) temperature between the burner and the surface, calculated by the Cantera code. The flame location is indicated by the increase in velocity and temperature. . . . .	141
6.17	Derivative of the flow velocity along the $z$ -axis, with the strain rate indicated . . . . .	141
6.18	Maximum temperature versus strain rate near extinction for a 15% hydrogen-air mixture calculated using detailed chemistry and a second-order one-step model . . . . .	143
6.19	Maximum temperature versus strain rate near extinction for a 15% hydrogen-air mixture using detailed chemistry, the 2-species one-step model with $Le = 1.14$ , and the four-species one-step model with $Le = 0.42$ . . . . .	145
6.20	Comparison of the flame profiles for (a) flow speed and density and (b) temperature calculated using the four-species one-step model and detailed chemistry . . . . .	146
7.1	One-dimensional flame profiles from Cantera and AMROC simulations for a 15% hydrogen-air mixture: (a) velocity, (b) temperature, and (c) density . . . . .	148
7.2	Mass diffusivity versus temperature from Cantera and using an empirical relation (Equation 7.10) . . . . .	150

7.3	Ignition of a 15% hydrogen-air mixture using wire electrodes: (a) images from high-speed schlieren visualization and (b) simulations of the reaction product ( $\text{H}_2\text{O}$ ). The simulation region corresponds to the quadrant outlined in white on the upper left schlieren image. . . . .	152
7.4	Ignition of a 15% hydrogen-air mixture using conical electrodes: (a) images from high-speed schlieren visualization and (b) simulations of the reaction product ( $\text{H}_2\text{O}$ ). The simulation region corresponds to the quadrant outlined in white on the upper left schlieren image. . . . .	153
7.5	Ignition of a 15% hydrogen-air mixture using flanged electrodes: (a) images from high-speed schlieren visualization and (b) simulations of the reaction product ( $\text{H}_2\text{O}$ ). The simulation region corresponds to the quadrant outlined in white on the upper left schlieren image. . . . .	154
7.6	Images from the ignition simulation with flanged electrodes at later times: (a) vorticity field showing the formation of the vortex pair and (b) product ( $\text{H}_2\text{O}$ ) showing ingestion of gas back towards the spark gap	155
8.1	New heated, stainless steel combustion vessel for jet fuel ignition tests .	163
A.1	Spark ignition test results for a mixture with 7% $\text{H}_2$ , $\text{Ar}/(\text{Ar} + \text{O}_2) = 0.226$ . . . . .	181
A.2	Probability distribution for ignition versus spark energy obtained using the data in Figure A.1 for a 7% $\text{H}_2$ , 21% $\text{O}_2$ , 72% $\text{Ar}$ mixture. The $p = 0.01$ point and corresponding 95% confidence interval is shown, as well as the MIE result obtained by Lewis and von Elbe (Lewis and von Elbe, 1951). . . . .	182
A.3	Illustration of using normal distributions at the 1 <sup>st</sup> , 50 <sup>th</sup> , and 99 <sup>th</sup> percentiles to test hypotheses for the mean energy . . . . .	188
J.1	(a) Flamespeed versus small changes in initial temperature calculated using full chemistry and one-step models with two different activation energies and (b) the slopes of the flame speed curves . . . . .	241

J.2 (a) Flamespeed versus small changes in initial pressure calculated using full chemistry and one-step models with two different activation energies and (b) the slopes of the flame speed curves . . . . . 241

# List of Tables

3.1	Comparison of the results of the statistical analysis of the spark ignition tests in lean hydrogen mixtures with historical MIE data by Lewis and von Elbe (Lewis and von Elbe, 1961) . . . . .	58
3.2	Thermodynamic properties of the three hydrogen test mixtures calculated using Cantera software (Goodwin, 2005) . . . . .	59
3.3	Flame speeds and ignition energies calculated using simple theory compared with experimental results . . . . .	60
3.4	Flame speeds and ignition energies calculated using the analytical model for a cylindrical kernel compared with experimental results . . . . .	62
4.1	Comparison of the 10 <sup>th</sup> , 50 <sup>th</sup> , and 90 <sup>th</sup> percentile spark energy densities for the three test mixtures . . . . .	71
4.2	Thermodynamic properties of the two hexane test mixtures calculated using Cantera software (Goodwin, 2005) and the JetSurF 1.0 chemical mechanism (Sirjean et al.) . . . . .	72
4.3	Thermal diffusivities of the hexane-air mixtures at the unburned temperature ( $T_u = 300$ K) and at the average temperature $(T_b + T_u)/2$ . . . . .	74
4.4	Comparison of the ignition energy per length for the hexane-air mixtures calculated using the analytical cylindrical kernel model (Equation 4.5) and the results from the statistical analysis of the experiments. The laminar burning velocities $s_L$ are by Davis and Law (1998). . . . .	74
6.1	Comparison of parameters in the Lewis number for two one-step models and the detailed chemistry . . . . .	144

A.1	Probabilities for binomial trials with $p_0 = 0.01$ . . . . .	183
C.1	Test matrix of spark ignition tests performed in mixtures with 3 to 12% hydrogen in oxygen and argon . . . . .	194
D.1	Spark energy data for the short, fixed-length spark ignition tests in the 5% hydrogen test mixture . . . . .	197
D.2	Spark energy data for the short, fixed-length spark ignition tests in the 6% hydrogen test mixture . . . . .	199
D.3	Spark energy data for the short, fixed-length spark ignition tests in the 7% hydrogen test mixture . . . . .	202
E.1	Spark length and energy data for the variable-length spark ignition tests in the 6% hydrogen test mixture . . . . .	206
E.2	Spark length and energy data for the variable-length spark ignition tests in the stoichiometric (2.16% C <sub>6</sub> H <sub>14</sub> ) hexane-air mixture . . . . .	209
E.3	Spark length and energy data for the variable-length spark ignition tests in the rich (3.67% C <sub>6</sub> H <sub>14</sub> ) hexane-air mixture with $\phi = 1.72$ . . . . .	211
G.1	Percentiles and 95% upper confidence limit (UCL) and lower confidence limit (LCL) for the short, fixed-length spark ignition tests . . . . .	223
G.2	Logistic probability distribution parameters $\beta_0$ and $\beta_1$ for the short, fixed-length spark ignition tests . . . . .	224
G.3	Percentiles and 95% upper confidence limit (UCL) and lower confidence limit (LCL) for the variable-length spark ignition tests . . . . .	225
G.4	Logistic probability distribution parameters $\beta_0$ and $\beta_1$ for the variable-length spark ignition tests . . . . .	226
G.5	Spark charge percentiles and 95% upper confidence limit (UCL) and lower confidence limit (LCL) for the short, fixed-length spark ignition tests . . . . .	227
G.6	Spark charge percentiles and 95% upper confidence limit (UCL) and lower confidence limit (LCL) for the variable-length spark ignition tests . . . . .	228

I.1	Effective reaction orders and activation energies calculated using the constant pressure explosion method with reaction order dependence (Equations 6.18 and 6.23) . . . . .	236
I.2	Effective activation energies calculated using the constant pressure explosion method with constant volume initial conditions (Equation 6.28)	237
I.3	Effective activation energies calculated using the constant volume explosion method (Equation 6.34) . . . . .	238
L.1	First-order ( $n = 1$ ) one-step model parameters for hydrogen-air systems	247
L.2	Second-order ( $n = 2$ ) one-step model parameters for hydrogen-air systems	248

# Chapter 1

## Introduction

### 1.1 Motivation

Determining the risks posed by combustion hazards is a topic of tremendous importance in industry and aviation. There are three main categories of combustion hazards: fires, deflagrations, and detonations. Fire generally refers to the burning of pools of liquid or of solids. A deflagration, commonly called a flame, is a subsonic combustion wave in a gaseous mixtures of fuel and air. Deflagrations propagate at speeds on the order of 0.01 to 100 m/s with a large temperature rise (1000 to 3000 K) across the flame front at approximately constant pressure. A detonation is another type of combustion wave, but it propagates at supersonic speeds of 1000 to 3000 m/s. The temperature and pressure increase sharply across the detonation front by 2000 to 3000 K and up to 5 MPa, respectively. Images and pressure traces for an example deflagration and detonation are given in Figures 1.1 and 1.2. Deflagrations and detonations are generically referred to as explosions. These explosion hazards exist in any application where flammable material is either handled or generated, for example in power plants and on aircraft. Detonations cause a very large, very fast increase in pressure as the wave passes by. If a deflagration is contained, it too leads to a large pressure rise on the order of 5 to 10 times the initial pressure. Additionally, a deflagration can transition to a detonation through interaction with boundaries or obstacles. Therefore, explosion hazards can cause structural failure and pose a threat to human safety.

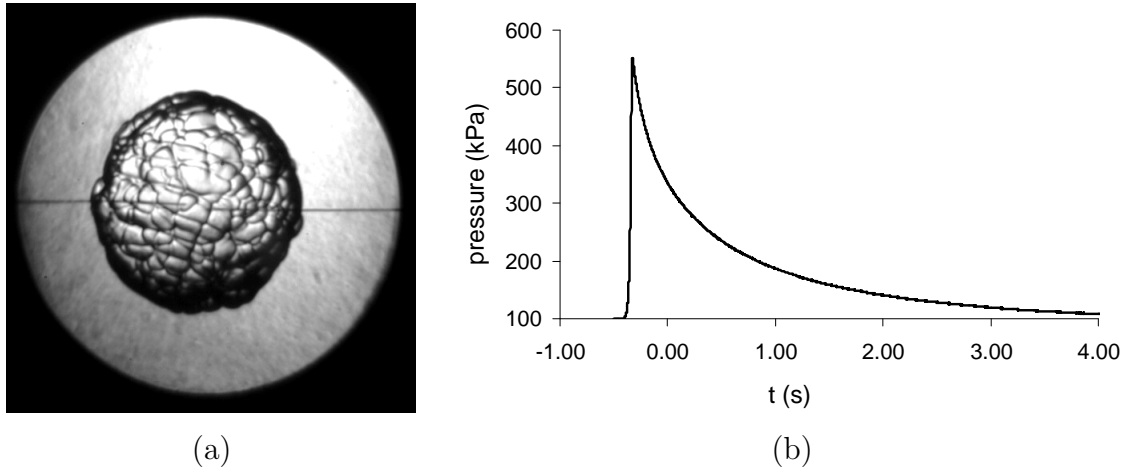


Figure 1.1: (a) Schlieren image of a deflagration wave propagating in a 10% hydrogen, 11.37% oxygen, 78.63% argon mixture in a closed vessel and (b) the pressure trace from the deflagration. The peak pressure in the vessel is 551 kPa.

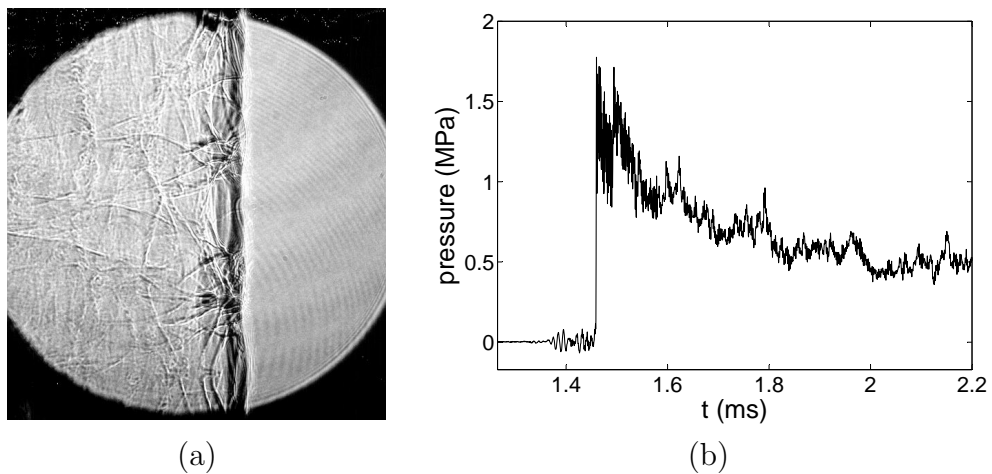


Figure 1.2: (a) Schlieren image of a detonation wave propagating in a  $2\text{H}_2 + \text{O}_2 + 17 \text{ Ar}$  mixture with  $p_0 = 20 \text{ kPa}$  (Akbar, 1997) and (b) the pressure trace from a detonation in stoichiometric ethylene-oxygen with  $p_0 = 50 \text{ kPa}$ . The peak pressure after the detonation is 1.78 MPa (1780 kPa).

To mitigate the risk of an accidental explosion certain knowledge about the particular conditions is required. First, the fuel of concern and the actual fuel-oxidizer mixture must be known to determine if the mixture is within the flammability limits. Secondly, the potential ignition sources must be identified, and some understanding of the physics of how and why the source causes ignition is needed. Finally, an ap-

appropriate method of quantifying the risk for the given conditions must be developed. Given all this knowledge, design criteria and rules and regulations can be determined to mitigate risks of accidental explosions.

In this work, the focus has been on explosion hazards on aircraft. In the aircraft fuel tank and flammable leakage zones, some of the liquid jet fuel will evaporate and mix with the air. Under certain conditions, if there is sufficient fuel vapor mixed with the air there will be flammable conditions in the fuel tank, as discussed by Shepherd, Nuyt, and Lee at Caltech (Shepherd et al., 2000). Shepherd and coauthors were performing a study as part of the investigation into the crash of flight TWA 800 and as part of their investigation it was noted that:

It is important to note that the combination of evaporation due to heating and the reduction in air pressure with increasing altitude created a flammable condition within the CWT [center wing tank]. The finding that the fuel-vapor air mixture within the CWT was flammable at 14 kft should not be considered surprising in view of previous work (Nestor, 1967, Ott, 1970) on Jet A flammability. Flammability of fuel-tank ullage contents, particularly at high altitudes or with low flashpoint fuels, has long been considered unavoidable (Boeing et al., 1997). Experiments (Kosvic et al., 1971, Roth, 1987) and simulations (Seibold, 1987, Ural et al., 1989, Fornia, 1997) indicate that commercial transport aircraft spend some portion of the flight envelope with the ullage in a flammable condition.

There are many potential ignition sources on aircraft that must be considered when designing safety criteria. There are electric sources: voltage arcs, capacitive sparks, loose wires, brush discharge, and other electrostatic sources. Other possible sources of ignition are hot surfaces on equipment, sparks from composites, and hot particle ejection from fasteners and metallic joints. Testing standards for certifying aircraft against accidental explosions have been developed by the SAE (International, 2005) and FAA (Administration, 1994). In these ignition tests described by these standards, a simple capacitive spark is used for the ignition source. However, these standards

rely on test methods and spark ignition data from the 1950s and were written with only limited understanding of the physics of the spark ignition process. In this work, the ignition of explosions (deflagrations) by electrostatic sparks is studied and the results are related to the issues surrounding aviation safety.

## 1.2 Spark Ignition of Flames

### 1.2.1 Spark Breakdown and Flame Formation

The schematics in Figure 1.3 give a simple overview of the spark breakdown process. Figure 1.3(a) shows an electrical circuit, in this case a capacitor that is charged by a high voltage power supply through a resistor. The circuit is connected in parallel with a pair of conductors some distance apart within a flammable gas mixture. If the voltage difference across the gap between the conductors is continually increased, electrons are released from the anode and eventually the breakdown voltage of the gas will be reached. At the breakdown voltage, the electric field is sufficiently strong to accelerate the electrons fast enough to ionize the entire gap through collisions (see Figure 1.3(b)). The ionization of the gap is a highly unstable process commonly referred to as the “electron avalanche”. After the breakdown, the gap between the conductors is now bridged by a plasma channel, as shown in Figure 1.3(c). The channel is extremely thin, on the order of 10 to 100  $\mu\text{m}$  in radius, and can be up to 50,000 K and 10 MPa in temperature and pressure. The plasma is also highly electrically conductive, and so the impedance of the gap drops and the current rises sharply, causing stored electrical energy in the circuit to discharge across the channel as a spark. The spark breakdown and plasma formation process occurs in an extremely short amount of time on the order of 10 to 100 ns.

The initial conditions created by the spark channel are similar to those in the cylindrical shock tube problem, and so a blast wave is emitted following the spark discharge as shown in Figure 1.4(a). The shock wave travels outward and decays quickly; following the wave the gas kernel initially expands rapidly (Figure 1.4(b)).

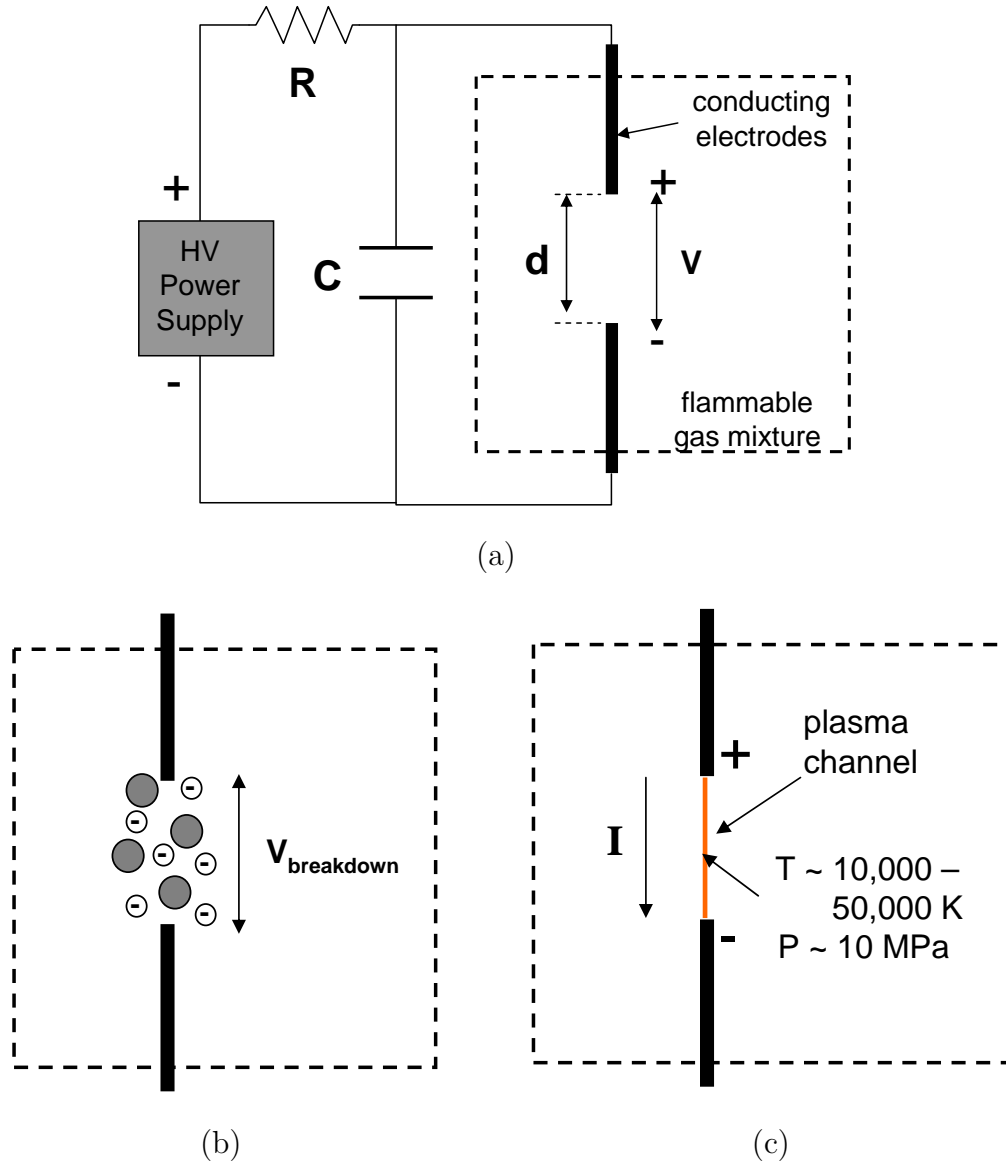


Figure 1.3: Schematics of the spark breakdown process. (a) A circuit is connected to two conductors a distance apart and the voltage difference across the gap is increased; (b) the breakdown voltage is reached, causing the gap to ionize through the “electron avalanche”; (c) a high-temperature, high-pressure, electrically conductive plasma channel forms across the gap.

After a few microseconds, chemical reactions begin inside the kernel and generate heat. The kernel continues to expand and cold unreacted gas is entrained along the electrodes. Diffusion of both heat and mass occurs at the boundary between the hot kernel and the cold outer gas (Figure 1.4(c)). After a period of time on the order of 10 to 100  $\mu\text{s}$ , if the proper conditions exist, a self-propagating flame front will form. In Figure 1.4(d) the flame front is shown on the surface of the kernel, but the details of exactly how and where the flame front forms are not completely understood. The process of flame formation is a complicated problem involving chemistry, fluid mechanics, and transport effects.

## 1.2.2 Flame Structure

The expanding flame induces radial flow in the cold surrounding gas because the burned gas has a higher specific volume, and the flame “rides” on top of this flow. Therefore, the flame propagation speed is the sum of radial flow velocity and the laminar burning velocity,  $s_L$ . The laminar burning velocity is a property of a given flammable mixture and is dependent on the initial conditions. Laminar burning velocities are typically on the order of 1–100 cm/s for hydrocarbon fuels under atmospheric conditions, but can be more than 1 m/s for some hydrogen mixtures. The flame velocity,

$$V_F = u_r + s_L \quad (1.1)$$

can also be written as proportional to the laminar burning velocity,

$$V_F = \epsilon s_L \quad (1.2)$$

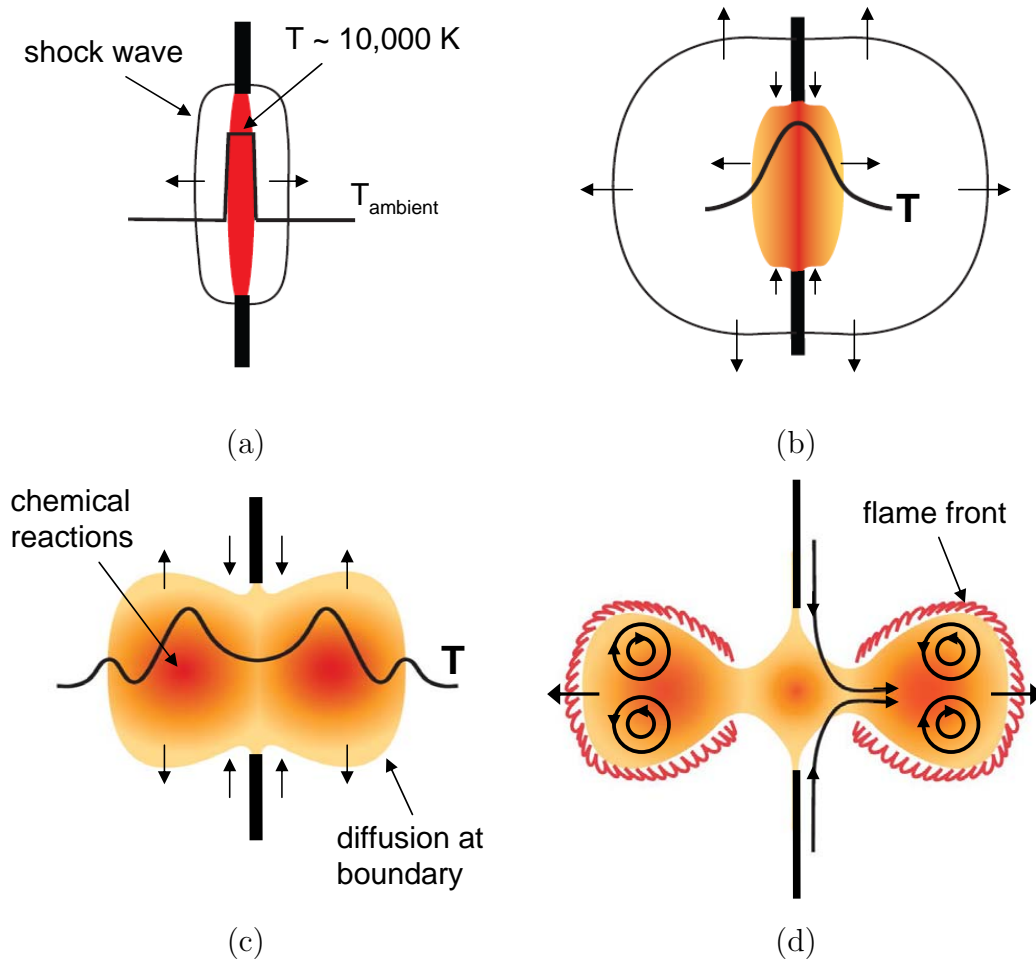


Figure 1.4: Schematics of the flame formation process. (a) A blast wave is emitted due to the high temperature, high pressure spark channel; (b) the hot gas kernel expands rapidly following the blast wave and fluid is entrained along the electrodes; (c) chemical reactions produce heat inside the gas kernel and diffusion of heat and species occurs at the boundary; (d) if the proper conditions exist, a self-sustaining flame forms after approximately 10 to 100  $\mu\text{s}$ .

where  $\epsilon$  is the *expansion ratio* and is equal to the ratio of the density of the unburned gas to the density of the burned gas, i.e.,

$$\epsilon = \frac{\rho_b}{\rho_u} . \quad (1.3)$$

The structure of a one-dimensional flame front in a flame-fixed reference frame is shown in Figure 1.5. Across the flame front, the temperature increases from the unburned temperature  $T_u$  to the burned temperature, or adiabatic flame temperature,  $T_b$ . The flow enters the flame front with a velocity equal to the laminar burning velocity, and as it expands across the flame, the flow is accelerated to the speed  $V_F$ . The mass of the products increases across the flame front as the reactants are consumed, and intermediate species are produced by the chemical reactions.

The flame structure is governed by the steady one-dimensional energy equation including mass diffusion and chemical reactions:

$$\dot{m}c_p \frac{\partial T}{\partial z} = \frac{\partial}{\partial z} \left( \kappa \frac{\partial T}{\partial z} \right) - \sum_{i=1}^N c_{pi} j_{i,z} \frac{\partial T}{\partial z} - \sum_{i=1}^N h_i \dot{\omega}_i W_i \quad (1.4)$$

where  $z$  is the distance through the flame. The diffusive flux of species  $i$ ,  $j_i$ , is often modelled using Fick's Law,

$$j_i = -D_i \frac{\partial Y_i}{\partial z} \quad (1.5)$$

and  $\dot{\omega}_i$  is the molar production rate per unit volume of species  $i$  due to chemical reaction. The thickness of the flame front is on the order of a millimeter and can be divided into three main regions as shown in Figure 1.5. Just upstream of the flame, cold reactants are flowing in at the laminar burning velocity and heat is diffusing out into the cold gas through conduction. In this region, there is minimal chemical reaction and therefore the gradients of the species mass fractions and hence the diffusive flux are negligible. This region is called the *preheat zone* and is characterized by a

balance between convection of cold reactants in and heat conduction out, i.e.,

$$\dot{m} \frac{\partial T}{\partial z} \approx \frac{\partial}{\partial z} \left( \kappa \frac{\partial T}{\partial z} \right). \quad (1.6)$$

Following the preheat zone the flowing reactants enter the *main reaction zone*, where the majority of the chemical reactions take place. The curvature of the temperature profile is large in this zone, and therefore, in this region the energy release by the chemical reactions is balanced by energy loss by diffusion, i.e.,

$$-\kappa \frac{\partial^2 T}{\partial x^2} \approx \sum h_i \dot{\omega}_i W_i. \quad (1.7)$$

Finally, downstream of the flame is the equilibrium zone, where there is no chemical reaction and no gradients in the temperature or species. These balances among convection, diffusion, and chemical reactions must be achieved for a self-propagating flame front to exist.

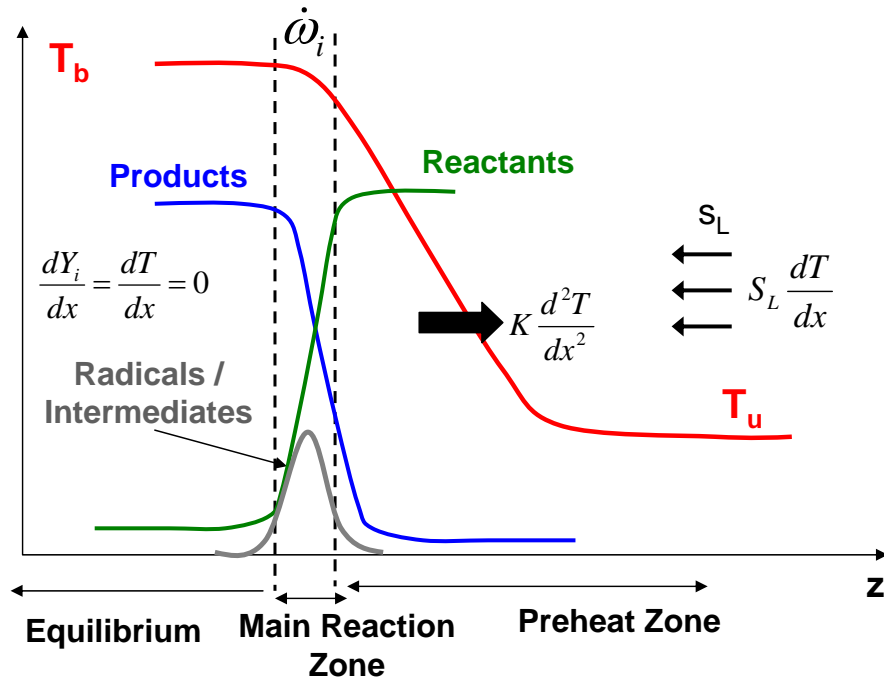


Figure 1.5: A schematic showing the profiles of temperature and species across a flame front in a flame-fixed frame

### 1.3 Minimum Ignition Energy

Determining the risk of accidental ignition of flammable mixtures is a topic of tremendous importance in industry and in aviation safety. Extensive work has been done (Coward and Jones, 1952, Britton, 2002, Babrauskas, 2003) to determine the flammability limits of various mixtures in terms of mixture composition. These studies were all performed using a very high energy ignition source that was assumed strong enough to ignite any mixture with a composition inside the flammability limits. The results of these tests defined ranges of compositions for various fuels where, if a very strong ignition source is present, the mixture will ignite. However, for mixtures with compositions within the flammability limits, there also exists a limiting strength of the ignition source. If an ignition source is not strong enough, or is below the minimum ignition energy (MIE) of the particular mixture, the mixture will not ignite. Just as for flammability limits in terms of mixture composition, there have also been extensive studies to determine the minimum ignition energies of many different flammable mixtures.

In combustion science, the concept of a minimum ignition energy (MIE) has traditionally formed the basis for studying ignition hazards of fuels. The viewpoint is that fuels have specific ignition energy thresholds corresponding to the MIE, and ignition sources with energy below this threshold value will never be able to ignite the fuel. Standard test methods for determining the MIE have been developed (Babrauskas, 2003, Magison, 1990) which use a capacitive spark discharge for the ignition source. The MIE is determined from energy stored in a capacitor at a known voltage that is then discharged through a specified gap. The pioneering work using this ignition method to determine MIE was done at the Bureau of Mines in the 1940s by Guest, Blanc, Lewis, and von Elbe (Lewis and von Elbe, 1961). They obtained MIE data for many different fuels and mixture compositions, and this data is still extensively cited in the literature and ignition handbooks (Babrauskas, 2003, Magison, 1990). This technique is also used to study ignition hazards in the aviation industry and standardized testing is outlined to determine the MIE of aviation test fuels (Intern-

tional, 2005, Administration, 1994). Following the work at the Bureau of Mines, other authors have performed MIE tests with methods similar to those used by Lewis and von Elbe (Calcote et al., 1952, Metzler, 1952a,b, Moorhouse et al., 1974) and found comparable results. Other authors have proposed improvements on the technique for determining MIE using capacitive spark discharge, most recently Ono et al. (Ono et al., 2005, 2007) and Randeberg et al. (Randeberg et al., 2006).

### 1.3.1 Analytical Models

Since the 1950s, several authors have attempted to develop analytic models to predict the minimum ignition energy. Lewis and von Elbe (Lewis and von Elbe, 1961) proposed an empirical relationship for the required ignition energy,

$$E_{ign} \approx \frac{\kappa_u q}{(c_P/m) s_L} = \frac{\kappa_u}{s_L} (T_b - T_u) \quad (1.8)$$

where  $\kappa_u$  is the thermal conductivity of the unburned gas,  $q$  is the heat of reaction at constant pressure,  $c_P$  is the specific heat,  $m$  is the mass, and  $T_u$  and  $T_b$  are the temperatures of the unburned and burned gas, respectively. This relation was also discussed in Strehlow (1979) and derived from unsteady conservation equations in Rosen (1959). The basis for the model was the idea that combustion waves have excess enthalpy that maintains the balance between the heat flow into the preheat zone by conduction and the heat release in the reaction zone. This excess enthalpy is required for the flame to grow spherically until it reaches a planar state. It was postulated that the excess enthalpy is usually provided by the burned gas, but when the diameter of the flame ball is less than the minimum diameter required for propagation, there is not enough excess enthalpy being generated by chemical reactions. In this case, the temperature in the core would drop, reactions would stop, and the flame would be extinguished. Therefore, Lewis and von Elbe concluded that for the flame to grow to the minimum size, the required excess enthalpy must be provided by an ignition source. Hence, the minimum ignition energy would be equal to the excess enthalpy of the minimum diameter flame.

A second analytical model for the ignition energy is discussed in combustion textbooks by Williams (1985), Glassman (1996), and Turns (2000). In this model the flame is considered to be a spherical volume of gas ignited by a point spark, and a critical radius is defined under which the spherical wave cannot propagate. To determine the critical radius,  $r_{crit}$ , it is assumed that there is a balance between the heat generated by chemical reactions inside the gas volume and the heat lost to the surrounding cold gas through conduction:

$$-\frac{dm'''_{fuel}}{dt}\Delta h_c \left(\frac{4}{3}\pi r_{crit}^3\right) \approx -\kappa \left.\frac{dT}{dr}\right|_{r_{crit}} (4\pi r_{crit}^2) \quad (1.9)$$

where  $m'''_{fuel}$  is the fuel per unit volume,  $\Delta h_c$  is the heat of combustion, and  $\kappa$  is the thermal conductivity. The following approximations are made:

$$\left.\frac{dT}{dr}\right|_{r_{crit}} \approx \frac{-(T_b - T_u)}{r_{crit}} \quad (1.10)$$

$$\Delta h_c \approx mc_P (T_b - T_u) \quad (1.11)$$

$$s_L \approx \left(\frac{-2m\alpha}{\rho_u} \frac{dm'''_{fuel}}{dt}\right)^{\frac{1}{2}} \quad (1.12)$$

$$p_u = p_b = p = \rho_u R_u T_u \quad (1.13)$$

$$= \rho_b R_b T_b \quad (1.14)$$

where

$$\alpha = \frac{\kappa}{\rho c_P} \quad (1.15)$$

is the thermal diffusivity,  $\rho_u$  and  $\rho_b$  are the densities of the unburned and burned gas, respectively,  $m$  is the mass, and

$$R_b = \frac{\tilde{R}}{MW_b} \quad (1.16)$$

where  $\tilde{R}$  is the universal gas constant and  $MW_b$  is the average molecular weight of the burned gas. Using these approximations, the critical flame radius is found to be

$$r_{crit} \approx \sqrt{6} \frac{\alpha}{s_L} \approx \sqrt{6} \frac{\delta_{flame}}{2} \quad (1.17)$$

where  $\delta_{flame}$  is the flame thickness. It is then assumed that the required ignition energy is the energy needed to heat the critical gas volume to the adiabatic flame temperature, i.e.,

$$E_{ign} = m_{crit} c_P (T_b - T_u) \quad (1.18)$$

$$= \left( \frac{4}{3} \pi r_{crit}^3 \right) \rho_b c_P (T_b - T_u) . \quad (1.19)$$

Substituting Equation 1.17 gives

$$E_{ign} = 61.6 (p) \left( \frac{c_P}{R_b} \right) \left( \frac{T_b - T_u}{T_b} \right) \left( \frac{\alpha}{s_L} \right)^3 . \quad (1.20)$$

These analytical models greatly simplify the spark ignition process and do not include important aspects such as mass diffusion, geometry of the electrodes and spark gap, and turbulence in the surrounding gas. Therefore, determining ignition energy remains primarily an experimental issue. The oversimplification of analytical models for the minimum ignition energy is demonstrated by the comparison of calculations with experimental results in Section 3.4.3.

### 1.3.2 Ignition as a Statistical Phenomenon

The view of the ignition where the MIE is considered to be a single threshold value is the traditional viewpoint in combustion science and extensive tabulations of this kind of MIE data are available (Babrauskas, 2003, Magison, 1990). However, particularly in the aviation safety industry, a different approach to ignition characterization is being used that is more consistent with experimental observations of engineering

test data (Administration, 1994). In standardized testing guidelines published by the FAA and SAE International (Administration, 1994, International, 2005) ignition is not treated as a threshold phenomenon, but rather as a statistical event. The outcome of a series of ignition tests is used to define the probability of ignition as a function of stored energy, peak current, or some other characteristic of the ignition source. It is reasonable and useful to recognize that engineering test results have inherent variability, and hence using statistical methods to analyze these variable results provides a good basis for assessing the ignition hazard of flammable mixtures.

Simple statistical methods have been applied to Jet A ignition tests performed by Lee and Shepherd at the California Institute of Technology using a standard capacitive spark discharge system as the ignition source (Lee and Shepherd, 1999). A set of 25 ignition tests were performed while varying only the spark energy, and the data points were then used to derive a mean value and standard deviation for the MIE, rather than a single threshold value. This data set is used in Section 3.3.2 as an example to illustrate statistical analysis resulting in a probability distribution for ignition versus spark energy and confidence intervals. Statistical analysis of ignition data has also been applied to ignition of automotive and aviation liquid fuels as a means of assessing the risk of accidental ignition by hot surfaces (Colwell and Reza, 2005). Taking on the viewpoint of ignition tests as being statistical in nature raises a key question: is the statistical nature of the data due to an intrinsic characteristic of the ignition process, or is it due only to variability in the test methods? To answer this question, the experimental variability must be minimized and quantified, and the ignition source must be well-controlled.

In ignition testing, there are many uncontrolled sources of variability in the experiment itself separate from the ignition energy. These uncertainties can lead to inaccurate test results and the appearance of variability in the results that has no correlation with the ignition energy. One major cause of variability in the test results is uncertainty in the mixture composition. Not only do changes in mixtures lead to changes in combustion characteristics (flame speeds, peak pressures, etc.), as shown in the previous MIE studies (Babrauskas, 2003, Magison, 1990), even small changes

in mixture composition can lead to large differences in MIE values. Therefore, it is important to precisely control and accurately measure composition during ignition experiments. Another cause of variability is the degree of turbulence near the ignition source, as the process of flame initiation and propagation can be affected by pre-existing turbulence. Finally, a third important source of variability in the test data is the method used to detect ignition. If the detection method is unreliable or unsuitable for the combustion characteristics of the mixture being tested, a given ignition energy may be perceived as not igniting a mixture when in fact combustion did occur. In this work test methods are proposed that minimize these uncertainties to isolate the statistical nature of the ignition process itself (Kwon et al., 2007). The sources of uncertainty are not limited to the three discussed here, but these three sources are major contributors to variability in the data that is unrelated to the ignition source. It is therefore necessary to quantify and minimize the uncertainties from these three sources before the variability of ignition with respect to ignition source energy can be examined.

### 1.3.3 Probability and Historical Spark Ignition Measurements

The large volume of historical minimum ignition energy data for capacitive spark discharge ignition has been extensively used in the chemical and aviation industry to set standards and evaluate safety with flammable gas mixtures. However, there is scant information on the experimental procedures, raw data or uncertainty consideration, or any other information that would enable the assignment of a statistical meaning to the minimum ignition energies that were reported. However, some researchers have claimed that the historical data can be interpreted as corresponding to a certain level of ignition probability. For example, in a paper by Moorhouse et al. (1974) the authors claim that the MIE results of Lewis and von Elbe (1961), Metzler (1952a,b), and Calcote et al. (1952) all correspond to an ignition probability of 0.01, i.e., 1 ignition in 100 tests. However, in all three studies the authors make no mention of

ignition probability and a specific probability of 0.01 is never discussed. In addition, the authors do not provide information about the number of tests performed nor the number of ignitions versus non-ignitions. Therefore, it is impossible to prescribe probabilities to historical minimum ignition energy data, as statistical analysis was never addressed in the literature, and there is not enough information on the number of tests performed and the experimental procedures. Also, obtaining a probability of ignition of only 0.01 with a reasonable level of confidence requires a large number of tests with very few ignitions, which does not appear to be consistent with the descriptions of the testing performed in the discussed literature (Calcote et al., 1952, Metzler, 1952a,b, Lewis and von Elbe, 1961). This issue of probability and historical MIE data is discussed in detail in Appendix A.

## 1.4 Spark Ignition Modeling and Experimental Investigations

A great deal of work has been done by many investigators on deriving models for ignition and on developing numerical simulations. Ballal and Lefebvre (1979) presented analytical expressions for minimum ignition energy and quench time assuming a spherical spark kernel. Maas and Warnatz (1988) developed a method for simulating ignition for generalized one-dimensional geometries, and several authors have performed simulations of ignition for one-dimensional spherical kernels (Maly, 1980, Akindele et al., 1982, Champion et al., 1986, Sloane, 1990, Kusharin et al., 1996, 2000) and cylindrical kernels (Maly, 1980, Sher and Refael, 1982, Refael and Sher, 1985, Sher and Keck, 1986). Two-dimensional simulations of spark discharge in a non-reactive gas have been performed by Kono et al. (1988), Akram (1996), Reinmann and Akram (1997), and Ekici et al. (2007) to investigate the fluid mechanics involved in the spark ignition process. Two-dimensional simulations of ignition have been developed by several authors (Ishii et al., 1992, Kravchik et al., 1995, Thiele et al., 2000b,a, 2002, Yuasa et al., 2002). In all the two-dimensional studies the clas-

sic toroidal shape of the evolved kernel is observed, which occurs due to the inward fluid flow toward the gap center resulting from the shock wave structure. However, the simulations are not sufficiently resolved to capture all aspects of the fluid motion including laminar mixing. Also, in most of these studies only one electrode geometry is considered. Akram (1996) and Thiele et al. (2000b) performed simulations for several electrode geometries, however, the geometries were limited to blunt and cone-shaped electrodes with diameters of 1 to 2 mm.

Many investigators have also performed experimental studies on visualizing spark discharge and ignition using optical and laser techniques. Experiments have been done to visualize the fluid mechanics of the evolving spark and ignition kernels using schlieren visualization (Olsen et al., 1952, Bradley and Critchley, 1974, Champion et al., 1986, Kono et al., 1988, Pitt et al., 1991, Au et al., 1992, Arpaci et al., 2003, Ono et al., 2005) and interferometry (Maly and Vogel, 1979, Kono et al., 1988). Laser diagnostics, such as laser-induced fluorescence (LIF) (Thiele et al., 2002, Ono et al., 2005, Ono and Oda, 2008) and spectroscopy (Ono et al., 2005, Ono and Oda, 2008), have also been implemented to measure characteristics of the spark kernel such as temperature and magnitude of OH radicals. In all of these studies, the electrode geometry is not varied, and there is no direct comparison with two-dimensional simulations.

## 1.5 Goals of the Investigation

The primary goals of this investigation are to examine the statistical nature of spark ignition and gain further insight into the physics of the ignition process. Statistical tools are developed for analyzing ignition test results to obtain probability distributions for ignition versus three measures of the spark strength: energy, energy density, and charge. Ignition tests were performed in five different flammable test mixtures, and when possible the results of the statistical analysis are compared qualitatively and quantitatively with historical minimum ignition energy results. To relate the current experimental study specifically to hazards on aircraft, the flammable test mixtures

were chosen based on current aircraft certification testing standards. Test methods were also developed to improve on existing test standards, and the results of the current work have been used to make recommendations for improving the test standards through collaboration with Boeing. High-speed visualization is used to examine both the characteristics of the flame propagation in the different test mixtures as well as study spark discharge and ignition at very early times. The latter visualization allows for investigation of the effect of electrode geometry on the fluid mechanics following spark discharge and provides insight into possible reasons for the statistical nature of the ignition process near the minimum ignition energy. Finally, knowledge gained while performing the experimental investigations is used to develop numerical models of spark discharge and ignition. Visualization of spark discharges are used to validate the fluid mechanics in the simulation, and one-step chemistry models are developed to use in highly resolved simulations of ignition and flame formation.

## 1.6 Thesis Outline

A discussion on spark breakdown, the spark ignition process, and flame structure was presented in Chapter 1. Chapter 1 also included background information on historical minimum ignition energy (MIE) studies and previous experimental and numerical investigations of spark ignition. Chapter 2 describes the experimental setup and test procedures used to perform spark ignition tests. The test diagnostics, including optical visualization, and the two low-energy capacitive spark ignition systems are described.

The results of short, fixed-length spark ignition tests performed in three flammable test mixtures are discussed in Chapter 3. Schlieren visualization and pressure measurements are used to study the combustion characteristics of very lean hydrogen test mixtures based on the recommended test mixture in the aircraft certification standards. Chapter 3 also describes the statistical tools developed for analysis of spark ignition test results, and probability distributions for ignition versus spark energy are presented and compared with historical MIE data and calculations using an analytical

model. Chapter 4 presents results of ignition tests performed using a variable-length spark ignition system and probability distributions for ignition versus both spark energy density and spark charge. Also, schlieren visualization is used in a discussion of ignition variability.

In Chapter 5, the details of numerical simulations of the fluid mechanics following spark discharge in air are presented. The results using three different electrode geometries are discussed and the simulations are compared with schlieren visualization. The development of one-step chemistry models for simulation of flames and ignition is discussed in Chapter 6, and a one-step model for a hydrogen-air mixture is implemented in a two-dimensional simulation of spark ignition in Chapter 7. Also presented in Chapter 7 are the results of simulations of ignition using the three different electrode geometries and the simulations are compared with schlieren visualization. Finally, the major conclusions of the investigation and possible future work are discussed in Chapter 8.

# Chapter 2

## Experimental Setup

### 2.1 Combustion Vessel

The spark ignition experiments were conducted in a rectangular constant-volume steel combustion vessel shown in Figure 2.1. The vessel is constructed of 31.75 mm thick steel plates bolted together to form a rectangular chamber approximately 33.7 cm in height with a 25.4 cm square cross-section. The internal dimensions are approximately 19 cm by 19 cm by 30.5 cm, giving a gas volume of approximately 11 liters. Each wall has a 11.7 cm diameter port hole and bolt circle for mounting flanges and other fixtures. Two parallel walls have 25.4 mm thick BK7 glass windows in the port holes for visualization. The remaining two walls are used for mounting the the ignition systems. A feed-through for a fan mixture and all the plumbing connections are in the lid of the vessel. The plumbing in the lid includes connections for the vacuum and gas-fill lines, static pressure gauge and pressure transducer, thermocouple, and a septum for injecting liquid fuels.

A remotely-controlled gas plumbing system is used to fill the combustion chamber precisely. A 25.4 mm ball valve separates the lab vacuum manifold from the chamber and is opened to evacuate the vessel. The gas feed line in the vessel is connected to gas bottles outside of the lab through a series of valves. The static pressure is measured by a Heise 901A manometer and a precise digital readout allowing for precise filling of the gases by the method of partial pressures to within 0.01 kPa. The gas lines are also connected to the vacuum manifold so that they can be evacuated between gases

to eliminate errors in composition due to dead volume. All the valves are controlled remotely from a control panel outside of the experiment room.

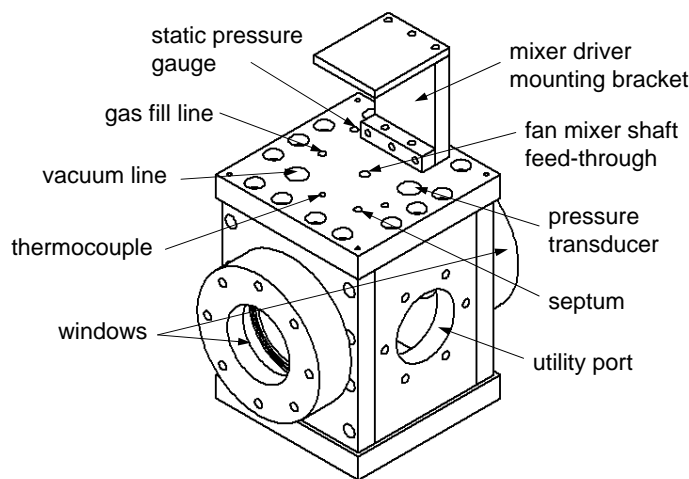


Figure 2.1: A schematic of the constant volume combustion vessel used for the spark ignition testing

## 2.2 Diagnostics

### 2.2.1 Pressure and Temperature Measurement

Whether or not ignition occurred was determined by measuring the dynamic pressure and temperature inside the combustion vessel. The transient pressure rise from the combustion was measured using a model 8530B Endevco piezoresistive pressure transducer mounted at the top of the vessel. The pressure transducer had a sensitivity of 1.57 mV/psi (approximately 0.228 mV/kPa), a full scale output of 314 mV, and non-linearity of 0.04% of the full scale output. The output voltage of the transducer was amplified by a factor of 50 and then read by a National Instruments PCI-MIO-16E-1 12-bit data acquisition card. The card was used with a voltage range of  $\pm 50$  mV, giving a measurement resolution of approximately 0.024 mV. Therefore, the smallest change in pressure that could be detected and accurately measured was approximately 0.11 kPa. Hence, the pressure measurement provided an extremely

sensitive and accurate ignition detection method. The maximum pressure in the vessel and the explosion time could also be obtained from the pressure traces. Ignition was also detected through measurement of the temperature inside the vessel using an Omega K type thermocouple inserted through the lid of the vessel. The voltage output of the thermocouple was converted to temperature and displayed using an Omega DP116 electronic readout. The temperature voltage was also digitized using the data acquisition card, and both the dynamic pressure and temperature measurements were recorded using LabVIEW Data Acquisition software. The response time of the thermocouple is in excess of 100 ms (1.5 mm bead size with 24 AWG wires), so the recorded temperature was not quantitatively accurate; the temperature measurement was used only as a secondary method of ignition detection. The Heise gauge and precise digital readout were used to monitor the static pressure inside the vessel during the gas filling process as well as the post-combustion pressure of the products.

### 2.2.2 Schlieren Visualization

Visualization of the spark discharge and flame propagation was achieved using a schlieren optical system. Two different schlieren systems were developed. The first schlieren system (Figure 2.2(a)) was designed to visualize the flame propagation and therefore had a field-of-view with full view of the vessel windows, approximately 12 mm in diameter. The light source used was an 150 watt Ealing xenon arc lamp, and the light was focused onto a pin-hole by a 50 mm focal length condenser lens. A 1.5 mm focal length concave mirror was used to collimate the light prior to passing through the test section, and an identical mirror was used as the schlieren focusing mirror. A round aperture was used as the schlieren edge, and the image was focused onto the camera CCD using a 50 mm Nikon lens. A Phantom v7.3 high-speed video camera was used to record the schlieren images at a rate of 1000 frames per second at a resolution of 512 x 512. The second schlieren system (Figure 2.2(b)) was developed to visualize the very early stages of the spark discharge and flame kernel development using a very small field-of-view. To obtain close-up images of the spark gap, the 1.5

m concave mirror used to collimate the light was replaced by a 100 mm focal length achromatic doublet lens 2 inches in diameter. The optical assembly mounted on the xenon arc lamp was used to focus the light onto a thin vertical slit formed by two parallel razor blades. The light was then collimated by the 100 mm focal length lens and passed through an aperture, producing a beam approximately 20 mm in diameter that was then directed by mirrors through the test section and centered on the spark gap. A 1 m focal length concave mirror focused the light onto both vertical and horizontal schlieren knife edges. The camera was placed at a defined distance from the knife edges such that the schlieren image was focused directly on the CCD. A Phantom v7.10 camera was used to record high-speed schlieren videos at a rate of 10,000 frames per second with 800 x 800 resolution and up to 79,000 frames per second at a resolution of 256 x 256.

## 2.3 Low-Energy Capacitive Spark Ignition Systems

Traditional MIE testing ([ASTM, 2009](#), [Magison, 1990](#), [Lewis and von Elbe, 1961](#), [Babrauskas, 2003](#)) used capacitive spark ignition systems with a fixed-length spark gap, and the goal was determining the minimum spark energy required for ignition using that particular gap size. In this work, however, the objective was to investigate the statistical nature of ignition with both fixed and variable spark lengths. Therefore, very low-energy spark ignition system was first developed to produce short sparks with a fixed length of 1 to 2 mm to study ignition versus spark energy. To perform ignition tests with sparks near the traditional MIE values, the ignition system needed to generate sparks with energy as low as 50  $\mu\text{J}$ . Generating such low energy capacitive sparks presented several design challenges, including obtaining extremely low capacitances and limiting charge leakage from the circuit. A second ignition system was developed to generate sparks with variable lengths from 1 mm to 10 mm or longer to examine ignition versus spark energy density (spark energy divided by the

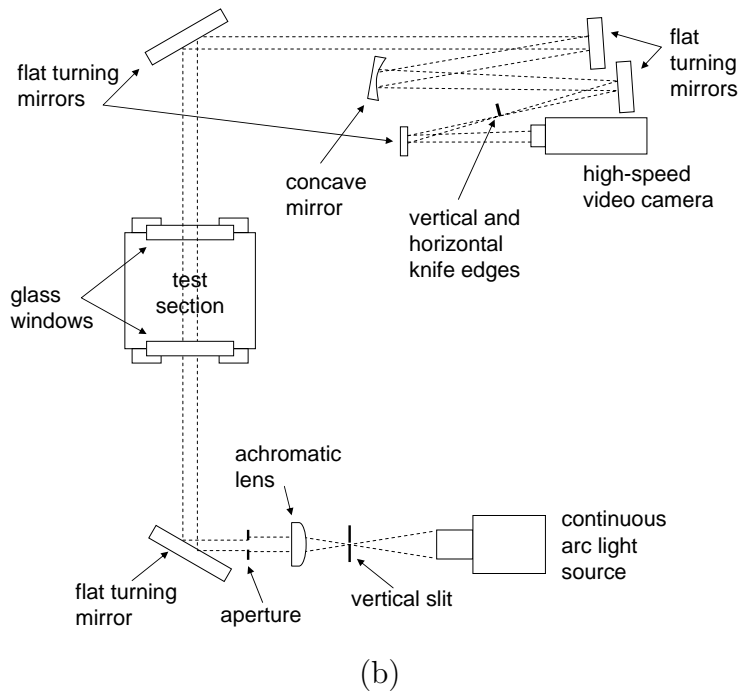
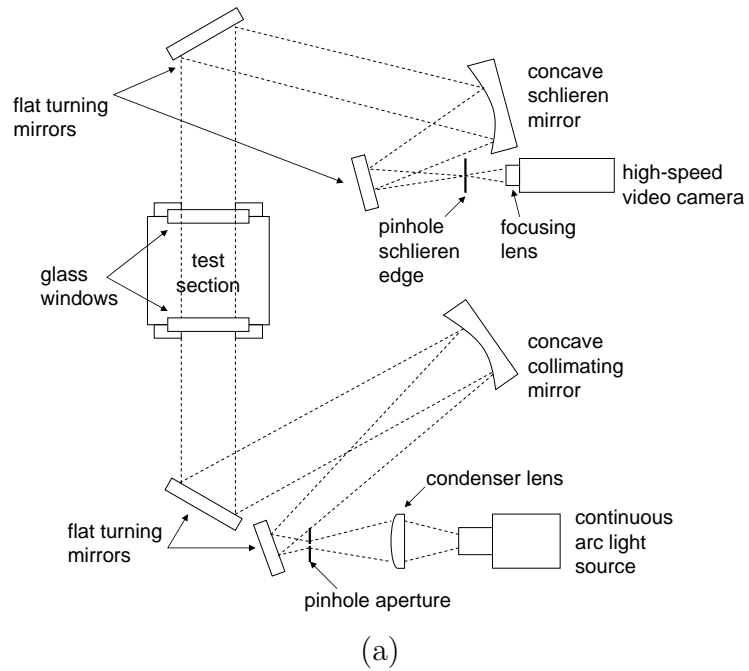


Figure 2.2: Large field-of-view (a) and small field-of-view (b) schlieren systems used for spark and flame visualization

spark length).

### 2.3.1 Short, Fixed-Length Spark Ignition System

The discharge circuit used in the short spark ignition system was based on the ideas of Ono et al. (Ono et al., 2005, 2007, Ono and Oda, 2008). The basis of the design was a simple capacitive discharge circuit, but many features were implemented to improve the system performance in terms of reliability, consistency, and repeatability so that the spark energy could be reasonably predicted and measured.

The capacitive discharge circuit consisted of a Glassman model MJ15P1000 high-voltage power supply (0–15 kVDC range) connected to two 50 G $\Omega$  7.5 kV charging/isolation resistors in series with a Jennings CADD-30-0115 variable vacuum capacitor with a range of 3 to 30 pF. The capacitor was then connected in parallel with the spark gap, so that when the capacitor was charged to the gap breakdown voltage it would discharge through the gap producing a low-energy spark. The high-voltage power supply output was controlled by supplying a 0–10 V input voltage provided by a function generator. The function generator output a ramp signal that rose from 0 to 7.32 V in 50 seconds, which caused the high-voltage power supply to output a ramp voltage increasing from 0 to 11 kV in 50 seconds. The ramp time was chosen to be more than 10 times longer than the maximum capacitor charging time. This choice of ramp time allowed sufficient time for the capacitor to charge so that the voltage could be measured at the output of the high-voltage power supply instead of measuring the voltage directly on the capacitor. It was important to be able to measure the voltage in this manner because of the extremely large isolation resistance (100 G $\Omega$ ); if a probe with much lower impedance was connected directly in parallel with the capacitor, a voltage divider was formed where the probe draws the majority of the current. By using a sufficiently long voltage ramp to charge the capacitor, it was possible to measure the capacitor voltage on the other side of the resistors. A Tektronix P6015A high-voltage probe was connected to the output of the power supply to measure the capacitor voltage at breakdown, and the output of the probe was

digitized by a Tektronix TDS460A oscilloscope at a sampling rate of 1 MS/s. The spark current was measured using a Bergoz CT-D1.0 fast current transformer, and the current waveform was digitized by a second oscilloscope (Tektronix TDS 640A) with a sampling rate of 2 GS/s. The faster oscilloscope was triggered by the spark current directly and then triggered the second oscilloscope to record the breakdown voltage.

It was necessary to implement a high-voltage relay in the circuit to disconnect the capacitor from the high-voltage power supply after a spark occurred to prevent multiple sparks. A Gigavac GR5MTA 15 kV load switching relay was connected between the positive output of the high-voltage power supply and the first 50 G $\Omega$  charging resistor. The relay required 12 VDC to close, which was provided by a lab power supply and a Grayhill 70-ODC5 solid-state relay mounted on a Grayhill 70RCK4 rack. A timing diagram illustrating the triggering of the devices and the opening of the high-voltage relay is shown in Figure 2.3. A 4 V power supply and a delay generator were used to provide the logic inputs to the relay; the 4 V signal leaves the relay closed during charging, so that the high-voltage relay receives the 12 V signal and remains closed. When the spark begins, the current signal triggers the oscilloscope which in turn triggers the delay generator to open the solid state relay. This causes the high-voltage relay to open, disconnecting the charging circuit from the high-voltage ramp and preventing multiple capacitor discharges. A schematic of the circuit is shown in Figure 2.4 and the important circuit features are indicated in the photograph in Figure 2.5. All the circuit components were mounted on a 0.5 inch thick acrylic plate, and the resistors, capacitor, and high-voltage relay were mounted on Teflon standoffs to limit any leakage current. A round acrylic face plate was attached to the end of the circuit board to hold all the connections to the external power supplies, delay and function generators, and high-voltage probe. All electrical connections with corners or sharp edges were coated with high-voltage putty to prevent corona losses.

The spark gap, shown in the photographs in Figure 2.6, was constructed using brass and stainless steel rods that were threaded at the ends so that different electrode tips could be used. One of the brass screws was mounted in a piece of fiberglass in

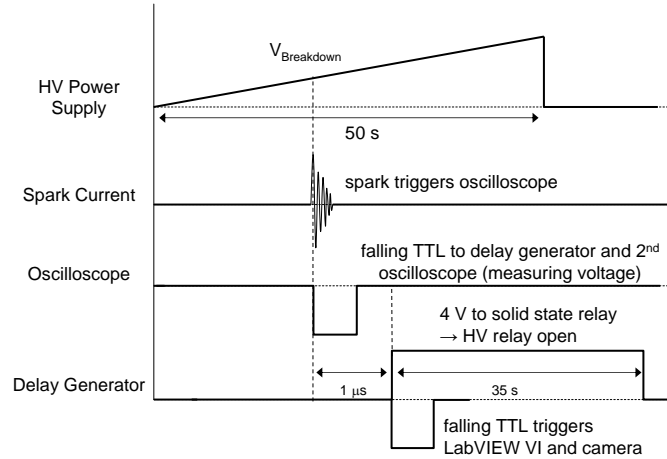


Figure 2.3: Timing diagram illustrating the triggering of the oscilloscope and the opening of the high-voltage relay after the spark discharge

front of the other electrode tip on a stainless steel extender rod. The spark gap could then be adjusted by threading the brass screw further in or out through the fiberglass. The brass screw and extender arm were mounted on brass rods fed through Teflon bushings in a circular fiberglass plate, and on the other side of the plate high-voltage leads were attached to the rods for connecting the spark gap to the discharge circuit. The fiberglass plate mounted on an aluminum fixture that held the spark gap on one side and the circuit board on the other side. The fiberglass plate, teflon bushings, and feed-through rods were all mounted using O-rings ensuring that the assembly was vacuum tight. As with the circuit board, all sharp edges on the connections were insulated with high-voltage putty. An acrylic tube enclosed the circuit board and air from a desiccant dryer was pumped through a connection in the face plate and into the enclosed circuit. The dry air was necessary to control the humidity so that the extremely sensitive high-voltage components, particularly the capacitor surface, remained dry while testing to minimize leakage current. Every time the tube was removed and adjustments to the circuit made, the surfaces of the resistors, capacitor, and Teflon parts were cleaned using isopropyl alcohol. The spark gap side of the aluminum fixture fit through a flange on the combustion vessel and clamps were used to hold the fixture against the flange with an O-ring seal. The spark ignition system

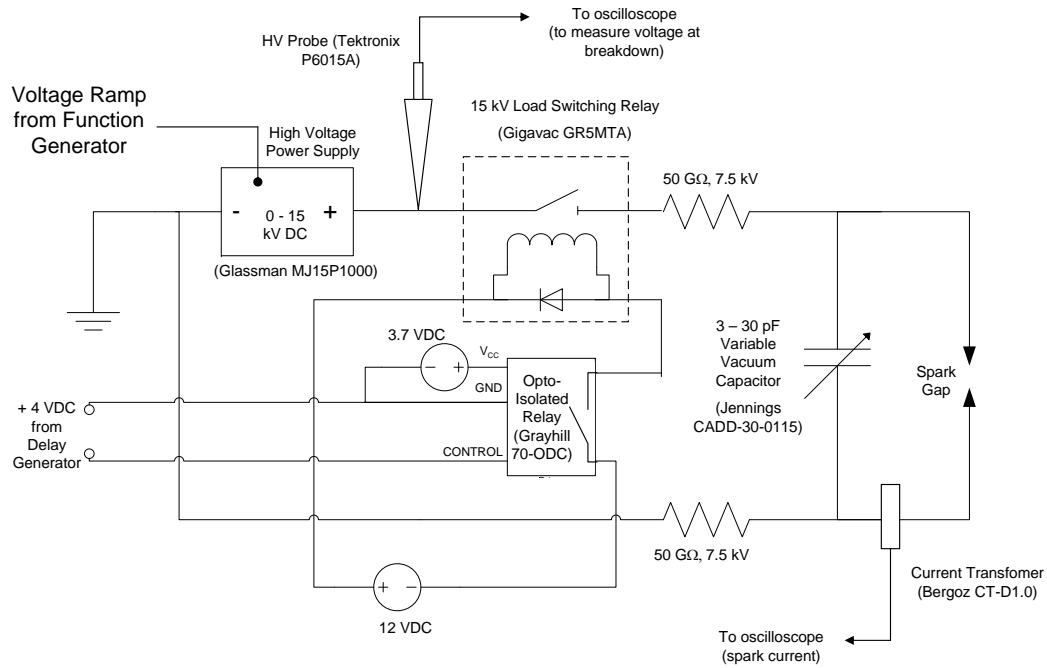


Figure 2.4: Schematic of the short, fixed-length, low-energy spark ignition system

mounted on the combustion vessel is shown in Figure 2.7.

### 2.3.2 Variable-Length Spark Ignition System

A second low-energy spark ignition system was developed to generate sparks with lengths varying from approximately 1 to 10 mm. The ignition system was designed to simulate the sparks due to an isolated conductor in a grounded aircraft fuel tank, as illustrated in the schematic in Figure 2.8. While fueling an aircraft, the fuel is sent through filters before entering the fuel tank. During the filtering process, electrons are ripped off of the fuel molecules in a process referred to as tribocharging, resulting in positively charged fuel in the tank. While the aircraft fuel tank is grounded, the fuel is not highly conductive and so it can take several minutes for the positive charge to leak to ground. The positively charged fuel induces a large electromagnetic field, as illustrated in Figure 2.8. If there are any conductors within the electric field that are electrically insulated from the grounded tank, for example a metal bolt or bracket,

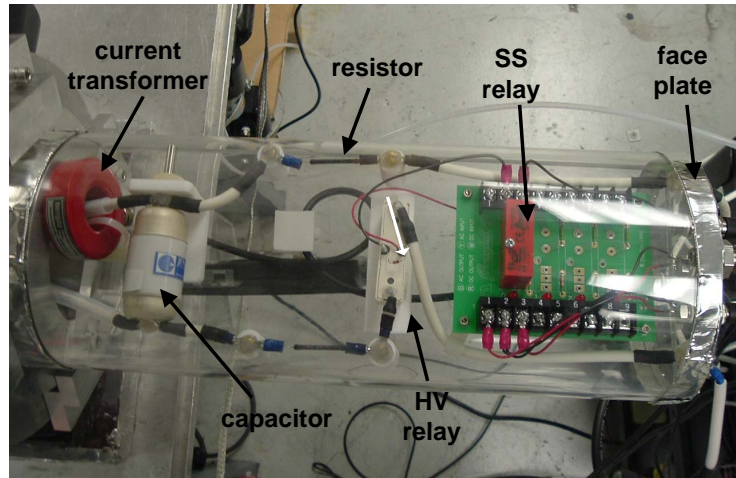


Figure 2.5: Photograph of the short, fixed-length, low-energy spark ignition system

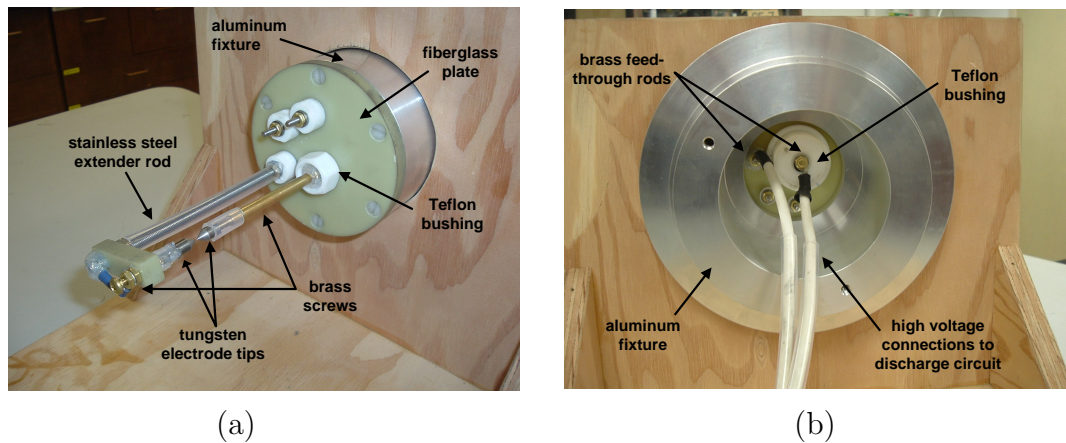


Figure 2.6: (a) Front and (b) back views of the spark gap fixture

the conductor will become charged up to tens of kilovolts. The capacitance of the isolated conductor is extremely small, on the order of picofarads, so the stored energy will be in the range of microjoules to millijoules. If the voltage of the conductor is high enough, the conductor may discharge the stored energy through a long spark to the wall of the fuel tank. Therefore, the threat posed by isolated conductors is ignition by long (several millimeters), low-energy spark discharges.

A schematic of the circuit used in the experiments to simulate the isolated conductor hazard is shown in Figure 2.9. In this circuit, the isolated conductor was a

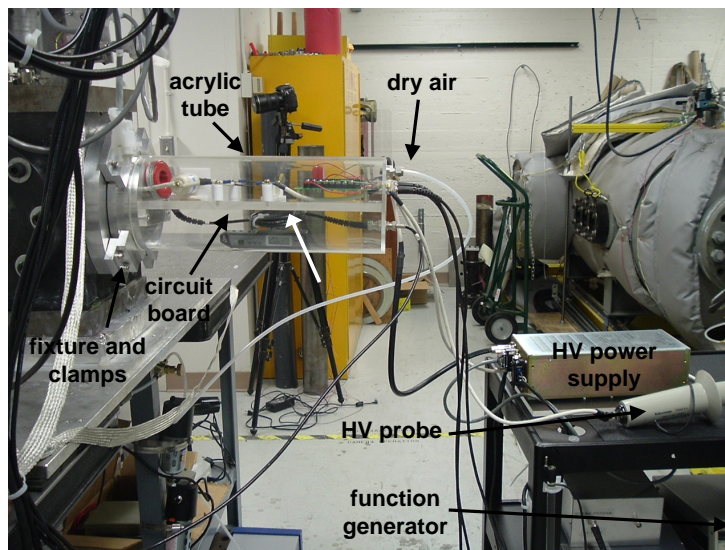


Figure 2.7: The short, low-energy spark ignition system mounted on the combustion vessel

round aluminum plate with an electrode suspended inside the combustion vessel. An electrode was mounted on a screw threaded into the center of the plate. The plate was mounted on a Teflon tube to electrically isolate it from the vessel, which was grounded and hence acted like the grounded fuel tank. A  $20\text{ G}\Omega$  high-voltage resistor housed inside the Teflon tube was connected in series with the plate to isolate it from the rest of the high-voltage circuit. The vessel wall and aluminum plate formed a capacitor, and the capacitance could be varied from approximately 5 to 20 pF by changing the separation distance between the plate and the vessel wall or by changing the plate diameter. For ignition tests that required larger spark energies, a 20 to 450 pF variable vacuum capacitor was connected in parallel with the isolated conductor. A high-voltage power supply with a range of 0 to -30 kV was connected in series with the isolation resistor through a high-voltage relay (Ross Engineering E40-DT-40-0-15-BD). The relay remained open, disconnecting the capacitor from the power supply, until it received a 120 VAC signal provided by remotely closing a Grayhill 70-0AC5 solid state relay on the 120 VAC power line. The voltage was set using a variable transformer, and the high-voltage relay was closed for several seconds to charge the isolated conductor to the desired negative voltage. A grounded electrode

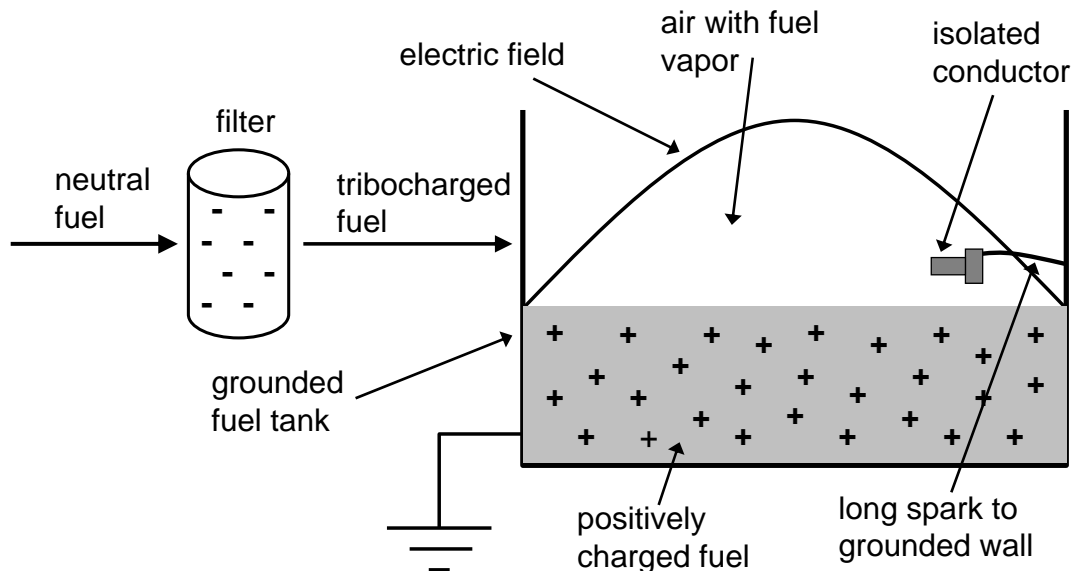


Figure 2.8: Schematic of the isolated conductor phenomenon in aircraft fuel tanks

was mounted on a Teflon tube and held inside the vessel by a fixture on the opposite wall from the aluminum plate. The Teflon tube was mounted on a motorized linear stage (Arrick Robotics X Positioning Table with MD-2 Dual Stepper Motor System) that was controlled remotely to step the electrode in towards the negatively charged electrode. A special dynamic gland seal was used between the fixture and tube to prevent leaking while the electrode was moving. When the grounded electrode reached the breakdown distance it induced a spark across the gap between the electrodes. The breakdown voltage was measured by a high-voltage probe at the output of the high-voltage power supply and the spark current was measured using the fast current transformer. The spark gap length was determined by analyzing a schlieren image using image processing tools in MATLAB. The aluminum plate and electrodes are shown in Figure 2.10(a) and the linear stage is shown in Figure 2.10(b). The length of the spark was varied by changing the charging voltage, and the spark energy was varied by changing the voltage and the capacitance. By varying these parameters, ignition tests could be performed using not only a range of spark energies but also a range of spark energy densities.

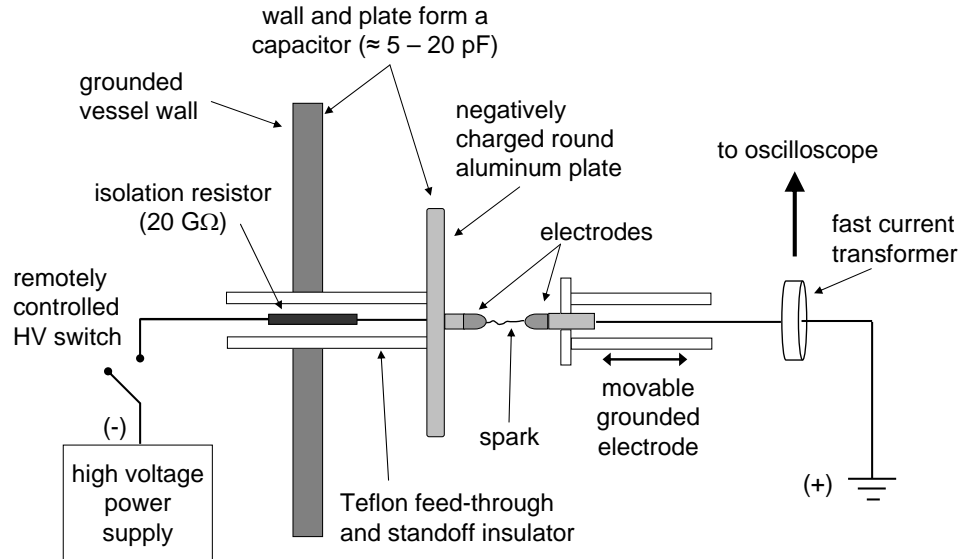


Figure 2.9: Schematic of the variable-length spark ignition system

## 2.4 Spark Energy and Charge

Traditionally, in spark ignition testing, e.g., [Lewis and von Elbe \(1961\)](#), the spark energy was considered to be equal to the energy stored in the capacitor,

$$E_{stored} = \frac{1}{2}CV^2. \quad (2.1)$$

However, there are many sources of energy loss, such as electromagnetic radiation, production of shock waves, residual energy in the capacitor, and circuit losses. As a result, only a fraction of the stored energy is delivered to the spark channel to heat the volume of gas and initiate combustion. These sources of loss are very difficult to quantify and depend strongly on the particular spark discharge circuit. Therefore, measuring the amount of energy of a low-energy, short duration capacitive spark is extremely difficult ([Strid, 1973](#)).

One possible method of quantifying the energy dissipated in the spark is by mea-

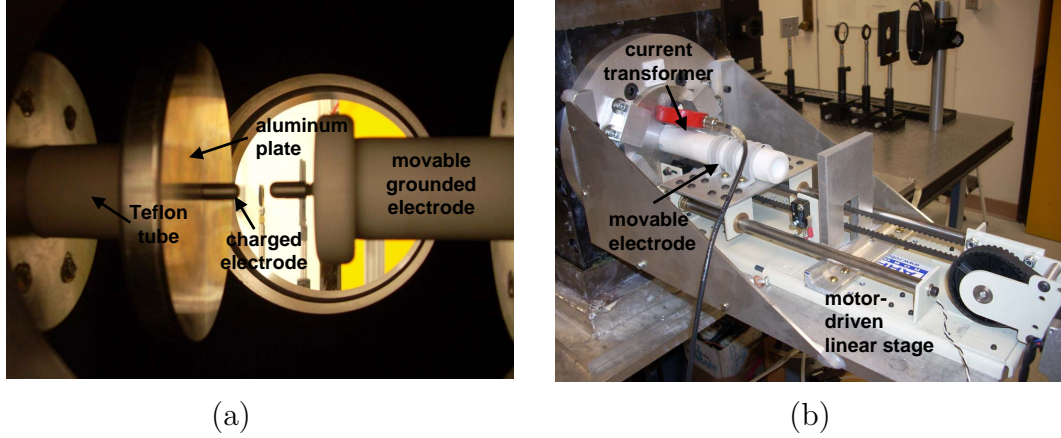


Figure 2.10: Front (a) and back (b) views of the spark gap fixture

asuring the current and voltage trace of the spark and calculating the energy as

$$E_{spark} = \int_0^{\infty} i_{spark}(t) v_{spark}(t) dt . \quad (2.2)$$

However, using this method is difficult because a measuring circuit is required to measure the voltage. This circuit would add additional capacitance and resistance to the overall discharge circuit. Also, with short-duration sparks one must be concerned with the effects of the frequency response introduced by the measuring circuit which can lead to phase shifts in the signals. Finally, the voltage measurement cannot be taken directly across the spark gap because the spark current would flow into the ground of the measuring circuit. There, measurement resistors must be connected in series with the spark gap, resulting in additional power losses that must be calculated. The difficulties associated with measuring the spark energy using this method are discussed further in [Shepherd et al. \(1999\)](#) and [Lee and Shepherd \(1999\)](#).

Another way to calculate the spark energy is using the spark charge. As discussed in Section 2.3.1, a passive measurement of the spark current trace is made using a current transformer. The total charge in the spark is then simply:

$$Q_{spark} = \int_0^{\infty} i_{spark}(t) dt . \quad (2.3)$$

The charge is related to the voltage through

$$Q = CV \quad (2.4)$$

and substituting this expression into the equation for the energy (Equation 2.1) gives:

$$\begin{aligned} E_{spark} &= \frac{1}{2} Q_{spark} V^2 \\ &= \frac{1}{2} \frac{Q_{spark}^2}{C} . \end{aligned} \quad (2.5)$$

However, the capacitance  $C$  in this case is the time-dependent capacitance of the spark gap during the discharge, which is prohibitively complicated.

The spark charge, however, can be used to calculate the residual energy left in the capacitor that is not dissipated in the spark:

$$\begin{aligned} Q_{res} &= Q_{stored} - Q_{spark} \\ &= CV_{breakdown} - \int i_{spark}(t) dt . \end{aligned} \quad (2.6)$$

Therefore, in this work the spark energy was approximated as the difference between the stored energy in the capacitor and the residual energy in the capacitor after discharge:

$$E_{spark} \approx E_{stored} - E_{residual} \quad (2.7)$$

where

$$E_{stored} = \frac{1}{2} CV_{breakdown}^2 \quad (2.8)$$

and

$$E_{residual} = \frac{1}{2} \frac{Q_{residual}^2}{C} . \quad (2.9)$$

The voltage on the capacitor at spark breakdown was measured as described in Section 2.3.

The capacitance,  $C$ , includes not only the contribution of the capacitor but also the stray capacitance in the circuit due to electrical leads and the spark gap. In the short-spark ignition system, the capacitance was measured using a BK Precision 878A LCR meter by disconnecting the leads from the capacitor to the isolation resistors but keeping the spark gap connected to include the stray capacitance. The variable-spark ignition system, however, had a more complicated geometry, and therefore instead of a simple LCR meter, a Keithley 6517A electrometer was used to accurately measure the total capacitance. The capacitor was charged to 1 kV using the electrometer's precision power supply, then discharged using a grounded probe connected to the electrometer which records the charge. The capacitance is then calculated simply as

$$C = \frac{Q}{V} = \frac{Q_{electrometer}}{1000 \text{ V}}. \quad (2.10)$$

The residual charge in the capacitor,  $Q_{residual}$  is calculated by subtracting the spark charge from the original stored charge,

$$Q_{residual} = Q_{stored} - Q_{spark} = CV_{breakdown} - \int i_{spark}(t) dt \quad (2.11)$$

where the integral of the spark current  $i_{spark}(t)$ , the spark charge, was calculated by numerical integration of the waveform from the current transformer as demonstrated in Figure 2.11. The spark charge could also be determined precisely using the electrometer by discharging the spark into a second capacitor and measuring the resulting charge on the capacitor. The spark charge calculations using the current trace were verified by inserting a 10 nF capacitor between the spark gap and ground and taking measurements of the spark charge using the electrometer.

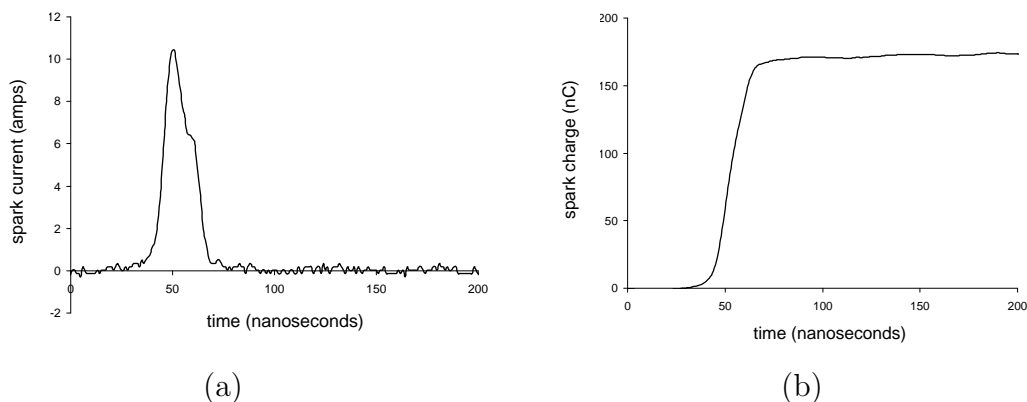


Figure 2.11: (a) Current waveform from an example spark and (b) spark charge versus time obtained by numerically integrating the current waveform

## 2.5 Experimental Procedure

A checklist (example given in Appendix B) was used for each spark ignition experiment to ensure strict adherence to the experimental procedure and to record data from the test. Each spark ignition experiment began by evacuating the combustion vessel and gas line to a pressure of less than 50 mTorr, at which time the Heise pressure gauge readout and the pressure transducer amplifier were set to zero. The relevant gas bottles and gas line hand valves were opened, and the vessel was filled with the desired mixture using the method of partial pressures. If only gases were used, the diluent was filled first, followed by the oxygen and the fuel last. If a liquid fuel, such as hexane, was used, the fuel was injected first into the evacuated chamber through a septum using a needle syringe. In all cases, the gas line was evacuated between each gas to eliminate errors in composition due to the dead volume. The partial pressures of each gas were recorded on both the checklist and in the LabVIEW virtual instrument (VI). Once the gases were filled, a fan mixer was turned on for three minutes to ensure homogeneous composition followed by a three minute waiting period to allow any turbulent fluctuations in the gas to dissipate. The final temperature and pressure were recorded on the checklist and in the VI and all valves were closed.

After the three minute waiting period, the Phantom camera software, LabVIEW

VI, and the oscilloscope(s) were all set to wait for a trigger. In the short-spark ignition tests, the “fireset” key was turned to supply power to the high-voltage power supply and the “fire” button on the control panel was pressed to trigger the function generator. The function generator output initiated the high-voltage ramp, and when the breakdown voltage was reached a spark was induced between the electrodes. The spark current triggered the faster oscilloscope and a falling TTL signal from the first oscilloscope triggered the second oscilloscope recording the breakdown voltage and the delay generator. The delay generator then opened the high-voltage relay to disconnect the power supply from the capacitor to prevent multiple sparks. Signals from the delay generator also triggered the LabVIEW VI and Phantom camera.

In the variable-length spark ignition tests, the “fireset” was again used to turn on the high-voltage power supply and the “arm” switch was held up for approximately three seconds to close the high-voltage relay and charge the capacitor. After the “arm” switch was released, the motorized stage was activated using a computer to step in the grounded electrode. When the breakdown distance was reached and the spark induced, the spark current once again triggered the fast oscilloscope. A falling TTL signal from the oscilloscope then triggered the LabVIEW VI and the delay generator, which in turn triggered the camera and the linear stage motor to turn off. In all tests, following the spark and triggering sequence, the schlieren video was saved and the current waveform was imported to a computer using a GPIB program. The post-shot pressure, peak pressure, and test result (ignition or no ignition) was recorded on the checklist and the vessel was evacuated.

## Chapter 3

# Results & Analysis: Short, Fixed-Length Spark Ignition Tests

1

### 3.1 Flammable Test Mixtures

In assessing the ignition threat to fuel tank vapor spaces due to lightning strikes on aircraft, the industry refers to the SAE Aerospace Recommended Practice 5416 Aircraft Lightning Test Methods ([International, 2005](#)), and the European equivalent ED 105 Lightning Testing Document. The recommended method for testing ignition sources is to use a flammable test mixture consisting of 5% hydrogen, 12% oxygen, and 83% argon by volume. This mixture has been selected to meet the requirement that the flammable mixture has a 90% or greater probability of ignition with a 200  $\mu\text{J}$  voltage spark source. The foundation of this work is published in the DOT/FAA/CT94/74 Aircraft Fuel System Lightning Protection Design and Qualification Test Procedures Development ([Administration, 1994](#)). The mixture recommended by the SAE in ARP 5416 is deliberately close to the lean flammability limit. Using mixtures so close to the lean flammability limit to determine incendiarity creates a serious problem due to the difficulty of defining ignition limits in these situations. [Britton \(2002\)](#) has discussed this issue in regards to standardized testing for determining flammability limits and the disparity between the results of various test methods. He pointed out

---

<sup>1</sup>Significant portions of this chapter were also presented in [Kwon et al. \(2007\)](#) and [Bane et al. \(2009\)](#).

the difficulty of defining a combustion event, even when the pressure rise is measured, for near-limit cases for which only a narrow cone of the reactants is burned, producing a very small pressure rise. This same issue has been identified in this work while using mixtures with less than 6% hydrogen, which also have the added complication of the unusual behavior of flames in lean hydrogen mixtures. These issues are described in more detail in Section 3.2.

Flames in near-limit hydrogen-oxygen-diluent mixtures are a special case (Ronney, 1990). The high mass diffusivity of hydrogen molecules in the reactant mixture enables combustion to take place for extremely lean mixtures with very low flame temperatures as compared to hydrocarbon fuels near the flammability limit (Coward and Jones, 1952). The low temperature results in very low flame speeds, and the flames are sensitive to fluid motion (e.g., turbulence), flame stretching due to motion associated with the buoyant rise of the hot combustion products (Lamoureux et al., 2003, Kumar, 1985), and radiation losses (Kusharin et al., 1996). As a consequence, the extent of combustion and resulting pressure rise are very sensitive to the experimental setup, as discussed in (Cashdollar et al., 2000). This behavior has been known since the earliest studies on hydrogen flammability (Coward and Jones, 1952) and leads to the substantial difference between the lower flammability limits for “upward” flame propagation (4% H<sub>2</sub>) and “downward” flame propagation (8% H<sub>2</sub>) in hydrogen-air mixtures (Coward and Jones, 1952). This issue has been extensively studied in the context of nuclear safety and the potential for hydrogen explosions following loss-of-coolant accidents.

Motivated by the testing standards, the first flammable mixture that was considered in this work was the the ARP-recommended mixture of 5% H<sub>2</sub>, 12% O<sub>2</sub>, 83% Ar. To investigate the effect of small changes in the composition on ignition for very lean mixtures, two additional mixtures where the hydrogen concentration was increased by just 1% were also considered. Therefore, in addition to the 5% hydrogen mixture recommended by the SAE, tests were performed in a 6% H<sub>2</sub>, 12% O<sub>2</sub>, 82% Ar mixture and in a 7% H<sub>2</sub>, 12% O<sub>2</sub>, 81% Ar mixture.

## 3.2 Schlieren Visualization and Pressure Measurement

High-speed schlieren visualization of the ignition and flame propagation in the three hydrogen test mixtures was performed. Schlieren images were recorded at a rate of 1000 frames per second with a resolution of 512 x 512. The transient pressure was also measured using the transducer and the traces were recorded using LabVIEW software. The visualization and pressure measurements were used to examine the combustion characteristics of the test mixtures and to investigate the effect of small changes in the composition near the lower flammability limit on the flame propagation. The effect of turbulence was also briefly examined.

### 3.2.1 5% Hydrogen Mixture

Schlieren images of flame propagation in the 5% hydrogen mixture are shown in Figure 3.1. This mixture is very close to the lean flammability limit and so the flame speed is very low, approximately 5.4 cm/s compared to 2.3 m/s for stoichiometric hydrogen-air. Therefore, the inertia of the flame front is overcome by buoyancy, causing the flame to rise slowly and be extinguished at the top of the vessel with no further downward propagation. The quenching of the flame prevents complete combustion, with only a small cone of the fuel being consumed resulting in a modest pressure rise on the order of 10%. Due to the incomplete combustion the pressure trace, shown in Figure 3.2 has a much lower peak pressure than those for mixtures with higher hydrogen concentrations. Alternative detection methods such as aluminum foil deformation or thermal flame front measurements may not be able to detect these partial combustion events due to insufficient overpressures or misplacement of the detection device relative to the flame motion.

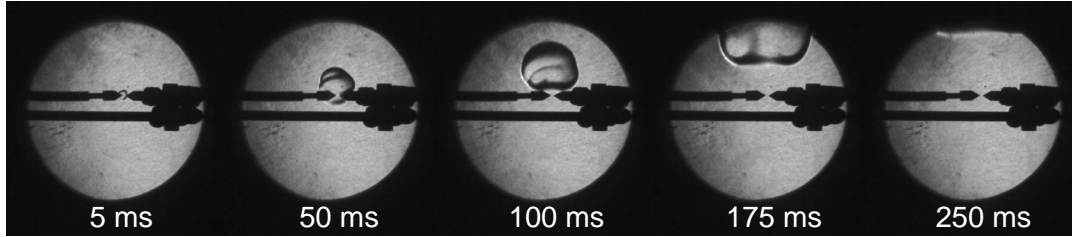


Figure 3.1: Schlieren images from high-speed visualization of ignition in the 5% hydrogen test mixture recommended by the ARP standards (International, 2005)

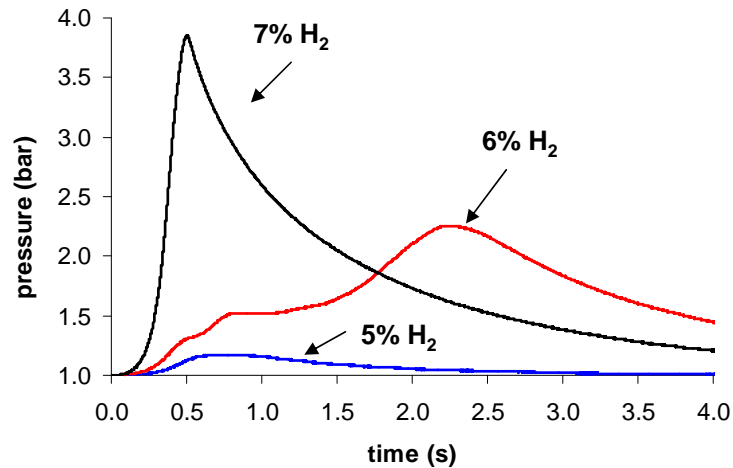


Figure 3.2: Pressure versus time during combustion of the three hydrogen test mixtures

### 3.2.2 6% Hydrogen Mixture

The case of 6% hydrogen concentration, as shown in Figure 3.3, is a transitional case where the effect of buoyancy is nearly balanced by flame front propagation. The flame is still slow enough that buoyancy has a large effect. Therefore, the flame propagates upwards, and the top surface of the flame is quenched at the top of the vessel. However, unlike the 5% hydrogen case, the flame has enough inertia and the flame speed is high enough that the flame can continue to propagate downwards, and with assistance from convection induced by the flame, nearly complete combustion occurs. This leads to the two-peak pressure trace (Figure 3.2) that exhibits a higher overall peak pressure (approximately 150% of the initial pressure) and a smaller time-

to-peak than the 5% hydrogen mixture.

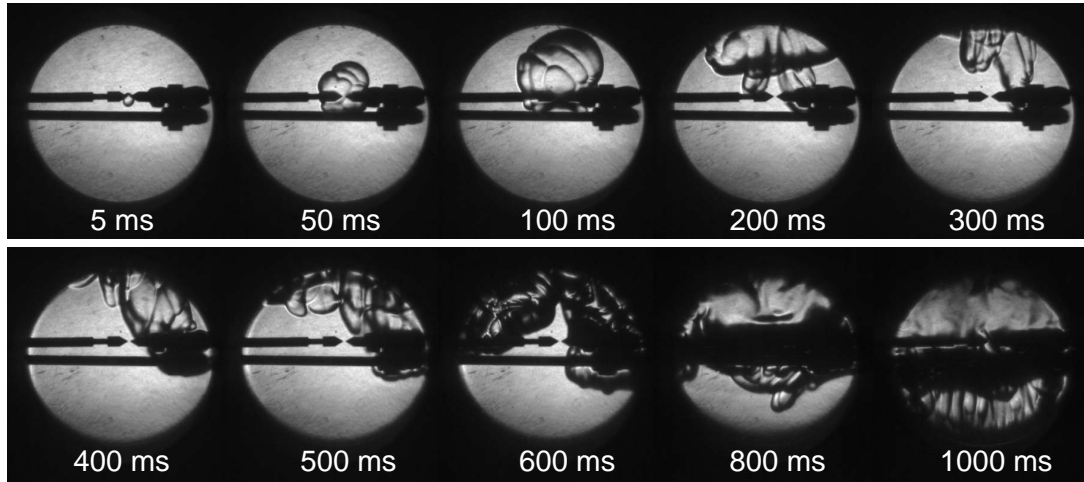


Figure 3.3: Schlieren images from high-speed visualization of ignition in the 6% hydrogen test mixture

### 3.2.3 7% Hydrogen Mixture

At a 7% hydrogen concentration (Figure 3.4) the flame speed is high enough (approximately 12 cm/s) to counteract the buoyancy effects. Therefore the combustion is characterized by a quasi-spherical flame front that propagates outward with a small amount of upward motion of the flame ball due to buoyancy. The flame is highly unstable under these conditions and a cellular or folded structure of the flame front is observed. Complete combustion is achieved and a large pressure rise of approximately 400% is observed, as shown in Figure 3.2. Also, because the flame speed for this mixture is significantly larger than for mixtures with lower hydrogen concentrations, the time to the peak pressure is significantly shorter.

### 3.2.4 Effect of Turbulence

Many studies have been conducted to assess the effects of turbulence on flammability, including extensive studies of hydrogen combustion under turbulent conditions

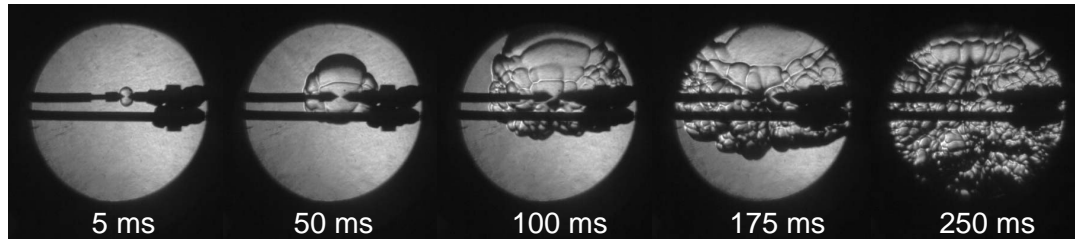


Figure 3.4: Schlieren images from high-speed visualization of ignition in the 7% hydrogen test mixture

in large scale testing (Cashdollar et al., 2000, Benedick et al., 1984). Turbulent motion of the gas in the vicinity of the spark discharge influences both the ignition and flame propagation processes (Benedick et al., 1984). Higher flow velocities and turbulence intensities may increase the minimum ignition energy (MIE) (Heywood, 1988). However, once a flame is initiated, flame front folding by turbulence can significantly increase the effective flame speed compared to values observed in quiescent systems (Benedick et al., 1984). The effect of having some initial gas motion versus a quiescent mixture was briefly examined in the present tests for a 6% hydrogen mixture. Gas motion was introduced by operating a mixing fan at the top of the vessel, and the spark was initiated immediately after the fan was stopped, leaving some initial gas motion at the time of ignition. From comparison of pressure traces from both the quiescent and non-quiescent cases (Figure 3.5), it is clear that the initial gas motion increases the initial energy release leading to a higher flame speed. Thus, more of the fuel is burned earlier in the event, and the pressure increases faster initially than in the quiescent case, consistent with observations in hydrogen-air testing (Cashdollar et al., 2000, Benedick et al., 1984). Differences in the flame front evolution can also be clearly seen in the schlieren images shown in Figure 3.6, with increased initial downward propagation of the flame in the non-quiescent case. While the gas motion and turbulence are not quantified in this study, it has been shown qualitatively that turbulence is another aspect of the ignition experiment that must be controlled to reduce test variability.

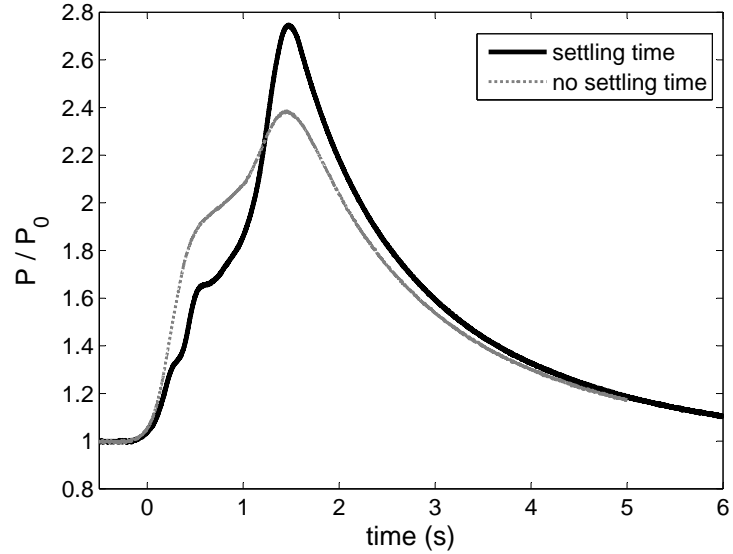


Figure 3.5: Normalized pressure traces for ignition in the 6% hydrogen mixture with little initial gas motion (solid line) and with a higher degree of initial motion (dashed line)

### 3.2.5 Implications

The normalized peak pressures versus hydrogen concentrations for mixtures with 3 to 13% hydrogen are plotted in Figure 3.7. Also shown is the theoretical curve given by constant volume, adiabatic, equilibrium calculations performed using Cantera, a software package for problems involving chemically reacting flows (Goodwin, 2005). The peak pressures for hydrogen concentrations above 6% follow the same trend as the theoretical pressures, but the experimental values are on average 67 kPa lower than the theoretical values since the calculations do not account for heat losses. For these ignition tests, there is a threshold at a 6% hydrogen concentration where downward flame propagation and complete combustion occurs. This threshold concentration is strongly dependent on the vertical location of the ignition source within the combustion vessel. In these tests, the ignition source was located approximately in the center of the vessel; however, other work has found that the threshold concentration for a downward-propagating flame increases as the ignition source location approaches the top of the combustion vessel (Benedick et al., 1984). The case of 6% hydrogen

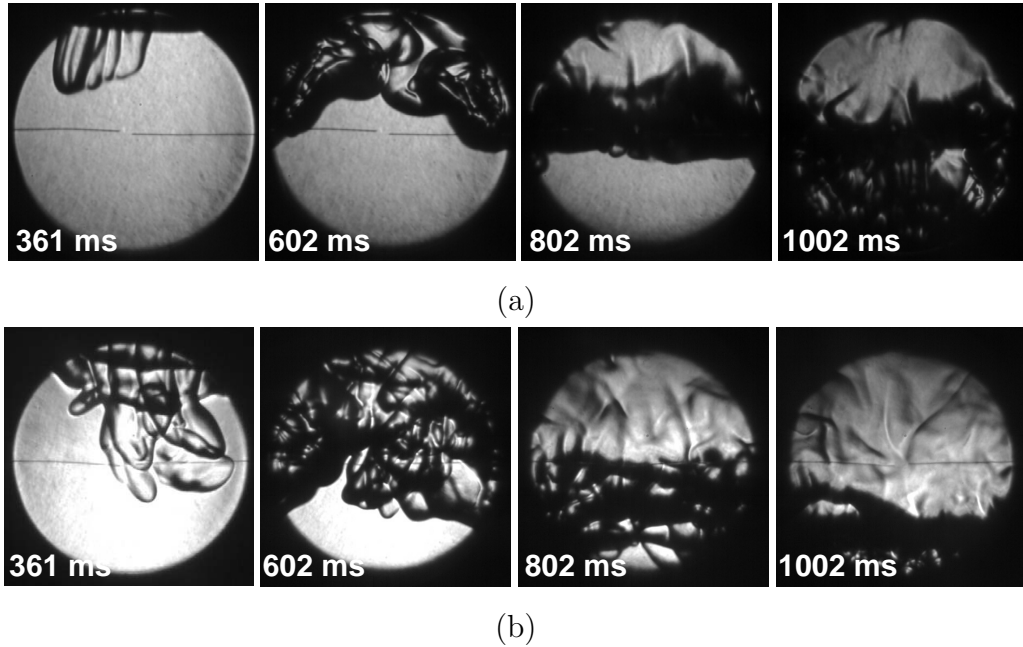


Figure 3.6: Schlieren images of combustion in the 6% hydrogen mixture with (a) little initial gas motion and (b) with a higher degree of initial gas motion induced by a fan mixer

concentration is a transitional case where the effects of buoyancy nearly counteract the flame speed and the inertia of the gases. The competition among these forces leads to a combustion event on the order of 1 second in length, with irregular flame front motion and a longer time-to-peak and lower peak pressure than cases above the threshold concentration. Mixtures with hydrogen concentrations below this threshold do not undergo complete combustion and the resulting peak pressures are small even when measured under constant volume conditions. These peak pressures are only about 30% of the theoretical pressures calculated assuming complete combustion.

For mixtures between 3 and 6% hydrogen (including the ARP-recommended mixture), the flame motion is dominated by buoyancy, only a fraction of the fuel volume burns, and relatively low pressure rises are observed. For hydrogen concentrations greater than 6%, the combustion is relatively fast, the entire gas volume burns, and the overpressures are sufficiently high that even the crudest methods will detect ignition. In mixtures with hydrogen concentrations lower than 6%, ignition and flame propagation are highly sensitive to igniter location, gas flow, and turbulence inten-

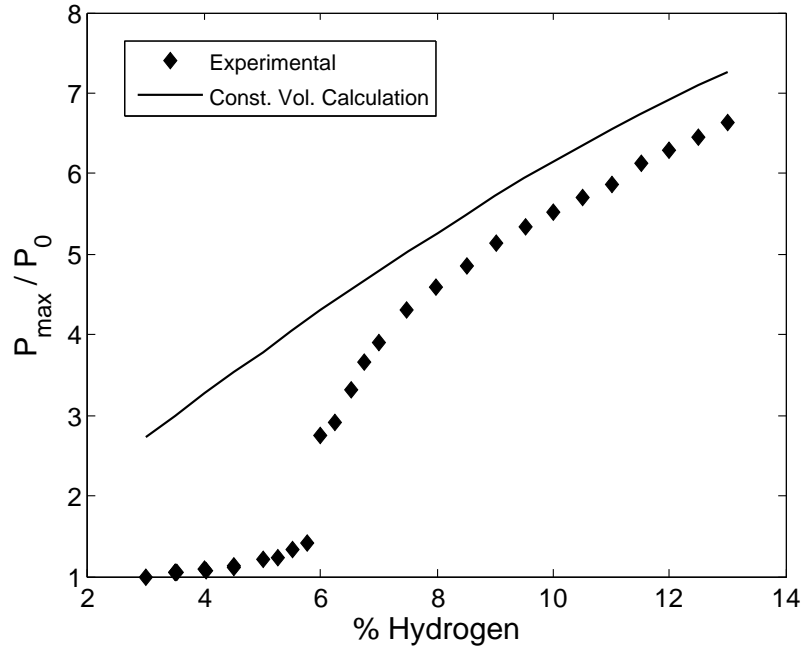


Figure 3.7: Normalized peak pressure versus hydrogen concentration near the lower flammability limit

sity, and the precise value of the hydrogen concentration. As a consequence, the test methods must be carefully designed to minimize variability. These results on the sensitivity to mixture composition and the influence of buoyancy have serious implications for the ARP testing standards. Many tests performed using the ARP standards may not be valid since ignitions near the top of the test vessel may go undetected for very lean mixtures, where flame buoyancy leads to extinction at the top of the vessel. Also, tests conducted with a mixture with less than 6% hydrogen and using an insensitive ignition detection method may give false no-ignition results. These types of ignition events were successfully detected by the three methods used in this work, but the overpressures generated by the buoyant flames may not be sufficient for a less sensitive method, such as observing the deformation of a thin film covering an aperture, as often done in lightning testing. Finally, these results demonstrate that a very small change in mixture composition near the flammability limit leads to drastically different combustion characteristics, so precise determination of the composition is extremely important. However, more typical engineering tests often use open or

vented combustion chambers and geometries which introduce additional variability.

### 3.3 Statistical Analysis

Ignition testing can be considered a sort of “sensitivity experiment”, where the goal is to measure the critical level of a stimulus that produces a certain result in a test sample. In the case of spark ignition testing, the test sample is the combustible mixture under consideration, the stimulus level is the spark energy, and the result above the critical stimulus level is ignition of the mixture. The ignition tests produce a binary outcome, where the result is either a “go” (ignition) or a “no go” (no ignition) for a given stimulus level (spark energy). It has been suggested in other work (Lee and Shepherd, 1999, Administration, 1994) that when doing ignition testing with spark energies near the reported MIE, the energy levels for “go” and “no go” results overlap, giving no clear critical stimulus level (spark energy) for ignition. The overlapping of data points suggests that statistical tools are the appropriate approach to analyzing the binary test results.

#### 3.3.1 Choosing Stimulus Levels: Bruceton Technique and Langlie Method

When performing ignition testing with the goal of using statistics to analyze the outcomes, it is desirable to generate data that produces meaningful statistical results with the fewest number of tests possible. Two possible methods for choosing the stimulus levels of each test are the Bruceton “Staircase” Technique (or the “Up and Down” Method) (Zukas and Walters, 1998, Dixon and Jr., 1983) and the “Langlie” Method (or the “One-Shot” Method) (Langlie, 1962), both of which were used by Lee and Shepherd when studying spark ignition of Jet A (Lee and Shepherd, 1999). Both of these methods have the same basic requirements for the data, including that each test is performed on a new sample (i.e., a new flammable mixture), that there is a consistent criteria for determining a “go” or “no go” (i.e., pressure detection

of ignition or visualization), and that the test stimuli (spark energies) are normally distributed.

For the Bruceton Technique, the minimum and maximum stimulus levels and the stimulus level increments must be chosen a priori. So, if this method is applied to spark ignition tests, the minimum and maximum spark energies as well as the energy increments between tests must be determined before testing begins. The conditions of each test depend on the result of the previous test, and the dependence follows a simple rule: if a “go” is obtained on the previous test, decrease the stimulus level on the next test by one increment, and if a “no go” is obtained on the previous test, then increase the stimulus level by one increment. This method is repeated until enough data points are obtained for meaningful statistics; this method usually requires large (50–100) numbers of data points, though there is some evidence that much fewer data points can be sufficient in some cases (Dixon and Jr., 1983).

For the Langlie Method, only the minimum and maximum stimulus levels, and not the stimulus increments, must be determined a priori. As with the Bruceton Technique, the conditions of each test depend on the result of the previous test, but by a more complicated rule. When counting backwards through the previous tests, if an equal number of “go” and “no go” results can be found, then the next stimulus level is the average of that level with equal “go”/“no go” results and the level of the last test performed. If a level with equal “go”/“no go” results after it cannot be found, then the next stimulus level is the average of the level of the last test and a limiting level (the minimum level if the last test produced a “go,” and the maximum level if the last test produced a “no go”). This technique is more complicated, but using it can produce meaningful statistical results with only 10–15 data points.

### 3.3.2 Logistic Regression Method

After employing one of the two methods for choosing stimulus levels discussed in the previous section, a set of data points exists for statistical analysis. The goal is to derive a probability distribution for the probability of a “go” result (ignition) versus

stimulus level (spark energy). In this work, the logistic regression method (Hosmer and Lemeshow, 1989, Neter et al., 1996) is used to calculate a cumulative probability distribution for the ignition data; this same statistical method has also been used for analyzing hot surface ignition of automotive and aviation fuels (Colwell and Reza, 2005). Once a probability distribution is obtained, percentiles and confidence intervals can also be calculated.

A binary outcome model is used for spark ignition tests with a binary result,  $y$ , where  $y = 1$  for a “go” (ignition) and  $y = 0$  for a “no go” (no ignition) for a given stimulus level (spark energy)  $x$ . If  $W$  is the threshold stimulus for a “go” result, then

$$y = 1 \quad \text{if} \quad x \geq W \quad (3.1)$$

$$y = 0 \quad \text{if} \quad x < W . \quad (3.2)$$

Then a cumulative probability distribution for a “go” (ignition) at stimulus level  $x$  (spark energy) can be defined

$$P(x) = \text{Probability}(y = 1; x) . \quad (3.3)$$

For  $n$  tests, all with new samples (mixtures), the following parameters are then defined:

$$x_i = \text{stimulus level (spark energy) for the } i^{\text{th}} \text{ test} \quad (3.4)$$

$$y_i = \text{result for the } i^{\text{th}} \text{ test (= 0 or 1)} \quad (3.5)$$

$$P(x_i) = \text{probability that } y_i = 1 \text{ for the } i^{\text{th}} \text{ test} . \quad (3.6)$$

All the stimulus levels and the binary results for the  $n$  tests are represented collectively using the likelihood function

$$L = \prod_{i=1}^n P(x_i)^{y_i} (1 - P(x_i))^{1-y_i} . \quad (3.7)$$

Then  $P(x)$  can be represented with the parametric logistic distribution function

$$P(x) = \frac{1}{1 + \exp(-\beta_0 - \beta_1 x)} \quad (3.8)$$

where  $\beta_0$  and  $\beta_1$  are parameters that are estimated by maximizing the likelihood function. The  $100q^{th}$  percentile,  $x_q$ , can be calculated using the logistic distribution with known parameter values

$$P(x_q) = q = \frac{1}{1 + \exp(-\beta_0 - \beta_1 x_q)} \quad (3.9)$$

and solving for  $x_q$  gives

$$x_q = \frac{1}{\beta_1} \ln \left[ \frac{q}{1 - q} - \beta_0 \right]. \quad (3.10)$$

Finally, the upper confidence limit (UCL) and lower confidence limit (LCL) for the  $100(1 - \frac{\alpha}{2})\%$  confidence interval for the percentile  $x_q$  can be calculated using the large sample approach for a two-sided interval

$$UCL/LCL = x_q \pm Z_{\alpha/2} \sqrt{(\sigma_{00} + 2x_q\sigma_{01} + x_q^2\sigma_{11})/\beta_1^2} \quad (3.11)$$

where  $\sigma_{00}$  and  $\sigma_{11}$  are the variances and  $\sigma_{01}$  is the covariance of  $\beta_0$  and  $\beta_1$ ,  $\alpha$  is 1 minus the confidence level (i.e.,  $\alpha = 1 - 0.95 = 0.05$  for 95% confidence) and  $Z_{\alpha/2}$  is the  $100(1 - \frac{\alpha}{2})^{th}$  percentile from a standard cumulative Gaussian distribution ( $\mu = 0$ ,  $\sigma = 1$ ). The result of this analysis is a cumulative probability distribution of the  $n$  spark ignition tests and a confidence envelope on the probability of ignition versus spark energy.

As an example, this statistical analysis method has been applied to Jet A ignition data at 38–39°C, 0.585 bar, and a mass-volume ratio of 200 kg/m<sup>3</sup> obtained by Lee and Shepherd using the One-Shot method (Lee and Shepherd, 1999). Figure 3.8 (a) shows the results of 25 spark ignition tests plotted versus the spark energy, and Figure

3.8 (b) shows the tabulated results represented in the binary form required for the statistical analysis. The likelihood function was calculated for these  $n = 25$  tests, then values for  $\beta_0$  and  $\beta_1$  were found such that those values maximized the likelihood function. These two parameters then defined a logistic probability distribution for the data, shown in Figure 3.9 along with the original data points. Then, 10<sup>th</sup>, 30<sup>th</sup>, 50<sup>th</sup>, 70<sup>th</sup>, and 100<sup>th</sup> percentiles were calculated using Equation 3.10 and the corresponding 95% confidence envelope was found by calculating the upper and lower 95% confidence limits for each percentile using Equation 3.11 with  $\alpha = 0.05$ . The resulting confidence envelope is also shown in Figure 3.9. While the distribution can be characterized by a mean value of spark energy, there is no single threshold value as in the MIE view of ignition.

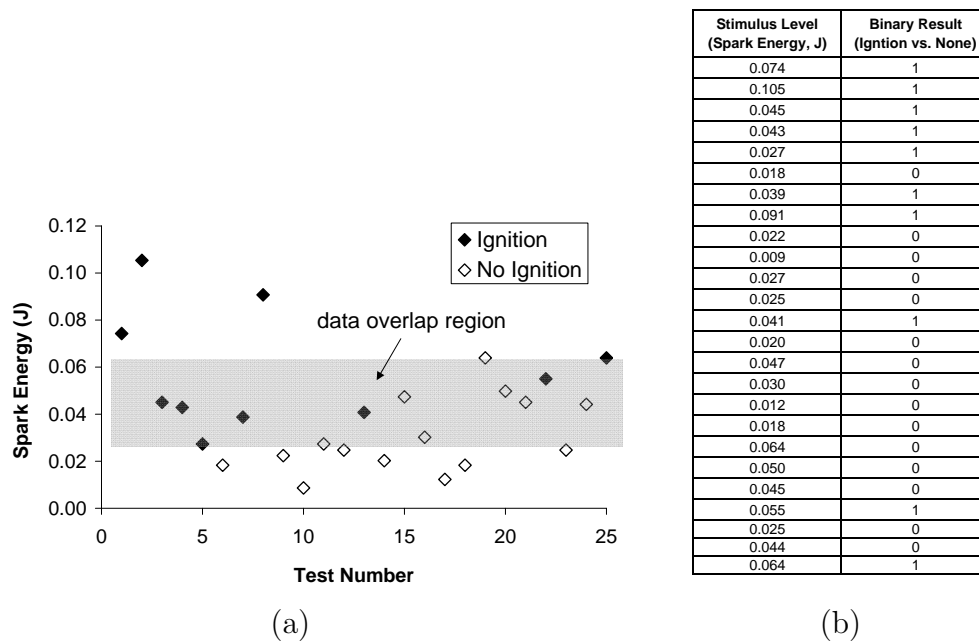


Figure 3.8: Jet A spark ignition data (Lee and Shepherd, 1999) shown as (a) a plot of 25 tests versus spark energy and (b) as tabulated results in binary form

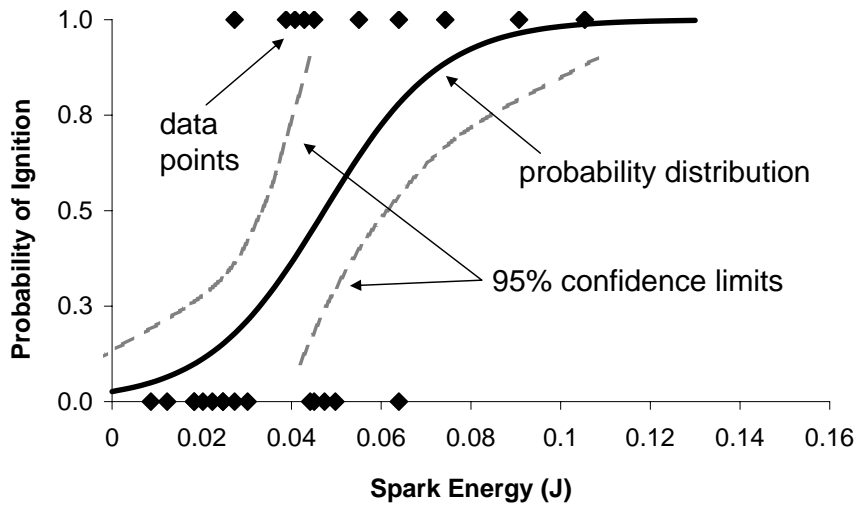


Figure 3.9: Logistic probability distribution and 95% confidence envelope for the Jet A spark ignition data

### 3.4 Probability of Ignition Versus Spark Energy

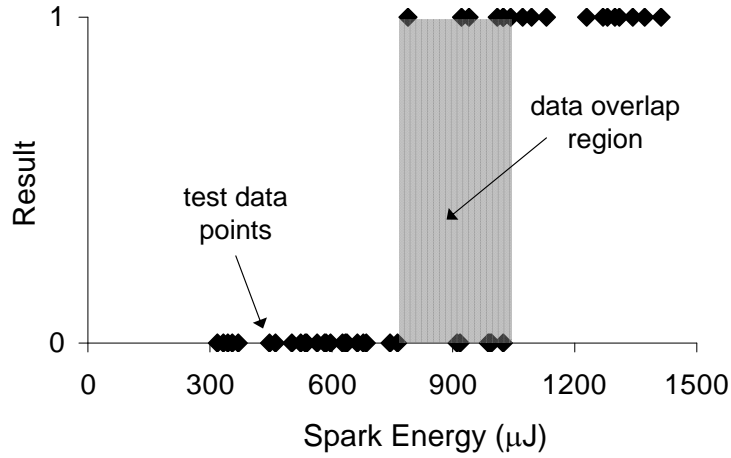
The first set of ignition tests was performed in the aviation test mixture recommended in the ARP testing standards (International, 2005), 5% H<sub>2</sub>, 12% O<sub>2</sub>, 83% Ar. The test set consisted of 47 tests with spark energies ranging from approximately 300  $\mu$ J to 1.4 mJ. The electrodes used were made of tungsten and were conical in shape with a base diameter of 6.35 mm, cone angle of 53°, and a tip radius of 0.8 mm. The spark gap length was fixed at 2 mm, motivated by the 1.5 to 2 mm gap range recommended in the ARP standards. Two further sets of ignition tests were performed in the same mixture but with 6 and 7% hydrogen as described in Section 3.1. The test set for the 6% H<sub>2</sub> mixture consisted also of 47 tests with spark energies ranging from approximately 150 to 600  $\mu$ J, and the test set for the 7% H<sub>2</sub> mixture consisted of 41 tests with spark energies of approximately 70 to 330  $\mu$ J. The same tungsten electrodes that were used in the first set of ignition tests were used also for the 6 and 7% H<sub>2</sub> mixtures, and the spark gap was fixed at 1.5 mm and 1 mm, respectively. The gap had to be shortened to 1 mm for the 7% mixture in order to obtain spark energies low enough that the mixture did not ignite. The stored energy in the discharge circuit

was varied by changing the capacitance and the spark energy was estimated using the method described in Section 3.2. If ignition did occur at a given spark energy, that data point was assigned a result of “1” (a “go”), and if ignition did not occur the result was a “0” (a “no go”). The results were analyzed using the statistical tools described in Section 3.3.2 to obtain distributions for the probability of ignition as a function of the spark energy.

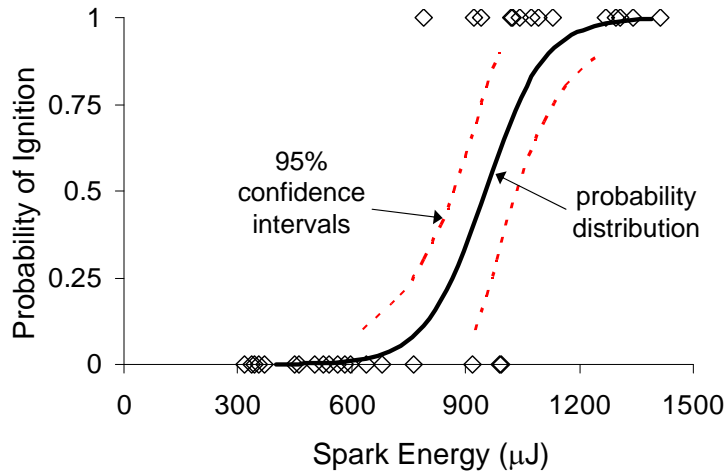
### 3.4.1 Results for Hydrogen Test Mixtures

The test data points and resulting probability distribution for ignition versus spark energy for the 5% hydrogen ARP-recommended mixture are shown in Figures 3.10 (a) and (b). The “go” and “no go” data points overlap significantly with the highest non-ignition occurring for a spark energy of 1022  $\mu\text{J}$  and the lowest ignition occurring for a spark energy of 790  $\mu\text{J}$ ; this overlap is reflected in the broadness of the probability curve. In the ARP standards, it is assumed that this mixture “has a demonstrated greater than 90% probability of ignition when exposed to a 200  $\mu\text{J}$  voltage spark source” with a gap between 1.5 and 2 mm (International, 2005). However, these results show that a significantly higher energy is required for ignition. According to the statistical analysis, the probability of ignition with a spark energy of 200  $\mu\text{J}$  is negligible, and a 90% ignition probability requires a spark energy of approximately 1120  $\mu\text{J}$ .

The data points and resulting probability distributions and 95% confidence intervals for the 6% and 7% hydrogen mixtures are shown in Figures 3.11 and 3.12, respectively. For comparison, the probability distributions and data overlap regions for all three test mixtures are shown on the same scale in Figure 3.13. Qualitatively, the probability distribution for the 5%  $\text{H}_2$  mixture is broad and the curves for the 6% and 7%  $\text{H}_2$  mixtures are much narrower and closer to representing a threshold MIE value. Quantitatively, the degree of variability can be described using a measure of the width of the distribution. To compare the variabilities of the three distributions,



(a)



(b)

Figure 3.10: Results for ignition of the 5% ARP-recommended test mixture: (a) ignition test data points with data overlap region and (b) probability distribution and 95% confidence intervals

the *relative width* of a distribution can be defined as:

$$\text{Relative Width} = \frac{(E)_{P=0.90} - (E)_{P=0.10}}{(E)_{P=0.50}} \quad (3.12)$$

where  $(E)_{P=q}$  is the spark energy corresponding to an ignition probability  $q$ , or the  $100q^{\text{th}}$  percentile, as illustrated in Figure 3.14. Using Equation 3.12 to calculate the relative widths of the distributions gives values of 0.36, 0.23, and 0.64 for the

5, 6, and 7% hydrogen mixtures, respectively. In other words, the width of the 5% hydrogen distribution is approximately 36% of the mean, etc. While the 5% hydrogen distribution qualitatively appears more variable than the other two distributions, in fact, the distribution for the 7% hydrogen mixture has the largest relative distribution with the 5 and 6% mixtures being nearly comparable. These results demonstrate that ignition in all three mixtures exhibits considerable statistical variation, suggesting that a statistical approach to analyzing ignition test data is more appropriate than the traditional MIE approach. The statistical analysis also shows significant margin in the spark energy required for ignition because the probability distributions are centered at very different spark energies; the 50% probability of ignition for the 5%, 6%, and 7% H<sub>2</sub> mixtures are 952  $\mu$ J, 351  $\mu$ J, and 143  $\mu$ J, respectively. It was shown in Section 3.2 that a very small change in the composition near the flammability limit leads to drastic changes in the flame propagation characteristics. These results demonstrate that very small changes in the hydrogen concentration also lead to significant differences in the required ignition energy. Therefore, when performing ignition tests in lean hydrogen mixtures it is imperative that the composition be well-defined if testing using a spark energy chosen for a specific mixture.

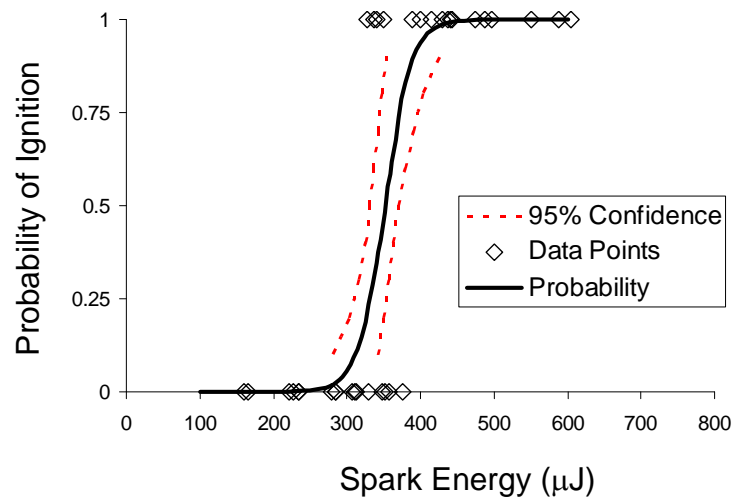


Figure 3.11: Data points and resulting probability distribution and 95% confidence intervals for the 6% hydrogen test mixture

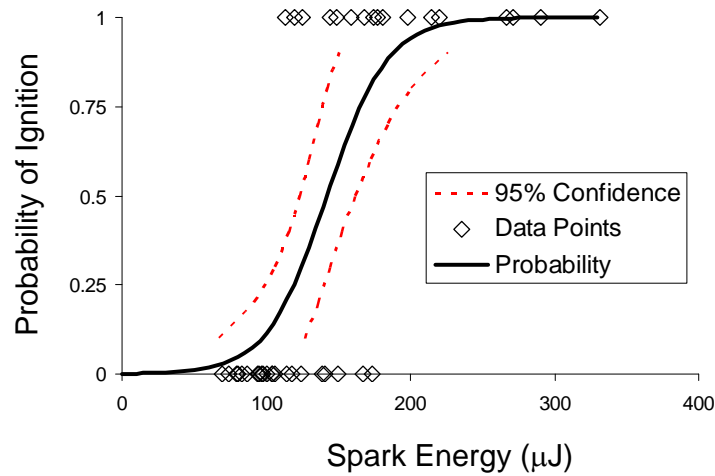


Figure 3.12: Data points and resulting probability distribution and 95% confidence intervals for the 7% hydrogen test mixture

### 3.4.2 Comparison to Historical MIE Data

The results of these tests can be compared with the classic MIE results of [Lewis and von Elbe \(1961\)](#), who obtained MIE curves for various hydrogen, oxygen, diluent mixtures. The results of the statistical analysis, specifically the 10<sup>th</sup> and 90<sup>th</sup> percentile spark energies, are compared with the MIE values from Lewis and von Elbe in [Table 3.1](#) for the 5, 6, and 7% H<sub>2</sub> mixtures. The results for the 7% H<sub>2</sub> mixtures agree extremely well—in this work, it was found that a spark energy of 97 μJ had a 10% probability of igniting the mixture, and this is nearly equal to the MIE value of 100 μJ found by Lewis and von Elbe. The 7% H<sub>2</sub> mixture was the leanest mixture for which Lewis and von Elbe presented an actual MIE data point, but they extrapolated the MIE curve to leaner compositions. According to their curve, the MIE for the 6% mixture is approximately 150 μJ. However, in these tests a spark energy of 312 μJ only has a 10% probability of ignition. Similarly, Lewis and von Elbe present an MIE of only 100 μJ for the 5% H<sub>2</sub> mixture, which is nearly 8 times smaller than even the 10<sup>th</sup> percentile of the probability distribution found in this work. These differences can be explained by two factors, the first being that Lewis and von Elbe did not directly test the 5% or 6% mixtures, but rather extrapolated a curve. The

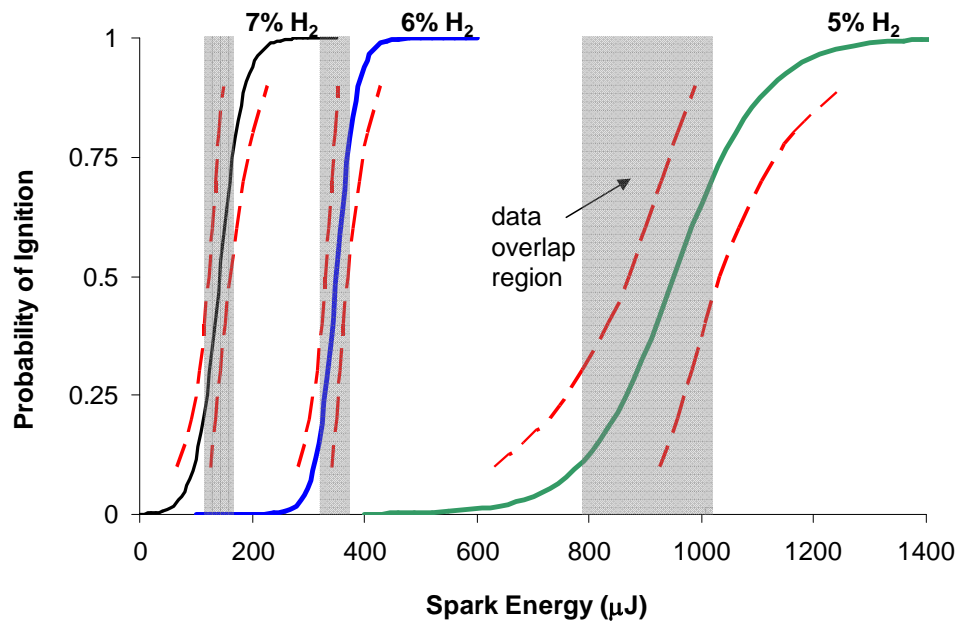


Figure 3.13: Probability distributions of ignition versus spark energy for the three hydrogen test mixtures

MIE curves are presented in Lewis and von Elbe (1961) on a logarithmic scale, so even a small error in the slope of the extrapolated curve could drastically change the MIE values for mixtures leaner than 7% H<sub>2</sub>. Also, the electrodes used by Lewis and von Elbe had glass flanges which contained the heated gas kernel for a longer period of time, producing ignition at lower energy values than with the conical electrodes used in this work. These findings raise additional issues with the ARP testing standards, where it is assumed that a 200  $\mu\text{J}$  spark will ignite the 5% mixture 90% of the time. This assumption was based on the MIE curves from Lewis and von Elbe, but, as demonstrated in this work, the required ignition energy for this mixture is substantially larger. Therefore, it is imperative to perform independent tests with any mixture under consideration for use in standard tests to correctly characterize not only the combustion characteristics but also the ignition energy.

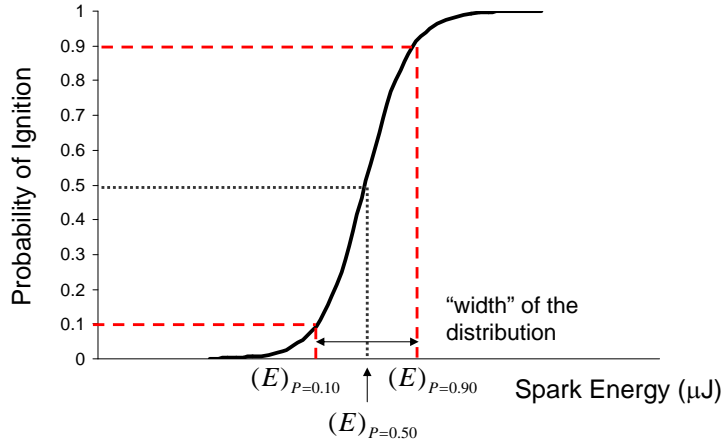


Figure 3.14: Illustration of the percentiles used to calculate the relative width of the probability distribution

Table 3.1: Comparison of the results of the statistical analysis of the spark ignition tests in lean hydrogen mixtures with historical MIE data by Lewis and von Elbe (Lewis and von Elbe, 1961)

% H <sub>2</sub>	$(E)_{P=0.10}$ ( $\mu\text{J}$ )	$(E)_{P=0.90}$ ( $\mu\text{J}$ )	MIE (Lewis and von Elbe, 1961) ( $\mu\text{J}$ )
7% H <sub>2</sub>	97	188	100
6% H <sub>2</sub>	312	391	150
5% H <sub>2</sub>	780	1123	200

### 3.4.3 Comparison with Analytical Ignition Energy

In Section 1.3.1 an analytical expression for the minimum ignition energy was given (Equation 1.20):

$$\begin{aligned}
 E_{ign} &= 61.6p \left( \frac{c_P}{R_b} \right) \left( \frac{T_b - T_u}{T_b} \right) \left( \frac{\alpha}{s_L} \right)^3 \\
 &= \frac{\xi}{s_L^3}
 \end{aligned} \tag{3.13}$$

where all the thermodynamic parameters have been combined in the coefficient  $\xi$ . This expression can be used to estimate values of the ignition energy for comparison with the experimental results obtained in this work. All the thermodynamic quantities

in the coefficient  $\xi$  were calculated for the three hydrogen test mixtures using constant pressure equilibrium calculations in Cantera (Goodwin, 2005). It is unclear what gas temperature should be used when evaluating the thermal diffusivity, so for the initial calculations it is evaluated at the ambient, unburned temperature  $T_u = 300$  K. The results of the Cantera calculations for the three mixtures are given in Table 3.2. The laminar burning velocity,  $s_L$ , is related to the speed of the flame front,  $V_f$  through the expansion ratio,

$$\epsilon = \frac{\rho_u}{\rho_b} \quad (3.14)$$

with the simple linear relation:

$$V_f = \epsilon s_L . \quad (3.15)$$

The expansion ratio is calculated in Cantera, and the flame front velocity is estimated using schlieren images by measuring the distance the flame front propagates horizontally over several frames and taking the average velocity.

Table 3.2: Thermodynamic properties of the three hydrogen test mixtures calculated using Cantera software (Goodwin, 2005)

Mixture	$c_P$ (J/kg·K)	$R_b$ (J/kg·K)	$T_b$ (K)	$\alpha$ (m <sup>2</sup> /s)	$\epsilon$
5% H <sub>2</sub>	598.9	218.5	847.7	$2.651 \times 10^{-5}$	2.755
6% H <sub>2</sub>	607.2	219.6	955.2	$2.746 \times 10^{-5}$	3.088
7% H <sub>2</sub>	615.8	220.8	1062	$2.842 \times 10^{-5}$	3.415

The flame speeds, expansion ratios, and calculated ignition energies are given in Table 3.3 for the three test mixtures. Also shown in Table 3.3 are the spark energies corresponding to the 10<sup>th</sup> and 90<sup>th</sup> percentiles from the probability distributions obtained in this work. The analytical model overestimates the ignition energy for the 5 and 6% hydrogen mixtures, most significantly for the 6% hydrogen mixture where the estimated value is approximately 2 times larger than the 90<sup>th</sup> percentile ignition en-

ergy. In the case of the 7% hydrogen mixture, the analytical model gives a reasonable estimate for the ignition energy, with 161  $\mu\text{J}$  corresponding to approximately 70% probability of ignition in the current results. If the calculation is performed using the thermal diffusivity evaluated at an elevated temperature, e.g., the average of the ambient and burned temperatures, the calculated ignition energies become even larger. The thermal conductivity increases with temperature, the density decreases with temperature, and so the thermal diffusivity increases by a factor of 3 to 4. Since in the model  $E_{ign} \sim \alpha^{-3}$ , the calculated ignition energies increase by factors of 30 to 70 to extremely unrealistic values. These calculations are based on an extremely simplified model of the spark ignition process that does not include important aspects such as mass diffusion, the geometry of the electrodes, gap size, and turbulence. In these cases, it is most likely the exclusion of mass transport that leads to the overestimated ignition energies because hydrogen has such a high mass diffusivity. Neglecting the effect of preferential diffusion results in larger ignition energies than those observed in the experiments.

Table 3.3: Flame speeds and ignition energies calculated using simple theory compared with experimental results

Mixture	$V_f$ (cm/s)	$\epsilon$	$s_L$ (cm/s)	$\xi$ ( $\mu\text{J}\cdot\text{m}^3/\text{s}^3$ )	$E_{ign}$ ( $\mu\text{J}$ )	$E_{P=0.1}$ ( $\mu\text{J}$ )	$E_{P=0.9}$ ( $\mu\text{J}$ )
5% H <sub>2</sub>	15	2.755	5.4	0.203	1291	780	1123
6% H <sub>2</sub>	21	3.088	6.8	0.242	769	312	391
7% H <sub>2</sub>	41	3.415	12	0.279	161	97	188

Additionally, the analytical model assumes that the kernel of hot gas created by the spark is spherical, while schlieren visualization shows that the kernel is more cylindrical in shape initially. To re-derive the critical kernel radius for a cylindrical kernel, the volume and surface area terms in the energy balance (Equation 1.9) must be rewritten. The volume term on the left side of the equation,  $4/3\pi r_{crit}^3$  for a sphere, must be changed to the volume of a cylinder,  $\pi r_{crit}^2 L$  where  $L$  is the length of the kernel. Also, the surface area term on the right side of the equation must be changed

from  $4\pi r_{crit}^2$  for a sphere to  $2\pi r_{crit}L$  for the surface of the cylinder in contact with the cold outer gas. The energy balance equation then becomes

$$-\frac{dm_{fuel}'''}{dt}\Delta h_c(\pi r_{crit}^2 L) \approx -\kappa \left. \frac{dT}{dr} \right|_{r_{crit}} (2\pi r_{crit}L) . \quad (3.16)$$

Using the same approximations given in Equations 1.10 to 1.14, the critical kernel radius is found to be

$$r_{crit} \approx 2 \frac{\alpha}{s_L} \quad (3.17)$$

which is approximately 18% smaller than the critical radius for a spherical kernel. To calculate the required ignition energy, the volume term in Equation 1.19 must also be changed to  $\pi r_{crit}^2 L$  for a cylinder, i.e.,

$$E_{ign} = (\pi r_{crit}^2 L) \rho_b c_P (T_b - T_u) . \quad (3.18)$$

Substituting Equation 3.17 into Equation 3.18 and solving for the ignition energy gives

$$E_{ign} = 12.6 (p) \left( \frac{c_P}{R_b} \right) \left( \frac{T_b - T_u}{T_b} \right) \left( \frac{\alpha}{s_L} \right)^2 L . \quad (3.19)$$

Therefore, in the case of a cylindrical flame kernel,

$$E_{ign} \sim \left( \frac{\alpha}{s_L} \right)^2 \quad (3.20)$$

and is proportional to the kernel length  $L$ . The ignition energies were calculated using Equation 3.19 for a cylindrical kernel and using the thermodynamic parameters and laminar burning velocities given in Tables 3.2 and 3.3. The calculated ignition energies are compared with the experimental results in Table 3.4.

The ignition energies calculated using the cylindrical kernel model are within 13% and 2% of the 50<sup>th</sup> percentile energies for the 5% and 7% hydrogen mixtures,

respectively. While the model still significantly overestimates the ignition energy for the 6% hydrogen mixture, the value found using the cylindrical kernel (585  $\mu\text{J}$ ) is closer to the experimental values than the result using the spherical kernel (769  $\mu\text{J}$ ). Modest improvements in the estimated ignition energy were obtained for all three mixtures by using a cylindrical kernel model instead of a spherical kernel. In these tests, the spark gaps used were only 1 to 2 mm in length, and so the spark length was on the same order as the initial kernel radius. Therefore, using a spherical kernel model did not lead to substantial errors in the calculations. However, for longer sparks the cylindrical kernel model should be used, as demonstrated in Section 4.3.1.

Table 3.4: Flame speeds and ignition energies calculated using the analytical model for a cylindrical kernel compared with experimental results

Mixture	$L$ (mm)	$E_{ign}$ ( $\mu\text{J}$ )	$E_{P=0.1}$ ( $\mu\text{J}$ )	$E_{P=0.5}$ ( $\mu\text{J}$ )	$E_{P=0.9}$ ( $\mu\text{J}$ )
5% $\text{H}_2$	2	1076	780	952	1123
6% $\text{H}_2$	1.5	585	312	351	391
7% $\text{H}_2$	1	141	97	143	188

## Chapter 4

# Results & Analysis: Variable-Length Spark Ignition Tests <sup>1</sup>

It is well known that the length of the spark gap will affect the energy required for ignition (Lewis and von Elbe, 1961). With a longer spark gap the energy heats a larger cylindrical volume of gas which suggests that a higher spark energy will be required for ignition than with a shorter gap. Traditional minimum ignition energy data are given for ignition tests performed with the optimal spark gap length, i.e., the spark gap that gives the lowest overall ignition energy (Lewis and von Elbe, 1961). However, in realistic physical situations, the ignition hazard is often posed by sparks with lengths different from and exceeding the minimum ignition energy spark length. For example, in the isolated conductor situation, the conductor has an extremely low capacitance and the voltage can be tens of thousands of volts, resulting in sparks several millimeters in length. Therefore, high-voltage, low-energy spark discharges are the more realistic threat, and so the spark energy may not be the most appropriate quantity to characterize the risk of ignition for real-life situations. The spark length must also be considered, and so in the second phase of ignition tests the risk of ignition versus the spark energy density (the spark energy divided by the spark length) was examined. Ignition tests were performed over a range of spark energies and spark lengths using the variable-length spark ignition system described in Section 2.3.2.

---

<sup>1</sup>Significant portions of this chapter were also presented in Bane and Shepherd (2009).

The spark length and energy were varied by varying the voltage and capacitance, respectively, producing sparks with a range of spark energy densities.

## 4.1 Capacitance Measurement

The capacitance of the short, fixed-spark ignition system described in Section 2.3.1 was measured using a simple LCR meter. However, the geometry of the variable-length spark ignition system is more complicated with the vessel acting as the circuit ground, so measurements taken with a simple LCR meter are not reliable. To accurately measure the total capacitance in the circuit a Keithley 6517A electrometer was used, a device which can measure charges on the order of nanocoulombs. The capacitor was charged to 1 kV by connecting a lead to the electrometer's precision high voltage power supply and holding that lead in contact with the electrode on the isolated plate for several seconds. A probe connected to the input of the electrometer was used to discharge the capacitor. When the probe was put in contact with the charged electrode the circuit discharged and the electrometer recorded the total charge. The discharge probe was kept inside of a Faraday cage made by connecting a metal can to the circuit ground, and after discharging the capacitor the probe was returned to the cage before reading the charge off the electrometer. The capacitance is then determined from

$$C = \frac{Q}{V} = \frac{Q_{electrometer}}{1000 \text{ V}} . \quad (4.1)$$

## 4.2 Flammable Test Mixtures

Ignition tests were performed using the variable-length spark ignition system in three flammable test mixtures. The first set of tests were performed using the 6% hydrogen mixture (6% H<sub>2</sub>, 12% O<sub>2</sub>, 82% Ar) investigated previously using short spark ignition system, as presented in Chapter 3. The second and third set of ignition tests were performed in two hexane-air test mixtures to compare ignition of a hydrocarbon

fuel with the hydrogen results. The first hexane-air mixture tested was 3.67% C<sub>6</sub>H<sub>14</sub>, 20.24% O<sub>2</sub>, 76.09% N<sub>2</sub> which is fuel-rich with an equivalence ratio,  $\phi$ , of approximately 1.72, where the equivalence ratio is defined as:

$$\begin{aligned}\phi &= \frac{\text{fuel-to-oxidizer ratio in test mixture}}{\text{stoichiometric fuel-to-oxidizer ratio}} \\ &= \frac{m_{\text{fuel}}/m_{\text{ox}}}{(m_{\text{fuel}}/m_{\text{ox}})_{\text{stoic}}} = \frac{n_{\text{fuel}}/n_{\text{ox}}}{(n_{\text{fuel}}/n_{\text{ox}})_{\text{stoic}}}\end{aligned}\quad (4.2)$$

where  $n$  is the number of moles. This particular mixture was chosen because according to the classical MIE data, this equivalence ratio gives the overall minimum ignition energy for all hexane mixtures (Lewis and von Elbe, 1961). Finally, the last set of ignition tests were performed using a stoichiometric ( $\phi = 1$ ) hexane-air mixture, 2.16% C<sub>6</sub>H<sub>14</sub>, 20.55% O<sub>2</sub>, 77.29% N<sub>2</sub>.

### 4.3 Probability Versus Spark Energy Density

The first set of ignition tests in the 6% H<sub>2</sub>, 12% O<sub>2</sub>, 82% Ar test mixture were performed using the long spark ignition system over a range of spark energies (100 to 2400  $\mu$ J) and spark lengths (1 to 11 mm). The electrodes used for the hydrogen mixture were made of tungsten with a 6.35 mm base diameter, and the tips are not conical but rather hemispherical with a radius of 3.2 mm. Using these electrodes was necessary to better control breakdown at higher voltages in the argon mixture. The energy density was obtained by dividing the spark energy by the spark gap length which was measured from schlieren images taken immediately before the gap breakdown. The results were analyzed, using the same statistical tools as employed in the short spark testing (Section 3.3), to obtain the probability distribution for ignition versus energy density, shown in Figure 4.1.

These initial tests demonstrated that the spark energy is not an appropriate quantity for investigating incendivity with sparks of variable lengths. In several of the tests, no ignition occurred even though the spark energy was significantly larger than the required ignition energies obtained using a fixed spark length. An example of this

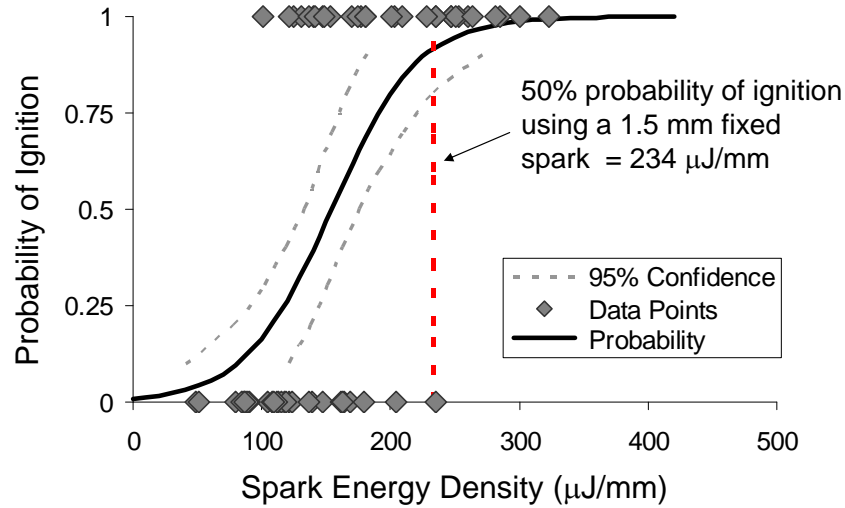


Figure 4.1: Probability distribution of ignition versus spark energy density (energy per unit spark length) for the 6% H<sub>2</sub> mixture. The 50th percentile ignition energy density for the fixed-length spark tests, obtained by dividing the energy by 1.5 mm, is indicated by the dashed line.

phenomenon is given in Figure 4.2. The spark shown in Figure 4.2(a) was 6 mm in length and had an energy of 1000  $\mu\text{J}$  and did not cause ignition. The spark shown in Figure 4.2(b) was 3 mm in length and had a significantly lower energy, 740  $\mu\text{J}$ , but did cause ignition. These seemingly contradictory results are explained when the sparks are quantified in terms of the energy density; the shorter spark had a higher energy density (247  $\mu\text{J}/\text{mm}$  versus 167  $\mu\text{J}/\text{mm}$  for the longer 6 mm spark) and therefore was more incendive and caused ignition. The probability distributions for ignition versus spark energy for the 6% H<sub>2</sub> mixtures using the fixed 1.5 mm sparks and the variable length sparks are shown in Figure 4.3. The spark energy with a 50% probability of ignition for the 1.5 mm sparks is 351  $\mu\text{J}$ , while the 50% probability energy for the variable length (1 to 10 mm) sparks was 745  $\mu\text{J}$ , nearly twice as large. Therefore, the spark energy cannot be used to compare the fixed length sparks and the variable length sparks. Instead, the long spark results were analyzed again to obtain a probability distribution for ignition versus spark energy density. The 50th percentile energy density from the 1.5 mm spark tests is 234  $\mu\text{J}/\text{mm}$  (obtained by dividing the 50th percentile energy, 351  $\mu\text{J}$ , by the spark length of 1.5 mm), while the

results of the variable long spark tests give a 50th percentile energy density of  $154 \mu\text{J}/\text{mm}$ , which is much more comparable. The energy density is lower for the long sparks because all the long spark tests where ignition occurred with a spark energy density less than  $234 \mu\text{J}/\text{mm}$  involved spark gaps of 4 mm or longer, so the quenching effect of the electrodes is reduced. Also, it was observed in the schlieren videos that for several of the longer sparks localized ignition occurred in one region of the spark channel. This phenomenon, a key source of variability in the spark ignition tests, is discussed further in Section 4.5.

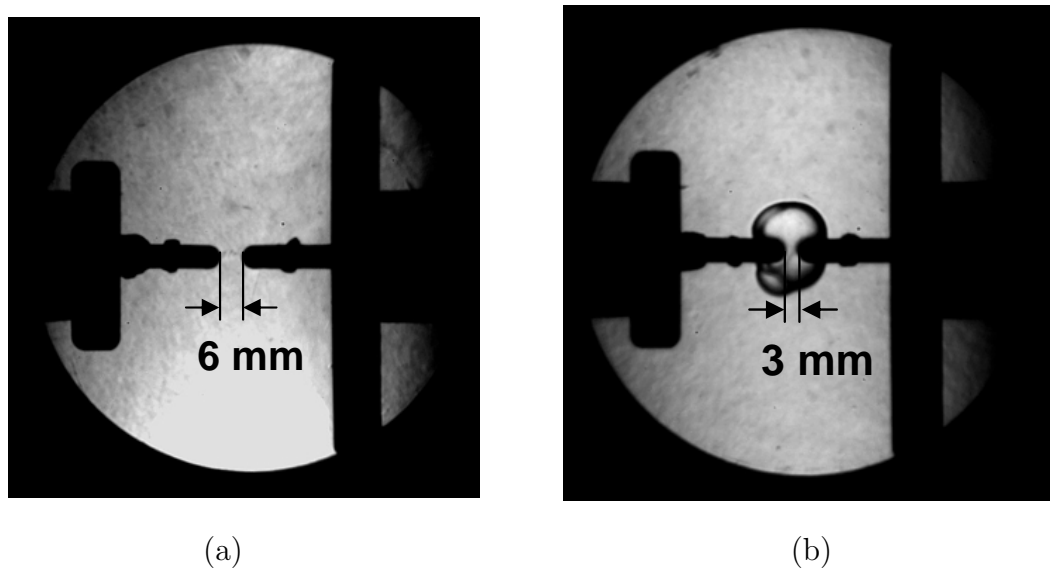


Figure 4.2: Schlieren images from two spark tests in the 6% test mixture; (a) a spark with a higher energy where no ignition occurs and (b) a spark with lower energy but larger energy density so ignition does occur

The second set of ignition tests in the rich hexane-air mixture (3.67%  $\text{C}_6\text{H}_{14}$ , 20.24%  $\text{O}_2$ , 76.09%  $\text{N}_2$ ) test mixture were performed using the long spark ignition system over a range of spark energies (180 to 1830  $\mu\text{J}$ ) and spark lengths (1.6 to 8.4 mm). The third and final set of ignition tests in the stoichiometric hexane-air mixture (2.16%  $\text{C}_6\text{H}_{14}$ , 20.55%  $\text{O}_2$ , 77.29%  $\text{N}_2$ ) test mixture were performed using a range of spark energies (1090 to 6000  $\mu\text{J}$ ) and spark lengths (2.0 to 12 mm). The resulting probability distributions for ignition versus the spark energy density for the rich and stoichiometric hexane-air mixtures are shown in Figures 4.4 and 4.5, respectively. The

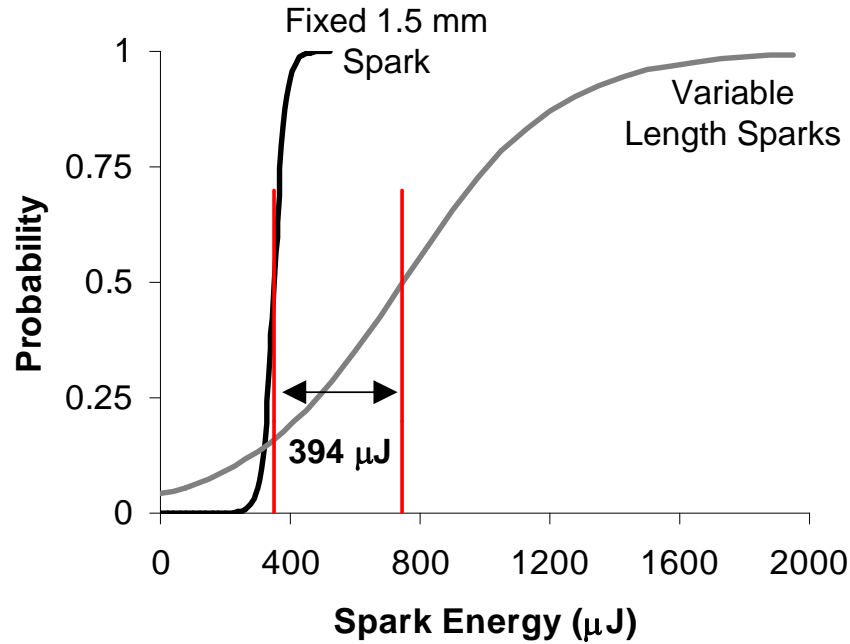


Figure 4.3: Probability distributions for ignition versus spark energy for the 6% H<sub>2</sub> test mixture with the 50th percentiles indicated by the red lines

distributions are centered (50% probability) at  $342 \mu\text{J}/\text{mm}$  and  $656 \mu\text{J}/\text{mm}$  for the rich ( $\phi = 1.71$ ) and stoichiometric ( $\phi = 1.0$ ) mixtures, respectively.

According to ignition energy curves in [Lewis and von Elbe \(1961\)](#) the MIE for the  $\phi = 1.71$  mixture is approximately  $250 \mu\text{J}$  and the MIE for the stoichiometric mixture is approximately  $900 \mu\text{J}$ . We cannot directly compare this data with our results, however, because the gap length used in the Lewis and von Elbe tests is unknown, so the energy density cannot be determined. Also, there is no information on the ignition probabilities that correspond to the historical MIE data. Therefore, only a very qualitative comparison can be made. While the spark gap used by Lewis and von Elbe is not indicated, it must have been at least as large as the quenching distance,  $d_q$ . According to [Potter \(1960\)](#) the quenching distance for the stoichiometric ( $\phi = 1$ ) mixture is approximately 1.9 mm and the quenching distance for the  $\phi = 1.72$  mixture is approximately 2.2 mm. Since the gap lengths had to have been larger than the quenching distances, the maximum possible energy densities corresponding to the

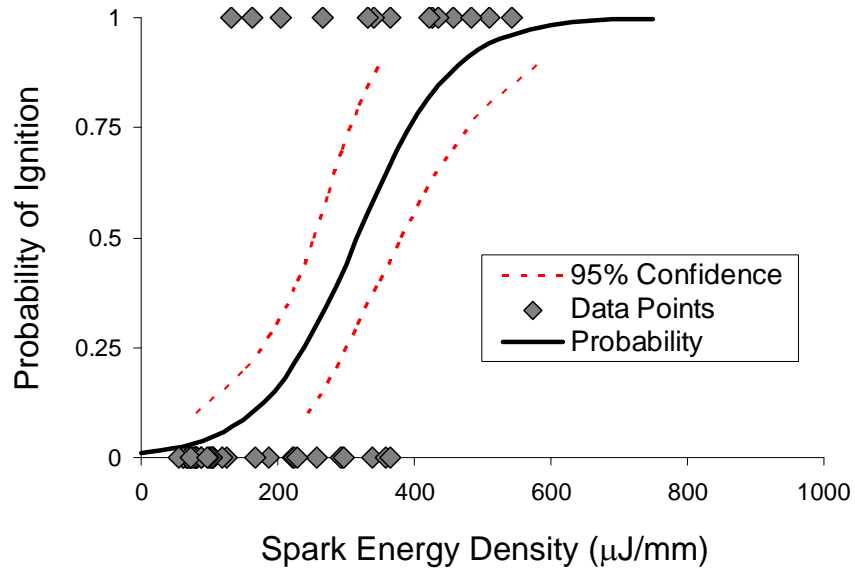


Figure 4.4: Data points and probability distributions for ignition versus spark energy density for the rich hexane-air ( $\phi = 1.72$ ) test mixture

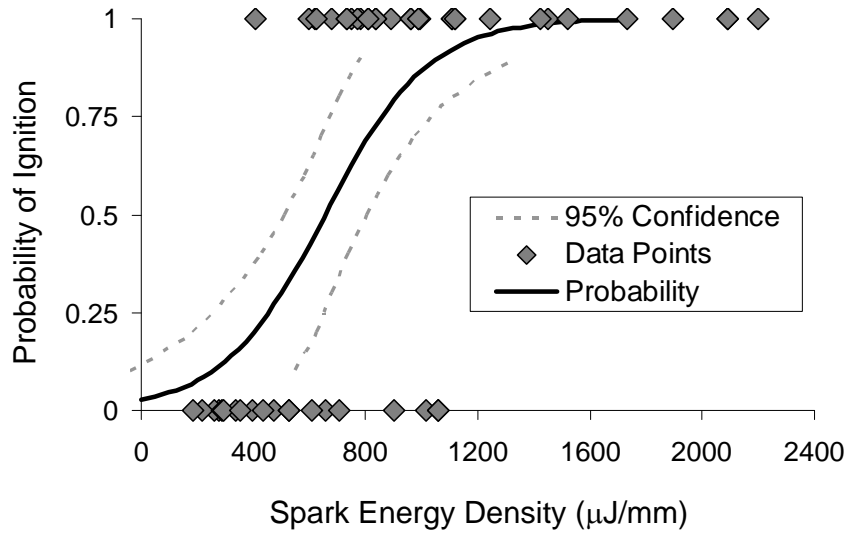


Figure 4.5: Data points and probability distributions for ignition versus spark energy density for the stoichiometric hexane-air ( $\phi = 1$ ) test mixture

MIE values obtained by Lewis and von Elbe would have been:

$$(E/d)_{max} = \frac{E_{spark}}{d_{min}} = \frac{E_{spark}}{d_q} . \quad (4.3)$$

Dividing the MIE values by their respective quenching distances gives maximum energy densities of  $114 \mu\text{J}/\text{mm}$  and  $474 \mu\text{J}/\text{mm}$  for the  $\phi = 1.72$  and  $\phi = 1$  mixtures, respectively. Comparing these energy densities to the statistical results in this work,  $114\mu\text{J}/\text{mm}$  corresponds to a 7% probability of ignition in the rich mixture and  $474\mu\text{J}/\text{mm}$  corresponds to a 27% probability of ignition. Clearly, this comparison is not exact because only rudimentary assumptions can be made about the spark gap size, but it does show some qualitative agreement between the current work and the classic MIE results. According to [Lewis and von Elbe \(1961\)](#), to obtain the MIE values the capacitance was gradually increased until ignition occurred and that stored energy was recorded as the MIE. As discussed in Section 1.3.3, there is not enough information to assign probabilities to the MIE values presented in [Lewis and von Elbe \(1961\)](#). However, the ranges of spark energy densities encompassed by the probability distributions derived in this work are comparable to the MIE results.

Finally, the probability distributions for the three test mixtures are shown together in Figure 4.6. As expected, the 6% hydrogen requires, in general, the lowest energy density to ignite while the stoichiometric hexane-air mixture requires the highest energy density to ignite. The spark energies corresponding to 10, 50, and 90% probability of ignition for the three mixtures are given in Table 4.1. The energy densities where the distributions are centered (50th percentile) differ approximately by a factor of two. To compare the relative variability of the distributions, the *relative width* of the distributions can again be used (as in Section 3.4) by changing energy to energy density in Equation 3.12:

$$\text{Relative Width} = \frac{(E/d)_{P=0.90} - (E/d)_{P=0.10}}{(E/d)_{P=0.50}} . \quad (4.4)$$

The relative widths of the distributions for the 6%  $\text{H}_2$  mixture and the rich and stoichiometric hexane-air mixtures are approximately 0.94, 1.22, and 1.13, respectively. The distribution widths are fairly comparable, suggesting that the mixture does not have a significant effect on the variability of the test results. If the specific mixture was a factor in producing variability in the ignition test results, one would expect to

see a significant difference in the relative variability, especially between the hydrogen and hexane mixtures.

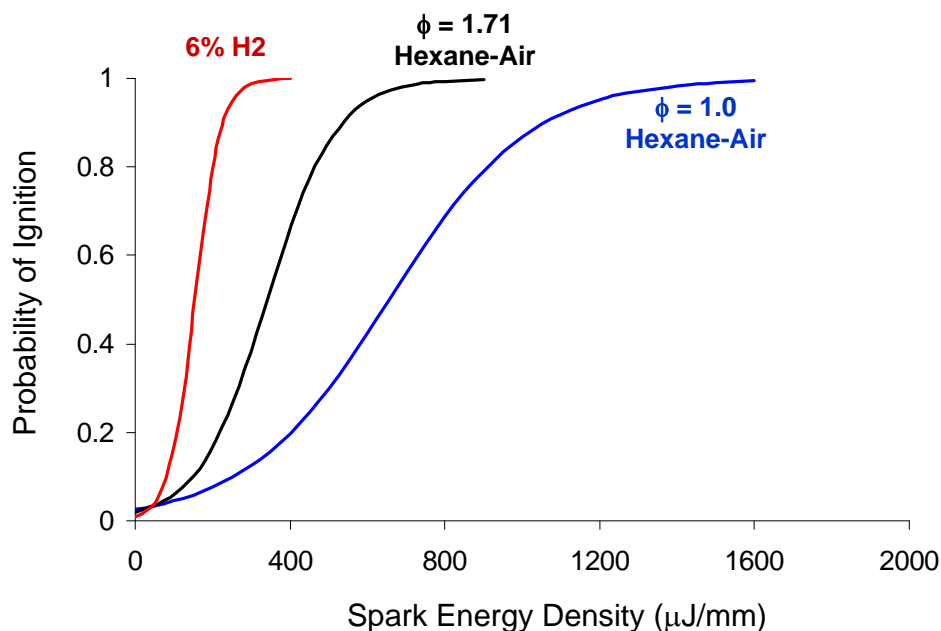


Figure 4.6: Comparison of the probability distributions for the 6% hydrogen mixtures and two hexane-air mixtures

Table 4.1: Comparison of the 10<sup>th</sup>, 50<sup>th</sup>, and 90<sup>th</sup> percentile spark energy densities for the three test mixtures

Mixture	$(E/d)_{P=0.1}$ ( $\mu\text{J}/\text{mm}$ )	$(E/d)_{P=0.5}$ ( $\mu\text{J}/\text{mm}$ )	$(E/d)_{P=0.9}$ ( $\mu\text{J}/\text{mm}$ )
6% H <sub>2</sub> , 12% O <sub>2</sub> , 83% Ar	81	154	227
$\phi = 1.72$ Hexane-Air	149	342	535
$\phi = 1$ Hexane-Air	255	656	1057

### 4.3.1 Comparison With Analytical Model

The analytical model for the ignition energy of a cylindrical kernel as described in Section 3.4.3 can be used to estimate the required energy density for ignition of the

hexane mixtures. Equation 3.19 can be used to calculate the energy density needed for ignition, i.e.

$$\frac{E_{ign}}{L} = \frac{\xi'}{s_L^2} \quad (4.5)$$

where  $L$  is the spark length and

$$\xi' = 12.6p \left( \frac{c_P}{R_b} \right) \left( \frac{T_b - T_u}{T_b} \right) \alpha^2. \quad (4.6)$$

The terms in the coefficient  $\xi'$  were calculated in Cantera using the JetSurF 1.0 chemical mechanism for  $n$ -alkane oxidation (Sirjean et al.). The results of the Cantera calculations for the two hexane mixtures are given in Table 4.2.

Table 4.2: Thermodynamic properties of the two hexane test mixtures calculated using Cantera software (Goodwin, 2005) and the JetSurF 1.0 chemical mechanism (Sirjean et al.)

Mixture	$c_P$ (J/kg·K)	$R_b$ (J/kg·K)	$T_b$ (K)	$\alpha$ (m <sup>2</sup> /s)
$\phi = 1$ Hexane-Air	1051	359.5	2278	$2.057 \times 10^{-5}$
$\phi = 1.72$ Hexane-Air	1077	428.9	1823	$1.93 \times 10^{-5}$

For the laminar burning velocities, the data obtained by Davis and Law (1998) was used. According to Davis and Law (1998), the laminar burning velocities for the stoichiometric ( $\phi = 1$ ) and rich ( $\phi = 1.72$ ) hexane-air mixtures were approximately 38.2 and 11.3 cm/s, respectively. However, when the ignition energy per length was calculated for the hexane mixtures using Equation 4.5, the values were extremely low: approximately 9.6  $\mu$ J/mm and 77  $\mu$ J/mm for the stoichiometric and fuel-rich hexane-air mixtures, respectively. It was postulated that the values were so low because of the choice to evaluate the thermal diffusivity,  $\alpha$ , at the unburned gas temperature ( $T_u = 300$  K) as done in previous calculations. The thermal diffusivity is a strong function of temperature, and due to the high adiabatic flame temperature of the mixtures, the loss of energy through conduction will be more significant for the hexane-air mixtures than

for the lean hydrogen mixtures. Therefore, as suggested by [Turns \(2000\)](#), the thermal diffusivity was re-evaluated at the average of the unburned and burned temperatures,

$$\begin{aligned}\alpha_{ave} &= \alpha(T_{ave}) \\ &= \alpha\left(\frac{T_b + T_u}{2}\right) .\end{aligned}\tag{4.7}$$

The ignition energy increases with the square of the thermal diffusivity, so the higher value of  $\alpha_{ave}$  will result in a significant increase in the energy. The values of the thermal diffusivity of the unburned gas and evaluated at the temperature  $T_{ave}$  are given in [Table 4.3](#). The laminar burning velocities ([Davis and Law, 1998](#)), values of the coefficient  $\xi'$  evaluated using  $\alpha_{ave}$ , and the ignition energies per length are given in [Table 4.4](#). Also shown in [Table 4.4](#) are the 10<sup>th</sup> and 90<sup>th</sup> percentile energy densities obtained from the experiments. The value calculated by the analytical model is within approximately 2% of the energy density corresponding to 90% probability of ignition. However, the model grossly overestimates the ignition energy density for the rich hexane-air mixture; the model predicts that the fuel-rich mixture requires a 4 times higher energy density for ignition than the stoichiometric mixture. However, the results of both [Lewis and von Elbe \(1961\)](#) and the current work demonstrate that the rich hexane-air mixture in fact has a significantly lower ignition energy than the stoichiometric mixture. The fuel-rich mixture has a lower ignition energy because of the preferential diffusion of oxygen versus hexane. In the rich hexane-air mixture, the diffusion coefficient of O<sub>2</sub> is approximately  $1.93 \times 10^{-5}$  m<sup>2</sup>/s, while the coefficient for hexane is approximately  $7.20 \times 10^{-6}$  m<sup>2</sup>/s, nearly 3 times smaller. Therefore, the oxygen will diffuse into the reaction zone much more quickly than the hexane will diffuse out, and so an excess of hexane is required to react with the additional oxygen. The analytical model does not take into account the effect of the preferential diffusion, and therefore gives a reasonable estimate for a stoichiometric mixture but would overestimate the ignition energy for lean or rich mixtures.

Table 4.3: Thermal diffusivities of the hexane-air mixtures at the unburned temperature ( $T_u = 300$  K) and at the average temperature  $(T_b + T_u) / 2$

Mixture	$\alpha_u$ (m <sup>2</sup> /s)	$T_{ave}$ (K)	$\alpha_{ave}$ (m <sup>2</sup> /s)
$\phi = 1$ Hexane-Air	$2.057 \times 10^{-5}$	1289	$2.200 \times 10^{-4}$
$\phi = 1.72$ Hexane-Air	$1.930 \times 10^{-5}$	1062	$1.450 \times 10^{-4}$

Table 4.4: Comparison of the ignition energy per length for the hexane-air mixtures calculated using the analytical cylindrical kernel model (Equation 4.5) and the results from the statistical analysis of the experiments. The laminar burning velocities  $s_L$  are by [Davis and Law \(1998\)](#).

Mixture	$s_L$ (cm/s)	$\xi'$ (J·m/s <sup>2</sup> )	$E_{ign}/L$ ( $\mu$ J/mm)	$(E/d)_{P=0.1}$ ( $\mu$ J/mm)	$(E/d)_{P=0.9}$ ( $\mu$ J/mm)
$\phi = 1$ Hexane-Air	38.2	0.1547	1071	255	1057
$\phi = 1.72$ Hexane-Air	11.3	0.0555	4346	149	535

## 4.4 Probability Versus Spark Charge

It was suggested by [von Pidoll et al. \(2004\)](#) that the charge is a more appropriate parameter than the energy or energy density for characterizing the incendivity of electrostatic discharges because it is less dependent on the voltage and gap size. Von Pidoll and the coauthors base this hypothesis on the following argument. Historical ignition energy data shows that the ignition energy increases approximately linearly with the gap distance, i.e.,

$$E \sim C_1 d \quad (4.8)$$

where  $C_1$  is a constant. Therefore the electrical stored energy is:

$$E = \frac{1}{2} CV^2 \sim C_1 d. \quad (4.9)$$

Paschen's law states that the breakdown voltage of the gap also scales approximately linearly with the spark gap size, therefore,

$$V \sim C_2 d \quad (4.10)$$

where  $C_2$  is a second constant. Substituting Equation 4.10 into Equation 4.9 gives:

$$E \sim \frac{1}{2} CV (C_2 d) \sim C_1 d \quad (4.11)$$

and combining the constants results in:

$$CV = Q \sim \text{constant} . \quad (4.12)$$

Therefore, it is hypothesized in [von Pidoll et al. \(2004\)](#) that the charge required for ignition does not vary when the voltage,  $V$ , or gap distance,  $d$ , is changed.

To investigate this hypothesis, the ignition test results for the 6% H<sub>2</sub> test mixture and the two hexane-air test mixtures were sorted by the spark length. The minimum spark charge and energy that caused ignition for each spark length was identified, and these minimum ignition values are plotted versus the spark length in Figure 4.7. The values shown in the plot are not necessarily the absolute minimum ignition charge or energy for that spark gap, only the minimum values from the tests performed in this work. However, this data can still provide insight into the dependence of the charge or energy required for ignition on the spark length. As the gap size increases the minimum charge required for ignition does increase by approximately 15%, 71%, and 39% for the  $\phi = 1.72$  hexane-air mixture,  $\phi = 1$  hexane-air mixture, and 6% hydrogen mixture, respectively. However, the percent increase in the required energy is 2.3 to 4 times larger than the percent increase in the charge. The minimum energy increases by approximately 51%, 160%, and 153% for the  $\phi = 1.72$  hexane-air mixture,  $\phi = 1$  hexane-air mixture, and 6% hydrogen mixture, respectively. These results, though only approximate given the limited number of tests, suggest that while the minimum charge for ignition may not remain exactly constant, it is less dependent on the voltage

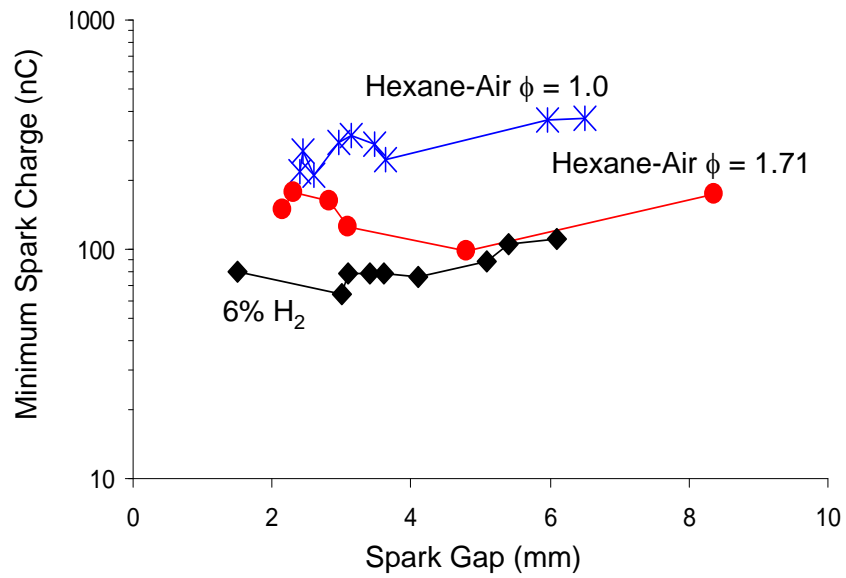
and gap size than the spark energy, and therefore may be a more appropriate measure of the incendiarity.

Probability distributions for ignition versus the spark charge were calculated for the three test mixtures, and are shown next to the probability distributions versus spark energy density in Figure 4.8(a) and (b) (6% H<sub>2</sub> mixture), Figure 4.10(a) and (b) ( $\phi = 1.0$  hexane-air mixture), and Figure 4.9 ( $\phi = 1.71$  hexane-air mixture). To directly compare the broadness of the two distributions, and therefore the variability of the test results with respect to energy density versus charge, the energy density and charge must be normalized. We normalize the energy density and charge by dividing by the 50<sup>th</sup> percentiles (50% probability of ignition). This normalization results in the probability versus  $(E/d) / (E/d)_{P=0.50}$  and  $Q/Q_{P=0.50}$  where  $(E/d)$  and  $Q$  are the energy density and charge, respectively, and  $(E/d)_{P=0.50}$  and  $Q_{P=0.50}$  are the energy density and charge corresponding to 50% ignition probability. The two probability distributions are then both centered at  $(E/d) / (E/d)_{P=0.50} = Q/Q_{P=0.50} = 1.0$  and can be shown on the same plot for comparison, as in Figures 4.8(c), 4.10(c), and 4.9(c). For all three test mixtures, the probability distribution versus charge is significantly more narrow than the distribution versus energy density, demonstrating that ignition is less variable with respect to the spark charge. For a more quantitative comparison of the two distributions, we can once again compare the broadness of curves using the relative width:

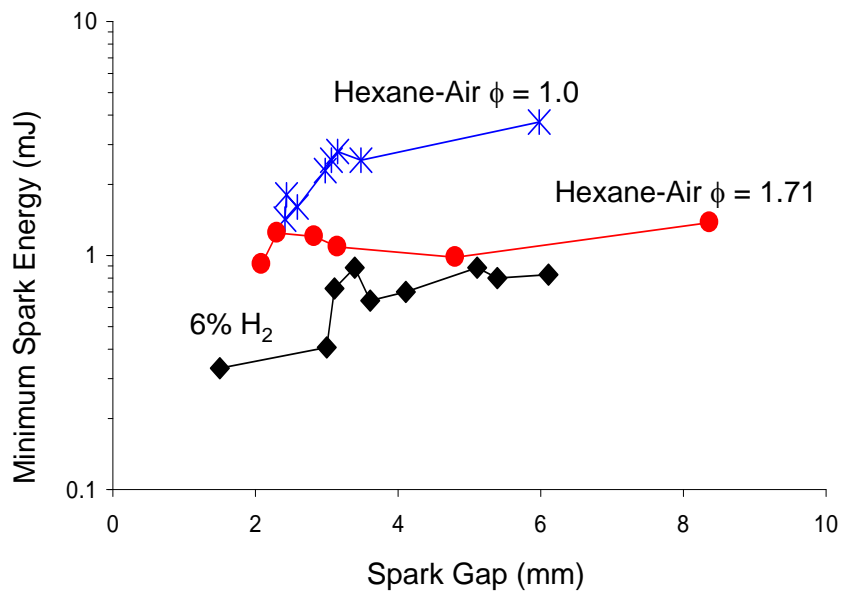
$$\text{Relative Width} = \frac{(E/D)_{P=0.90} - (E/D)_{P=0.10}}{(E/D)_{P=0.50}} \quad (4.13)$$

$$= \frac{Q_{P=0.90} - Q_{P=0.10}}{Q_{P=0.50}} \quad (4.14)$$

Using Equation 4.14, the relative widths of the distributions for ignition versus energy density are 0.94, 1.13, and 1.22 for the 6% H<sub>2</sub> mixture and rich ( $\phi = 1.72$ ) and stoichiometric hexane mixtures, respectively. The relative widths for the distributions versus charge, however, are 0.50, 0.82, and 0.77. Therefore the relative widths of the spark charge distributions are 27 to 47% smaller than the widths of the spark energy density distributions.



(a)



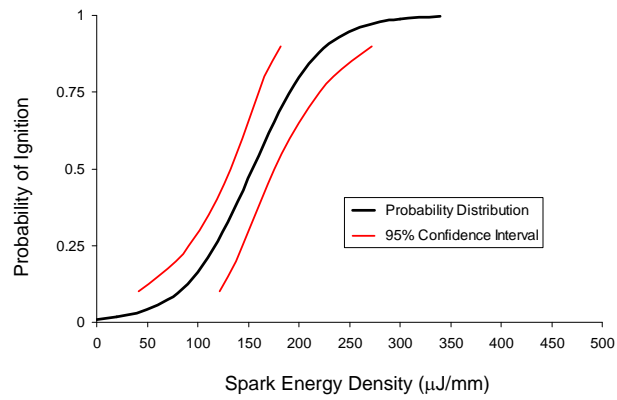
(b)

Figure 4.7: Approximate minimum spark charge (a) and spark energy (b) required for ignition versus spark gap length for the 6% H<sub>2</sub> test mixture and the two hexane-air test mixtures

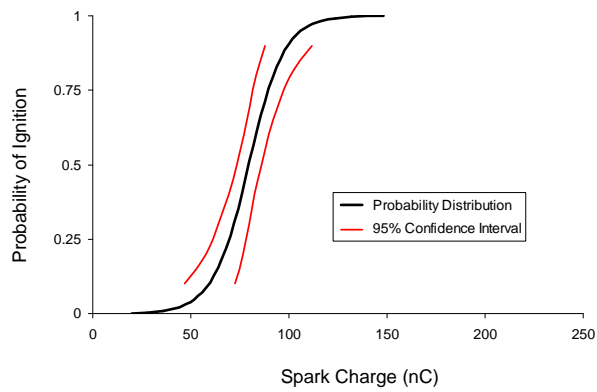
Figure 4.11 shows a comparison of the spark energy and spark charge distributions for the ignition tests using short, fixed-length sparks. In these cases, the probability distributions versus charge shows no improvement over the distributions versus spark energy due to the fact that in these tests both the voltage and the spark gap were held approximately constant. A comparison can also be made between the probability distributions for ignition versus spark charge for the short, fixed-length spark ignition tests and the variable-length spark ignition tests. The two distributions are shown in Figure 4.12, and the agreement between the results of the two sets of tests shows improvement over the comparisons using spark energy and even energy density. For example, the 50<sup>th</sup> percentile spark charge obtained from the short, fixed spark ignition tests (94 nC) is only 15% larger than the value from the variable-length spark tests (80 nC). Also, the results from the two tests give a 99% probability of ignition at approximately the same spark charge (120 nC). All these results support the idea by von Pidoll et al. that the charge may be a better characterization of the incendivity of the sparks for tests with varying voltage and gap distance. The variability of the test results was reduced significantly when the probability was analyzed in terms of the spark charge versus the energy density. Also, the charge may be a more convenient quantity for comparing the incendivity of different electrostatic discharges because the charge transfer is often easier to measure directly than energy. However, there was still a considerable degree of variability of ignition with respect to charge, the possible sources of which are discussed in Section 4.5.

## 4.5 Ignition Variability

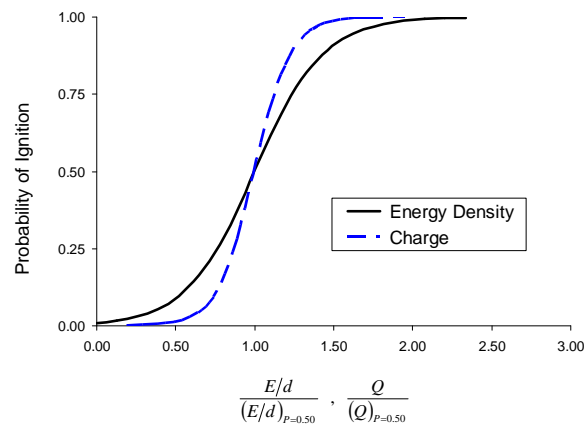
The results of the statistical analysis clearly demonstrate that there exists a significant degree of variability in the spark ignition process. In Section 4.3 it was shown the specific mixture is not the primary cause of the statistical nature of the test results, so there must be another aspect of the spark ignition process that contributes variability. The schlieren visualization revealed that variability of the initial spark channel geometry is likely an important source of variability in the ignition process.



(a)

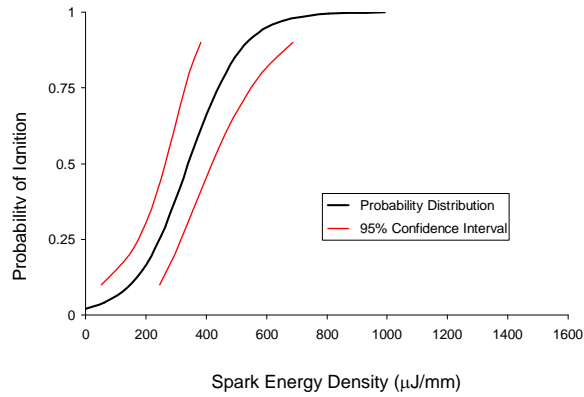


(b)

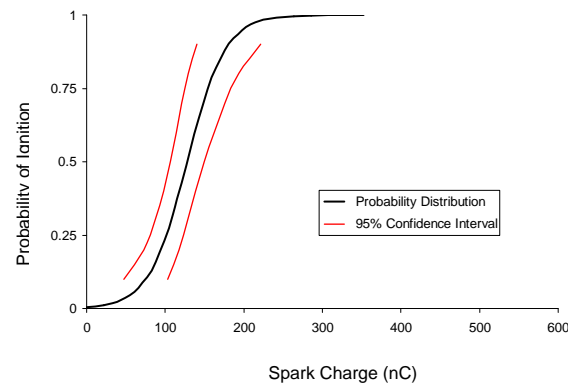


(c)

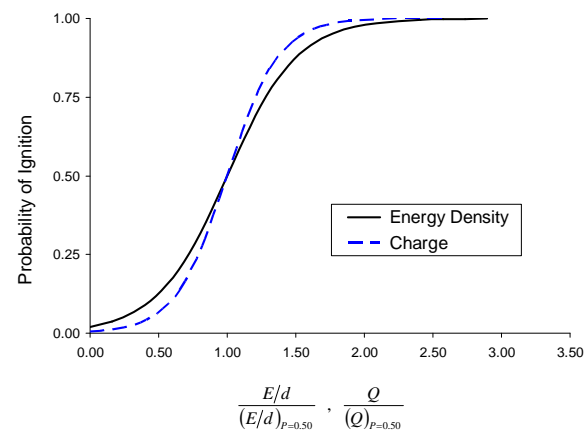
Figure 4.8: Statistical analysis of the ignition test results for the 6% H<sub>2</sub>-12% O<sub>2</sub>-82% Ar mixture. (a) Probability of ignition versus spark energy density; (b) probability of ignition versus spark charge; (c) probability versus normalized energy density and normalized charge shown on the same axis



(a)

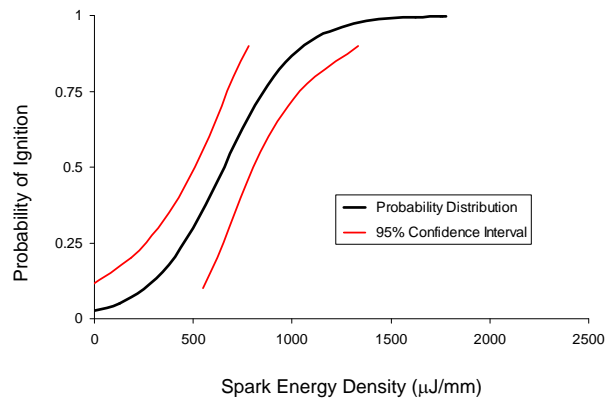


(b)

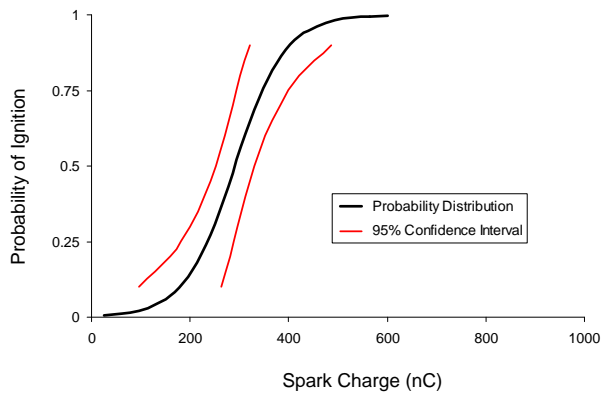


(c)

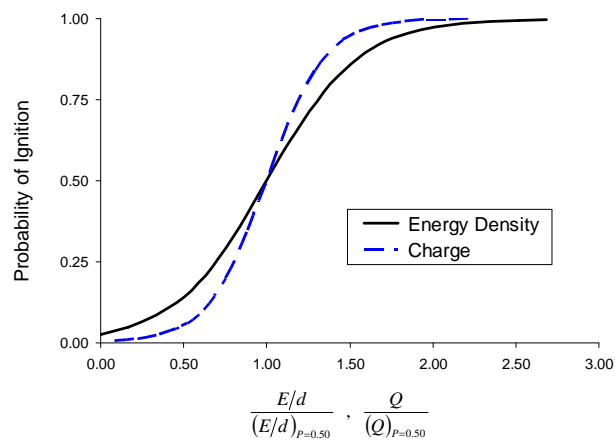
Figure 4.9: Statistical analysis of the ignition test results for the rich ( $\phi=1.72$ ) hexane-air mixture. (a) Probability of ignition versus spark energy density; (b) probability of ignition versus spark charge; (c) probability versus normalized energy density and normalized charge shown on the same axis



(a)

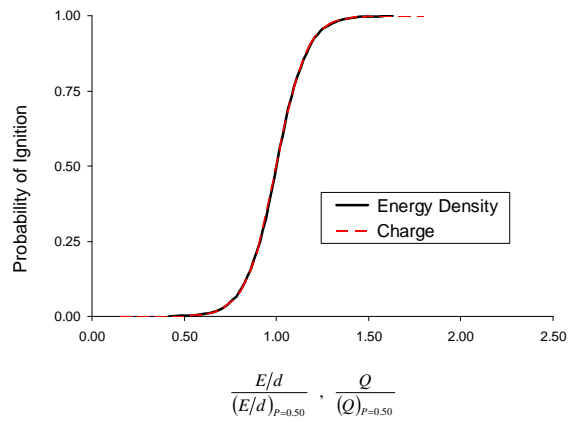


(b)

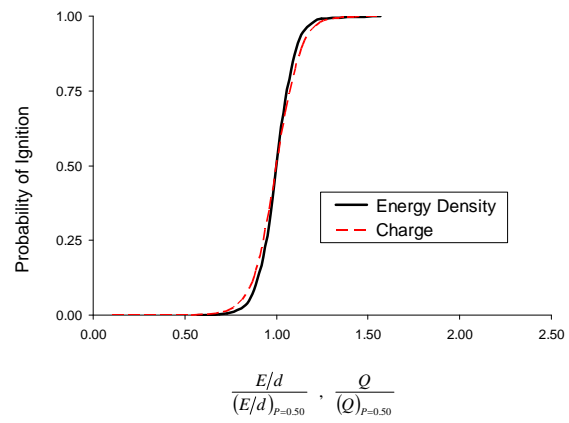


(c)

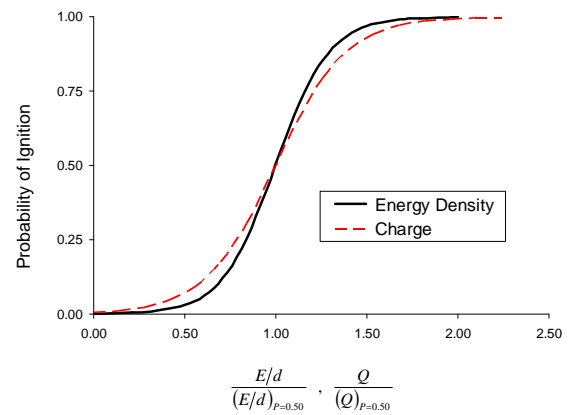
Figure 4.10: Statistical analysis of the ignition test results for the stoichiometric ( $\phi=1$ ) hexane-air mixture. (a) Probability of ignition versus spark energy density; (b) probability of ignition versus spark charge; (c) probability versus normalized energy density and normalized charge shown on the same axis



(a)



(b)



(c)

Figure 4.11: Comparison of the probability distributions for ignition versus normalized energy and charge for the short, fixed spark tests in the three hydrogen-based test mixtures. (a) 5% H<sub>2</sub>; (b) 6% H<sub>2</sub>; (c) 7% H<sub>2</sub>

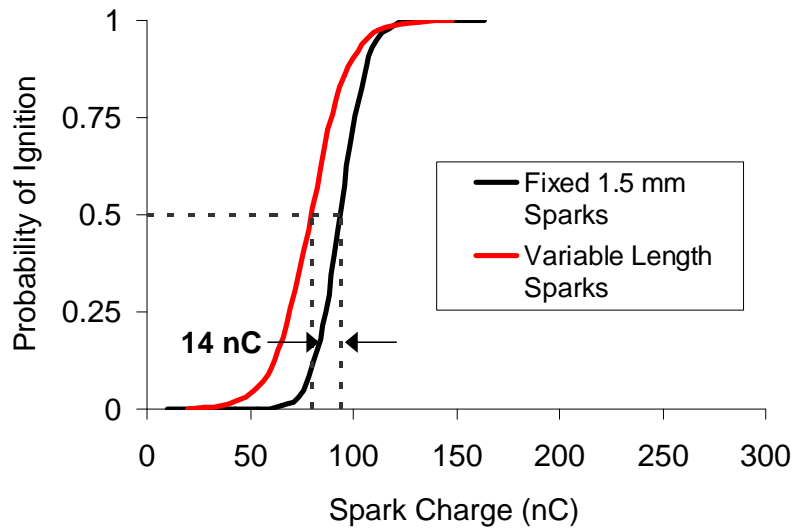


Figure 4.12: Comparison of the probability distributions for ignition versus spark charge for the short and variable-length spark ignition tests

In the tests with longer sparks, it can be seen in the schlieren videos that the spark channel is not homogeneous, and that in some cases the ignition kernel forms in only part of the channel where the channel is significantly thicker. In a number of tests, long sparks with low energy densities still caused ignition due to a bulging of the spark channel. The bulge would appear at the cathode where the electrons are bombarding the electrode surface or at some location along the spark channel where the channel is thicker due to an instability in the plasma. It is believed that these bulges in the spark channel have a higher energy density than the rest of the channel, leading to localized ignition kernels. Examples of localized ignition are presented in Figures 4.13 and 4.14. Figure 4.13 shows schlieren images of an ignition in the 6% hydrogen mixture (shot 15) with a spark energy of  $754 \mu\text{J}$ , length of 5.8 mm, and resulting energy density of  $130 \mu\text{J}/\text{mm}$ . In this test the whole spark channel does form a flame kernel, but rather a localized flame kernel forms near the center of the channel. Figure 4.14 shows close-up schlieren images of ignition in the rich ( $\phi = 1.72$ ) hexane-air mixture (shot 22) with a spark 8.4 mm in length and with a very low energy density of  $163 \mu\text{J}/\text{mm}$ . The schlieren visualization shows a large bulge in the

spark channel near the cathode (right electrode) that leads to ignition in only a fraction of the spark channel. Figure 4.15 shows magnified schlieren images of a 11.4 mm long spark channel in the 6% hydrogen mixture (shot 21). Multiple bulges along the spark channel due to instabilities of the plasma are visible, and the instabilities result in four distinct ignition kernels. In this case, the entire spark channel ultimately ignites, but the flame formation is extremely inhomogeneous. The three examples of different spark channel geometry presented in this section suggest that variability in the spark channel geometry leads to non-constant energy density along the length of the spark and leads to variability in the ignition.

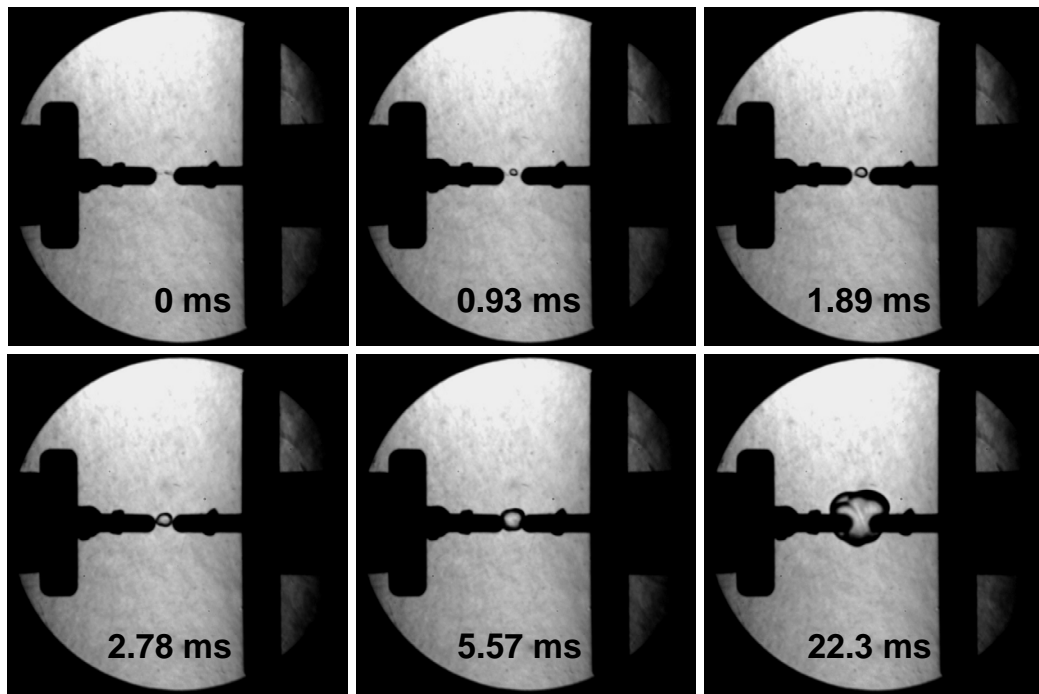


Figure 4.13: Schlieren images from high-speed video of localized ignition in the 6% hydrogen test mixture

Further evidence that the spark channel geometry is a source of variability can be found by comparing consecutive sparks with identical electrical parameters. Schlieren images of spark channels formed by three consecutive sparks in air with the same spark length, breakdown voltage, energy, and charge are shown in Figure 4.16. Even though the electrical parameters of the sparks are the same, the three spark channels have

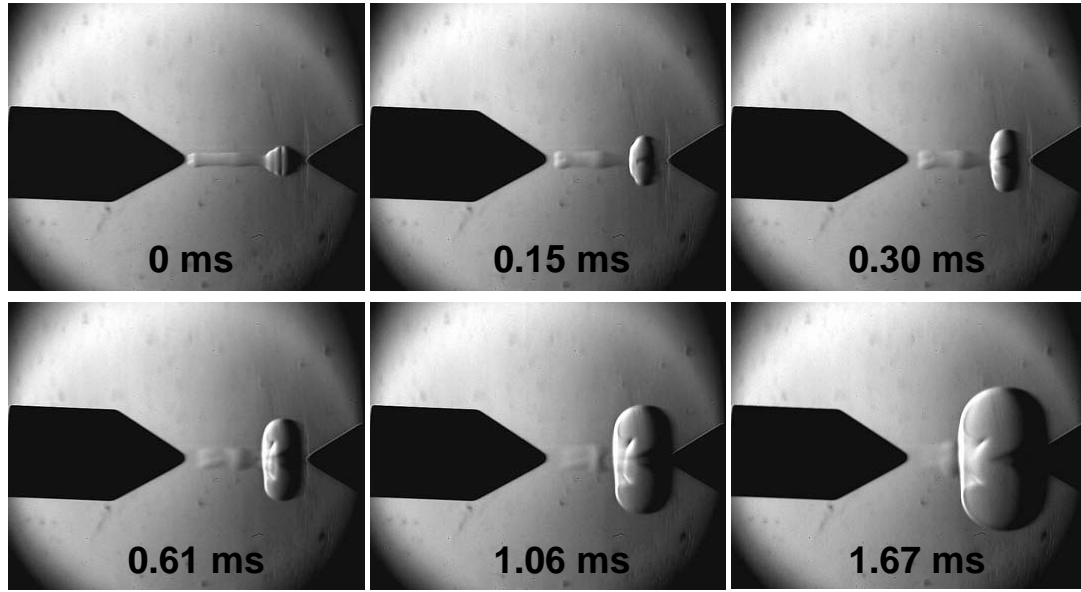


Figure 4.14: Schlieren images from high-speed video of localized ignition in the rich ( $\phi = 1.72$ ) hexane-air mixture

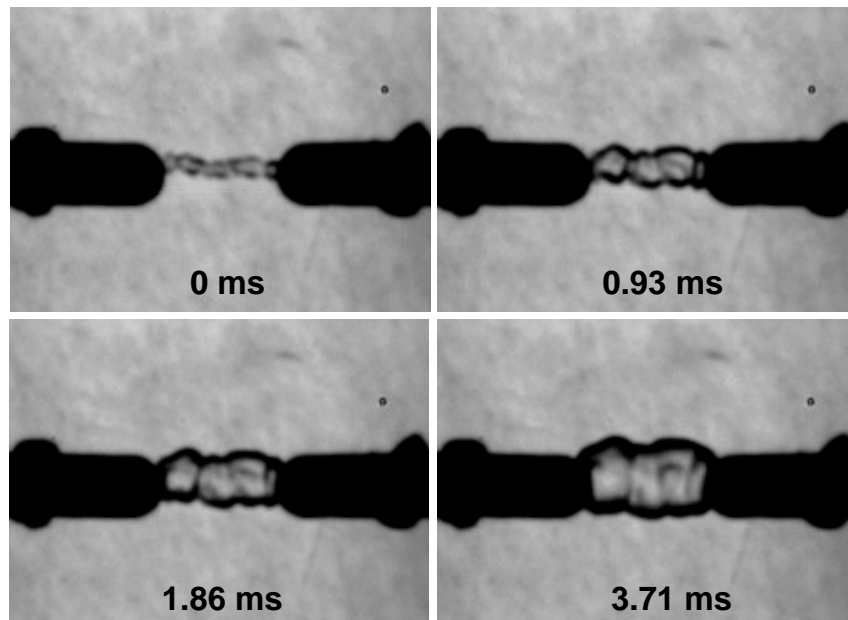


Figure 4.15: Magnified schlieren images of a spark channel in the 6% hydrogen mixtures with multiple plasma instabilities and flame kernels

three distinctly different shapes. The subsequent flow fields will therefore also be different, leading to variability in the ignition process. These images explain why the

ignition is still variable with respect to the spark charge as discussed in Section 4.4. Spark breakdown is an extremely unstable process and electromagnetic effects due to the electrical parameters, the electrode and spark gap geometry, and the condition of the electrode surfaces will affect the shape of the resulting spark channel.

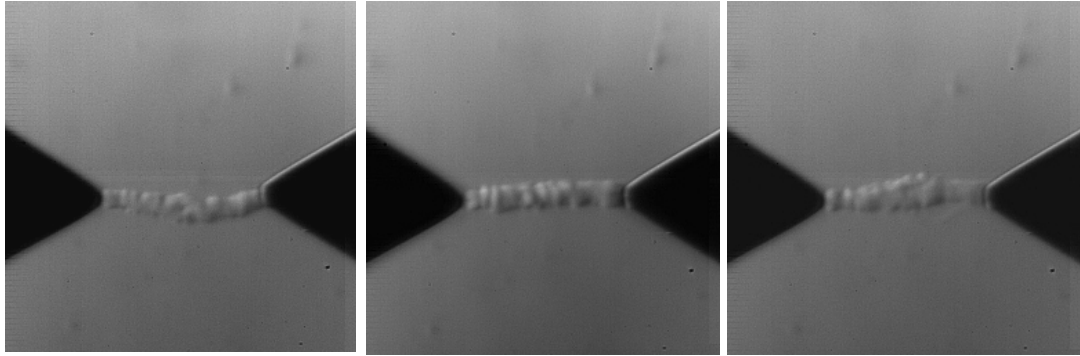


Figure 4.16: Three consecutive sparks in air with the same gap length, breakdown voltage, energy, and charge

## Chapter 5

# Numerical Modeling: Spark Discharge in Non-Reactive Gas

The energy of a spark required to ignite a gaseous mixture depends strongly on the specifics of the geometry and the electrical discharge, complicating experimental investigations. Also, as shown in this work, quantifying the statistics of ignition for a single flammable mixture, a single set of initial conditions, and one electrode geometry requires a large number of tests and a great deal of time. Therefore, in the past couple of decades several authors have done work on developing numerical tools to simulate and predict ignition. As discussed in Section 1.4, much of the previous work on simulating ignition has idealized the problem and treated one-dimensional spherical and cylindrical spark kernels. There have been some two-dimensional simulations of spark discharge in a non-reactive gas performed by [Kono et al. \(1988\)](#), [Akram \(1996\)](#), [Reinmann and Akram \(1997\)](#), and [Ekici et al. \(2007\)](#) to investigate the fluid mechanics involved in the spark ignition process and two-dimensional simulations of ignition have been performed by [Ishii et al. \(1992\)](#), [Kravchik et al. \(1995\)](#), [Thiele et al. \(2000b,a, 2002\)](#), and [Yuasa et al. \(2002\)](#). In all the two-dimensional studies, the classic toroidal shape of the hot gas kernel is observed, which occurs due to fluid flow inward toward the gap center. In most of these studies only one electrode geometry is considered and the simulations are not sufficiently resolved to capture all aspects of the fluid motion. [Akram \(1996\)](#) and [Thiele et al. \(2000b\)](#) performed simulations for several electrode geometries, however, the geometries were limited to blunt and

cone-shaped electrodes with diameters of 1 to 2 mm. Due to the complexity of modeling the ignition process, predicting ignition remains primarily an experimental issue. Developing numerical tools to reliably predict ignition in different geometries is one of the outstanding issues in combustion science.

In this work, through collaboration with Explosion Dynamics Laboratory doctoral student Jack Ziegler, the objective was to develop a numerical model of the spark ignition process that accurately captures both the chemistry and the fluid dynamics over a range of physical scales. The AMROC (Adaptive Mesh Refinement in Object-Oriented C++) software package developed by R. Deiterding (Deiterding, 2003) was used to solve the non-reactive and reactive Navier-Stokes equations including diffusion with high resolution. The first simulations were of spark discharge in a non-reactive gas (combustion air, 79% N<sub>2</sub> and 21% O<sub>2</sub>) to investigate the flow field resulting from the spark. High-speed schlieren visualization of sparks in air was also performed for comparison with and validation of the numerical model.

## 5.1 Electrode Geometries and Spark Duration

The effect of electrode geometry on the flow field subsequent to the spark discharge and was investigated for three distinctly different electrode types: thin wire, conical, and blunt cylindrical electrodes with Teflon flanges. Schematics of the electrodes are shown in Figure 5.1. The first geometry considered was very thin wire electrodes (Figure 5.1(a)) with a 0.38 mm diameter. The second electrodes studied (Figure 5.1(b)) were conical with a base diameter of 6.35 mm, a cone angle of 53 degrees, and rounded tips with a radius of curvature of approximately 0.8 mm. Finally, the flanged electrodes have a cylindrical electrode with a diameter of 1.6 mm surrounded by a round 19 mm diameter flange. These electrode shapes were used with a fixed spark gap of 2 mm in both the numerical simulations and the experiments. The conical electrodes used in the experiments were the same tungsten electrodes used in the short spark ignition testing (described in Section 3.4). The wire electrodes were made of tungsten welded to the end of a threaded rod. For the flanged electrodes, the cylindrical

electrode was made of tungsten and the flanges were made of Teflon so they would not conduct heat from the spark kernel.

Only a few authors have considered conical electrodes (Akram, 1996, Thiele et al., 2000b) and in these studies the base diameters of the electrodes were 1 to 2 mm. Thin cylindrical electrodes have been considered by several authors (Kono et al., 1988, Akram, 1996, Ekici et al., 2007, Ishii et al., 1992, Kravchik et al., 1995, Thiele et al., 2000b). In all the studies except Kono et al. (1988) the diameters of the cylindrical electrodes were 1 or 2 mm; in the present study the diameter is 0.38 mm, on the order of the thickness of the initial spark channel. Finally, in our work, flanged electrodes are also considered. This geometry is particularly important because flanged electrodes were used to obtain the classic minimum ignition energy and quenching distance data (Lewis and von Elbe, 1961) that is still relied on extensively in scientific literature and safety standards. The role of the flanges in the ignition process is not well understood and there have been few studies which consider flanged electrodes.

In both the simulations and experiments in the current study only very short sparks (on the order of 100 ns) are considered. In some of the previous modeling work (Ishii et al., 1992, Thiele et al., 2000b, 2002) sparks with a breakdown phase followed by a long arc phase (10 to 100  $\mu$ s) are used to simulate sparks from circuits with a significant inductance component, e.g., an automotive spark plug. Shorter duration ( $< 1 \mu$ s) sparks are more consistent with electrostatic discharge hazards in aviation and other industries.

## 5.2 Numerical Simulation

### 5.2.1 Model Description

For the simulations of spark discharge in a non-reactive gas, the Navier-Stokes equations for two-dimensional, compressible, viscous, heat-conducting flow were solved in cylindrical coordinates. With  $x_1 = x$ ,  $x_2 = r$  and  $u_1 = u$ ,  $u_2 = v$  representing the positions and velocities in the axial and radial directions, respectively, the continuity

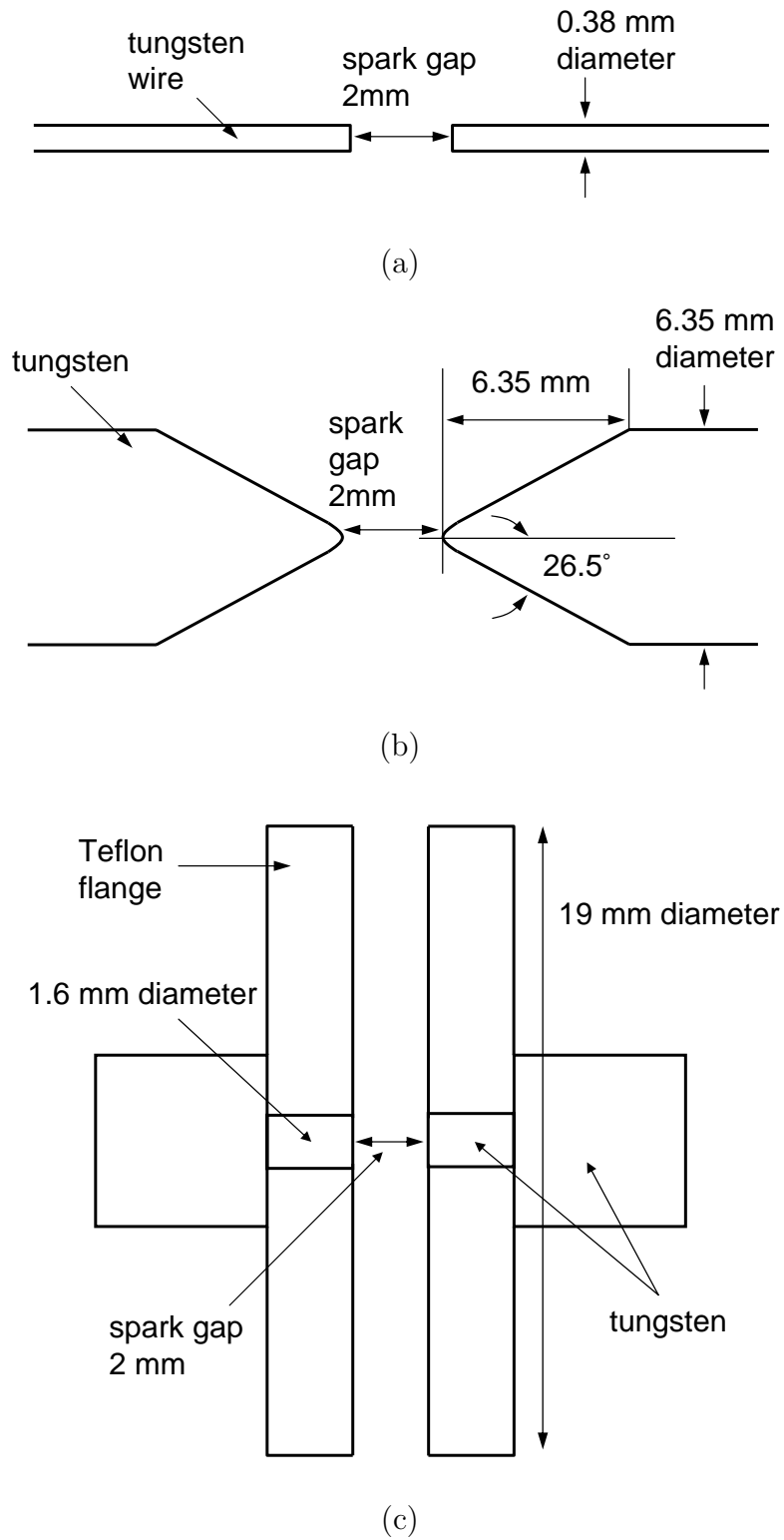


Figure 5.1: Three electrode configurations used in the experiments and numerical simulations: (a) wire electrode; (b) conical electrode; and (c) flanged electrode

equation in differential form is

$$\frac{\partial \rho}{\partial t} + \frac{\partial (\rho u_i)}{\partial x_i} = -\frac{1}{r} \rho v \quad (5.1)$$

where  $\rho$  is the gas density. The momentum equations in the axial and radial directions are

$$\frac{\partial (\rho u_j)}{\partial t} + \rho \frac{\partial (u_i u_j)}{\partial x_i} + \frac{\partial p}{\partial x_j} = \frac{\partial \tau_{ij}}{\partial x_j} - \frac{1}{r} \rho v^2 \quad (5.2)$$

where  $p$  is the pressure  $\tau_{ij}$  is the viscous stress tensor. Finally, the energy equation including viscosity and heat conduction

$$\frac{\partial (\rho e_t)}{\partial t} + \frac{\partial (\rho u_i e_t)}{\partial x_i} + \frac{\partial (u_i p)}{\partial x_i} = \frac{\partial (\tau_{ij} u_j)}{\partial x_i} - \frac{\partial q_i}{\partial x_i} - \frac{1}{r} (\rho e_t + p) v \quad (5.3)$$

where  $e_t$  is the total internal energy and  $\partial q_i / \partial x_i$  is the heat flux described by Fourier's law:

$$\frac{\partial q_i}{\partial x_i} = \frac{\partial}{\partial x_i} \left( -\kappa \frac{\partial T}{\partial x_i} \right) \quad (5.4)$$

where  $\kappa$  is the thermal conductivity of the gas. The system of 4 scalar equations (Equations 5.1–5.3) is closed using the ideal gas relations:

$$e_t = -\frac{p}{\rho(\gamma - 1)} + \frac{u_i u_i}{2} \quad (5.5)$$

$$p = \rho R T \quad (5.6)$$

where  $\gamma$  is the ratio of specific heats and  $R$  is the specific gas constant.

The temperature dependence of the thermal conductivity and viscosity were described using the Sutherland law,

$$\kappa = \kappa_{ref} \left( \frac{T}{T_{ref}} \right)^{3/2} \frac{T_{ref} + s_\kappa}{T + s_\kappa} \quad (5.7)$$

and

$$\mu = \mu_{ref} \left( \frac{T}{T_{ref}} \right)^{3/2} \frac{T_{ref} + s_{\mu}}{T + s_{\mu}}. \quad (5.8)$$

The parameters  $T_{ref}$ ,  $s_{\kappa}$ , and  $s_{\mu}$  were chosen to fit the temperature dependence to calculations performed using Cantera software (Goodwin, 2005), as shown in Figure 5.2. Thermodynamic properties were evaluated as a function of temperature using a standard subroutine library. The properties model was valid up to 5000 Kelvin, and constant properties were assumed for the high temperature phase.

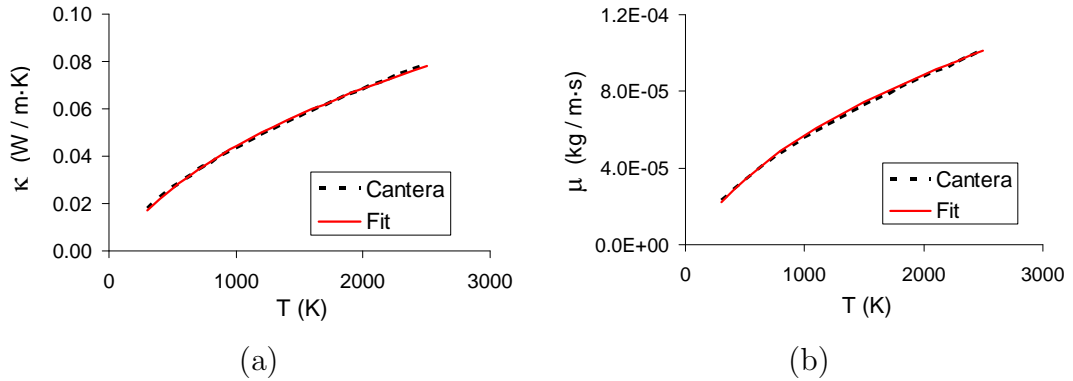


Figure 5.2: Fits of the temperature dependence of (a) the thermal conductivity and (b) the viscosity to Cantera calculations

## 5.2.2 Initial and Boundary Conditions

Simulation of the spark breakdown phase is beyond the scope of this work. Therefore, the imposed initial conditions were used to model the plasma channel between the electrodes that results from the spark breakdown. The initial conditions are based on those used in Kravchik et al. (1995) and Thiele et al. (2000b), which in turn were motivated by the work of Maly and Vogel (Maly and Vogel, 1979, Maly, 1984). The initial conditions are those of a plasma channel at thermodynamic equilibrium approximately 60 ns after breakdown (Maly and Vogel, 1979, Maly, 1984). The plasma is modeled as a thin cylindrical channel between the electrodes with a temperature of

35,000 K and a pressure of 1 MPa. The channel is 2 mm long, the length of the spark gap, and the radius of the channel is determined from the spark energy. Assuming the spark energy is deposited under constant volume conditions, the volume of the spark channel is

$$V_c = \frac{E_{spark}}{c_V \rho_0 (T_c - T_0)} \quad (5.9)$$

where  $T_c$  is the temperature of the channel and  $\rho_0$  and  $T_0$  are the density and temperature of the ambient gas. Taking a cylindrical channel of length  $d_{gap}$ , then the channel radius is

$$r_c = \left( \frac{V_c}{\pi d_{gap}} \right)^{1/2}. \quad (5.10)$$

In the spark discharge studies without ignition, the gas used in the simulations is air (79% nitrogen, 21% oxygen) and the following values were assumed within the spark channel:  $c_V = 721$  J/kg·K,  $\rho_0 = 1.15$  kg/m<sup>3</sup>,  $T_k = 35,000$  K; and outside the channel  $T_0 = 300$  K and  $p_0 = 0.1$  MPa.

In both the experiments and simulations the spark energy used is  $E_{spark} = 2$  mJ and the spark gap is  $d_{gap} = 2$  mm. Using Equations 5.9 and 5.10, the volume and radius of the spark channel used for the initial condition is approximately 0.07 mm<sup>3</sup> and 0.1 mm, respectively. The Ghost Fluid Method (GFM) is used to model the solid electrode boundary and to enforce the no slip boundary condition, and the electrode is modeled as an adiabatic boundary so heat loss to the electrode is neglected. There are two planes of symmetry, the boundaries  $r = 0$  and  $x = 0$ , and so only one quadrant of the flow domain must be computed. A schematic of the computational domain and boundary conditions is given in Figure 5.3, and the initial pressure field for the simulation is shown in Figure 5.4.

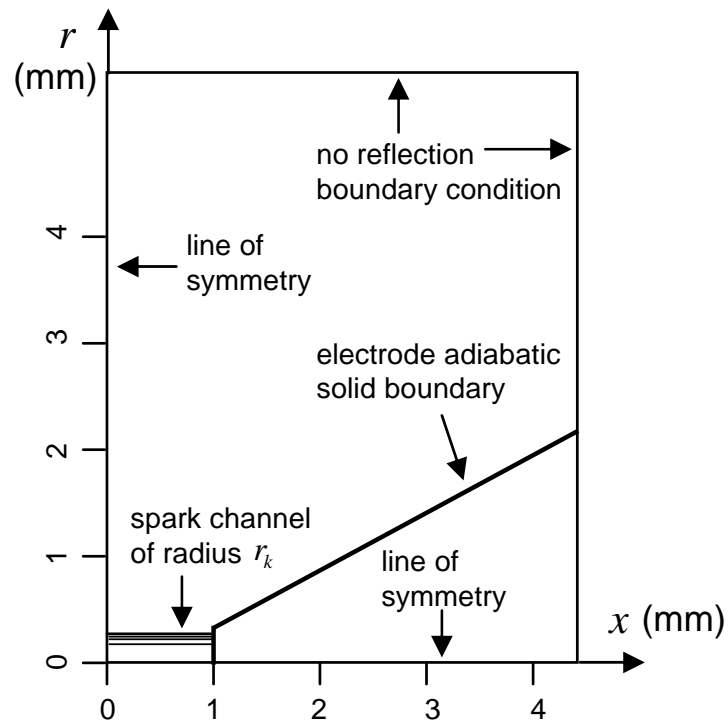


Figure 5.3: Computational domain and boundary conditions for the numerical simulation

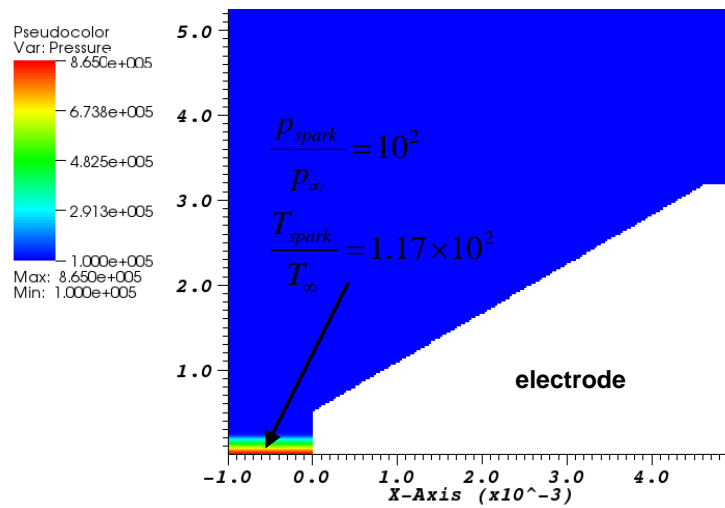


Figure 5.4: Initial pressure field for the spark discharge and ignition simulations

### 5.2.3 Numerical Solution

The computational fluid dynamics code AMROC (Adaptive Mesh Refinement in Object-Oriented C++) (Deiterding, 2003) was used when solving the equations described in Section 5.2.1. AMROC uses an improved version of the blockstructured adaptive mesh refinement algorithm of Berger and Olinger (Berger and Olinger, 1984) and Berger and Colella (Berger and Colella, 1988), allowing for highly resolved simulations. The algorithm used in AMROC was developed especially for the solution of hyperbolic partial differential equations of the form

$$u_{i,t} + f(u_i)_{i,i} = \Phi_i(u_i) . \quad (5.11)$$

The finite volume scheme used in this work was MUSCL, a variant of Roe’s second-order slope-limited method. Diffusion was modeled in the simulation using second-order finite differences. The finite volume method solves for the convective fluxes, and then a diffusive flux was added before updating with forward Euler integration. The diffusive flux includes the viscous shear and heat conduction. Second-order accuracy in time is obtained using the Strang splitting method. The Strang time splitting procedure was also applied to the cylindrical source terms using a second-order, two-step Runge-Kutta method.

For the grid refinement, criteria were used that capture the physics of each length scale in the problem. The gradients of the density, radial and axial velocities, and energy were used for the convective, viscous, and conductive length scales, respectively. When a gradient across two cells becomes larger than a user-specified tolerance, a refinement level is added.

## 5.3 Schlieren Visualization

High-speed schlieren visualization of spark discharge in air was performed using the schlieren system with a close-up view of the spark gap described in Section 5.2.1. Sparks with energies of 2 mJ and 2 mm in length were generated using the spark

ignition system described in Section 2.3.2. A Vision Research Phantom v710 high-speed camera was used to take schlieren video at rates of 10,000 to 79,000 frames per second with resolutions from 800 x 800 to 256 x 256, respectively. High-speed schlieren video was obtained of spark discharges in air using multiple camera speeds for the three different electrode geometries.

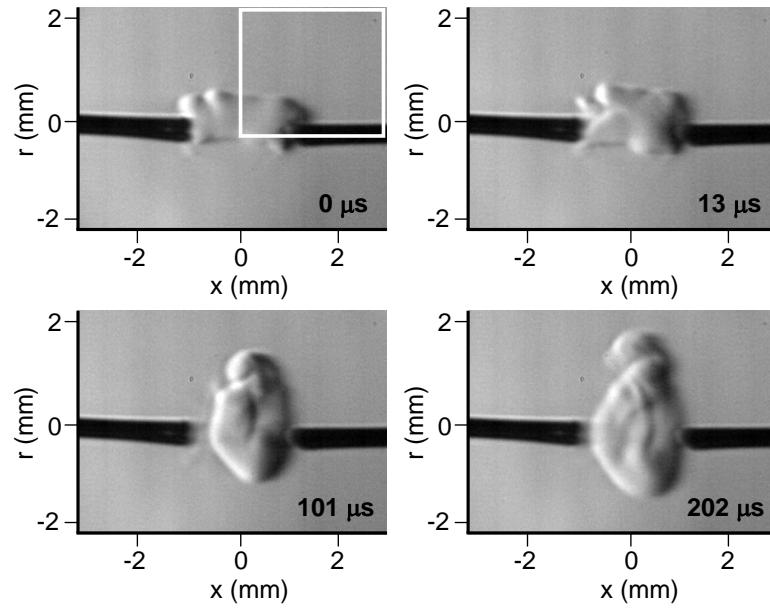
## 5.4 Results: Spark Discharge in Air

Images from high-speed schlieren visualization of a 2 mJ spark discharge in air using the 0.38 diameter cylindrical electrodes and images of the density field from the two-dimensional simulation at approximately the same time steps are shown in Figures 5.5(a) and (b), respectively. The video was taken at a rate of 79,069 frames per second with a total field of view of approximately 6.7 mm x 6.7 mm. Dimensions are given on the images in millimeters, and the computational region is indicated on the first schlieren image by a white box. The first image is taken less than 12.6  $\mu$ s after the spark breakdown and for this discussion corresponds to time  $t = 0$ . The spark breakdown creates a thin plasma channel at high temperature and pressure, as described in Section 5.2.2, and when the channel expands, a blast wave propagates outward while a rarefaction wave propagates inward toward the center of the channel. The rarefaction reflects at the center of the channel and propagates back outward and is seen trailing the blast wave in the pressure contours from the simulation. Initially, the shock wave is nearly a pure cylindrical wave except for very close to the electrode surface, where the wave is spherical in nature. Because the pressure gradient following a cylindrical shock wave is smaller than that following a spherical shock wave, the pressure is higher in the middle of the channel than next to the electrodes, causing gas to flow outward toward the electrode surface, as illustrated in Figure 5.6. The flow separates and creates a clockwise-rotating vortex at the corner of the face and cylindrical body of the electrode, and additional vorticity is generated from the boundary layer due to the flow along the electrodes. The pressure gradient rapidly decreases and as the outward flow stops, the vortices propagate outward from the corner and

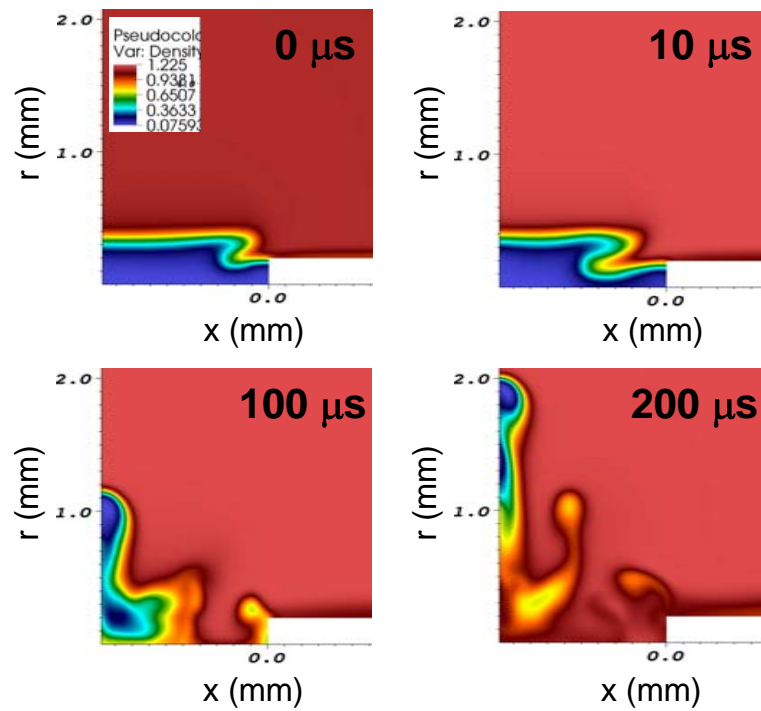
pull fluid inward along the electrode as shown in both the schlieren visualization and simulation at approximately  $10 \mu\text{s}$ .

The vorticity contours from the computation reveal that by  $10 \mu\text{s}$  a counter-rotating vortex pair has formed near the tip of the electrode, shown in Figure 5.7. The clockwise rotating vortex (top) is a result of the flow separation, and the counter-clockwise rotating vortex (bottom) is a result of the shear layer that develops due to flow moving outward against the inflow. The clockwise rotating vortex is convected towards the center of the channel by the inflow, and when the inflowing gas reaches the vertical plane of symmetry at approximately  $40 \mu\text{s}$ , it turns vertical and convects the vortex up out of the channel until it is dissipated. Because there is a vertical plane of symmetry at the center of the channel, it is expected that a counter-clockwise rotating vortex would be generated from the other electrode and propagate upwards as part of a vortex pair. The schlieren visualization of the kernel clearly shows this phenomenon, as well as the symmetry about the  $r = 0$  plane. The temperature results from the simulation, shown in Figure 5.8 reveal that the vortex trapped a kernel of hot gas, preventing it from being cooled by the gas inflow, and this hot kernel continues to propagate vertically from the center of the channel. The kernel cools quickly and its temperature decreases below  $1000 \text{ K}$  by  $80 \mu\text{s}$ . There is also a mixing region near the channel and the inflow of cool gas causes this region to be significantly cooler than the rising kernel. The major features of the flow field in the simulation are also observed in the schlieren visualization, including the inflow of cold gas immediately following expansion of the spark channel, the rising hot kernel, and the mixing region.

Images from schlieren visualization of the spark discharge with the conical electrodes and the density fields from the two-dimensional simulation are shown in Figures 5.9(a) and (b), respectively. The images were taken at the same time steps as those for the cylindrical electrode case for comparison. In this geometry, the competition between spherical and cylindrical expansion is more predominant than in the cylindrical electrode case. Once again, clockwise-rotating vortices are generated near the tip of the electrode due to flow separation and boundary layer vorticity and induce inflow into the channel. The vortices are weaker in this geometry than in



(a)



(b)

Figure 5.5: Spark discharge in air using wire electrodes: (a) images from high-speed schlieren visualization and (b) density fields from the simulation. The simulation region corresponds to the quadrant outlined in white on the upper left schlieren image

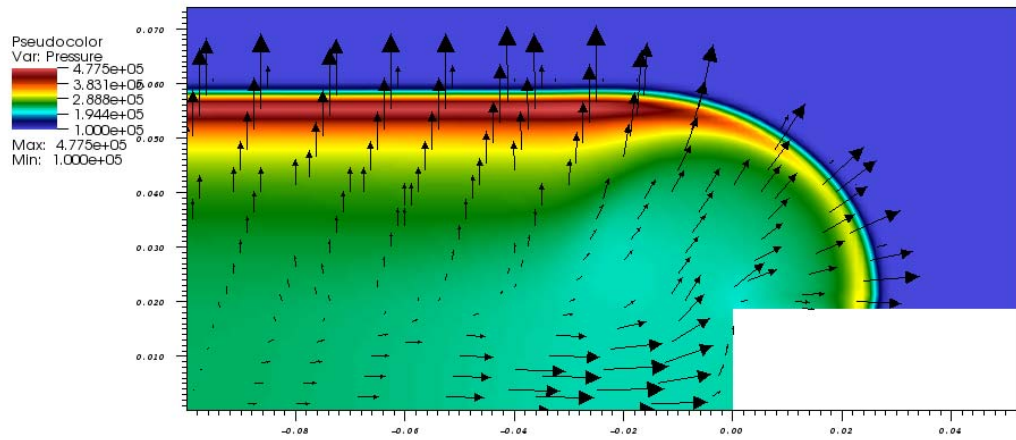


Figure 5.6: Simulated pressure field and velocity vectors showing the cylindrical and spherical portions of the blast wave at time  $t = 0.5 \mu s$

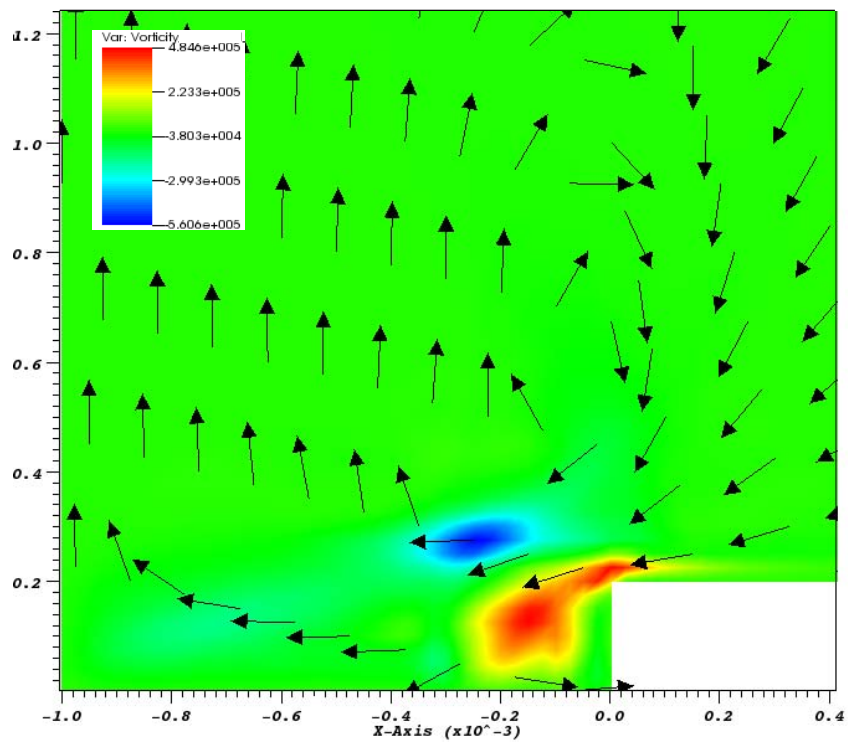


Figure 5.7: Simulation results (vorticity and velocity vectors) showing the vortex pair generated near the tip of the cylindrical electrode at time  $t = 10 \mu s$

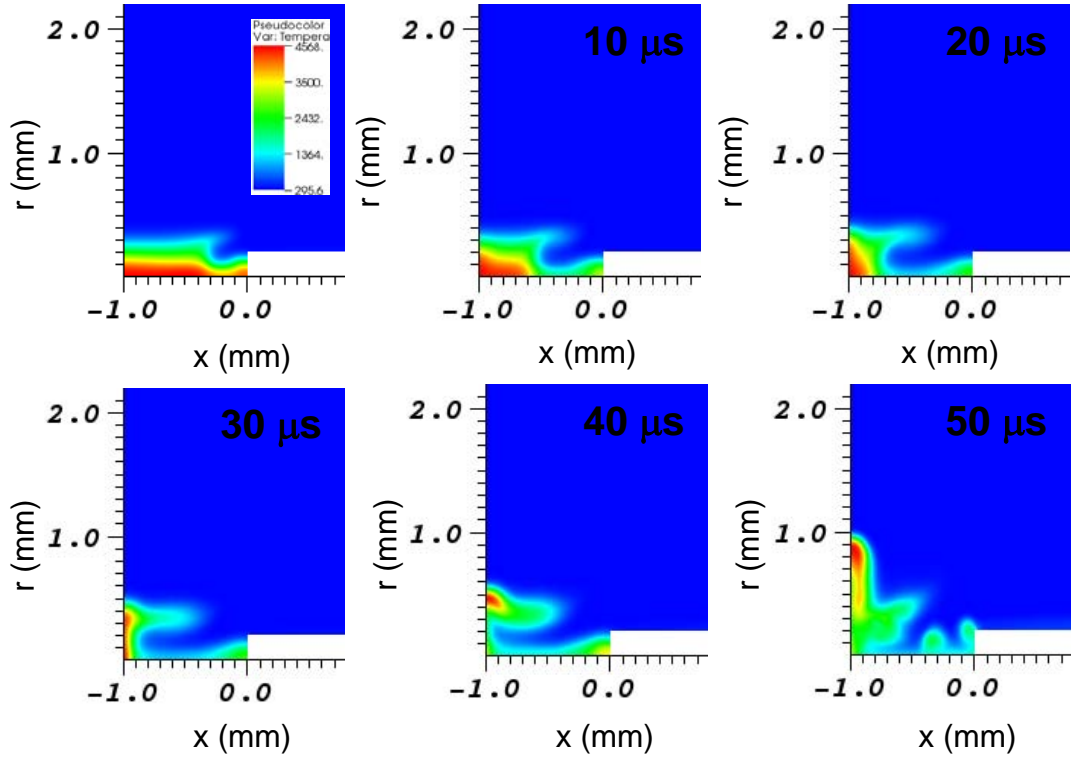
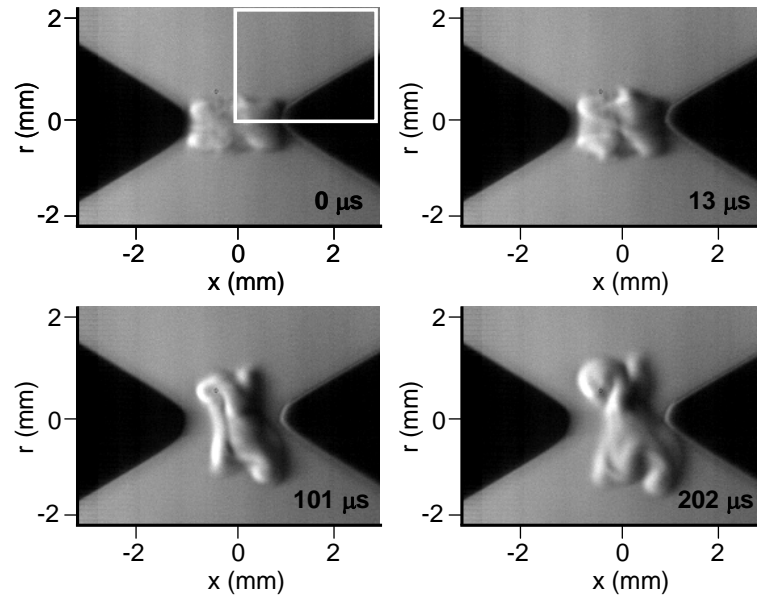


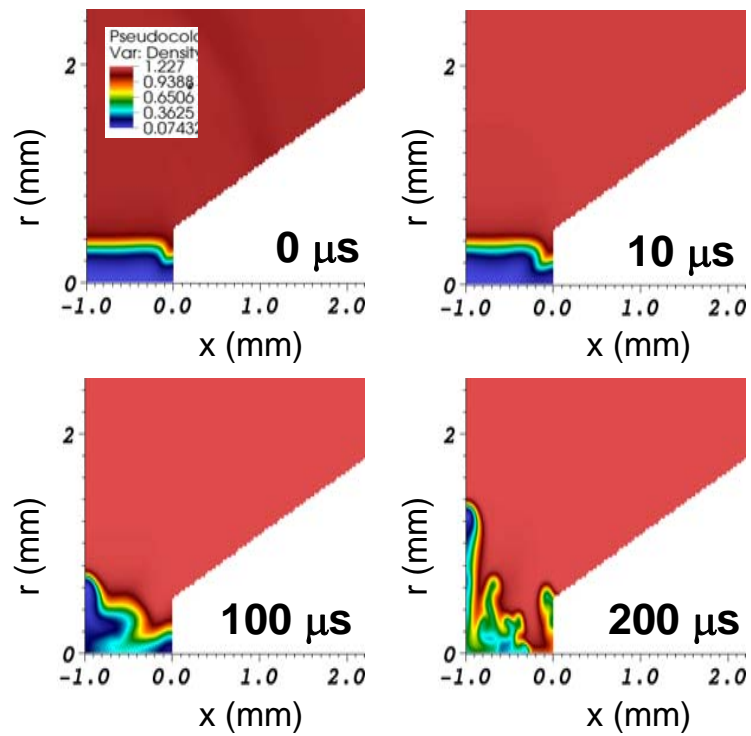
Figure 5.8: Simulation results of the temperature showing the hot gas trapped by the vortex

the cylindrical geometry due to less flow separation, and as a result the inflow has a lower velocity. The vortex created by the flow separation is convected towards the center of the channel and then upward. Due to the lower rates of convection and entrainment of cold gas, the kernel cools slower than in the cylindrical electrode case, maintaining a temperature above 1000 K until  $140 \mu\text{s}$ . The mixing region that forms near the gap is larger and at higher temperatures than in the cylindrical case. These flow features are also seen in the schlieren visualization, including the larger mixing region and slower propagation of the hot gas kernel. In comparison to the cylindrical electrodes, we have for the same energy a higher temperature gas kernel and larger mixing region, suggesting that for a given mixture, a lower spark energy would be needed for ignition.

The results of the schlieren visualization and computations for the third geometry, 1.6 mm diameter electrodes with Teflon flanges, are shown in Figure 5.10. In this



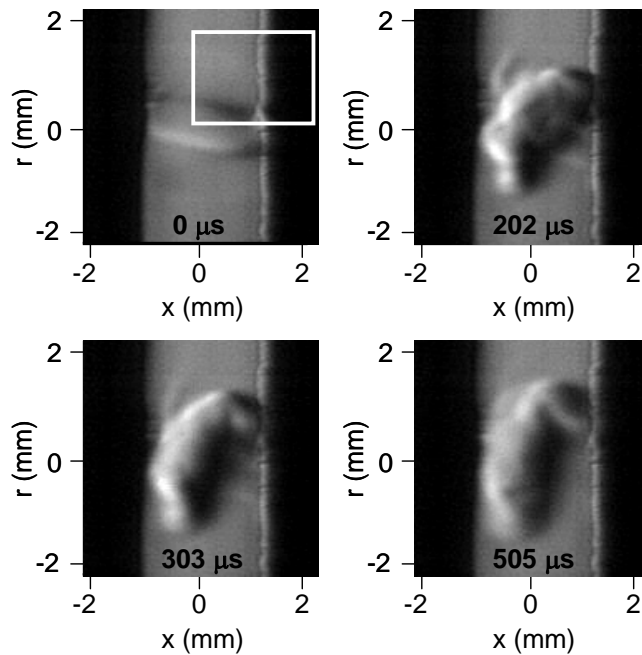
(a)



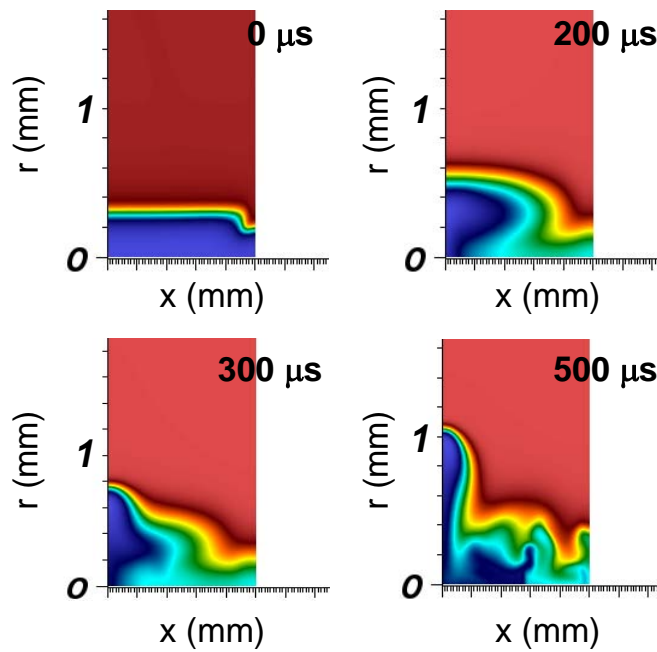
(b)

Figure 5.9: Spark discharge in air using conical electrodes: (a) images from high-speed schlieren visualization and (b) density fields from the simulation. The simulation region corresponds to the quadrant outlined in white on the upper left schlieren image.

geometry the expanding spark channel generates a purely cylindrical blast wave, and therefore there is no pressure gradient along the spark channel. However, in both the simulation and the schlieren visualization there is clearly inflow of gas towards the center of the channel caused by viscous effects. The vorticity field from the simulation, shown in Figure 5.11, indicates that there is negative vorticity originating in the boundary layer at the right-hand flange and positive vorticity originating in the boundary layer at the left-hand flange. The vorticity diffuses into the flow to form a vortex pair which is clearly visible in the experiments. This weak vortex pair moves slowly outward. The kernel is hotter for a longer time than in the other cases, maintaining a temperature above 1000 K until 340  $\mu\text{s}$ . The confinement of the gas also results in a larger and hotter mixing region. Therefore, these results suggest that the lowest ignition energy would be required in this configuration, and that the overall minimum ignition energy for a flammable gas is obtained using this geometry, as done by Lewis and von Elbe (1961). The generation of this vortex and subsequent hot kernel is a result not seen in previous simulations, and was captured by these simulations due to the high resolution and inclusion of viscous effects.



(a)



(b)

Figure 5.10: Spark discharge in air using flanged electrodes: (a) images from high-speed schlieren visualization and (b) density fields from the simulation. The simulation region corresponds to the quadrant outlined in white on the upper left schlieren image.

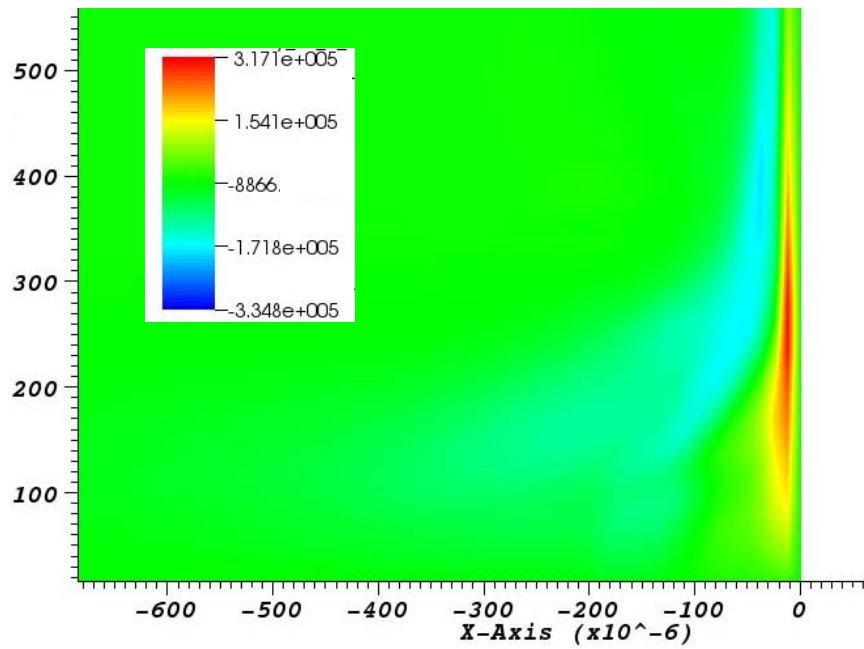


Figure 5.11: Simulation results (vorticity field) showing the vortex pair generated at the surface of the flanged electrode at time  $t = 10 \mu s$

## Chapter 6

# One-Step Chemistry Models for Flame and Ignition Simulation

The numerical model described in Chapter 5 was extended to reacting flow simulations to model ignition. To perform highly-resolved simulations quickly and with limited processing resources, simplified chemistry must be used. In this work the simplest possible chemistry was chosen, a one-step reaction model. One-step chemistry models are often used in large-scale simulations such as combustion in HCCI engines (e.g., [Hamosfakidis et al. \(2009\)](#)), ramjet engines (e.g., [Roux et al. \(2010\)](#)), and swirl gas combustors (e.g., [Grinstein and Fureby \(2005\)](#)), and in simulations involving turbulence such as turbulent flames (e.g., [Sankaran and Menon \(2005\)](#)). Work has been done recently at FM Global Research by Dorofeev and Bauwens ([Bauwens, 2007](#)) and also by [Fernández-Galisteo et al. \(2009\)](#) to develop one-step chemistry models for hydrogen-air mixtures, but no single scientific method exists for extracting physically reasonable parameters for one-step models.

In collaboration with Sergey Dorofeev and Carl Bauwens at FM Global Research, one-step models for hydrogen-air mixtures have been constructed for use in ignition and explosion simulations. Methods based on thermal explosion theory have been developed for extracting physically reasonable effective activation energies and reaction orders for one-step models. The one-step models were implemented into a steady 1D laminar flame code using Cantera software for chemically reacting flow ([Goodwin, 2005](#)), and the models were validated by comparing the flame properties with those

calculated using a detailed chemical mechanism. The one-step model for stoichiometric hydrogen-air was then implemented into the AMROC software to perform a preliminary simulation of a 1D laminar flame. Finally, the model transport properties were improved and the one-step model was used in AMROC simulations of ignition, presented in Chapter 7.

## 6.1 Model Parameters

The first goal of this work was to develop very simple one-step models that would produce flame properties matching those of flames modeled using large multi-step chemical mechanisms. Therefore, to develop the simplest possible one-step model the following assumptions were used:

1. There are only two species, R (reactant) and P (product).
2. Both species consist of one argon atom, so the molecular weights and transport properties of R and P are the same.
3. The two species have constant specific heat capacity (no temperature dependence). The constant pressure heat capacity of argon at 300 K is used for both R and P (20.785 J/mol·K).
4. The mechanism has one overall reaction  $R_1 + \dots + R_n \xrightarrow{k_f} P_1 + \dots$  where  $n$  is the order of the reaction and  $k_f$  is the reaction rate coefficient in the modified Arrhenius form

$$k_f = AT^m \exp\left(-\frac{E_a}{RT}\right). \quad (6.1)$$

5. The temperature dependence of the reaction rate is only in the Arrhenius term, i.e.,  $m = 0$ .

These assumptions determine the thermodynamic and transport parameters for the model, leaving four variables: the effective activation energy  $E_a$ , effective reaction order  $n$ , pre-exponential coefficient  $A$ , and the heat released by the reaction  $q$ . The

effective activation energy and reaction order,  $E_a$  and  $n$ , are calculated using one of the methods described in the following sections and the pre-exponential coefficient  $A$  and the heat release  $q$  can be adjusted to produce the desired flame properties. In this work, the one-step models were chosen to match the flame speed and flame temperature obtained using a detailed chemical mechanism.

## 6.2 Constant Pressure Explosion Method

In this section expressions are derived for the effective activation energy and reaction order based on thermal explosion theory. The derivation of the effective reaction order is given in the first section and reaction orders for hydrogen-air mixtures are estimated using the results of constant pressure explosion computations performed with Cantera software (Goodwin, 2005). In the second section the derivation of the effective activation energy is presented and values of the activation energy for hydrogen-air mixtures are estimated using the calculated reaction orders and Cantera computations.

### 6.2.1 Estimating Effective Reaction Order

In a constant pressure explosion the enthalpy is also constant and can be expressed as a function of temperature and mass fraction

$$h = h(T, Y) . \quad (6.2)$$

Differentiating the enthalpy with respect to time relates the change in temperature to the change in mass fraction:

$$\begin{aligned} \frac{dh}{dt} &= \frac{\partial h}{\partial T} \frac{dT}{dt} + \frac{\partial h}{\partial Y} \frac{dY}{dt} \\ &= c_p \frac{dT}{dt} - q \frac{dY}{dt} = 0 \end{aligned} \quad (6.3)$$

where  $q$  is the heat release per unit mass and

$$\frac{dY}{dt} = \frac{W\dot{\omega}}{\rho} . \quad (6.4)$$

The molar production rate of product per unit volume,  $\dot{\omega}$ , is assumed to have an Arrhenius form:

$$\dot{\omega} = A[O]^{n_O}[F]^{n_F} \exp\left(\frac{-E_a}{\tilde{R}T}\right) \quad (6.5)$$

where  $[O]$  and  $[F]$  are molar concentrations of the oxidizer and fuel, respectively, and  $n_O$  and  $n_F$  are empirical reaction orders. Using the ideal gas law, the concentration of a component  $i$  can be represented in terms of the density:

$$[i] = \frac{n_i}{V} = \frac{p_i}{\tilde{R}T} = \frac{x_i p}{\tilde{R}T} = \frac{x_i}{W_i} \rho \quad (6.6)$$

where  $p_i$ ,  $x_i$ , and  $W_i$  are the partial pressure, mole fraction, and molar mass of component  $i$ , respectively. Using this definition of molar concentration in Equation 6.5 gives

$$\begin{aligned} \dot{\omega} &= A \left[ \frac{x_O}{W_O} \rho \right]^{n_O} \left[ \frac{x_F}{W_F} \rho \right]^{n_F} \exp\left(\frac{-E_a}{\tilde{R}T}\right) \\ &= \left( A \frac{x_O^{n_O} x_F^{n_F}}{W_O^{n_O} W_F^{n_F}} \right) \rho^{n_O+n_F} \exp\left(\frac{-E_a}{\tilde{R}T}\right) \end{aligned} \quad (6.7)$$

and therefore

$$\frac{dY}{dt} = \frac{W\dot{\omega}}{\rho} = \left( AW \frac{x_O^{n_O} x_F^{n_F}}{W_O^{n_O} W_F^{n_F}} \right) \rho^{n_O+n_F-1} \exp\left(\frac{-E_a}{\tilde{R}T}\right) . \quad (6.8)$$

If the effective activation energy  $n$  is defined as  $n = n_O + n_F$  and the terms in the parenthesis are combined into a parameter  $Z$ , then the expression for the change in temperature versus time becomes:

$$\frac{dT}{dt} = \frac{q}{c_p} Z \rho^{n-1} \exp\left(\frac{-E_a}{\tilde{R}T}\right) . \quad (6.9)$$

The Frank-Kamenetskii approximation is now applied by assuming a small temperature rise, i.e.,

$$T = T_0 + T' \quad (6.10)$$

where  $T' \ll T_0$ . Substituting this definition of temperature into Equation 6.9 gives

$$\frac{dT'}{dt} = \frac{q}{c_p} Z \rho^{n-1} \exp\left(\frac{-E_a}{\tilde{R}T_0 \left(1 + \frac{T'}{T_0}\right)}\right) \quad (6.11)$$

and if the quantity  $1/(1 + T'/T_0)$  in the exponential is expanded in a series in  $T'$  about  $T' = 0$  and the first two terms are retained, the following differential equation is obtained:

$$\begin{aligned} \frac{dT'}{dt} &= \frac{q}{c_p} Z \rho^{n-1} \exp\left(\frac{-E_a}{\tilde{R}T_0} \left(1 - \frac{T'}{T_0}\right)\right) \\ &= \frac{q}{c_p} Z \rho^{n-1} \exp\left(\frac{-E_a}{\tilde{R}T_0}\right) \exp\left(\frac{E_a}{\tilde{R}T_0^2} T'\right). \end{aligned} \quad (6.12)$$

Now define a new variable  $\phi$  such that

$$\phi = \frac{E_a}{\tilde{R}T_0^2} T' \quad (6.13)$$

and

$$\frac{d\phi}{dt} = \frac{E_a}{\tilde{R}T_0^2} \frac{dT'}{dt} \quad (6.14)$$

then Equation 6.12 can be rewritten as

$$\frac{d\phi}{dt} = \left(\frac{q}{c_p} Z \rho^{n-1} \frac{E_a}{\tilde{R}T_0^2} \exp\left(\frac{-E_a}{\tilde{R}T_0}\right)\right) \exp(\phi) = \left(\frac{1}{\tau_i}\right) \exp(\phi) \quad (6.15)$$

where

$$\tau_i = \frac{c_p}{q} \frac{\tilde{R}T_0^2}{E_a} \rho^{-n+1} \frac{1}{Z} \exp\left(\frac{E_a}{\tilde{R}T_0}\right) \quad (6.16)$$

is called the *explosion time*. Differentiating Equation 6.16 with respect to the density  $\rho$  while keeping  $T_0$  constant and simplifying results in:

$$\begin{aligned} \left(\frac{\partial\tau_i}{\partial\rho}\right)_{T_0} &= \left(\frac{c_p}{q} \frac{\tilde{R}T_0^2}{E_a}\right) (-n+1) \rho^{-n} \frac{1}{Z} \exp\left(\frac{E_a}{\tilde{R}T_0}\right) \\ &= \left\{ \frac{c_p}{q} \frac{\tilde{R}T_0^2}{E_a} \rho^{-n+1} \frac{1}{Z} \exp\left(\frac{E_a}{\tilde{R}T_0}\right) \right\} \frac{(-n+1)}{\rho} \\ &= \frac{\tau_i}{\rho} (-n+1) . \end{aligned} \quad (6.17)$$

From Equation 6.17 an expression for the effective reaction order is obtained:

$$n = -\frac{\rho}{\tau_i} \left(\frac{\partial\tau_i}{\partial\rho}\right)_{T_0} + 1 . \quad (6.18)$$

The computation to apply this method to calculate  $n$  proceeds as follows:

1. First a composition is chosen and the pressure is set to 1 bar and the temperature to the initial temperature  $T_0$ . The density, determined by the pressure and temperature through the ideal gas law, is stored in the variable  $\rho_0$ . Cantera is then used to compute a constant pressure explosion and a plot of temperature versus time.
2. The explosion time  $\tau_i$  is approximated as the time to the maximum temperature gradient.
3. Then a slightly larger initial density  $\rho'_0 = \rho_0 + \rho'$ , where  $\rho' \ll \rho_0$ , is chosen and the same initial temperature  $T_0$  is prescribed to keep the temperature constant for calculation of the derivative  $(\partial\tau_i/\partial\rho)_{T_0}$ . Another constant pressure explosion is computed, obtaining a slightly different explosion time  $\tau'_i$ .

4. The derivative of explosion time with respect to initial density is then approximated as:

$$\left(\frac{\partial \tau_i}{\partial \rho}\right)_{T_0} \approx \frac{\Delta \tau_i}{\Delta \rho} = \frac{\tau_i' - \tau_i}{\rho'}. \quad (6.19)$$

5. The effective reaction order is then calculated from:

$$n \approx -\frac{\rho_0}{\tau_i} \frac{(\tau_i' - \tau_i)}{\rho'} + 1. \quad (6.20)$$

A MATLAB script was written to perform the calculation described above, and the code is given in Appendix H.

The method described above was used to calculate effective reaction orders for a range of hydrogen-air compositions using several different density intervals,  $\rho'$ . The results for  $\rho' = 0.05\rho_0$ ,  $0.1\rho_0$ ,  $0.15\rho_0$ , and  $0.2\rho_0$ , shown in Figure 6.1, are all comparable, while the results for  $\rho' = 0.01\rho_0$  are erratic because the density interval is too small to correctly approximate the derivative. Therefore, a density interval in the range of  $0.05\text{--}0.30\rho_0$  is acceptable, and  $\rho' = 0.10\rho_0$  was used for all subsequent calculations. Values for the effective reaction order calculated for hydrogen-air mixtures using the constant pressure explosion method (Equation 6.18) are shown in Figure 6.2. The constant pressure explosion method gives values for  $n$  on the order of 2 for all compositions.

### 6.2.2 Estimating Effective Activation Energy

Applying the ideal gas law to rewrite the density in Equation 6.16 in terms of pressure and temperature gives

$$\begin{aligned} \tau_i &= \frac{c_p}{q} \frac{\tilde{R}T_0^2}{E_a} \left(\frac{p}{RT_0}\right)^{-n+1} \frac{1}{Z} \exp\left(\frac{E_a}{\tilde{R}T_0}\right) \\ &= \frac{c_p}{q} \frac{\tilde{R}T_0^{n+1}}{E_a} \left(\frac{p}{R}\right)^{-n+1} \frac{1}{Z} \exp\left(\frac{E_a}{\tilde{R}T_0}\right). \end{aligned} \quad (6.21)$$

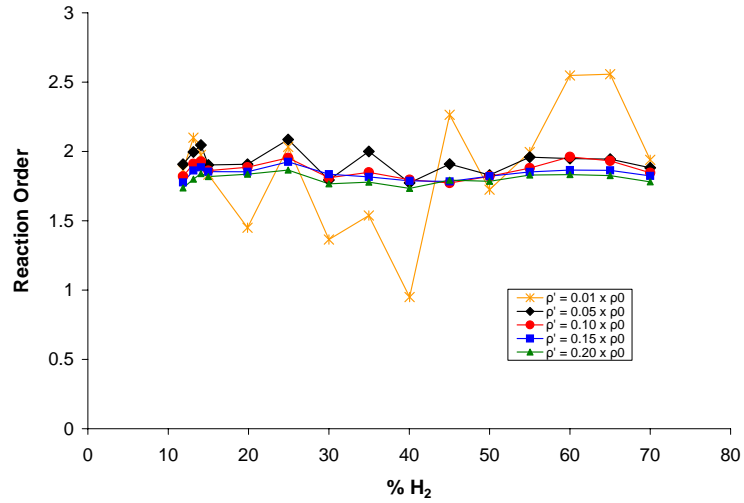


Figure 6.1: Effective reaction orders for H<sub>2</sub>-air mixtures calculated using the constant pressure explosion method (Equation 6.18) using 5 different density intervals

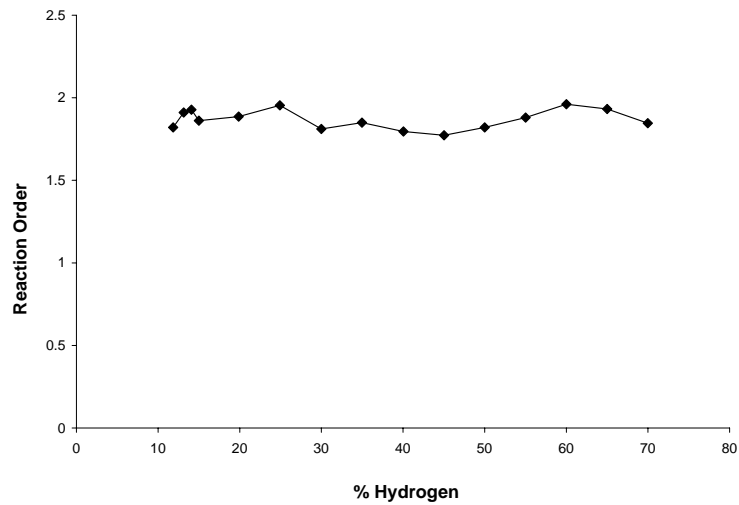


Figure 6.2: Effective reaction orders for H<sub>2</sub>-air mixtures calculated using the constant pressure explosion method (Equation 6.18) with  $\rho' = 0.10\rho_0$

Differentiating Equation 6.21 with respect to the temperature  $T_0$  while keeping pressure constant and simplifying results in the following expression for the derivative of

the explosion time:

$$\begin{aligned}
\left(\frac{\partial\tau_i}{\partial T_0}\right)_p &= \frac{c_p}{q} \frac{\tilde{R}T_0^{n+1}}{E_a} \left(\frac{p}{R}\right)^{-n+1} \frac{1}{Z} \left(-\frac{E_a}{\tilde{R}T_0^2}\right) \exp\left(\frac{E_a}{\tilde{R}T_0}\right) \\
&+ \frac{c_p}{q} (n+1) \frac{\tilde{R}T_0^n}{E_a} \left(\frac{p}{R}\right)^{-n+1} \frac{1}{Z} \exp\left(\frac{E_a}{\tilde{R}T_0}\right) \\
&= \left\{ \frac{c_p}{q} \frac{\tilde{R}T_0^{n+1}}{E_a} \left(\frac{p}{R}\right)^{-n+1} \frac{1}{Z} \exp\left(\frac{E_a}{\tilde{R}T_0}\right) \right\} \left(-\frac{E_a}{\tilde{R}T_0^2}\right) \\
&+ \left\{ \frac{c_p}{q} \frac{\tilde{R}T_0^{n+1}}{E_a} \left(\frac{p}{R}\right)^{-n+1} \frac{1}{Z} \exp\left(\frac{E_a}{\tilde{R}T_0}\right) \right\} \frac{(n+1)}{T_0} \\
&= \left(-\frac{E_a}{\tilde{R}T_0}\right) \frac{\tau_i}{T_0} + (n+1) \frac{\tau_i}{T_0}. \tag{6.22}
\end{aligned}$$

Equation 6.22 can then be solved for the activation energy  $E_a$ :

$$E_a = \tilde{R}T_0 \left( -\frac{T_0}{\tau_i} \left(\frac{\partial\tau_i}{\partial T_0}\right)_p + (n+1) \right). \tag{6.23}$$

The computation to apply this method to calculate  $E_a$  proceeds as follows:

1. First a composition is chosen and the pressure is set to 1 bar and the temperature to the initial temperature  $T_0$ . Cantera is then used to compute a constant pressure explosion and a plot of temperature versus time.
2. The explosion time  $\tau_i$  is approximated as the time to the maximum temperature gradient.
3. Then a slightly larger initial temperature  $T'_0 = T_0 + T'$ , where  $T' \ll T_0$  ( $T' = 30$  K was used in these calculations), is chosen and the pressure is set to 1 bar to keep the pressure constant for calculation of the derivative  $(\partial\tau_i/\partial T_0)_p$ . Another constant pressure volume explosion is computed, obtaining a slightly different explosion time  $\tau'_i$ .
4. The derivative of explosion time with respect to initial temperature is then

approximated as:

$$\left(\frac{\partial \tau_i}{\partial T_0}\right)_p \approx \frac{\Delta \tau_i}{\Delta T_0} = \frac{\tau'_i - \tau_i}{T'}. \quad (6.24)$$

5. The activation energy is then calculated from:

$$E_a \approx \tilde{R}T_0 \left( -\frac{T_0}{\tau_i} \frac{(\tau'_i - \tau_i)}{T'} + (n + 1) \right) \quad (6.25)$$

where the reaction order  $n$  is the value calculated from Equation 6.18.

This calculation is also performed in the MATLAB script given in Appendix H.

Figure 6.3(a) shows the effective activation energies for hydrogen-air mixtures calculated using the constant pressure explosion method (Equation 6.23) with the reaction order values shown in Figure 6.2. The corresponding Zeldovich numbers,  $\beta$ , are given in Figure 6.3(b) where

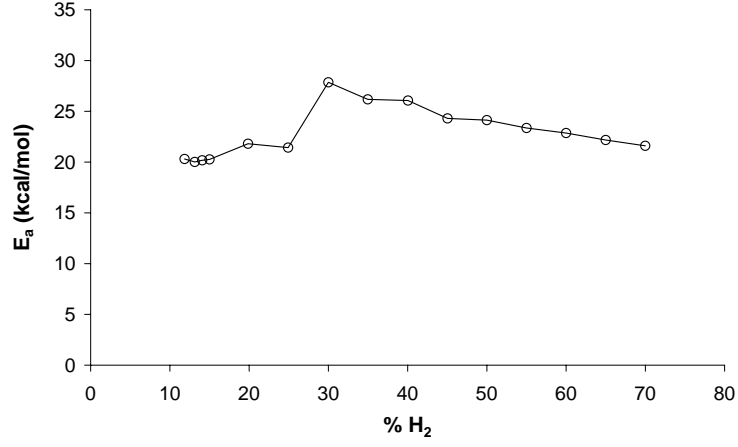
$$\beta = \frac{E_a}{\tilde{R}T_b^2} (T_b - T_u) \quad (6.26)$$

and  $T_u$  and  $T_b$  are the temperature of the unburned and burned gas, respectively.

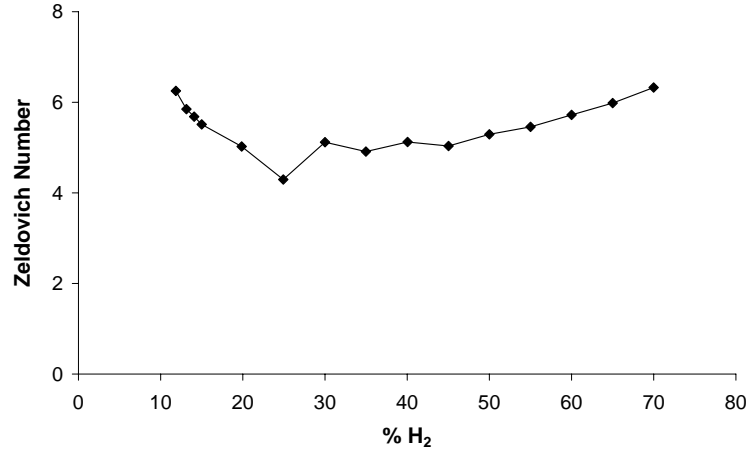
### 6.3 Constant Pressure Explosion Method with Constant Volume Initial Conditions

The effective activation energy can also be calculated using constant pressure explosion calculations with constant volume initial conditions. Since mass is conserved, the constant volume condition is imposed by keeping the initial density constant while perturbing the temperature. In this case, because the dependence of the explosion time on initial density is neglected, the reaction order does not appear in the expression for the activation energy, and so one variable is removed from the calculation.

Differentiating the constant pressure explosion time (Equation 6.16) with respect to initial temperature  $T_0$  while keeping the density (and hence the volume) constant



(a)



(b)

Figure 6.3: (a) Effective activation energies and (b) corresponding Zeldovich numbers calculated using the constant pressure explosion method (Equation 6.23) with reaction orders obtained from the constant pressure explosion method (Equation 6.18)

and simplifying gives:

$$\begin{aligned}
 \left( \frac{\partial \tau_i}{\partial T_0} \right)_\rho &= \frac{c_p}{q} 2 \frac{\tilde{R}T_0}{E_a} \rho^{-n+1} \frac{1}{Z} \exp\left( \frac{E_a}{\tilde{R}T_0} \right) \\
 &+ \frac{c_p}{q} \frac{\tilde{R}T_0^2}{E_a} \rho^{-n+1} \frac{1}{Z} \left( -\frac{E_a}{\tilde{R}T_0^2} \right) \exp\left( \frac{E_a}{\tilde{R}T_0} \right) \\
 &= \left\{ \frac{c_p}{q} \frac{\tilde{R}T_0^2}{E_a} \rho^{-n+1} \frac{1}{Z} \exp\left( \frac{E_a}{\tilde{R}T_0} \right) \right\} \left( -\frac{E_a}{\tilde{R}T_0^2} \right) \\
 &+ \left\{ \frac{c_p}{q} \frac{\tilde{R}T_0^2}{E_a} \rho^{-n+1} \frac{1}{Z} \exp\left( \frac{E_a}{\tilde{R}T_0} \right) \right\} \frac{2}{T_0} \\
 &= \left( -\frac{E_a}{\tilde{R}T_0} \right) \frac{\tau_i}{T_0} + 2 \frac{\tau_i}{T_0}.
 \end{aligned} \tag{6.27}$$

Equation 6.27 can then be solved for the effective activation energy  $E_a$ :

$$E_a = \tilde{R}T_0 \left( -\frac{T_0}{\tau_i} \left( \frac{\partial \tau_i}{\partial T_0} \right)_\rho + 2 \right). \quad (6.28)$$

The computation to apply this method to calculate  $E_a$  proceeds as follows:

1. First a composition is chosen and the pressure is set to 1 bar and the temperature to the initial temperature  $T_0$ . The density, determined by the pressure and temperature through the ideal gas law, is stored in the variable  $\rho_0$ . Cantera is then used to compute a constant pressure explosion and a plot of temperature versus time.
2. The explosion time  $\tau_i$  is approximated as the time to the maximum temperature gradient.
3. Then a slightly larger initial temperature  $T'_0 = T_0 + T'$ , where  $T' \ll T_0$ , is chosen and the same initial density  $\rho_0$  is prescribed to keep the density (and volume) constant for calculation of the derivative  $(\partial \tau_i / \partial T_0)_\rho$ . Another constant pressure explosion is then computed, obtaining a slightly different explosion time  $\tau'_i$ .
4. The derivative of explosion time with respect to initial temperature is then approximated as:

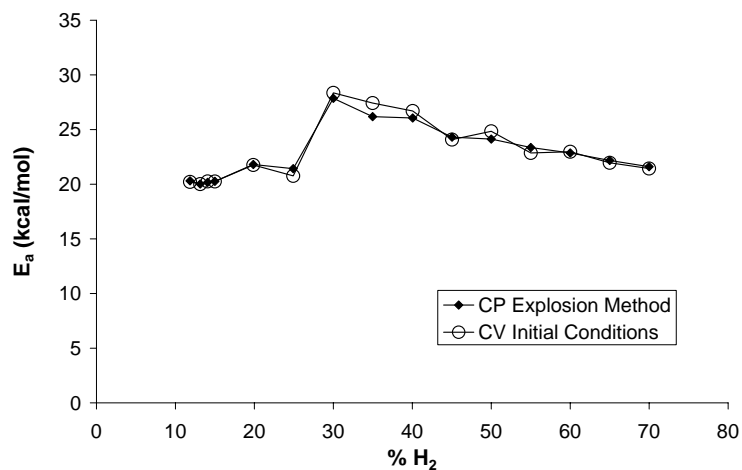
$$\left( \frac{\partial \tau_i}{\partial T_0} \right)_\rho \approx \frac{\Delta \tau_i}{\Delta T_0} = \frac{\tau'_i - \tau_i}{T'}. \quad (6.29)$$

5. The effective activation energy is then calculated from:

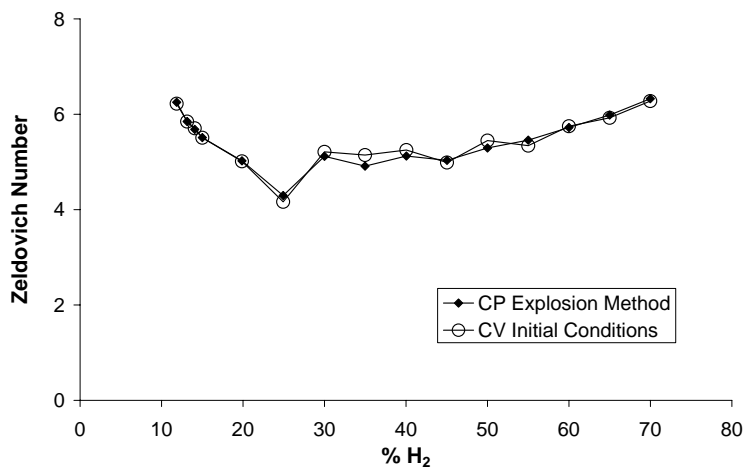
$$E_a \approx \tilde{R}T_0 \left( -\frac{T_0}{\tau_i} \frac{(\tau'_i - \tau_i)}{T'} + 2 \right). \quad (6.30)$$

Figure 6.4 shows effective activation energies and the corresponding Zeldovich numbers for hydrogen-air compositions calculated using the constant pressure explosion method with constant volume initial conditions (Equation 6.28). Also shown

are the values calculated using the constant pressure explosion method with reaction order dependence (Equation 6.23). The two slightly different methods produce nearly the same results, with the Zeldovich numbers differing by less than 0.25 and the activation energies differing by less than 1 kcal/mol over the full range of compositions.



(a)



(b)

Figure 6.4: (a) Effective activation energies and (b) corresponding Zeldovich numbers calculated using the constant pressure explosion method with reaction order dependence (Equation 6.23) and using the constant pressure explosion method with constant volume initial conditions (Equation 6.28)

## 6.4 Constant Volume Explosion Method

A third method for calculating the effective activation energy is to use constant *volume* explosion calculations instead of constant pressure calculations. Repeating the same derivation presented in Section 6.2.2 for the constant volume case, i.e.,  $e = \text{constant}$  where  $e$  is the internal energy, results in an expression for the constant volume explosion time:

$$\tau_i = \frac{c_v}{q} \frac{\tilde{R}T_0^2}{E_a} \rho^{-n+1} \frac{1}{Z} \exp\left(\frac{E_a}{\tilde{R}T_0}\right). \quad (6.31)$$

Differentiating the constant volume explosion time with respect to initial temperature  $T_0$  while keeping the density constant gives:

$$\begin{aligned} \left(\frac{\partial \tau_i}{\partial T_0}\right)_\rho &= \frac{c_v}{q} 2 \frac{\tilde{R}T_0}{E_a} \rho^{-n+1} \frac{1}{Z} \exp\left(\frac{E_a}{\tilde{R}T_0}\right) \\ &+ \frac{c_v}{q} \frac{\tilde{R}T_0^2}{E_a} \rho^{-n+1} \frac{1}{Z} \left(-\frac{E_a}{\tilde{R}T_0^2}\right) \exp\left(\frac{E_a}{\tilde{R}T_0}\right) \\ &= \left\{ \frac{c_v}{q} \frac{\tilde{R}T_0^2}{E_a} \rho^{-n+1} \frac{1}{Z} \exp\left(\frac{E_a}{\tilde{R}T_0}\right) \right\} \frac{2}{T_0} \\ &+ \left\{ \frac{c_v}{q} \frac{\tilde{R}T_0^2}{E_a} \rho^{-n+1} \frac{1}{Z} \exp\left(\frac{E_a}{\tilde{R}T_0}\right) \right\} \frac{1}{T_0} \left(-\frac{E_a}{\tilde{R}T_0}\right) \\ &= 2 \frac{\tau_i}{T_0} + \left(-\frac{E_a}{\tilde{R}T_0}\right) \frac{\tau_i}{T_0}. \end{aligned} \quad (6.32)$$

Equation 6.33 can then be solved for the effective activation energy:

$$E_a = \tilde{R}T_0 \left( -\frac{T_0}{\tau_i} \left(\frac{\partial \tau_i}{\partial T_0}\right)_\rho + 2 \right) \quad (6.34)$$

which is identical to Equation 6.28 except in this method the explosion time is found from a constant volume explosion instead of a constant pressure explosion.

1. First a composition is chosen and the pressure is set to 1 bar and the temperature to the initial temperature  $T_0$ . The density, determined by the pressure and temperature through the ideal gas law, is stored in the variable  $\rho_0$ . Cantera is

then used to compute a constant *volume* explosion and a plot of temperature versus time.

2. The explosion time  $\tau_i$  is approximated as the time to the maximum temperature gradient.
3. Then a slightly larger initial temperature  $T'_0 = T_0 + T'$ , where  $T' \ll T_0$ , is chosen and the same initial density  $\rho_0$  is prescribed to keep the density (and volume) constant for calculation of the derivative  $(\partial\tau_i/\partial T_0)_\rho$ . Another constant volume explosion is computed, obtaining a slightly different explosion time  $\tau'_i$ .
4. The derivative of explosion time with respect to initial temperature is then approximated as:

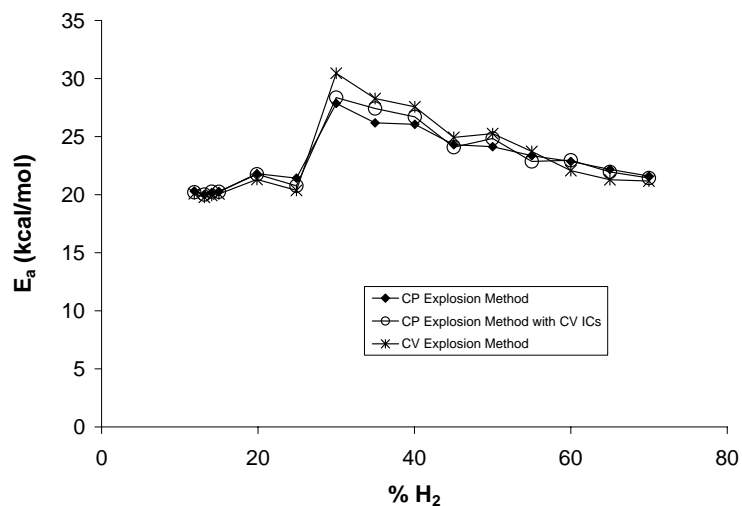
$$\left(\frac{\partial\tau_i}{\partial T_0}\right)_\rho \approx \frac{\Delta\tau_i}{\Delta T_0} = \frac{\tau'_i - \tau_i}{T'}. \quad (6.35)$$

5. The effective activation energy is then calculated from:

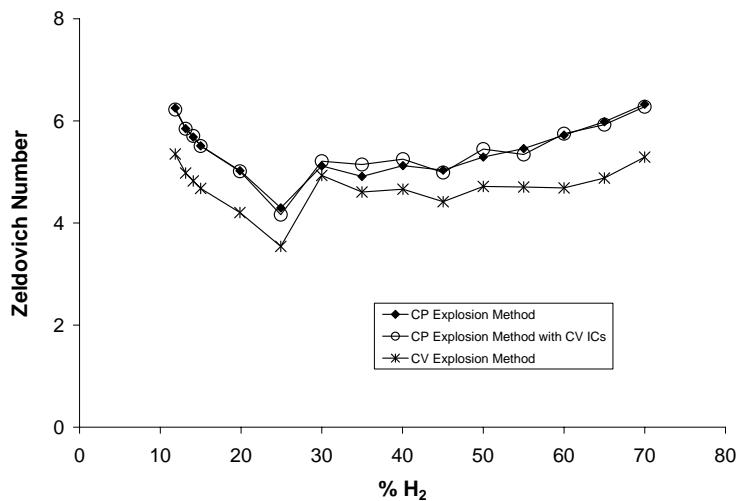
$$E_a \approx \tilde{R}T_0 \left( -\frac{T_0}{\tau_i} \frac{(\tau'_i - \tau_i)}{T'} + 2 \right). \quad (6.36)$$

Values of the effective activation energy and Zeldovich number calculated using the constant volume explosion method (Equation 6.34) are plotted in Figure 6.5 with results from the constant pressure explosion methods with reaction order dependence (Equation 6.23) and with constant volume initial conditions (Equation 6.28). The Zeldovich numbers calculated using the constant volume explosion approach are smaller than the values calculated using the constant pressure explosion methods by about 14% on average due to the higher burned temperature associated with equilibrating a mixture at constant volume versus constant pressure. The effective activation energies calculated using all three methods are comparable, differing by less than 3 kcal/mol over the full range of compositions. These results demonstrate that simple thermal explosion theory provides multiple schemes for extracting consistent and physically reasonable values of both the effective activation energy and effective reaction order

with very little computational cost. The complete set of effective reaction orders and activation energies calculated for hydrogen-air mixtures are tabulated in Appendix I.



(a)



(b)

Figure 6.5: (a) Effective activation energies and (b) corresponding Zeldovich numbers calculated using the three different methods: the constant pressure explosion method with reaction order dependence (Equation 6.23), the constant pressure explosion method with constant volume initial conditions (Equation 6.28), and the constant volume explosion method (Equation 6.34)

## 6.5 Development of One-Step Models for Flame Simulation

### 6.5.1 1D Flat Flame with One-Step Chemistry

The Cantera Python demo *adiabatic\_flame.py* calculates temperature and species profiles and flame speeds (laminar burning velocities) for freely-propagating flat flames with multicomponent transport properties. The code solves the 1D mass, species, and energy conservation equations,

$$\rho u = \rho_{in} s_L = \dot{m} = \text{constant} \quad (6.37)$$

$$\rho \frac{\partial Y_i}{\partial t} + \dot{m} \frac{\partial Y_i}{\partial z} = - \frac{\partial j_{i,z}}{\partial z} + \dot{\omega}_i W_i \quad (6.38)$$

$$\rho c_p \frac{\partial T}{\partial t} + \dot{m} c_p \frac{\partial T}{\partial z} = \frac{\partial}{\partial z} \left( \kappa \frac{\partial T}{\partial z} \right) - \sum_{i=1}^N c_{pi} j_{i,z} \frac{\partial T}{\partial z} - \sum_{i=1}^N h_i \dot{\omega}_i W_i. \quad (6.39)$$

The solution algorithm uses pseudo-time stepping and a Newton iteration scheme to implicitly solve for the steady-state solution vector (temperature  $T$  and the species mass fractions  $Y_i$ ) at each grid point in the domain. The flame speed (laminar burning velocity), related to  $\dot{m}$  as shown in Equation 6.37, is calculated as part of the solution. Figure 6.6 illustrates the problem domain.

The pressure is assumed to be constant in the problem, so the density can be found from the temperature and the mass fractions using the ideal gas law,

$$p = \text{constant} = \rho R T \quad (6.40)$$

so

$$\rho = \frac{p}{RT} \quad (6.41)$$

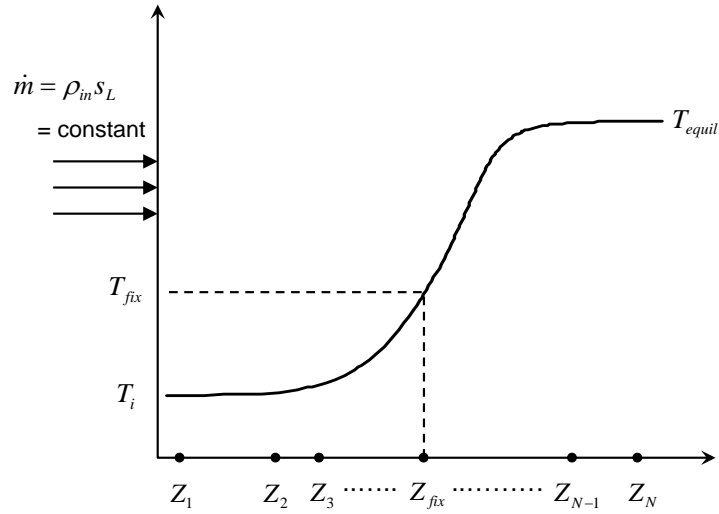


Figure 6.6: Problem domain for 1D flat flame calculation, with an example temperature profile shown. The flame is discretized into  $N$  grid points (at varying intervals), and the flame equations are solved for  $T$ ,  $u$ , and  $Y_i$  at each grid point. The temperature is fixed at one interior grid point as part of the solution algorithm.

where

$$R = \frac{\tilde{R}}{W_{mix}} = \frac{\tilde{R}}{\frac{1}{\sum_{i=1}^N \frac{Y_i}{W_i}}} . \quad (6.42)$$

To solve the problem, the following initial/boundary conditions must be supplied:

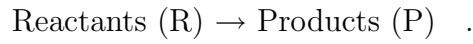
1. Pressure (constant throughout problem)
2. Temperature of reactants (at the inlet to the flame structure)
3. Initial guess for mass flow rate,  $\dot{m}$
4. Initial solution grid through the flame
5. Initial guess for temperature and species profiles on the initial grid.

The following terms in the conservation equations must also be modeled:

1. Specific heat of each species,  $c_{pi}$

2. Thermal conductivity of the mixture,  $\kappa$
3. Diffusive flux of each species,  $j_{i,z}$
4. Enthalpy of each species,  $h_i$
5. Net production rate of each species,  $\dot{\omega}_i$  .

The problem can be greatly simplified by making the assumption that all of the chemical kinetics can be simulated by a one-step global reaction



Making this assumption leads to the following simplifications:

1.  $\sum_{i=1}^N Y_i = Y_R + Y_P = 1$  and therefore  $Y_R = 1 - Y_P$
2.  $\dot{\omega}_R = -\dot{\omega}_P$  (rate of production of product P is equal to the rate of consumption of reactant R)
3.  $j_{i,z} = \rho Y_i V_i$  where  $V_i$  is the diffusion velocity of species  $i$ ; but  $\sum_{i=1}^N Y_i V_i = 0 = Y_R V_R + Y_P V_P$  which leads to  $j_{R,z} = -j_{P,z}$  .

In this model it is also assumed that both the reactants and products have the same molecular properties, i.e.,

1.  $c_{p,R} = c_{p,P}$
2.  $W_R = W_P$  .

Using these simplifications in the species conservation relationship (Equation 6.38) reduces the number of equations to just one, since the parameters  $Y_i$ ,  $j_{i,z}$ ,  $W_i$ , and  $\dot{\omega}_i$  of the two species can be related to each other. Writing the species conservation equation in terms of the mass fraction of the product,  $Y_P$ , gives,

$$\rho \frac{\partial Y_P}{\partial t} + \dot{m} \frac{\partial Y_P}{\partial z} = - \frac{\partial}{\partial z} (j_{P,z}) + \dot{\omega}_P W_P \quad . \quad (6.43)$$

It can be shown that the equation written in terms of the mass fraction of the reactant is completely equivalent. Now use the simplifications in the energy conservation equation (Equation 6.39) to give

$$\rho c_p \frac{\partial T}{\partial t} + \dot{m} c_p \frac{\partial T}{\partial z} - \frac{\partial}{\partial z} \left( \kappa \frac{\partial T}{\partial z} \right) = - (h_R \omega_R W_R + h_P \omega_P W_P) \quad (6.44)$$

where

$$W_R \omega_R = W_R (-k[R]) = -W_R k[R] \quad (6.45)$$

and

$$W_P \omega_P = W_R k[R] \quad (6.46)$$

where  $k$  is the rate of the one step reaction  $R \rightarrow P$ . The concentration of a species can be expressed in terms of the mass fraction,

$$[i] = \frac{\rho Y_i}{W_i} . \quad (6.47)$$

Substituting in the expressions for  $\omega_R$  and  $\omega_P$  and using Equation 6.47, the right-hand side of the energy equation (Equation 6.44) becomes

$$- (h_R W_R \omega_R + h_P W_P \omega_P) = - \left( -k W_R \frac{\rho Y_R}{W_R} h_R + k W_P \frac{\rho Y_R}{W_R} h_P \right) = -\rho Y_R (h_P - h_R) k . \quad (6.48)$$

Replacing  $Y_R$  with  $1 - Y_P$  gives the final form of the energy equation for the one-step reaction model

$$\rho c_p \frac{\partial T}{\partial t} + \dot{m} c_p \frac{\partial T}{\partial z} - \frac{\partial}{\partial z} \left( \kappa \frac{\partial T}{\partial z} \right) = -\rho (1 - Y_P) (h_P - h_R) k . \quad (6.49)$$

The equations for species (Equation 6.43) and energy (Equation 6.49) can also be

formulated in terms of one variable, called the “progress variable”  $\lambda$ , which in this case is set equal to the mass fraction of the product,  $Y_P$ . Therefore  $\lambda = 0$  at the start of the reaction (no product P) and  $\lambda = 1$  at the end (all product P). Substituting  $Y_P = \lambda$  into Equation 6.43 gives

$$\rho \frac{\partial \lambda}{\partial t} + \dot{m} \frac{\partial \lambda}{\partial z} = -\frac{\partial j_{,\lambda}}{\partial z} + \omega_P W_P . \quad (6.50)$$

But recall from the analysis of the energy equation, it was found that

$$\omega_P W_P = \rho Y_R k = \rho (1 - Y_P) k = \rho (1 - \lambda) k \quad (6.51)$$

so the final form for the species conservation equation is

$$\rho \frac{\partial \lambda}{\partial t} + \dot{m} \frac{\partial \lambda}{\partial z} = -\frac{\partial j_{,\lambda}}{\partial z} + \rho (1 - \lambda) k . \quad (6.52)$$

Substituting  $\lambda$  into the energy equation gives

$$\rho c_p \frac{\partial T}{\partial t} + \dot{m} c_p \frac{\partial T}{\partial z} - \frac{\partial}{\partial z} \left( \kappa \frac{\partial T}{\partial z} \right) = -\rho (1 - \lambda) (h_P - h_R) k . \quad (6.53)$$

## 6.5.2 Implementation of a One-Step Model in the 1D Flame Code

In this work the Python adiabatic 1D flame code included in the Cantera installation was used and is given in Appendix K. The code simulates a freely propagating planar flame, solving for the laminar flame speed and temperature and species profiles through the flame. Cantera requires a mechanism (.cti) file with thermodynamic and reaction rate data for the species of interest, and it is in this file that the one-step model is implemented as described in Section 6.1.

The structure of the Cantera input file, or .cti file, consists of three sections. In the

first section ideal gas is defined consisting of a set of chemical elements, species, and reactions with a chosen transport model and initial state (temperature and pressure). For the one-step model in this work there is one element argon (“Ar”) and two species (“R”, “P”) listed in this first section of the input file. The second section consists of the species ideal gas thermodynamic data: the specific heat  $c_{P_i} = c_{P_i}(T)$ , specific enthalpy  $h_i = h_i(T)$ , and the pressure-independent part of the entropy  $s_{oi} = s_{oi}(T)$ .

The Cantera software uses a piecewise polynomial representation of the specific heat at constant pressure in non-dimensional form

$$\frac{c_{P_i}}{R} = \begin{cases} \sum_{n=0}^4 a_{ni} T^n & T_{min} \leq T \leq T_{mid} \\ \sum_{n=0}^4 b_{ni} T^n & T_{mid} \leq T \leq T_{max} \end{cases} . \quad (6.54)$$

In complex mechanisms, the constants  $a_{ni}$  and  $b_{ni}$  have to be determined by fitting the polynomial representation to tabulated data. However, in this simple one-step model a constant specific heat is used that is the same for both the reactant (R) and product (P), so the coefficients  $a_1$ - $a_4$  are zero for both species R and P, and only the first coefficient  $a_0$  is nonzero

$$a_{0R} = a_{0P} = \frac{(c_P)_{Ar,300K}}{R} = \frac{20.785 \frac{J}{molK}}{8.314 \frac{J}{molK}} = 2.50 . \quad (6.55)$$

The enthalpy can be found simply by integrating the specific heat, giving a relationship between the enthalpy and the fifth constant in the thermodynamic data,  $a_{5i}$

$$a_{5i} = \frac{\Delta_f h_i^o}{R_i} - \sum_{n=0}^4 \frac{a_{ni}}{n+1} (T^o)^{n+1} . \quad (6.56)$$

In the one-step model, the heat release  $q$  is defined as the difference in the enthalpies

of the reactants and products

$$q = h_R - h_P \quad (6.57)$$

so the heat release is related to the constants  $a_{5i}$  and  $a_{0i}$  as follows:

$$\frac{q}{R} = (a_{5R} - a_{5P}) + (a_{0R} - a_{0P})T^o. \quad (6.58)$$

In the simple model in this work,  $a_{0R} = a_{0P}$  so the heat release was simply  $R(a_{5R} - a_{5P})$ . The last constant,  $a_{6i}$  is related to the pressure-independent portion of the entropy, and was left unchanged in this model.

The last section in the input file lists the chemical reactions along with the chemical rate coefficient parameters  $A$ ,  $m$ , and  $E_a$ . In the one step model there is only one reaction  $R_1 + \dots + R_n \xrightarrow{k_f} P_1 + \dots$ , and for this model  $m = 0$ . The one-step parameters  $q$  (implemented through the constants  $a_{5i}$ ),  $A$ , and  $E_a$  can be changed to produce a flame with the desired properties. An example set of flame profiles generated using a one-step model and profiles generated using detailed chemistry for stoichiometric hydrogen-air are shown in Figure 6.7. It was possible to match the flame speeds and temperatures over a range of compositions for hydrogen-air and propane-air systems. However, the density could not be matched since a complicated multi-species system is being modeled using a single species so the effects of varying molar mass cannot be simulated correctly; this issue is addressed in Section 6.7.

## 6.6 Two-Species One-Step Model for Hydrogen-Air Systems

One-step models were constructed for hydrogen-air systems using the effective activation energies calculated using the constant pressure explosion method (Equation 6.23) and listed in Table I.1 in Appendix I. The goal was to choose values for the heat release parameter  $q$  and the pre-exponential factor  $A$  in the one-step model to produce a

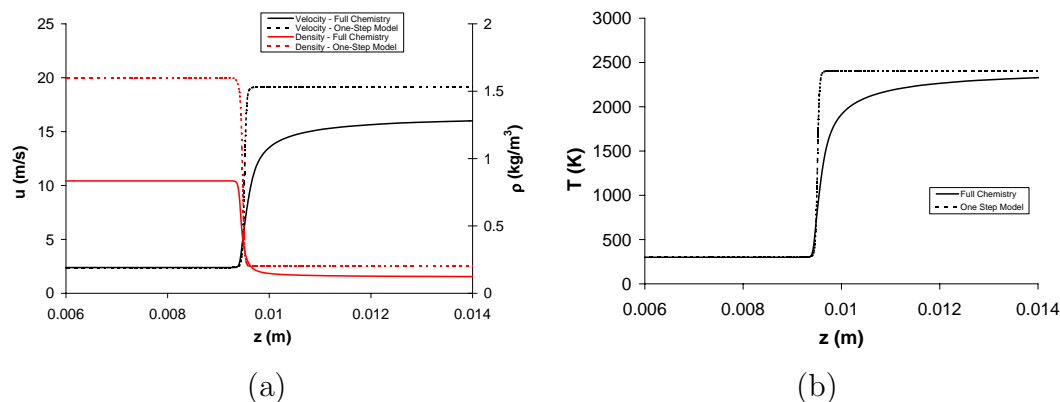


Figure 6.7: Profiles of the velocity and density (a) and temperature (b) through the flame generated using both the one-step model and full chemistry for stoichiometric hydrogen-air

flame with a laminar flame speed  $s_L$  and flame temperature  $T_b$  that match the values obtained using detailed chemistry. The heat release is found simply from the increase in temperature:

$$q = c_p (T_b - T_u) \quad (6.59)$$

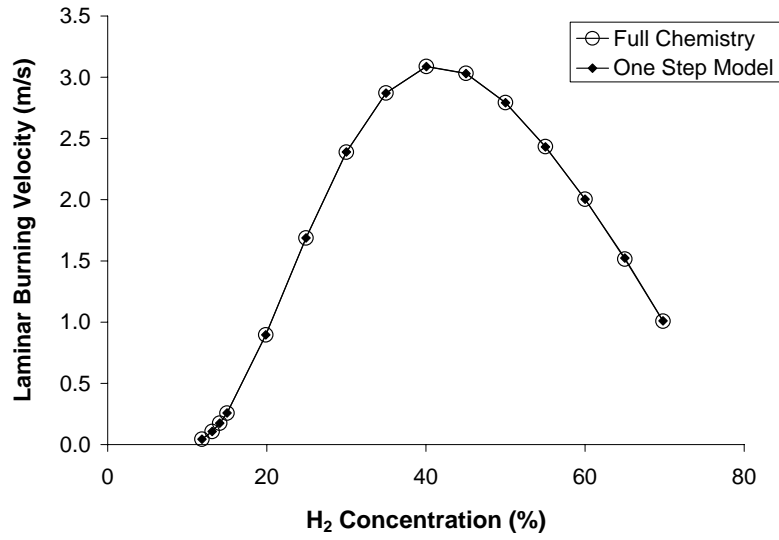
where  $c_p$  is the specific heat of the reactant and product in the one-step model,  $T_u$  is the initial unburned temperature of the reactant, and  $T_b$  is the burned temperature of the product (flame temperature). In the one-step model argon was used to represent both the reactant and the product, so the specific heat  $c_p$  used was 20.785 J/mol·K and the initial temperature  $T_u$  is 300 K. The flame temperature  $T_b$  was found from flame calculations performed using the H<sub>2</sub>/O<sub>2</sub> oxidation mechanism published by Li et al. (2004). The heat release calculated from Equation 6.59 was incorporated into the Cantera input (.cti) file through the coefficient  $(a_5)_P$ . Iteration was performed on  $A$  to match the flame speed from the flame calculations using detailed chemistry.

### 6.6.1 First-Order Reaction

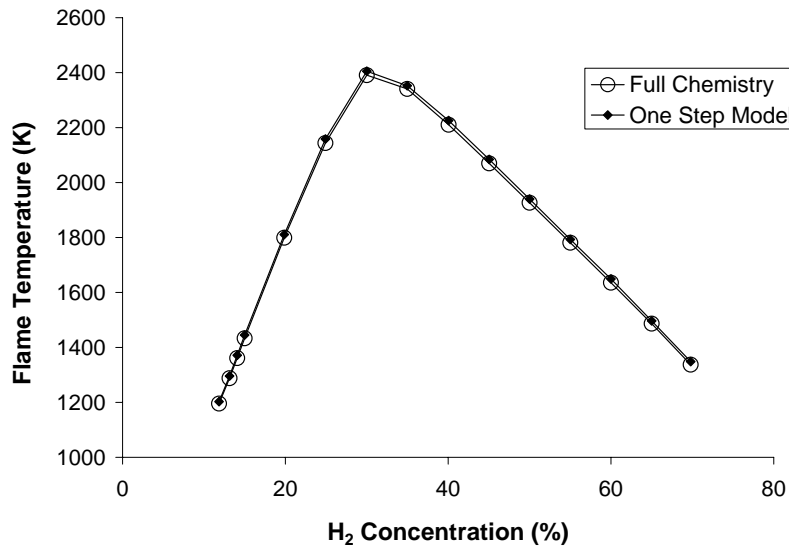
One-step models were constructed for the first-order reaction  $R \rightarrow P$ , and the results for the flame speed and flame temperature over a range of hydrogen-air compositions

are shown in Figure 6.8 with the results using detailed chemistry. The one-step model calculations were able to match the flame temperature from detailed chemistry to within 1% over the entire range of compositions, from very rich (70% hydrogen) to very lean (12% hydrogen). The one-step model flame speeds also matched the detailed chemistry values to within 1% over the entire range of hydrogen concentrations. The one-step model parameters  $E_a$ ,  $A$ ,  $q$ , and  $(a_5)_P$  for the range of hydrogen-air mixtures are tabulated in Appendix L.

The response of the flame speed and flame temperature to changes in the initial temperature and pressure was also examined using the one-step model versus the detailed chemistry behavior for a 30% hydrogen-air (near stoichiometric) mixture. Very small changes in the initial temperature and pressure, 10 K and 0.05 bar, respectively, were first considered. The response to small changes in initial temperature was then calculated by fixing the initial pressure at 1 bar and varying the initial temperature from 290 K to 350 K and computing flame speed and flame temperature using both the one-step model and detailed chemical mechanism. Similarly, the response to small changes in initial pressure were computed by fixing the initial temperature at 300 K and varying the pressure from 0.8 bar to 1.3 bar. The resulting flame speed and flame temperature response is shown in Figure 6.9. For small changes in initial temperature, both the flame speed and flame temperature response produced by the one-step model matched the results from detailed chemistry to within 5%. For small changes in initial pressure, the flame temperature response using the one-step model matched the detailed chemistry to within 1%. The flame speed response to small pressure change using the one-step model, while matching the detailed chemistry to within 11%, is clearly of a different functional form. The flame speed obtained using detailed chemistry is insensitive to small changes in the initial pressure (near 1 bar), staying nearly constant, while the flame speed calculated using the one-step model depends on the pressure like  $s_L \sim p^{-1/2}$ . This dependence is observed because in the one-step model a first-order reaction  $R \rightarrow P$  is used and from simple flame theory it



(a)



(b)

Figure 6.8: (a) Laminar flame speeds and (b) flame temperatures calculated using first-order one-step models and the Li et al. mechanism (Li et al., 2004) for hydrogen-air compositions

is known that

$$s_L \sim p^{\left(\frac{n-2}{2}\right)} \quad (6.60)$$

so with  $n = 1$  the flame speed dependence is  $s_L \sim p^{-1/2}$ . However, it was previously

calculated that the reaction order is closer to  $n = 2$  for stoichiometric hydrogen-air which gives no dependence of flame speed on pressure. This difference in effective reaction order between the one-step model and detailed chemistry calculations explains the notable difference in the flame speed response to changes in initial pressure.

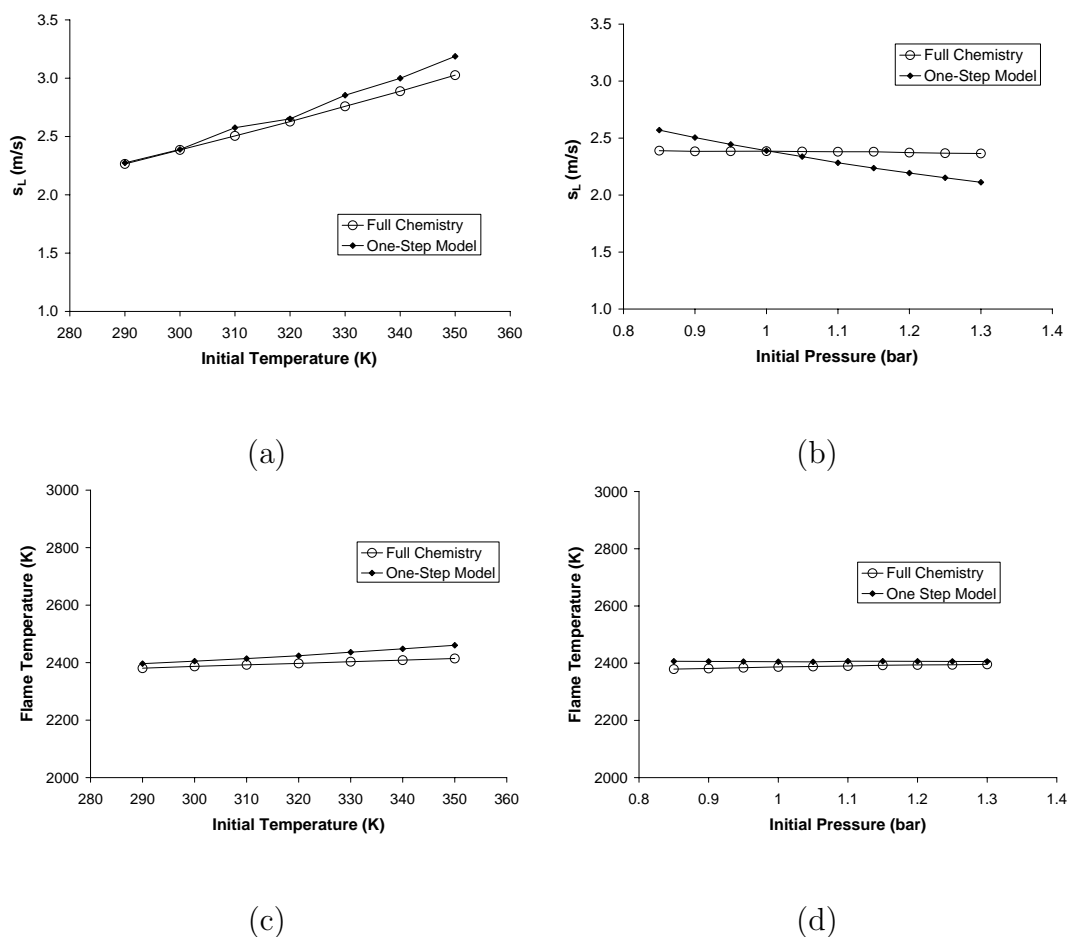


Figure 6.9: Flame speed response to small changes in initial (a) temperature and (b) pressure and flame temperature response to initial (c) temperature and (d) pressure calculated using first-order one-step models and detailed chemistry (Li et al., 2004) for 30% hydrogen-air

Also calculated were the flame speed and flame temperature response to large changes in initial temperature and pressure, extending the temperature to 800 K and pressure to 8 bar. The results from the one-step model and detailed chemistry are shown in Figure 6.10. The flame speed calculated using the one-step model was about 5 to 15% larger than the flame speed found using detailed chemistry as the initial

temperature is increased from 350 K to 800 K. The flame temperature from the one-step model was 3 to 11% larger than the detailed chemistry flame temperature, an effect that can be explained by examining the enthalpy. Across a flame the enthalpy is approximately constant, i.e.,

$$h_{Reactants}(T_{Reactants}) = h_{Products}(T_{Products}) \quad (6.61)$$

where

$$h(T) = \sum_{i=1}^K Y_i h_i(T) = \sum_{i=1}^K \left( Y_i h_{0,i} + Y_i \int_{T_0}^T c_{p,i}(T') dT' \right) \quad (6.62)$$

where  $Y_i$  is the mass fraction of species  $i$  and  $K$  is the total number of species. The flame temperature, or  $T_{Products}$ , is determined by the enthalpy balance, Equation 6.61. In the one-step model, the change in species mass fraction is simply  $Y_{Reactant} \rightarrow 0$  and  $Y_{Product} \rightarrow 1$  and the specific heats  $c_{p,Reactant}$  and  $c_{p,Product}$  are equal and constant. In flame calculations using detailed chemistry, however, there are many more species so the change in enthalpy due to the change in mass fractions,  $\sum Y_i h_{0,i}$  is different than in the one-step chemistry case. Additionally, in the detailed chemistry case the specific heats of all the species increase with temperature, resulting in a lower flame temperature than in the one-step calculation where the specific heat is constant. The flame temperature at an initial temperature 300 K is matched by choosing the heat release parameter in the one-step model, but the differences in the enthalpy change result in a different dependence of the flame temperature on initial temperature between the two models and a higher flame temperature for the one-step case. The slope of the flame temperature curve could be changed in the one-step case to better match the detailed chemistry curve by increasing the specific heat of the product. However, this change adds additional complexity to the one-step model and may not be necessary, as it was possible to match the flame temperature response to within 11% with the current model.

As expected, the flame temperature had little response to initial pressure, only

increasing by about 50 K from 1 bar to 8 bar, and the one-step model matched the detailed chemistry to within 1% over the entire range of pressure. The difference in the flame speed response to initial pressure calculated using the one-step model and detailed chemistry is more evident as the initial pressure increases. The one-step model flame speed clearly exhibits the dependence on pressure  $s_L \sim p^{-1/2}$ , deviating from the detailed chemistry flame speed by up to 50%. The detailed chemistry flame speed does notably decrease with increasing pressure, a trend that is due to the increasing rate of the 3-body reaction  $\text{H} + \text{O}_2 + \text{M} \rightarrow \text{HO}_2 + \text{M}$  slowing the energy release rate. This pressure dependence is a separate effect from the reaction order effect in Equation 6.60 and therefore cannot be reproduced with a simple one-step chemistry model.

### 6.6.2 Second-Order Reaction

To improve the flame speed response to pressure in the one-step model, the second-order reaction  $\text{R} + \text{R} \rightarrow \text{P} + \text{P}$  was implemented in the one-step Cantera input file, prescribing a reaction order  $n = 2$  that is closer to the effective reaction orders previously calculated. One-step models were then constructed for the entire range of hydrogen-air compositions using a second-order reaction with the same effective activation energies and heat release parameters found for the first-order ( $n = 1$ ) one-step models. Because of the larger reaction order the pre-exponential factor must increase, so the pre-exponential factor  $A$  was iterated on until the one-step model flame speed matched the detailed chemistry flame speed. Using the second-order one-step model it was possible once again to match the flame temperature and flame speed to the detailed chemistry results to within 1% over the entire range of compositions, as shown in Figure 6.11. The one-step model parameters for the second-order ( $n = 2$ ) reaction are tabulated in Appendix L, and an example Cantera input (.cti) file is given in Appendix N.

As in Section 6.6.1, the response of the flame speed and flame temperature to changes in the initial temperature and pressure was examined using the new second-

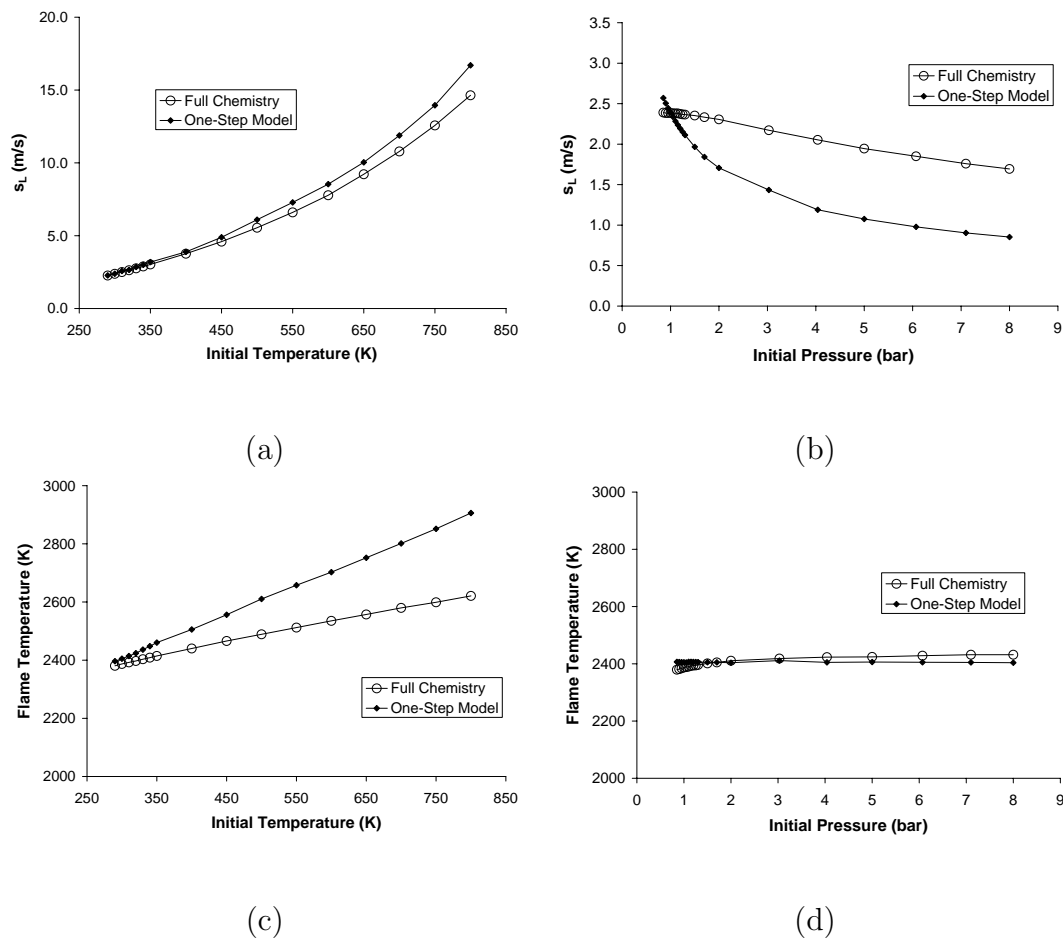
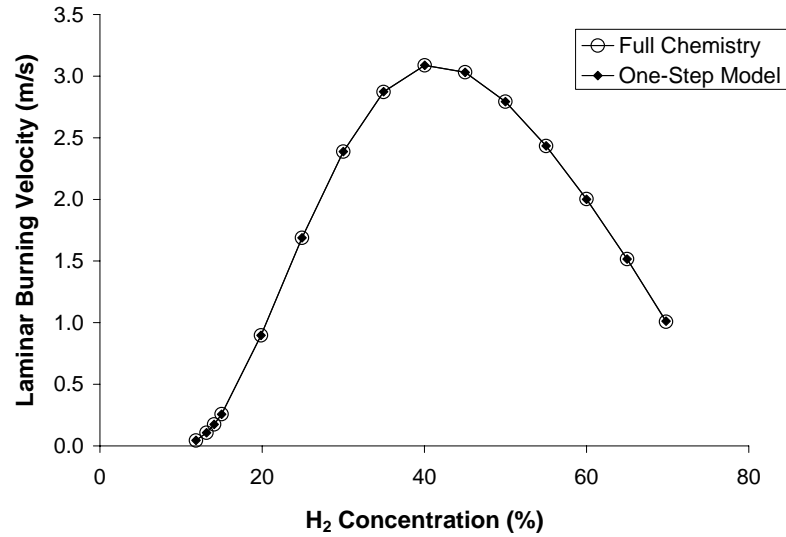
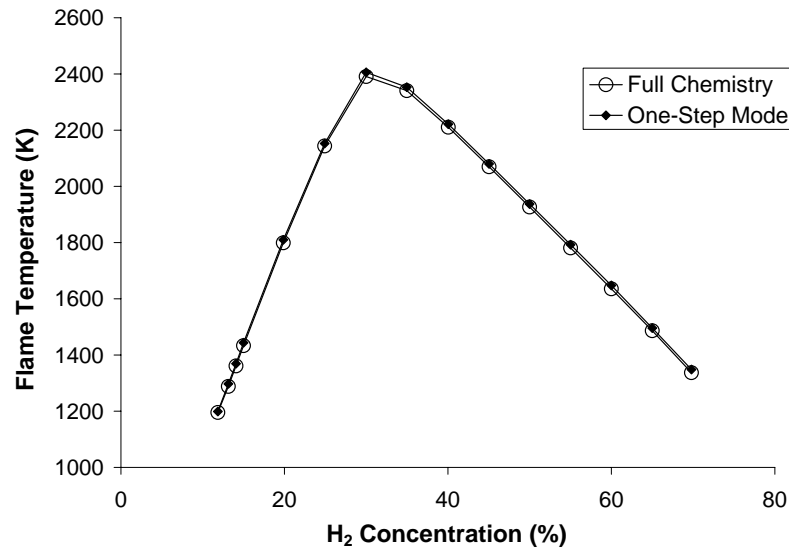


Figure 6.10: Flame speed response to large changes in initial (a) temperature and (b) pressure and flame temperature response to initial (c) temperature and (d) pressure calculated using first-order one-step models and detailed chemistry (Li et al., 2004) for 30% hydrogen-air

order one-step model compared with the detailed chemistry behavior for a 30% hydrogen-air mixture. Small changes in initial temperature and pressure were considered first by varying the temperature from 290 K to 350 K by 10K (with the pressure fixed at 1 bar) and the pressure from 0.8 bar to 1.3 bar by 0.05 bar (with the temperature fixed at 300 K). The resulting flame speed and flame temperature response is shown in Figure 6.12. Once again, for small changes in initial temperature both the flame speed and flame temperature response produced by the one-step model are in good agreement with the detailed chemistry, with the flame speed and temperature matching the detailed chemistry values to within 6% and 2%, respectively. Also, it



(a)



(b)

Figure 6.11: (a) Laminar flame speeds and (b) flame temperatures calculated using second-order one-step models and the Li et al. mechanism (Li et al., 2004) for hydrogen-air compositions

was possible once again to match the one-step flame temperature response to small pressure change to within 1%. Most notable was the change in the flame speed response to small pressure changes using a second-order one-step model. The agreement with the detailed chemistry behavior was greatly improved and the one-step model values match the detailed chemistry results to within 2.5%.

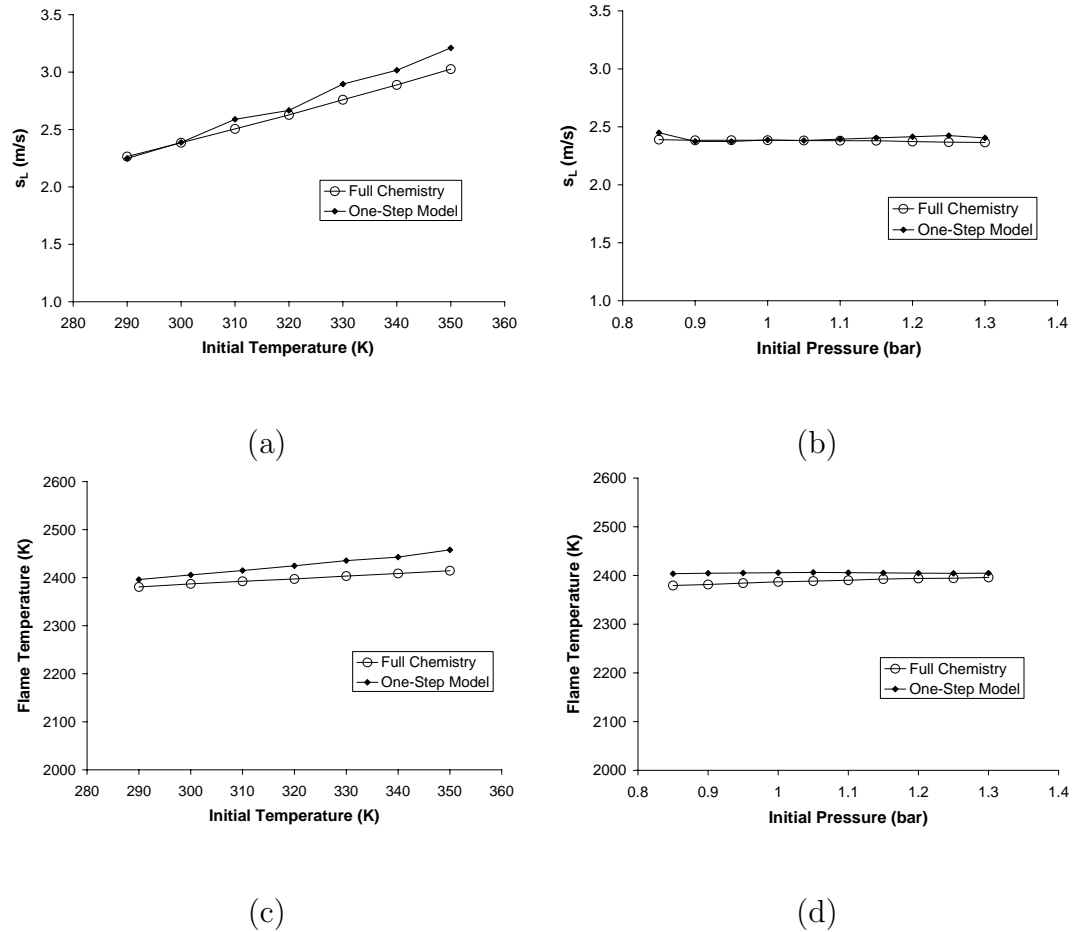


Figure 6.12: Flame speed response to small changes in initial (a) temperature and (b) pressure and flame temperature response to initial (c) temperature and (d) pressure calculated using second-order one-step models and detailed chemistry (Li et al., 2004) for 30% hydrogen-air

As in Section 6.6.1 the flame speed and flame temperature response to large changes in initial temperature and pressure were also calculated, and the results are shown in Figure 6.13. Like with the first-order one-step model, the one-step flame speed was about 5 to 15% larger than the detailed chemistry flame speed as the initial temperature was increased from 350 K to 550 K. For initial temperatures above 550 K the difference between the one-step and detailed chemistry flame speeds increases up to 33% until the one-step flame speed increases dramatically to 27 m/s and 76 m/s at initial temperatures of 750 K and 800 K, respectively. This phenomenon of rapidly increasing flame speed is a common issue with modeling high speed combustion waves

(see Singh et al. (2003)). As the flame speed increases the effects of diffusion decrease and the pre-heat region of diffusion-convection balance disappears, resulting in a predominant balance between convection and reaction. In this situation, the solution is no longer a typical flame, but rather the “fast flame” or “convected explosion” solution. The flame temperature from the one-step model is 2 to 10% larger than the detailed chemistry flame temperature due to the same reasons as described in Section 6.6.1 for the first-order one-step model.

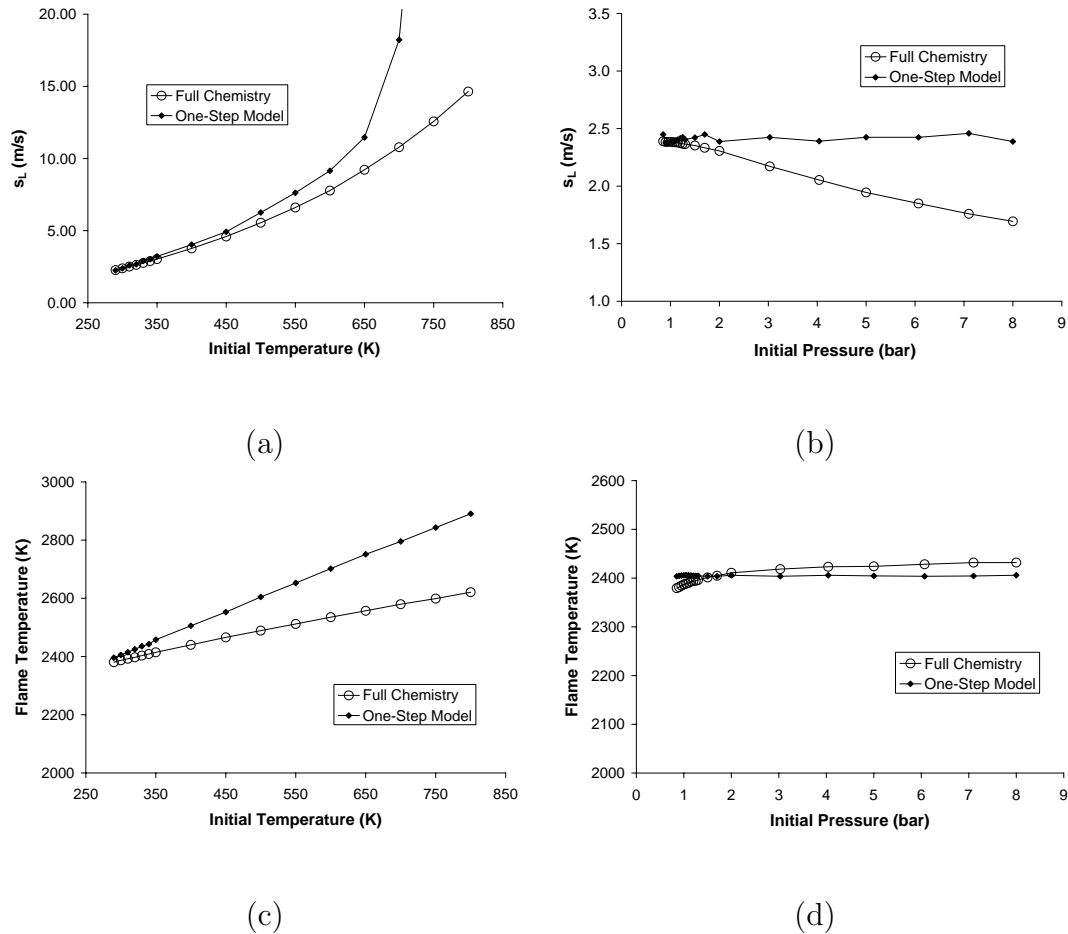


Figure 6.13: Flame speed response to large changes in initial (a) temperature and (b) pressure and flame temperature response to initial (c) temperature and (d) pressure calculated using second-order one-step models and detailed chemistry (Li et al., 2004) for 30% hydrogen-air

Once again, the flame temperature only increased by about 50 K for initial pressure increasing from 1 bar to 8 bar, and the one-step model matched the detailed chemistry

to within 1% over the entire range of pressure. While increasing the effective reaction order in the one-step model from  $n = 1$  to  $n = 2$  gave better agreement between the flame speeds calculated using the one-step model and detailed chemistry, there was still a large (up to 40%) difference for high initial pressures due to the decrease in the detailed chemistry flame speed. As described before, this flame speed decrease is due to the increasing rate of the 3-body reaction  $\text{H} + \text{O}_2 + \text{M} \rightarrow \text{HO}_2 + \text{M}$  as the initial pressure increases. Figure 6.14 shows the flame speed versus initial pressure calculated using detailed chemistry, the first-order one-step model, and the second-order one-step model for the 30% hydrogen case. Also shown is the flame speed calculated using the effective reaction order  $n = 1.8$  (found previously using the constant pressure explosion method, Equation 6.18) and the pressure dependence

$$s_L \sim p^{\left(\frac{n-2}{2}\right)} = p^{-0.1} \quad (6.63)$$

where the flame speed with  $n = 1.8$  was scaled to match the detailed chemistry flame speed at 1 bar. The flame speed versus pressure calculated using detailed chemistry lies between the first-order one-step model with pressure dependence  $s_L \sim p^{-1/2}$  and the second-order one-step model with no pressure dependence ( $s_L \sim p^0$ ). The scaled flame speed values generated using  $n = 1.8$  match the detailed chemistry results very closely (within 16% over the entire range of pressure), however, fractional reaction orders cannot be used in the one-step model. Therefore, the flame speed dependence on pressure cannot be properly modeled using one-step chemistry for large changes in initial pressure. The pressure dependence could be improved by using multi-step models, but a second-order one-step model is much easier to implement and the flame speed response to small changes in initial pressure (up to 2 bar) is reasonable, within 5% of the detailed chemistry results.

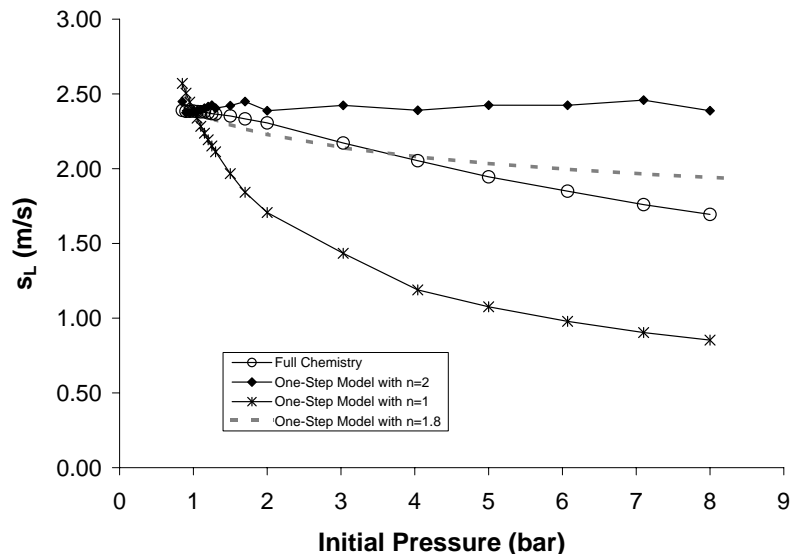


Figure 6.14: Flame speed response to changes in initial pressure calculated using detailed chemistry (Li et al., 2004), a first-order one-step model, and a second-order one-step model for 30% hydrogen-air. Also shown (red dashed line) is the predicted one-step model flame speed with effective reaction order  $n = 1.8$  obtained from the constant pressure explosion model (Equation 6.18).

## 6.7 Multi-Species One-Step Model: Flame Strain and Extinction

### 6.7.1 Strained Flame Calculations

In the first phase of this work, one-step chemistry models were used to accurately simulate the flame speed, flame temperature, and flame response to small changes in the initial pressure and temperature for a range of hydrogen-air mixtures. In these models, it was assumed that there were only two species, the reactant (R) and product (P), and that both of these species had the specific heat and transport properties of an argon atom. In the second phase of this work, the response of the one-step model flame to flame stretch was examined by performing simple strained flame simulations using the Cantera Python script *STFLAME1.py*. The script simulates a 1D flame in a strained flow field generated by an axisymmetric stagnation point, as illustrated in Figure 6.15. The flame starts out at a burner 6 mm above a non-reacting surface

and as the mass flow rate from the burner is increased, the flame moves closer to the surface until it is extinguished. The Python script is given in Appendix M.

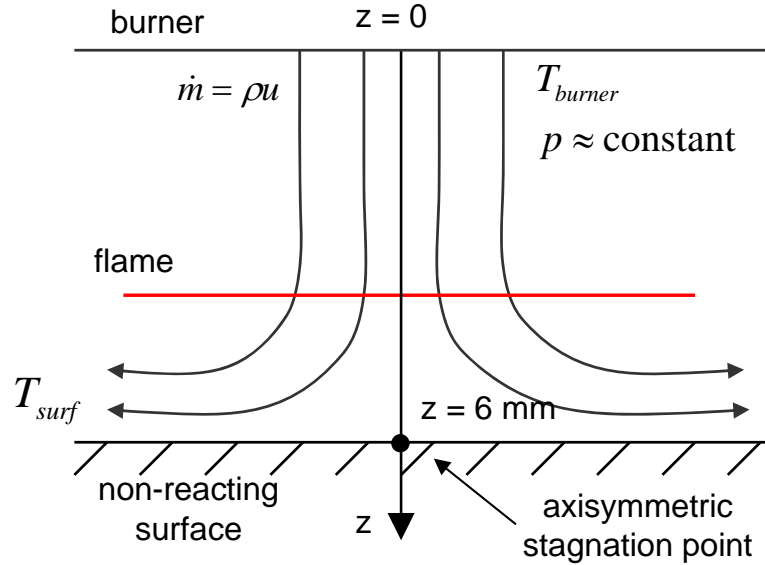


Figure 6.15: Schematic of axisymmetric stagnation point flow used to study flame strain in the Cantera script *STFLAME1.py*

An initial grid is defined along the  $z$ -axis from  $z = 0$  (the burner outlet) to  $z = 0.06 \text{ m}$  (the surface) and the code calculates the flow velocity, temperature, and species along the axis using grid refinement. Examples of the calculated velocity and temperature along the  $z$ -axis for a 15% hydrogen-air mixture with a mass flow rate  $\dot{m} = 2 \text{ kg/m}^2\cdot\text{s}$  are given in Figure 6.16. The slope of the velocity, plotted in Figure 6.17, provides a measure of the rate of strain in the flowfield, and so the highest rate of change of the velocity was taken as the strain rate,  $a$ , i.e.,

$$a = \left| \frac{du}{dz} \right|_{max} . \quad (6.64)$$

Taking the absolute value of the derivative was necessary because the slope of the velocity is negative upstream of the flame. The derivative of the velocity was calculated numerically, and the strain rate was recorded as well as the maximum temperature. The maximum temperature decreases as the mass flow rate, and hence the strain

rate, is increased until the flame is extinguished. Plotting the maximum temperature versus the strain rate allows for examination of the extinction behavior of strained flames.

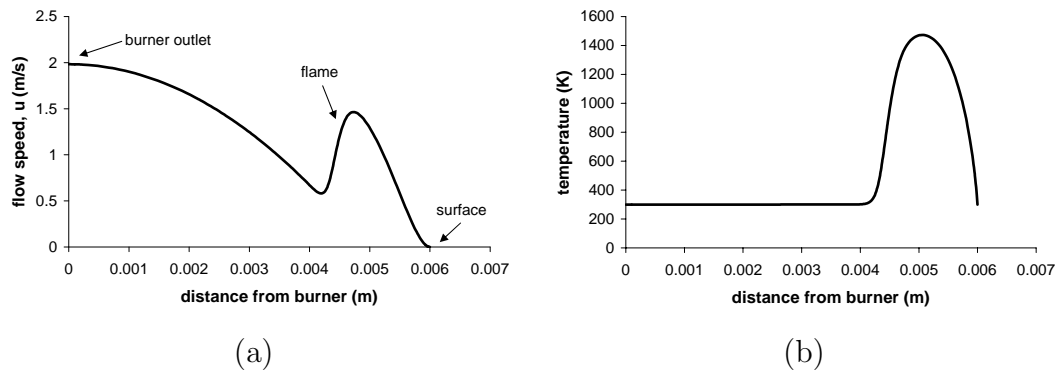


Figure 6.16: (a) Flow velocity and (b) temperature between the burner and the surface, calculated by the Cantera code. The flame location is indicated by the increase in velocity and temperature.

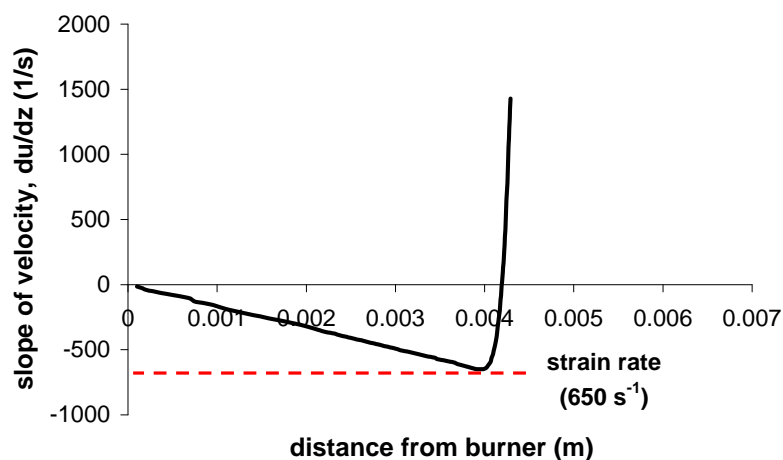


Figure 6.17: Derivative of the flow velocity along the  $z$ -axis, with the strain rate indicated

### 6.7.2 Two-Species One-Step Model

The Cantera code was used to calculate strained flames for a 15% hydrogen-air mixture using both detailed chemistry and a second-order one-step model, and the max-

imum temperature versus strain rate is plotted in Figure 6.18. The extinction strain rate with detailed chemistry was approximately  $1070 \text{ s}^{-1}$ , while the extinction strain rate with the one-step model was nearly 5 times lower, approximately  $223 \text{ s}^{-1}$ . This large difference is due to the different Lewis numbers in the two cases. The Lewis number of a mixture is defined as the ratio of the thermal diffusivity to the mass diffusivity:

$$Le = \frac{\alpha}{D} = \frac{\kappa / (\rho c_P)}{D} \quad (6.65)$$

where  $\kappa$  is the thermal conductivity,  $\rho$  is the density,  $c_P$  is the constant pressure specific heat, and  $D$  is the binary diffusion coefficient of the limiting species and the neutral diluent. In the case of the 15% hydrogen-air mixture, since the mixture is lean ( $\phi < 1$ ) the limiting species is hydrogen. For most gases, the Lewis number is close to unity, but for this mixture the Lewis number is less than 1 due to the large mass diffusivity of hydrogen. Using the detailed chemical mechanism, the Lewis number for the mixture can be calculated in Cantera:

$$Le = \frac{\frac{0.0405 \frac{\text{J}}{\text{s}\cdot\text{m}\cdot\text{K}}}{(0.9953 \frac{\text{kg}}{\text{m}^3})(1.1718 \times 10^3 \frac{\text{J}}{\text{kg}\cdot\text{K}})}}{9.24 \times 10^{-5} \frac{\text{m}^2}{\text{s}}} = 0.38 . \quad (6.66)$$

Therefore, for this lean hydrogen mixture the Lewis number is significantly less than 1, allowing for a much higher extinction strain rate than typical gas mixtures. In the one-step model the reactant was treated as an argon atom, so the mass diffusivity was nearly an order of magnitude smaller ( $1.895 \times 10^{-5} \text{ m}^2/\text{s}$  versus  $9.24 \times 10^{-5} \text{ m}^2/\text{s}$  for hydrogen) and thus the Lewis number was close to unity ( $Le = 1.14$  for the one-step model). Therefore, with the simple two-species (both argon) one-step model much lower extinction strain rates will be observed.

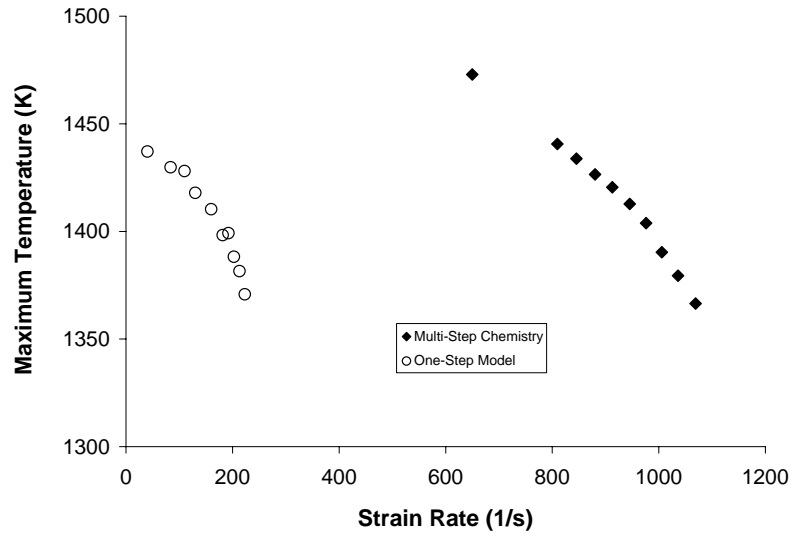


Figure 6.18: Maximum temperature versus strain rate near extinction for a 15% hydrogen-air mixture calculated using detailed chemistry and a second-order one-step model

### 6.7.3 Four-Species One-Step Model with Realistic Transport Properties

To simulate the straining behavior more accurately, the one-step model was changed in an attempt to match the Lewis number obtained with detailed chemistry. The new one-step model included the four species  $\text{H}_2$ ,  $\text{O}_2$ ,  $\text{H}_2\text{O}$ , and  $\text{N}_2$  instead of the two species R and P. The specific heats of  $\text{H}_2$ ,  $\text{O}_2$ , and  $\text{H}_2\text{O}$  were increased by a factor of approximately 3 to reduce the numerator of the Lewis number; for  $\text{N}_2$  the actual thermodynamic coefficients for a nitrogen molecule were used. Also, the actual transport coefficients for all 4 species were used so that the mass diffusivity matched that in the detailed chemistry case. The one-step reaction was changed from  $\text{R} + \text{R} \rightarrow \text{P} + \text{P}$  to the model reaction  $\text{H}_2 + \frac{1}{2}\text{O}_2 \rightarrow \text{H}_2\text{O}$  with effective parameters  $E_a = 20.263$  kcal/mol and  $A = 2.85 \times 10^{14} \text{ s}^{-1}$ . Finally, since all the actual species were included, the initial composition was the same as in the detailed chemistry case:  $0.42\text{H}_2 + 0.5\text{O}_2 + 1.88\text{N}_2$ . After these changes were implemented, the Lewis number of the mixture obtained with the new one-step model was 0.42, much closer to the actual Lewis number of 0.38. The parameters for the first one-step model, new four-species

one-step model, and the detailed chemistry model are summarized in Table 6.1 and the Cantera input file for the four-species one-step model is given in Appendix O.

Table 6.1: Comparison of parameters in the Lewis number for two one-step models and the detailed chemistry

	2-Species One-Step Model	4-Species One-Step Model	Detailed Chemistry
Reaction	$R + R \rightarrow P + P$	$\text{H}_2 + \frac{1}{2}\text{O}_2 \rightarrow \text{H}_2\text{O}$	
$\rho$	1.601 kg/m <sup>3</sup>	0.995 kg/m <sup>3</sup>	0.995 kg/m <sup>3</sup>
$c_P$	520 J/kg·K	1662 J/kg·K	1171 J/kg·K
$\kappa$	0.0181 W/m·K	0.0507 W/m·K	0.0405 W/m·K
$D_{H_2}$	$1.89 \times 10^{-5}$ m <sup>2</sup> /s	$9.24 \times 10^{-5}$ m <sup>2</sup> /s	$9.24 \times 10^{-5}$ m <sup>2</sup> /s
Le	1.14	0.42	0.38

As before, the effective activation energy was calculated using the constant pressure explosion method (Section 6.2) and the reaction was second order since  $n \approx 2$ . The heat release was determined to match the flame temperature, and the pre-exponential factor  $A$  was adjusted to match the flame speed. In addition to matching the flame temperature and speed, the four-species one-step model now also accurately simulates the density because it uses the correct molecular weights and initial composition, as shown by the flame profiles in Figure 6.20. While the post-flame velocity calculated using the one-step model overestimates the flow velocity by 11%, the profile fits are still greatly improved over the simpler one-step model. Strained flame computations for the 15% hydrogen-air mixture were performed again using the new four-species one-step model, and the maximum temperature versus strain rate is plotted in Figure 6.19 for both one-step models and detailed chemistry. As shown in the plot, with the four-species one-step model it was possible able to match the extinction strain rate obtained with detailed chemistry,  $a_{ext} = 1070 \text{ s}^{-1}$ . Therefore, flames modeled with the four-species model will more closely simulate flame front response to flame stretch than flames calculated using the initial 2-species one-step

model.

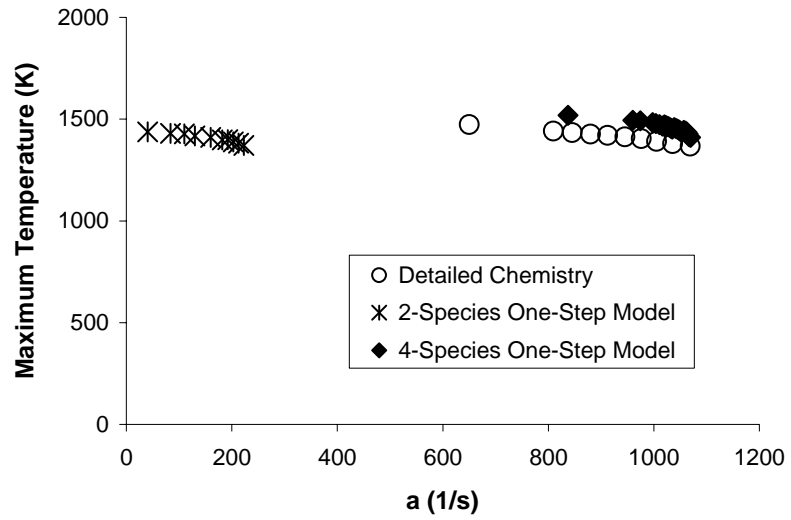


Figure 6.19: Maximum temperature versus strain rate near extinction for a 15% hydrogen-air mixture using detailed chemistry, the 2-species one-step model with  $Le = 1.14$ , and the four-species one-step model with  $Le = 0.42$

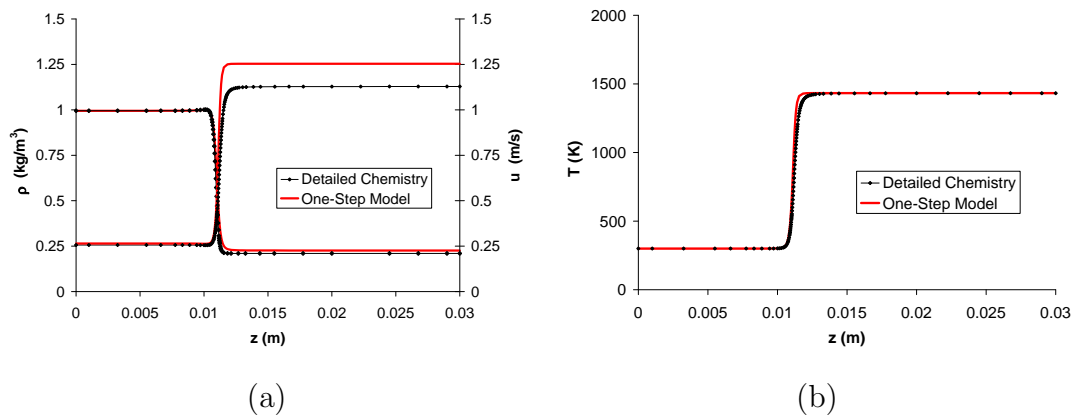


Figure 6.20: Comparison of the flame profiles for (a) flow speed and density and (b) temperature calculated using the four-species one-step model and detailed chemistry

## Chapter 7

# Numerical Modeling: Spark Ignition

### 7.1 Implementing One-Step Models in AMROC

To validate the implementation of one-step models in the AMROC software, a preliminary simulation of a one-dimensional steady flame was performed using the four-species one-step model described in Section 6.7.3. The initial condition for the AMROC simulation was a sixth-order interpolation of the Cantera solution for the flame profile, and after the errors dissipated, the AMROC simulation converged to a steady solution. The profiles of the velocity and temperature across the flame from AMROC and Cantera are compared in Figure 7.1. The flame profiles computed in AMROC agree with those calculated with Cantera to within 7% for the velocity and 1% for the temperature. These simple simulations indicated that the one-step model was correctly implemented in the AMROC software.

### 7.2 Numerical Model

The same model described in Section 5.2.1 for spark discharge in air is used for the ignition simulations, except that now the compressible Navier-Stokes equations are extended to multi-species, chemically reacting flows. The continuity (Equation 5.1) and momentum (Equation 5.2) equations are unchanged, but additional terms must

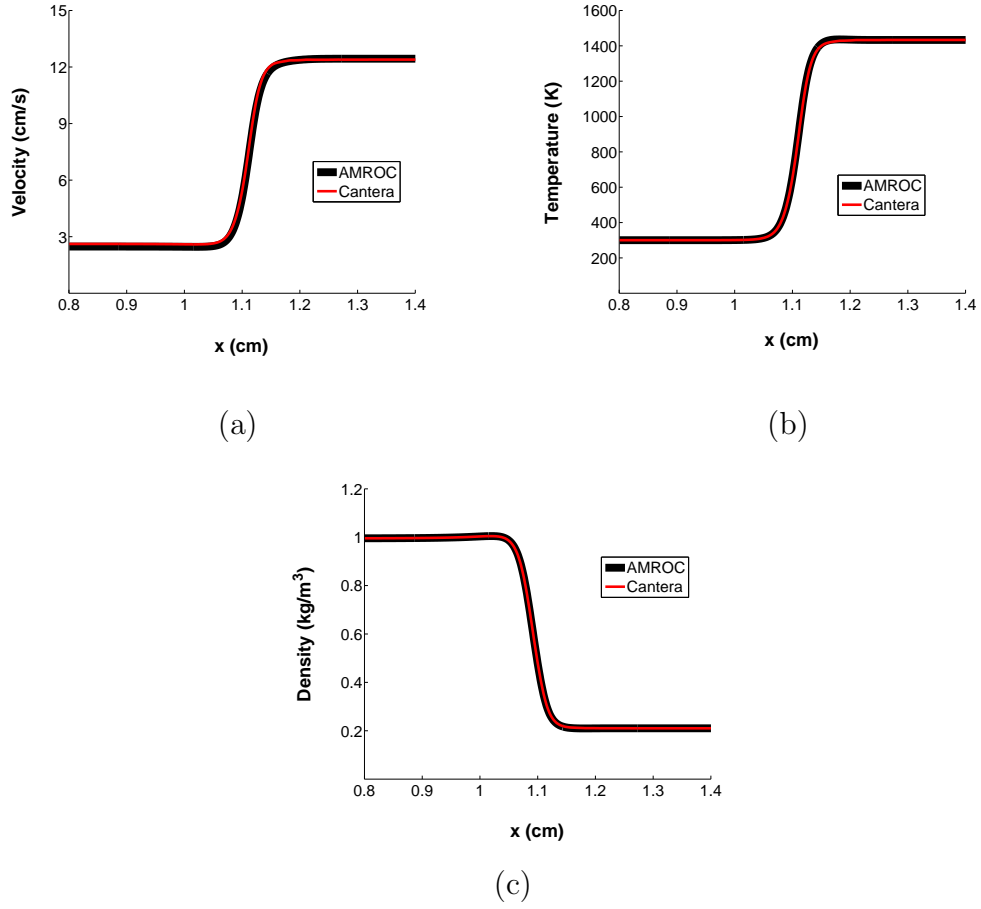


Figure 7.1: One-dimensional flame profiles from Cantera and AMROC simulations for a 15% hydrogen-air mixture: (a) velocity, (b) temperature, and (c) density

be included in the energy equation to account for energy flux through mass diffusion and changes in the total energy due to chemical reactions. Therefore, the reactive-diffusive energy equation is written (Chung, 1993):

$$\frac{\partial(\rho e_t)}{\partial t} + \frac{\partial(\rho u_i e_t)}{\partial x_i} + \frac{\partial(u_i p)}{\partial x_i} = \frac{\partial(\tau_{ij} u_j)}{\partial x_i} - \frac{1}{r}(\rho e_t + p)v - \frac{\partial q_i}{\partial x_i} - \sum_{k=1}^N h_k^0 \dot{\omega}_k \quad (7.1)$$

where  $h_k$  is the enthalpy of species  $k$  and  $\dot{\omega}_k$  is the mass production rate of species  $k$  through chemical reaction. Also, the heat flux  $q_i$  now includes not only heat flux due

to conduction but also due to species diffusion. Therefore, the total heat flux is

$$q_i = -\kappa \frac{\partial T}{\partial x_i} - \rho \sum_{k=1}^N h_k D_k \frac{\partial Y_k}{\partial x_i} \quad (7.2)$$

where  $D_k$  is the mass diffusivity and  $Y_k$  is the mass fraction for species  $k$ . Also, for  $N$  chemical species, there are  $N - 1$  conservation equations, where the equation for the  $k^{\text{th}}$  species is

$$\frac{\partial (\rho Y_k)}{\partial t} + \frac{\partial (\rho Y_k u_i)}{\partial x_i} + \frac{\partial}{\partial x_i} \left( \rho D_k \frac{\partial Y_k}{\partial x_i} \right) = \dot{\omega}_k . \quad (7.3)$$

The mass fraction of the  $N^{\text{th}}$  species is then determined separately by

$$Y_N = 1 - \sum_{i=1}^{N-1} Y_i . \quad (7.4)$$

Now that there are multiple species, the total energy is calculated using a mixture mass fraction averaged enthalpy,

$$e_t = -\frac{p}{\rho} + \frac{u_i u_i}{2} + h \quad (7.5)$$

$$= -\frac{p}{\rho} + \frac{u_i u_i}{2} + \sum_{k=1}^N Y_k h_k . \quad (7.6)$$

The total pressure is the sum of the partial pressures of the individual species, i.e.,

$$p = \sum_{i=1}^N p_i \quad (7.7)$$

and so the ideal gas law is now written

$$p = \rho R T = \sum_{i=1}^N \rho Y_i R_i T \quad (7.8)$$

where

$$R = \sum_{i=1}^N Y_i R_i \quad (7.9)$$

is the mixture-averaged gas constant, and  $R_i = \tilde{R}/W_i$ .

The temperature-dependent viscosity and thermal conductivity were modeled using the Sutherland law, as described in Section 5. For the reacting simulations, the pressure temperature dependence of the mass diffusivity was described using the empirical relation

$$D = D_{ref} \left( \frac{T}{T_{ref}} \right)^{1.71} \quad (7.10)$$

where the exponent 1.71 was determined by fitting the diffusivity to calculations from Cantera, as shown in Figure 7.2. The four-species one-step model described in Section 6.7.3 for a 15% hydrogen-air mixture was implemented in the simulation. The same initial conditions used in the non-reactive simulations were used, with a spark channel with a radius of 0.1 mm, 2 mm in length, and at a temperature of 35,000 K.

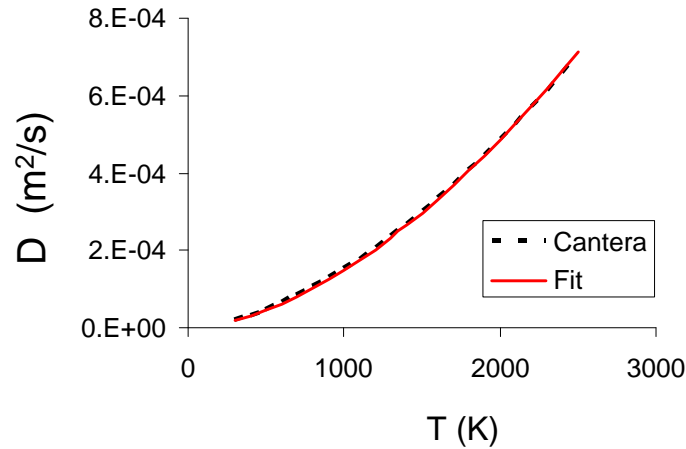


Figure 7.2: Mass diffusivity versus temperature from Cantera and using an empirical relation (Equation 7.10)

### 7.3 Spark Ignition in Hydrogen

Simulations of ignition were performed for the three electrode geometries described in Section 5.1: very thin cylindrical electrodes, conical electrodes, and flanged electrodes. Ignition experiments were also performed using electrodes of identical geometries to obtain high-speed visualization of the early stages of the flame formation. The simulation and experimental visualization were then compared at similar time steps to investigate the nature of the ignition in the different geometries.

Images from the schlieren visualization and images of the product (water in this case) from the simulation of ignition are shown in Figure 7.3 for the cylindrical electrode case. Both the experiment and computation show the inflow of cold reactant gas along the electrode, which then rolls up with the hot product gas expanding rapidly outward to form a large vortex with the flame front on its surface. This part of the flame continues to burn outward, while the small rising kernel in the center of the channel forms the rest of the flame front.

Figure 7.4 shows images from the schlieren visualization and of the simulated product ( $\text{H}_2\text{O}$ ) for the ignition with the conical electrodes. The flame formation is very similar to the cylindrical electrode case, as expected from the similarities in the fluid flow following spark discharge. Initially there is inflow along the electrode which forms a vortex with the outward flowing product gas. The flame front propagates outwards on the surfaces of this vortical structure and the rising gas kernel in the center of the channel.

Finally, the results for schlieren visualization and simulation of ignition with the flanged electrodes are shown in Figure 7.5. In the simulation, the flame front is curved due to the viscous flow velocity profile in the channel. The kernel shape is more pronounced in the schlieren images, and there is also some asymmetry of the flame. There are three possible causes of the asymmetry, the first being that it is an optical effect due to misalignment in the schlieren setup. Another possible cause is an actual fluid instability caused by the vortex pair being in close proximity. Finally, there may also be an asymmetry in the electrical discharge, as there are different

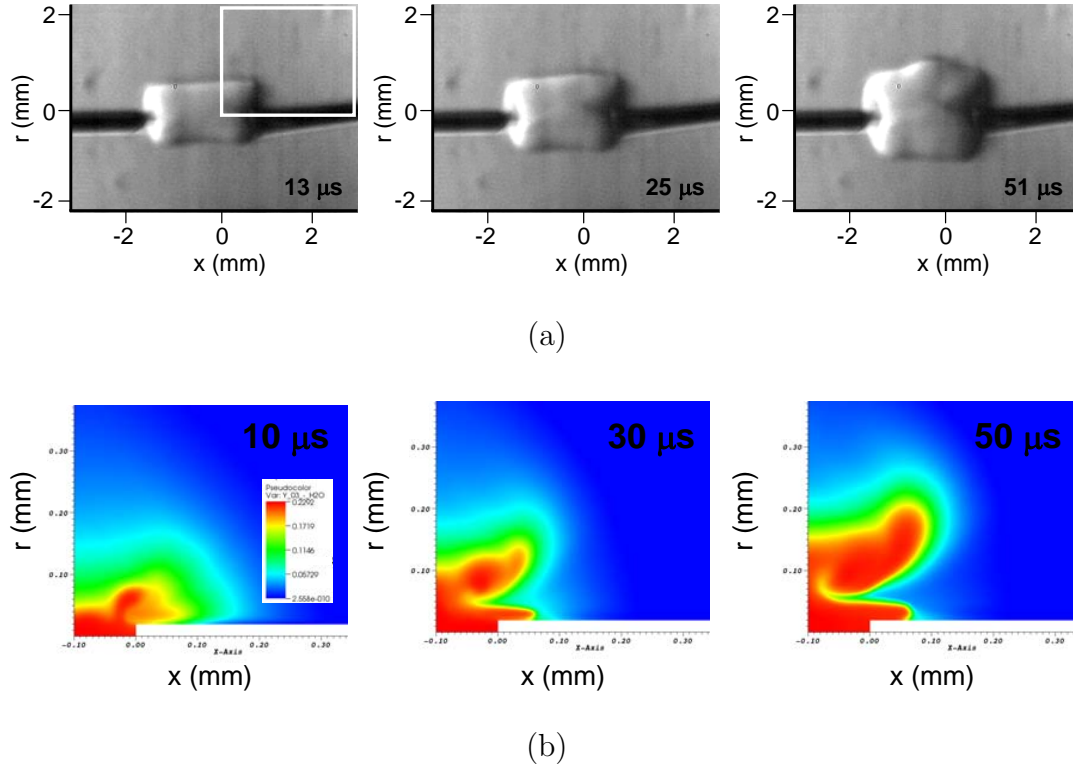


Figure 7.3: Ignition of a 15% hydrogen-air mixture using wire electrodes: (a) images from high-speed schlieren visualization and (b) simulations of the reaction product ( $\text{H}_2\text{O}$ ). The simulation region corresponds to the quadrant outlined in white on the upper left schlieren image.

physical processes that dominate at the anode versus the cathode. In this geometry there are some very interesting effects at late times, including the creation of a vortex pair at the outer edges of the flanges as shown in Figure 7.6(a). There is also ingestion of cold unburned gas back into the flanged region due to the pressure becoming sub-atmospheric, as observed in images of the product ( $\text{H}_2\text{O}$ ) in Figure 7.6(b). This phenomenon is only seen in the reacting simulations due to the higher velocities associated with the volume expansion of the burning gas.

## 7.4 Summary of Simulation Results

The flow field following a spark discharge is initially induced by the blast wave emitted from the high-temperature, high-pressure spark channel. The nature of the wave

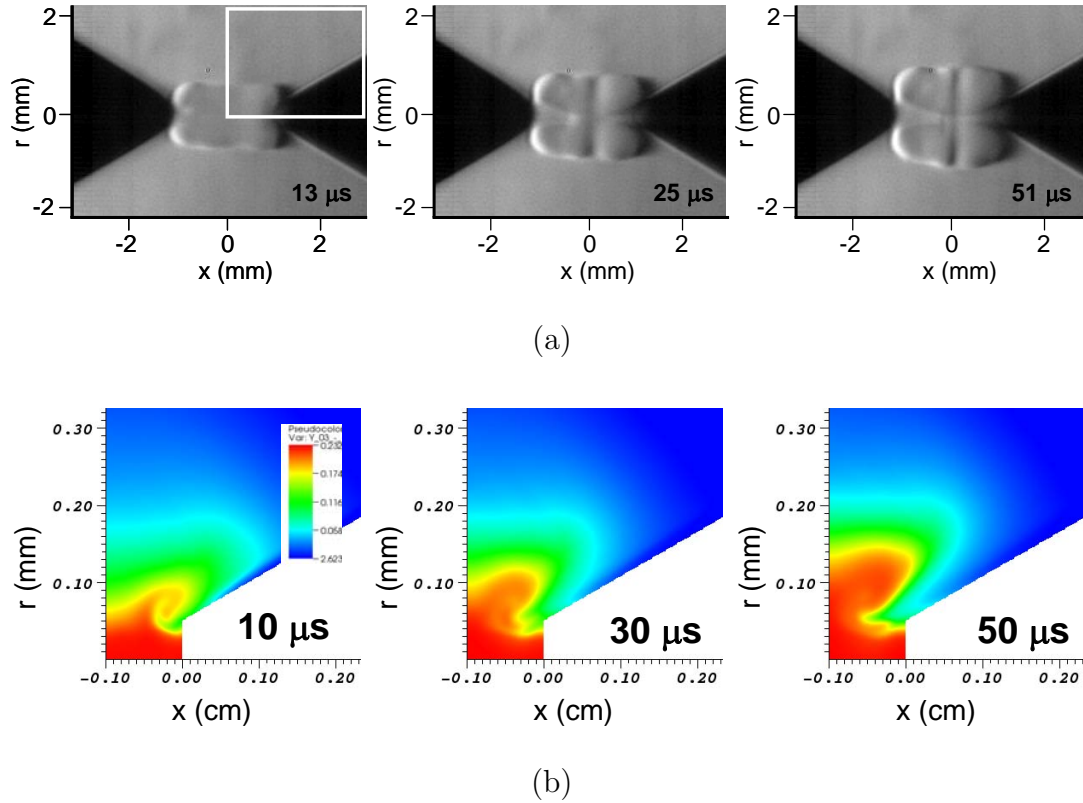
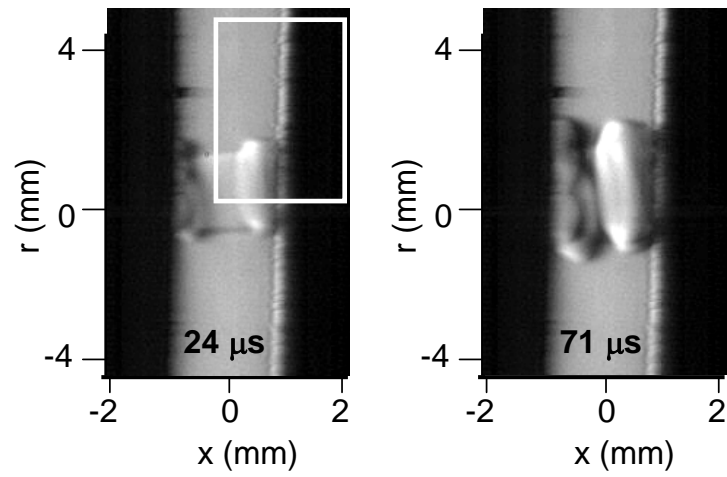
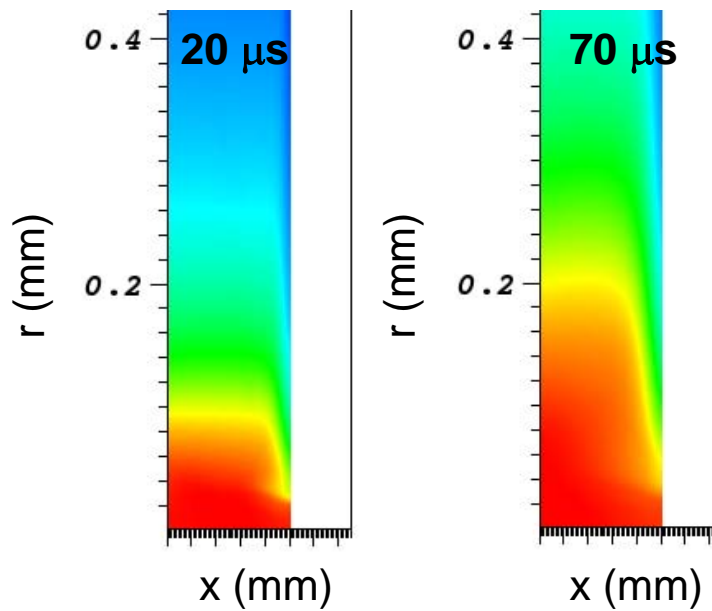


Figure 7.4: Ignition of a 15% hydrogen-air mixture using conical electrodes: (a) images from high-speed schlieren visualization and (b) simulations of the reaction product ( $\text{H}_2\text{O}$ ). The simulation region corresponds to the quadrant outlined in white on the upper left schlieren image.

depends on the geometry, and consequently the details of the fluid mechanics of the evolving kernel will be greatly influenced by the electrode shape and spacing. By simulating both the compressible flow aspects at very early times as well as the later viscous and chemical reaction effects, the important flow features seen in the schlieren visualization were captured by the simulations, including the blast and rarefaction waves, subsequent generation of inflow and vortices near the electrode tips, and formation of a rising hot gas kernel and mixing regions. It was determined that the inflow and vortex generation is a result of the competition between the geometric expansion of the kernel and the vorticity added to the flow due to viscous effects at the boundaries. The present experiments and simulations show that there are significant concentrations of vorticity and instabilities in the flow field that result in convoluted

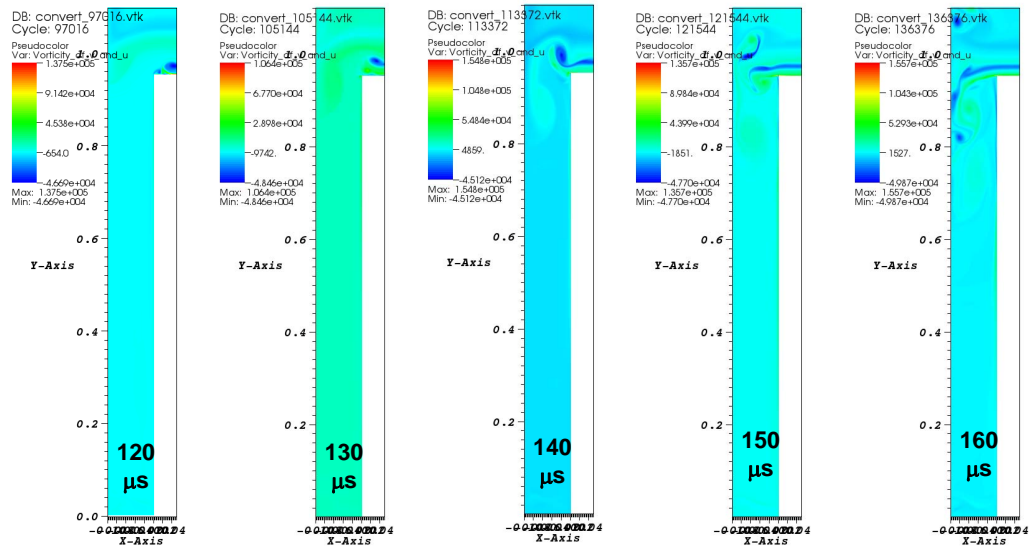


(a)

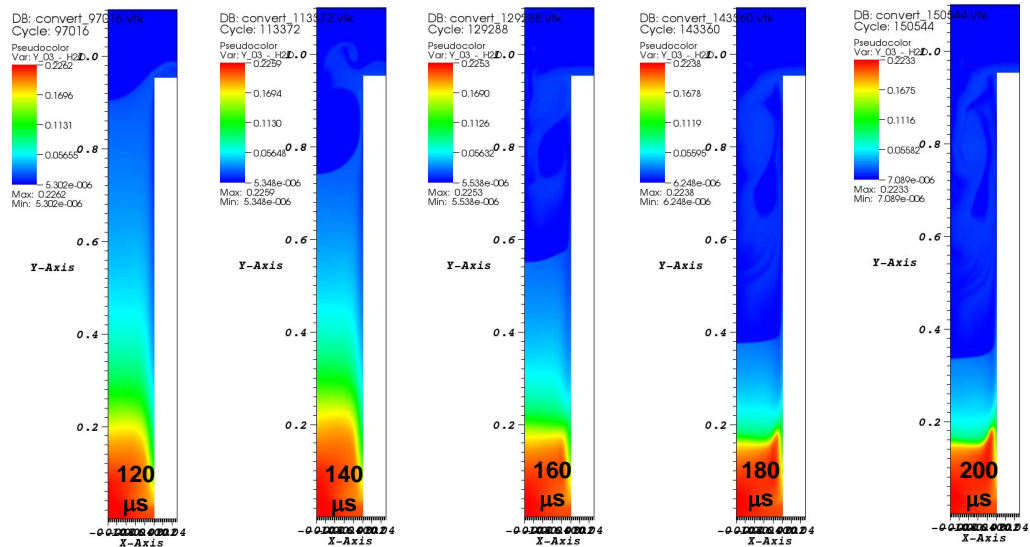


(b)

Figure 7.5: Ignition of a 15% hydrogen-air mixture using flanged electrodes: (a) images from high-speed schlieren visualization and (b) simulations of the reaction product ( $\text{H}_2\text{O}$ ). The simulation region corresponds to the quadrant outlined in white on the upper left schlieren image.



(a)



(b)

Figure 7.6: Images from the ignition simulation with flanged electrodes at later times: (a) vorticity field showing the formation of the vortex pair and (b) product ( $\text{H}_2\text{O}$ ) showing ingestion of gas back towards the spark gap

spark kernels and flame fronts.

In the flanged electrode geometry, it was expected that purely cylindrical expansion would be seen. However, both the simulations and experiments showed that even in this two-dimensional geometry, the viscous effects lead to multidimensional flow, a result not shown in previous modeling work. Therefore, including viscosity in simulations of ignition is extremely important as it has a large effect on the flow field in the flanged electrode case as well as in the other two geometries. The results indicate that the lowest minimum ignition energy would be obtained using the flanged electrodes due to a hotter gas kernel and confinement of the flow, and that the largest ignition energy would be required for the thin cylindrical electrode case. Schlieren visualization and two-dimensional simulations of ignition in a 15% hydrogen-air mixture demonstrated that the flame formation process was comparable in the cylindrical and conical electrode cases due to the similarities of the flow fields in the two geometries. The flame formation process was influenced by viscosity for the flanged electrode case, but the propagating flame ultimately appeared to be very similar to observations of steady flames in two-dimensional channels ([Jarosinski, 2009](#)).

# Chapter 8

## Conclusion

### 8.1 Summary

The work performed in this investigation included both an experimental phase and a numerical phase. The experimental phase of this work focused on investigating the phenomenon of spark ignition of flammable gases. Spark ignition tests were performed in various test mixtures to investigate the possible statistical nature of the spark ignition process. The effect of both the spark energy and length were studied, and the ignition and flame propagation were investigated using optical visualization. The second phase of this work focused on developing simplified chemistry models and implementing them in two-dimensional simulations of spark ignition.

In the first phase of experiments, the statistical nature of spark ignition with respect to the spark energy was investigated by performing ignition tests using sparks with energies on the order of historical minimum ignition energy (MIE) values. A very low-energy capacitive spark ignition source was developed to produce sparks 1 to 2 mm in length and with energies on the order of 50  $\mu\text{J}$  to 1 mJ. The test methods were carefully developed to minimize the experimental variability so that the probabilistic nature of the ignition process could be isolated and observed. Spark ignition tests were first performed using fixed-length (2 mm) sparks in the test mixture recommended by the ARP for aircraft certification testing: 5% hydrogen, 12% oxygen, and 83% argon ([International, 2005](#)). Tests were performed using a range of spark energies, and the results were analyzed using statistical tools to obtain a probability

distribution for ignition versus spark energy. The statistical analysis demonstrated that a single threshold MIE value did not exist, but rather that ignition was probabilistic at these very low spark energies, a feature manifested in the breadth of the probability distribution.

To investigate the effect of the fuel concentration on the required ignition energies and the flame propagation, further ignition tests were conducted in mixtures with 6 and 7% hydrogen and statistical analysis was performed on the results. Changing the fuel concentration by a mere 1% was found to have a significant effect on the required ignition energies and the resulting probability distributions. For example, increasing the hydrogen concentration from 5 to 6% resulted in a decrease in the 50<sup>th</sup> percentile (50% probability of ignition) spark energy by a factor of 2.7 (952  $\mu\text{J}$  to 351  $\mu\text{J}$ ). A further increase in the hydrogen concentration from 6 to 7% once again resulted in the 50<sup>th</sup> percentile energy decreasing significantly, in this case by a factor of 2.5 (351  $\mu\text{J}$  to 143  $\mu\text{J}$ ). The considerable dependence of the required spark ignition energy to small changes in the fuel concentration was not surprising, given that the ARP-recommended mixture is very close to the lower flammability limit of hydrogen (4% for “upward” flame propagation) (Coward and Jones, 1952). The ignition test results were also compared with the MIE data of Lewis and von Elbe (1961), and the range of ignition energies obtained in the current work for the 7% hydrogen mixture were in good agreement with the historical MIE value. However, the current and historical results for the 5% hydrogen mixture were inconsistent. Lewis and von Elbe gave an MIE value of 200  $\mu\text{J}$  for the 5% mixture, but the statistical analysis of the current tests showed the probability of ignition with a 200  $\mu\text{J}$  was negligible; a spark energy of 600  $\mu\text{J}$  was required to have even a 1% probability of ignition in the 5% hydrogen mixture. The discrepancy in the values could possibly be explained by the fact that in Lewis and von Elbe there is no data point for a 5% hydrogen mixture, only a 7% mixture. Therefore, the 200  $\mu\text{J}$  MIE value is obtained through extrapolation of an MIE curve versus spark energy on a logarithmic scale. Even a small error in the slope of the MIE curve could result in errors of an order of magnitude in the spark energy.

The flame propagation in the three test mixtures was also studied using schlieren

visualization and measurement of the pressure history in the combustion vessel. Varying the hydrogen concentration from 5 to 7% was also found to have a large influence on the nature of the flame propagation; in the 5% hydrogen mixture a buoyant flame is observed that extinguishes at the top of the vessel, while the flame propagation in the 7% hydrogen mixture is nearly spherical. The 6% hydrogen case was determined to be a sort of “threshold” case between entirely buoyant combustion characterized by modest pressure rises (on the order of 10% of the initial pressure) and quasi-spherical flame propagation with pressure rises of 200 to 600% of the initial pressure. The findings in this investigation regarding the spark energies required for ignition and the combustion characteristics have significant implications for aircraft safety testing and the ARP testing standards.

In the second phase of experiments, the effect of the spark length on ignition was investigated. A second low-energy capacitive spark ignition system was developed; this system was designed to produce sparks of varying lengths, from 1 mm up to 11 mm. The first flammable mixture tested was the 6% hydrogen mixture used in the short, fixed-spark ignition tests so that the two sets of results could be compared. Two additional mixtures with hexane ( $C_6H_{14}$ ) as the fuel were also tested—a stoichiometric hexane-air mixture and a fuel-rich ( $\phi = 1.72$ ) hexane-air mixture corresponding to the composition with the lowest overall MIE value according to [Lewis and von Elbe \(1961\)](#). Tests were performed using a range of spark energies and lengths, and the results were analyzed using statistical tools to obtain probability distributions for ignition versus the spark energy density (spark energy divided by spark length). It was found that the two sets of tests in the 6% hydrogen mixture could not be compared in terms of the spark energy, but rather were more comparable when considering the spark energy density, demonstrating the importance of considering the spark length. Qualitative agreement was also found between the current test results in the hexane mixtures and historical MIE data ([Lewis and von Elbe, 1961](#)).

The statistical analysis showed that the relative variability of ignition was comparable between the three test mixtures, suggesting that the variability is not influenced by the chemical composition. The test results were further analyzed in terms of the

spark charge, as it has been suggested (von Pidoll et al., 2004) that the required charge for ignition would be less dependent on the voltage and gap distance and therefore less variable. While the variability of the ignition was decreased when analyzed with respect to the spark charge, the probability distributions still did not approach a threshold MIE value. Experimental observations lend credence to the conclusion that the results will always have an associated probability distribution no matter which independent variable is considered.

The schlieren visualization of the early times following the spark breakdown revealed that the hot gas channel produced by the spark is not homogeneous, but rather has localized bulges due to electromagnetic effects such as plasma instabilities and cathode effects. Localized ignition along the spark channel was observed in several tests, and was more common as the spark length increased. Therefore, even though the test methods were carefully controlled, the electromagnetic effects were a significant contributor to the variability in the ignition data. The result of these phenomena is that long sparks with very low energy densities may still ignite locally, potentially leading to underestimation of explosion hazards.

The focus of the numerical portion of this work was on developing a two-dimensional simulation of spark discharge and flame ignition that accurately resolved all physical scales of the fluid mechanics and chemistry. In the first phase of the work, two-dimensional, axisymmetric simulations of the fluid mechanics following a spark in a non-reactive gas were performed. The Navier-Stokes equations including diffusion of heat and mass were solved, and using the AMROC (Adaptive Mesh Refinement in Object-Oriented C++ (Deiterding, 2003)) software package, highly resolved simulations were possible. The results of the computations were compared with close-up images of the spark discharge obtained using high-speed schlieren visualization. Both the simulations and experiments were performed using three different electrode geometries to examine the effect of the geometry on the flow field following the spark discharge. The high-pressure, high-temperature gas kernel created by the spark was used as the initial condition, and a shock wave is emitted as the kernel expands. The shock wave is cylindrical in nature near the center of the spark gap but spherical in

nature near the electrode surface. This shock structure initiates a complicated flow field. After the shock wave passes, initially the hot kernel of gas expands outward. However, due to the complicated shock structure, the pressure is higher in the center of the kernel, inducing outflow along the electrodes. A vortex forms due to the separation of the flow at the electrode, which then induces flow inward toward the center of the kernel. The vortex is convected towards the center of the channel and then up and out of the channel, trapping a kernel of hot gas. In addition, a mixing region forms near the end of the channel, mixing hot gas with the cold outer gas. Inflow of gas was observed even in a purely two-dimensional geometry (a spark between two flat walls, or flanges) due to viscous effects at the boundaries inducing vorticity into the flow. The major flow features observed in the simulation were also observed in the schlieren visualization.

To perform efficient, high-resolution simulations of spark ignition, one-step models were developed for hydrogen-air mixtures. Methods were developed based on constant pressure explosion calculations to extract physically reasonable values of the effective parameters for the one-step reaction. The thermodynamic and transport parameters in the models were then tuned to match the flame speed, temperature, and straining behavior of one-dimensional flames calculated using Cantera software (Goodwin, 2005) with a detailed chemical mechanism. The one-step chemistry model was implemented into AMROC and validated using one-dimensional, steady flame computations. Simulations were performed of ignition in a 15% hydrogen-air mixture using a four-species one-step model by solving the reactive Navier-Stokes equations including heat and mass diffusion. As expected, the flame front forms on both the hot rising gas kernel generated by the vortex but also in the mixing region. For the two-dimensional electrode geometry, a curved flame was observed due to the no-slip condition at the electrode flanges. Once again, the results of the simulations were compared with high-speed schlieren visualization of flame ignition, and the simulation and experiment demonstrated good qualitative agreement.

## 8.2 Future Work

For experimental work, the next step is to perform ignition tests in jet fuel, or aviation kerosene, to quantify the actual threat to aircraft. The results could then be compared with the results obtained using the hydrogen and hexane mixtures to determine the margin between the probability distributions for ignition. Once the risk of ignition in jet fuel is quantified, then an appropriate mixture can be chosen for safety testing that has the desired spark ignition energy. Experiments could also be performed over a range of mixture compositions and pressures to simulate actual flight conditions at different altitudes.

A new combustion vessel, shown in Figure 8.1, has been constructed for use in jet fuel ignition testing. The vessel is made of stainless steel to prevent corrosion, and it was manufactured by using a round pipe as the body and welding flanges to the pipe. The vessel was designed this way so that the inside would be smooth with no corners or crevices, allowing for easy cleaning between ignition tests. A lid-lifting assembly was also constructed to remove the lid using a counterweight for cleaning the inside of the vessel. Due to the low vapor pressure of jet fuel, the vessel must be heated to temperatures on the order of 100°C. Therefore, a heating system was also designed using flat silicone heaters and programmable temperature controllers. The vessel is insulated using custom manufactured fiberglass insulating jackets.

The numerical work in the current investigation formed a solid basis for future development of spark ignition simulations. For example, the simulations presented in Section 7 could be repeated on more powerful computers using detailed chemical mechanisms to examine how well the one-step model simulated the chemistry. Further one-step models could be developed for lean hydrogen mixtures like those used in this work, and for hexane and other hydrocarbons and implemented into the two-dimensional simulations. In addition, spark ignition of jet fuel could be studied using a surrogate fuel and a detailed chemical mechanism designed specifically for surrogate fuel chemistry.

Future numerical work could also include implementing an electrostatics model

into the spark ignition simulation. One of the major conclusions of this work was that electrodynamic effects contributed significantly to the variability and nature of the ignition process, so electrodynamics must be considered in any accurate model of spark ignition. The first steps toward simulating the localized ignition observed in the long spark ignition tests would be to include a localized hot region in the spark channel or increase the temperature of the cathode. There is still a great deal of work to be done before predicting spark ignition is possible using only numerical simulations.

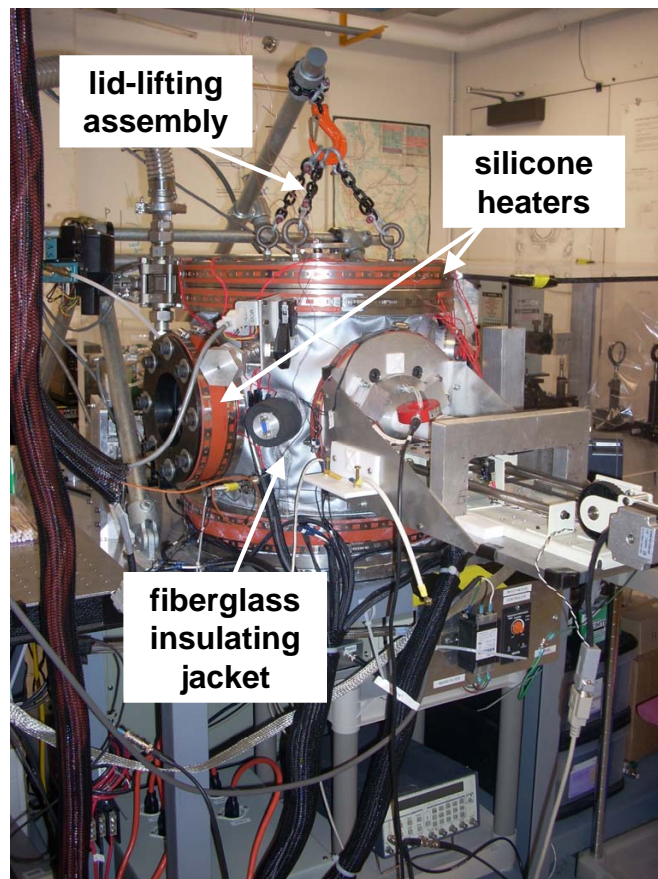


Figure 8.1: New heated, stainless steel combustion vessel for jet fuel ignition tests

# Bibliography

- Federal Aviation Administration. Aircraft fuel system lightning protection design and qualification test procedures development. Technical report, 1994. U.S. Dept. of Transportation Federal Aviation Administration Report DOT/FAA/CT-94/74. [3](#), [11](#), [14](#), [38](#), [47](#), [180](#)
- R. Akbar. *Mach Reflection of Gaseous Detonations*. PhD thesis, Rensselaer Polytechnic Institute, 1997. [xii](#), [2](#)
- O. O. Akindele, D. Bradley, P. W. Mak, and M. McMahon. Spark ignition of turbulent gases. *Combustion and Flame*, 47:129–155, 1982. [16](#)
- M. Akram. Two-dimensional model for spark discharge simulation in air. *AIAA Journal*, 34(9):1835–1842, 1996. [16](#), [17](#), [87](#), [89](#)
- V. S. Arpaci, Y. Ko, M. T. Lim, and H. S. Lee. Spark kernel development in constant volume combustion. *Combustion and Flame*, 135:315–322, 2003. [17](#)
- ASTM. Standard test method for minimum ignition energy and quenching distance in gaseous mixtures. Technical report, American Society for Testing and Materials International, 2009. E 582-07. [23](#)
- S. Au, R. Haley, and P. R. Smy. The influence of the igniter-induced blast wave upon the initial volume and expansion of the flame kernel. *Combustion and Flame*, 88: 50–60, 1992. [17](#)
- V. Babrauskas. *Ignition Handbook: Principles and Applications to Fire Safety Engineering, Fire Investigation, Risk Management and Forensic Science*. Fire Science Publishers, Issaquah, WA, 2003. [10](#), [13](#), [14](#), [23](#)

- D. R. Ballal and A. H. Lefebvre. Ignition and flame quenching of flowing heterogeneous fuel-air mixtures. *Combustion and Flame*, 35:155–168, 1979. [16](#)
- S. P. M. Bane and J. E. Shepherd. Statistical analysis of electrostatic spark ignition. 2009 Fall Meeting of the Western States Section of the Combustion Institute, October 26–27, University of California at Irvine, Irvine, CA, paper 09F-64, 2009. [63](#)
- S. P. M. Bane, J. E. Shepherd, E. Kwon, and A. C. Day. Statistical analysis of electrostatic spark ignition of lean H<sub>2</sub>-O<sub>2</sub>-Ar mixtures. International Conference on Hydrogen Safety, 2009. [38](#)
- C. R. Bauwens. Research technical memorandum, evaluation of flame properties (fp) program (Project no. 003025190). Technical report, 2007. FM Global. [105](#), [239](#)
- W. B. Benedick, J. C. Cummings, and P. G. Prassinis. Combustion of hydrogen-air mixtures in the vges cylindrical tank. Technical report, Sandia National Laboratories, Albuquerque, NM, and Livermore, CA, 1984. Report SAND-83-1022. [43](#), [44](#)
- M. Berger and P. Colella. Local adaptive mesh refinement for shock hydrodynamics. *Journal of Computational Physics*, 82:64–84, 1988. [95](#)
- M. Berger and J. Olinger. Adaptive mesh refinement for hyperbolic partial differential equations. *Journal of Computational Physics*, 53:484–512, 1984. [95](#)
- M. V. Blanc, P. G. Guest, G. von Elbe, and B. Lewis. Ignition of explosive gas mixtures by electric sparks. i. minimum ignition energies and quenching distances of mixtures of methane, oxygen, and inert gases. *Journal of Chemical Physics*, 15:798–802, 1947. [178](#)
- M. V. Blanc, P. G. Guest, G. von Elbe, and B. Lewis. Ignition of explosive gas mixtures by electric sparks. III. minimum ignition energies and quenching distances of mixtures of hydrocarbons and ether with oxygen and inert gases. In *Third*

- Symposium on Combustion, Flame, and Explosion Phenomena*, pages 363–367. The Combustion Institute, Pittsburgh, PA, 1949. [178](#)
- Boeing, Airbus, ATA, AEA, AAPA, EAAI, and AIA. Industry response to FAA on fuel system safety. Technical report, Boeing Commercial Airplane Group, <http://www.boeing.com/news/techissues/pdf/FAARESPONSE.PDF>, 1997. [3](#)
- D. Bradley and I. L. Critchley. Electromagnetically induced motion of spark ignition kernels. *Combustion and Flame*, 22:143–152, 1974. [17](#)
- L. G. Britton. Two hundred years of flammability limits. *Process Safety Progress*, 21:1–11, 2002. [10](#), [38](#)
- H. F. Calcote, Jr. C. A. Gregory, C. M. Barnett, and R. B. Gilmer. Spark ignition effect of molecular structure. *Industrial and Engineering Chemistry*, 44:2656–2662, 1952. [11](#), [15](#), [16](#), [177](#), [188](#)
- K. L. Cashdollar, I. A. Zlochower, G. M. Green, R. A. Thomas, and M. Hertzberg. Flammability of methane, propane, and hydrogen gases. *Journal of Loss Prevention in the Process Industries*, 13:327–340, 2000. [39](#), [43](#)
- M. Champion, B. Deshaies, G. Joulin, and K. Kinoshita. Spherical flame initiation: Theory versus experiments for lean propane-air mixtures. *Combustion and Flame*, 65:319–337, 1986. [16](#), [17](#)
- T. J. Chung. In *Numerical Modeling in Combustion*, Series in Computational and Physical Processes in Mechanics and Thermal Sciences. Taylor and Francis, 1993. [148](#)
- J. Colwell and A. Reza. Hot surface ignition of automotive and aviation fluids. *Fire Technology*, 41:105–123, 2005. [14](#), [49](#)
- H. F. Coward and G. W. Jones. The limits of flammability of gases and vapors. Technical report, Bureau of Mines, 1952. Bulletin 503. [10](#), [39](#), [158](#)

- S. G. Davis and C. K. Law. Determination of and fuel structure effects on laminar flame speeds of  $c_1$  to  $c_8$  hydrocarbons. *Combustion Science and Technology*, 140: 427–449, 1998. [xxii](#), [72](#), [73](#), [74](#)
- R. Deiterding. *Parallel Adaptive Simulation of Multi-dimensional Detonation Structures*. PhD thesis, Brandenburgische Technische Universität Cottbus, 2003. [88](#), [95](#), [160](#)
- W. J. Dixon and F. J. Massey Jr. *Introduction to Statistical Analysis*. McGraw-Hill, 1983. [47](#), [48](#)
- O. Ekici, O. A. Ezekoye, M. J. Hall, and R. D. Matthews. Thermal and flow fields modeling of fast spark discharges in air. *Journal of Fluids Engineering*, 129:55–65, 2007. [16](#), [87](#), [89](#)
- D. Fernández-Galisteo, A. L. Sánchez, A. Li nán, and F. A. Williams. One-step reduced kinetics for lean hydrogen-air deflagration. *Combustion and Flame*, 156: 985–996, 2009. [105](#)
- T. Fornia. Thermal modeling to predict fuel tank flammability. In *Transport Fuel Flammability Conference*. SAE/FAA, October 1997. [3](#)
- I. Glassman. *Combustion*. Academic Press, 3 edition, 1996. [12](#)
- D. Goodwin. Cantera: Object-oriented software for reacting flows, 2005. California Institute of Technology, <http://www.cantera.org>. [xxii](#), [44](#), [59](#), [72](#), [92](#), [105](#), [107](#), [161](#)
- F. F. Grinstein and C. Fureby. LES studies of the flow in a swirl gas combustor. *Proceedings of the Combustion Institute*, 30:1791–1798, 2005. [105](#)
- P. G. Guest. Apparatus for determining minimum energies for electric-spark ignition of flammable gases and vapors. Technical report, 1944. Bureau of Mines Report of Investigations 3753. [180](#)
- V. Hamosfakidis, H. G. Im, and D. N. Assanis. A regenerative multiple zone model for hcci combustion. *Combustion and Flame*, 156:928–941, 2009. [105](#)

- J. B. Heywood. *Internal Combustion Engine Fundamentals*. McGraw-Hill, 1988. 43
- D. Hosmer and S. Lemeshow. *Applied Logistic Regression*. John Wiley and Sons, 1989. 49
- SAE International. Aerospace recommended practice aircraft lightning test methods. Technical report, SAE International, 2005. Aerospace Report ARP5416. xiii, 3, 10, 14, 38, 41, 52, 53, 157
- K. Ishii, T. Tsukamoto, Y. Ujiie, and M. Kono. Analysis of ignition mechanism of combustible mixtures by composite sparks. *Combustion and Flame*, 91:153–164, 1992. 16, 87, 89
- J. Jarosinski. *Flammability Limits: History and Mechanism of Flame Extinction*, chapter 3. CRC Press, 2009. 156
- M. Kono, K. Niu, T. Tsukamoto, and Y. Ujiie. Mechanism of flame kernel formation produced by short duration sparks. In *Twenty-Second Symposium (International) on Combustion*, pages 1643–1649. The Combustion Institute, Pittsburgh, PA, 1988. 16, 17, 87, 89
- T. L. Kosvic, L. Zung, and M. Gerstein. Analysis of aircraft fuel tank fire and explosion hazards. Technical report, Air Force Aero Propulsion Laboratory, Wright-Patterson Air Force Base, Ohio, 1971. Report AFAPL-TR-71-7. 3
- T. Kravchik, E. Sher, and J. B. Heywood. From spark ignition to flame initiation. *Combustion Science and Technology*, 108:1–30, 1995. 16, 87, 89, 92
- R. K. Kumar. Flammability limits of hydrogen-oxygen-diluent mixtures. *Journal of Fire Sciences*, 3:245–262, 1985. 39
- A. Y. Kusharin, O. E. Popov, and G. L. Agafonov. Initiation of laminar flames in near-limit  $\text{H}_2/\text{O}_2/\text{H}_2\text{O}$  mixtures. In *Twenty-Sixth Symposium (International) on Combustion*, pages 985–991. The Combustion Institute, Pittsburgh, PA, 1996. 16, 39

- A. Yu. Kusharin, O. E. Popov, G. L. Agafonov, and B. E. Gelfand. Initiation of premixed flames in H<sub>2</sub>-air-H<sub>2</sub>O mixtures. *Experimental Thermal and Fluid Science*, 21:2–8, 2000. [16](#)
- E. Kwon, S. P. Moffett, J. E. Shepherd, and A. C. Day. Combustion characteristics of hydrogen as used in a flammable test mixture. Paper PPR-48, 2007. [15](#), [38](#)
- N. Lamoureux, N. Djebaili-Chaumeix, and C. E. Paillard. Laminar flame velocity determination for H<sub>2</sub>-air-He-CO<sub>2</sub> mixtures using the spherical bomb method. *Experimental Thermal and Fluid Science*, 27:385–393, 2003. [39](#)
- H. J. Langlie. A test-to-failure program for thermal batteries. In *Sixteenth Annual Power Sources Conference*. PSC Publications Committee, 1962. [47](#)
- R. J. Larsen and M. L. Marx. *An Introduction to Mathematical Statistics and its Applications*. Pearson Prentice Hall, 2006. [184](#)
- J. J. Lee and J. E. Shepherd. Spark energy measurements in Jet A part II. Technical report, 1999. technical report, Graduate Aerospace Laboratories, California Institute of Technology, Explosion Dynamics Laboratory Report FM 99-7. [xiv](#), [14](#), [33](#), [47](#), [50](#), [51](#)
- B. Lewis. Report of research and technological work on explosives, explosions, and flames, fiscal year 1946. Technical report, 1947. Bureau of Mines Report of Investigations 4176. [178](#)
- B. Lewis. Report of research and technological work on explosives, explosions, and flames, fiscal years 1947 and 1948. Technical report, 1949. Bureau of Mines Report of Investigations 4502. [178](#), [179](#)
- B. Lewis. Report of research and technological work on explosives, explosions, and flames, fiscal year 1949. Technical report, 1950. Bureau of Mines Report of Investigations 4667. [178](#), [179](#)

- B. Lewis and G. von Elbe. Ignition of explosive gas mixtures by electric sparks. II. theory of propagation of flame from an instantaneous point source of ignition. *Journal of Chemical Physics*, 15:803–808, 1947. [178](#)
- B. Lewis and G. von Elbe. *Combustion, Flames and Explosions of Gases*. Academic Press, 1951. [xx](#), [178](#), [179](#), [180](#), [182](#), [188](#)
- B. Lewis and G. von Elbe. *Combustion, Flames and Explosions of Gases*. Academic Press, New York, 2nd edition, 1961. [xxii](#), [10](#), [11](#), [15](#), [16](#), [23](#), [32](#), [56](#), [57](#), [58](#), [63](#), [65](#), [68](#), [70](#), [73](#), [89](#), [102](#), [158](#), [159](#)
- J. Li, Z. Zhao, A. Kazakov, and F. L. Dryer. An updated comprehensive kinetic model of hydrogen combustion. *International Journal of Chemical Kinetics*, 36: 566–575, 2004. [xviii](#), [xix](#), [128](#), [130](#), [131](#), [134](#), [135](#), [136](#), [137](#), [139](#)
- E. L. Litchfield. Minimum ignition-energy concept and its application to safety engineering. Technical report, 1960. Bureau of Mines Report of Investigations 5671. [180](#)
- E. L. Litchfield and M. V. Blanc. Recent developments in spark ignition. Technical report, 1959. Bureau of Mines Report of Investigations 5461. [180](#)
- E. L. Litchfield, M. H. Hay, T. A. Kubala, and J. S. Monroe. Minimum ignition energy and quenching distance in gaseous mixtures. Technical report, 1967. Bureau of Mines Report of Investigations 7009. [180](#)
- U. Maas and J. Warnatz. Ignition processes in hydrogen-oxygen mixtures. *Combustion and Flame*, 74:53–69, 1988. [16](#)
- E. C. Magison. *Electrical Equipment in Hazardous Locations*. Instrument Society of America, 3rd edition, 1990. [10](#), [13](#), [14](#), [23](#)
- R. Maly. Ignition model for spark discharges and the early phase of flame front growth. In *Eighteenth Symposium (International) on Combustion*, pages 1747–1754. The Combustion Institute, Pittsburgh, PA, 1980. [16](#)

- R. Maly. *Spark Ignition: Its Physics and Effect on the Internal Combustion Engine*, chapter 3. Springer, 1984. [92](#)
- R. Maly and M. Vogel. Initiation and propagation of flame fronts in lean  $\text{CH}_4$ -air mixtures by the three modes of the ignition spark. *Proceedings of the Combustion Institute*, 17:821–831, 1979. [17](#), [92](#)
- A. J. Metzler. Minimum ignition energies of six pure hydrocarbon fuels of the C2 and C6 series. Technical report, 1952a. NACA report RM E52F27. [11](#), [15](#), [16](#), [177](#), [188](#)
- A. J. Metzler. Minimum ignition energies of 12 pure fuels at atmospheric and reduced pressure. Technical report, 1952b. NACA report RM E53H31. [11](#), [15](#), [16](#), [177](#), [188](#)
- J. Moorhouse, A. Williams, and T. E. Maddison. An investigation of the minimum ignition energies of some C1 to C7 hydrocarbons. *Combustion and Flame*, 23:203–213, 1974. [11](#), [15](#), [176](#), [188](#)
- L. Nestor. Investigation of turbine fuel flammability within aircraft fuel tanks. Technical report, Naval Air Propulsion Test Center, Naval Base, Philadelphia, 1967. Final Report DS-67-6. [3](#)
- J. Neter, M. H. Kutner, W. Wasserman, and C. J. Nachtsheim. *Applied Linear Statistical Models*. McGraw-Hill/Irwin, 4th edition, 1996. [49](#)
- H. L. Olsen, R. B. Edmonson, and E. L. Gayhart. Microchronometric schlieren study of gaseous expansion from an electric spark. *Journal of Applied Physics*, 23:1157–1162, 1952. [17](#)
- R. Ono and T. Oda. Measurement of oh density and gas temperature in incipient spark-ignited hydrogen-air flame. *Combustion and Flame*, 152:69–79, 2008. [17](#), [25](#)
- R. Ono, N. Masaharu, S. Fujiwara, S. Horiguchi, and T. Oda. Gas temperature of capacitive spark discharge in air. *Journal of Applied Physics*, 97:123307, 2005. [11](#), [17](#), [25](#)

- R. Ono, M. Nifuku, S. Fujiwara, S. Horiguchi, and T. Oda. Minimum ignition energy of hydrogen-air mixture: Effects of humidity and spark duration. *Journal of Electrostatics*, 65:87–93, 2007. [11](#), [25](#)
- E. Ott. Effects of fuel slosh and vibration on the flammability hazards of hydrocarbon turbine fuels within aircraft fuel tanks. Technical report, Fire Protection Branch of the Fuels and Lubrication Division, Wright-Patterson Air Force Base, Ohio, 1970. Report AFAPL-TR-70-65. [3](#)
- P. L. Pitt, R. M. Clements, and D. R. Topham. The early phase of spark ignition. *Combustion Science and Technology*, 78:289–314, 1991. [17](#)
- A. E. Potter. Flame quenching. In *Progress in Combustion Science and Technology*, volume 1 of *International Series of Monographs in Aeronautics and Astronautics*, pages 145–181. CRC Press, 1960. [68](#)
- E. Randeberg, W. Olsen, and R. K. Eckhoff. A new method for generation of synchronised capacitive sparks of low energy. *Journal of Electrostatics*, 64:263–272, 2006. [11](#)
- S. Refael and E. Sher. A theoretical study of the ignition of a reactive medium by means of an electrical discharge. *Combustion and Flame*, 59:17–30, 1985. [16](#)
- R. Reinmann and M. Akram. Temporal investigation of a fast spark discharge in chemically inert gases. *Journal of Physics D—Applied Physics*, 30:1125–1134, 1997. [16](#), [87](#)
- P. D. Ronney. Near-limit flame structures at low lewis number. *Combustion and Flame*, 82:1–14, 1990. [39](#)
- G. Rosen. Ignition of combustible gases. *Journal of Chemical Physics*, 30:298–303, 1959. [11](#)
- A. J. Roth. Development and evaluation of an airplane fuel tank ullage composition model—volume II: Experimental determination of airplane fuel tank ullage com-

- positions. Technical report, Air Force Wright Aeronautical Laboratories, Wright-Patterson Air Force Base, Ohio, 1987. Report AFWAL-TR-87-2060, Volume II. [3](#)
- A. Roux, L. Y. M. Gicquel, S. Reichstadt, N. Bertier, G. Staffelbach, F. Vuillot, and T. J. Poinsot. Analysis of unsteady reacting flows and impact of chemistry description in large eddy simulations of side-dump ramjet combustors. *Combustion and Flame*, 157:176–191, 2010. [105](#)
- V. Sankaran and S. Menon. Subgrid combustion modeling of 3-d premixed flames in the thin-reaction-zone regime. *Proceedings of the Combustion Institute*, 30:575–582, 2005. [105](#)
- D. W. Seibold. Development and evaluation of an airplane fuel tank ullage composition model—volume I: Airplane fuel tank ullage computer model. Technical report, Air Force Wright Aeronautical Laboratories, Wright-Patterson Air Force Base, Ohio, 1987. Report AFWAL-TR-87-2060, Volume I. [3](#)
- J. E. Shepherd, J. C. Krok, and J. J. Lee. Spark energy measurements in Jet A. Technical report, Graduate Aerospace Laboratories, California Institute of Technology, Pasadena, California, 1999. Explosion Dynamics Laboratory Report FM97-9. [33](#)
- J. E. Shepherd, C. D. Nuyt, and J. J. Lee. Flash point and chemical composition of aviation kerosene (jet a). Technical report, Graduate Aerospace Laboratories, California Institute of Technology, Pasadena, California, 2000. Explosion Dynamics Laboratory Report FM99-4. [3](#)
- J. E. Shepherd, S. Bane, and J. Ziegler. Development of one-step chemistry models for hydrogen-air and propane-air systems. Technical report, Graduate Aerospace Laboratories, California Institute of Technology, Pasadena, California, 2008. Report for FM Global. [239](#)
- E. Sher and J. C. Keck. Spark ignition of combustible gas mixtures. *Combustion and Flame*, 66:17–25, 1986. [16](#)

- E. Sher and S. Refael. Numerical analysis of the early phase development of spark-ignited flames in  $\text{CH}_4$ -air mixture. In *Nineteenth Symposium (International) on Combustion*. The Combustion Institute, Pittsburgh, PA, 1982. 16
- S. Singh, D. Liberman, and J. E. Shepherd. Combustion behind shock waves. In *Fall 2003 Technical Meeting of the Western States Section of the Combustion Institute*, 2003. Paper 03F-29. 137
- B. Sirjean, E. Dames, D. A. Sheen, X.-Q. You, C. Sung, A. T. Holley, F. N. Egolfopoulos, H. Wang, S. S. Vasu, D. F. Davidson, R. K. Hanson, H. Pitsch, C. T. Bowman, A. Kelley, C. K. Law, W. Tsang, N. P. Cernansky, D. L. Miller, A. Violi, and R. P. Lindstedt. A high-temperature chemical kinetic model of n-alkane oxidation, JetSurF version 1.0, september 15, 2009. [http://melchior.usc.edu/JetSurF/Version1\\_0/Index.html](http://melchior.usc.edu/JetSurF/Version1_0/Index.html). xxii, 72
- T. M. Sloane. Numerical simulation of electric spark ignition in atmospheric pressure methane-air mixtures. *Combustion Science and Technology*, 73:367–381, 1990. 16
- R. A. Strehlow. *Fundamentals of Combustion*. Robert E. Kreiger Publishing Company, New York, 1979. 11
- K. G. Strid. Experimental techniques for determination of ignition energy. In *Oxidation and Combustion Reviews*, pages 1–46. Elsevier Publishing Company, 1973. 32
- M. Thiele, S. Selle, U. Riedel J. Warnatz, and U. Maas. Numerical simulation of spark ignition including ionization. *Combustion Theory and Modeling*, 4:413–434, 2000a. 16, 87
- M. Thiele, J. Warnatz, and U. Maas. Geometrical study of spark ignition in two dimensions. *Combustion Theory and Modeling*, 4:413–434, 2000b. 16, 17, 87, 89, 92
- M. Thiele, J. Warnatz, A. Dreizler, S. Lindenmaier, R. Schießl, U. Maas, A. Grant, and P. Ewart. Spark ignited hydrogen/air mixtures: Two dimensional detailed

- modeling and laser based diagnostics. *Combustion and Flame*, 128:74–87, 2002. [16](#), [17](#), [87](#), [89](#)
- S. R. Turns. *An Introduction to Combustion: Concepts and Applications*. McGraw-Hill, 2nd edition, 2000. [12](#), [73](#)
- E. A. Ural, R. G. Zalosh, and F. Tamanini. Ignitability of jet-a fuel vapors in aircraft. In *Aircraft Fire Safety*, AGARD Conference Proceedings, page 14, 1989. [3](#)
- U. von Pidoll, E. Brzostek, and H.-R. Froechtenigt. Determining the incendivity of electrostatic discharges without explosive gas mixtures. *IEE Transactions on Industry Applications*, 40:1467–1475, 2004. [74](#), [75](#), [160](#)
- F. A. Williams. *Combustion Theory*. The Benjamin/Cummings Publishing Company, Inc., 2 edition, 1985. [12](#)
- T. Yuasa, S. Kadota, M. Tsue, M. Kono, H. Nomura, and Y. Ujiej. Effects of energy deposition schedule on minimum ignition energy in spark ignition of methane/air mixtures. *Proceedings of the Combustion Institute*, 29:743–750, 2002. [16](#), [87](#)
- J. Zukas and W. Walters, editors. *Explosive Effects and Applications*, chapter 8. Springer-Verlag NY, 1998. [47](#)

# Appendix A

## Historical MIE Data and Probability

### A.1 Introduction

There is a large volume of historical data dating to the period 1947–1952 on the minimum ignition energy for capacitive spark discharge ignition. This data has been extensively used in the chemical and aviation industry to set standards and evaluate safety with flammable gas mixtures. There exists scant information on the experimental procedures, raw data, or uncertainty consideration, or any other information that would enable the assignment of a statistical meaning to the minimum ignition energies that were reported. However, some researchers have claimed that the historical data can be interpreted as corresponding to a certain level of ignition probability as discussed in Section 1.3.3. This appendix documents the investigation of these claims and compares the historical results with modern data.

### A.2 Claims and the Historical Record

In a paper by Moorhouse, Williams, and Maddison published in the journal *Combustion and Flame* (Moorhouse et al., 1974) the authors make the following statements on page 211 regarding the definition of minimum ignition energy:

The values of the minimum ignition energies given by these expressions at

25°C and 1 atm are higher than the values quoted by Lewis and von Elbe [1]. Their results, which are frequently taken as standards in relation to safety standards, relate to the case when one ignition occurs in a hundred tests, i.e. an ignition probability of 0.01. The present tests, those of Lewis and von Elbe [1] and Metzler [2,3] and some of the results given by Calcote et al. [4] are given in Table 2. [...] It should be noted that the results of Lewis and von Elbe and Metzler and Calcote refer to the same experimental technique, namely capacitor discharges and an ignition probability of 0.01.

The works by Metzler cited in Moorhouse et al. are two NACA reports published in 1952 (Metzler, 1952a,b). Metzler studied ignition of several fuels using a capacitive discharge circuit that includes a resistor in the series with the spark gap to vary the energy supplied to the gap. Metzler describes his method for determining the minimum ignition energy as follows:

All data were obtained on premixed fuel-air mixtures of known concentration, temperature, and pressure. The minimum ignition energy for such known conditions and a given gap width was approached from the low side by passing consecutive sparks and adjusting the capacitor voltage, R2 and R3. [...] For all data reported, ignition was obtained by a single spark in a mixture not previously sparked. Ignition energies so determined for a given mixture and various gap widths defined the minimum energy for that mixture. Repeating the procedure for various mixture strengths defined the minimum ignition energy as a function of fuel-air ratio.

Metzler does not state how many tests were performed for each data point and does not address probability of ignition at all in the reports.

Finally, Moorhouse cites a paper by Calcote et al. published in the journal *Industrial and Engineering Chemistry* in 1952 (Calcote et al., 1952). Calcote et al. examined the minimum ignition energy for a large number of fuels with varying

molecular structure, and the procedure for determining the minimum ignition energy is described as follows:

A known (3 to 4000 micro microfarads) condenser in parallel with the ignition gap is charged through a high resistance (approximately 109 to 1012 ohms) until a spark passes between the electrodes. [...] This process is repeated with a different electrode distance for a given mixture until the threshold energy is obtained. It was found much simpler to set the capacity and vary the distance than to vary the capacity at a fixed distance. [...] This procedure gives one point on the curve of ignition energy versus electrode distance and must be repeated with different capacities to obtain other points (Figure 3). The minimum of this curve is then taken as the minimum ignition energy for the particular mixture.

As with Metzler, the number of tests is not stated and the concept of an ignition probability of 0.01 is never discussed.

Finally, Moorhouse et al. reference the work done by Lewis and von Elbe as described in the book *Combustion, Flames and Explosion of Gases* in 1951 (Lewis and von Elbe, 1951). In the book, where the procedure to determine the minimum ignition energy is described in some detail, there is no mention of ignition probability or a  $p = 0.01$  probability criteria. The work described in the book in 1951 was first published in a series of three papers, two journal articles in 1947 (Blanc et al., 1947, Lewis and von Elbe, 1947) and a paper in a conference proceeding in 1949 (Blanc et al., 1949). As in Lewis and von Elbe (1951), there is no reference to ignition probability or to the number of tests performed. The work presented in these papers was not documented in a separate Bureau of Mines report, but was summarized in three reports for the years 1946 through 1949 authored by B. Lewis (Lewis, 1947, 1949, 1950). In the first report for the year 1946 (Lewis, 1947), the procedure for determining the minimum ignition energy is described as follows:

In the present series of experiments capacitance sparks are passed through a mixture of given composition and pressure at room temperature by

charging a condenser and electrode system to the breakdown voltage  $V$ , and the capacitance  $C$  of the circuit is gradually increased until ignition occurs. This is repeated for various accurately measured electrode distances, and a curve is obtained showing the electrical energy,  $1/2CV^2$ , at the ignition limit as a function of electrode distance.

The second report for the years 1947 and 1948 (Lewis, 1949) includes many of the figures published in the book by Lewis and von Elbe (1951). The procedure to determine the minimum ignition energy is again described:

After the bomb had been filled with an explosive mixture of accurately determined composition and pressure, the electrode and capacitor system was slowly charged, and the voltage  $V$ , at which the spark occurred, was observed. If the mixture did not ignite, the capacitance was increased until, by trial and error, the critical capacitance  $C$  for ignition was found. [...] The product  $(1/2)CV^2$  may be termed the minimum ignition energy. [...] The energy values corresponding to the horizontal part of the curves of minimum ignition energy versus electrode distance are functions of the variables of the gas mixtures only and may be regarded as absolute minimum values.

The third and final report that discusses the minimum ignition energy work is the report for the year 1949 (Lewis, 1950). Again, more figures from the book are published in this report. The procedure is described again in the same way as before:

The minimum ignition energy is determined by passing sparks through a mixture of given composition and pressure at room temperature and increasing the energy of the sparks until ignition occurs. The quenching distance is determined by repeating this procedure for various accurately measured electrode distances. The spark-gap is decreased progressively until a limit is reached beyond which ignition no longer occurs, no matter how great the energy of the spark is. The minimum energy may be expressed as  $1/2CV^2$ , where  $C$  is the capacitance of the condenser used as

the source of electrical energy, and  $V$  is the voltage for which the spark just occurs, or ‘break-down’ voltage.

Not a single reference to a criterion of a probability of ignition of 0.01 was found, and no reference was made to ignition probability at all. The number of tests and the individual test results were not presented in any of the documents, so determining what ignition probability the minimum ignition energy values correspond to is impossible. The work by Lewis and von Elbe and subsequent work on spark ignition are described in several additional Bureau of Mines reports. These documents include a report describing the apparatus used in the minimum ignition energy tests (Guest, 1944) and three later reports on spark ignition by Litchfield and others in the 1950s and 1960s (Litchfield and Blanc, 1959, Litchfield, 1960, Litchfield et al., 1967). Once again, there is no probability criterion given for determining the minimum ignition energy.

### A.3 Comparison of Historical and Modern Data

Spark ignition tests were performed in the 7% H<sub>2</sub>, 21% O<sub>2</sub>, 72% Ar mixture discussed in FAA document DOT/FAA/CT-94/74 (Administration, 1994). The choice of this mixture was based on the MIE curves obtained by Lewis and von Elbe for mixtures of hydrogen and oxygen with various diluents shown in Figure 187 in (Lewis and von Elbe, 1951). From the MIE curve it appears that Lewis and von Elbe obtained a minimum ignition energy of approximately 100  $\mu$ J for a mixture with 7% H<sub>2</sub> and O<sub>2</sub>/(O<sub>2</sub> + Ar) = 0.21, which is very close to the FAA mixture. The experimental setup and procedure for the spark ignition tests are described in Section 2.5. A series of 18 ignition tests were performed with stored energies ranging from 27 to 117  $\mu$ J and the results are shown in Figure A.1. A result of 0 indicates that no ignition occurred (a “no go”) and a result of 1 indicates that ignition did occur (a “go”). For the statistical analysis the test results were fit to a logistic distribution of the form

$$P(E) = \frac{1}{1 + \exp(-\beta_0 - \beta_1 \cdot E)} \quad (\text{A.1})$$

where  $P(E)$  is the probability of ignition at energy  $E$  and the parameters  $\beta_0$  and  $\beta_1$  are found using the maximum likelihood method. The statistical method is described in more detail in Section 3.3. The probability distribution and 95% confidence interval derived using the test data in Figure A.1 are shown in Figure A.2. The distribution is centered (50% probability of ignition) at  $56 \mu\text{J}$ , a value only half of that published by Lewis and von Elbe. To examine the  $p = 0.01$  for  $100 \mu\text{J}$  hypothesis, calculated the probability and 95% confidence interval for a probability of 0.01 was calculated using the probability distribution. The energy with a probability of 0.01 is  $39 \mu\text{J}$  with a lower 95% confidence limit of  $18 \mu\text{J}$  and an upper confidence limit of  $61 \mu\text{J}$ , far below  $100 \mu\text{J}$ . Even if the confidence interval is restricted to 99.9% confidence, the upper limit ( $75 \mu$ ) still does not come close to including the  $100 \mu\text{J}$  hypothesized to correspond to a probability of 0.01.

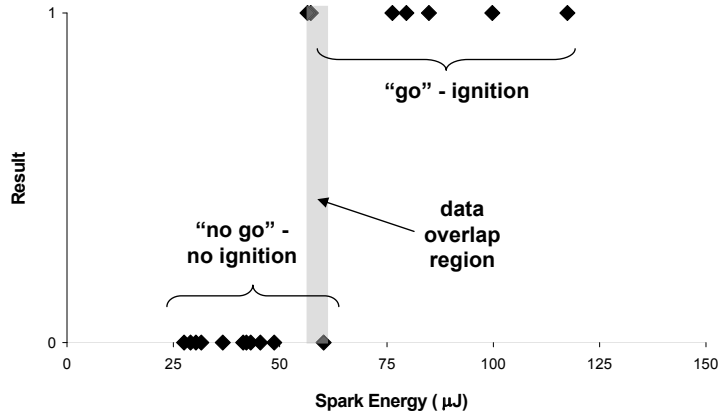


Figure A.1: Spark ignition test results for a mixture with 7%  $\text{H}_2$ ,  $\text{Ar}/(\text{Ar} + \text{O}_2) = 0.226$

To provide further statistical insight, the hypothesis  $H_0 : P(100 \mu\text{J}) = 0.01$  was tested using statistics of binomial trials. If we perform  $n$  ignition tests with an energy of  $100 \mu\text{J}$  the probability of having exactly  $k$  “successes” (ignitions) assuming a probability  $p_0$  is

$$P(k) = \binom{n}{k} p_0^k (1 - p_0)^{n-k} . \quad (\text{A.2})$$

To test the hypothesis, the probability was set to  $p_0 = 0.01$  and the probabilities

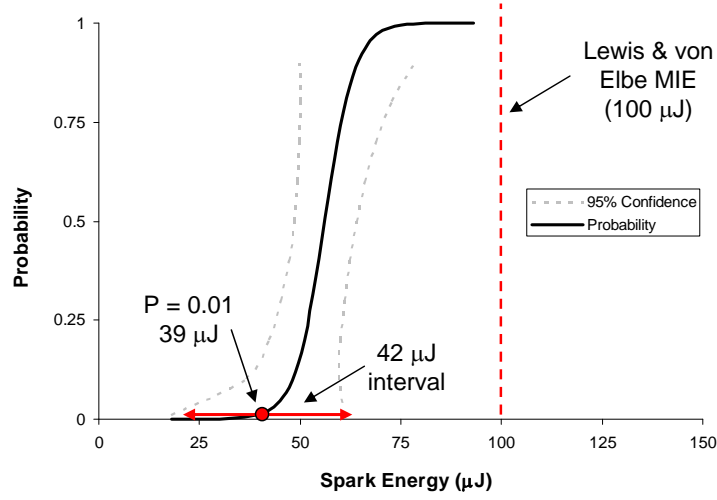


Figure A.2: Probability distribution for ignition versus spark energy obtained using the data in Figure A.1 for a 7% H<sub>2</sub>, 21% O<sub>2</sub>, 72% Ar mixture. The  $p = 0.01$  point and corresponding 95% confidence interval is shown, as well as the MIE result obtained by Lewis and von Elbe (Lewis and von Elbe, 1951).

for  $n = 5, 10,$  and  $20$  (small number of trials) were calculated. The results of the calculations are shown in Table A.1. Considering a level of significance  $\alpha = 0.05$  then the critical regions  $C$  for rejecting the hypothesis are

$$n = 5 : C = \{k : k \geq 1\} \quad (\text{A.3})$$

$$n = 10 : C = \{k : k \geq 2\} \quad (\text{A.4})$$

$$n = 20 : C = \{k : k \geq 2\} \quad (\text{A.5})$$

$$(\text{A.6})$$

with probabilities (assuming  $H_0$  to be true)

$$n = 5 : P(k \in C | H_0 \text{ is true}) = P(k \geq 1) = 0.048 < \alpha \quad (\text{A.7})$$

$$n = 10 : P(k \in C | H_0 \text{ is true}) = P(k \geq 2) = 0.004 < \alpha \quad (\text{A.8})$$

$$n = 20 : P(k \in C | H_0 \text{ is true}) = P(k \geq 2) = 0.017 < \alpha . \quad (\text{A.9})$$

Therefore, Bernoulli trials were performed with a  $100 \mu\text{J}$  energy level the hypothesis

being that  $p = 0.01$  would be rejected with 95% confidence if at least 1, 2, and 2 ignitions were observed for 5, 10, and 20 trials, respectively. Therefore, for a small number of trials one could not conclude with high confidence that  $p = 0.01$  if there were even 2 ignitions. While Lewis and von Elbe do not state the number of tests they performed at 100  $\mu\text{J}$ , the language in their publications implies that they obtained at least one ignition at the energy they determine to be the MIE. Therefore, to prescribe a probability of 0.01 to the MIE, it would have to be known that Lewis and von Elbe conducted at least 4 more tests at the same energy with no ignitions. However, there is no information in any of the documents that allow this conclusion to be drawn. While Bernoulli trials at a constant energy of 100  $\mu\text{J}$  have not been performed, 17 of the 18 tests performed had an energy equal to or less than 100  $\mu\text{J}$  and 6 ignitions were observed.

Table A.1: Probabilities for binomial trials with  $p_0 = 0.01$

n=5		n=10		n=20	
k	P(k)	k	P(k)	k	P(k)
0	0.951	0	0.904	0	0.818
1	0.048	1	0.091	1	0.165
2	0.000	2	0.004	2	0.016
3	0.000	3	0.000	3	0.001
4	0.000	4	0.000	4	0.000

Finally, hypothesis tests have been performed for the 1<sup>st</sup>, 50<sup>th</sup>, and 99<sup>th</sup> percentile (probability of ignition of 0.01, 0.50, and 0.99, respectively) using the logistic distribution and confidence intervals obtained from the current ignition data. A normal distribution of test spark energies is assumed about a percentile with a mean at the spark energy corresponding to that percentile. The null hypothesis is then stated:  $H_0: \mu = \mu_0$ , i.e., that the energy corresponding to the 100<sup>q</sup><sup>th</sup> percentile ( $q = 0.01, 0.50, \text{ and } 0.99$  in this case) is equal to  $\mu_0$ . The alternative hypothesis is then either

$H_1: \mu < \mu_0$  or  $H_1: \mu > \mu_0$ . The test statistic (a random variable normally distributed) used is

$$z = \frac{\bar{y} - \mu}{\sigma/\sqrt{n}} \quad (\text{A.10})$$

where  $\bar{y}$  is the observed mean, or observed energy for the percentile under consideration,  $\mu$  is the hypothesized mean from  $H_0$ ,  $\sigma$  is the standard deviation of the normal distribution, and  $n$  is the number of tests (Larsen and Marx, 2006). The null hypothesis is then rejected if

$$z \leq -z_\alpha \quad \text{for } H_1 : \mu < \mu_0 \quad (\text{A.11})$$

$$z \geq z_\alpha \quad \text{for } H_1 : \mu > \mu_0 \quad (\text{A.12})$$

where  $\alpha$  is the level of significance, typically 0.05 or 0.01, and  $z_\alpha$  has the property  $P(z \geq z_\alpha) = \alpha$ . For each percentile, the energy given by the logistic curve is used for the observed mean  $\bar{y}$  and the standard distribution is obtained from the 95% confidence intervals for the distribution using the fact that  $P(-1.96\sigma \leq z \leq 1.96\sigma) = 0.95$ , i.e., the probability that a test energy lies between  $-1.96\sigma$  and  $1.96\sigma$  is 95%. Therefore, the standard deviation can be defined in terms of the 95% confidence limits:

$$\pm 1.96\sigma = UCL/LCL - \bar{y} \quad (\text{A.13})$$

where the UCL and LCL are the upper and lower 95% confidence limits, respectively.

$$(\text{A.14})$$

### A.3.1 Probability = 0.01 (1<sup>st</sup> Percentile)

For the 1<sup>st</sup> percentile (1% probability of ignition), the null hypothesis that the energy corresponding to  $p = 0.01$  (1% probability of ignition) is 100  $\mu\text{J}$  was tested, with the

alternative hypothesis that the energy is lower as reflected by the current test results. Considering a normal distribution of test energies with a mean at the energy value corresponding to  $p = 0.01$ , as illustrated in Figure A.3, the hypothesis to test can be stated as

$$H_0 : \mu = 100\mu J \quad (\text{A.15})$$

$$H_1 : \mu < 100\mu J . \quad (\text{A.16})$$

The observed value of the mean,  $\bar{y}$ , is the energy with  $p = 0.01$  from the logistic distribution,  $E_{0.01} = 39 \mu J$ . The lower 95% confidence limit at  $p = 0.01$  is  $17 \mu J$ , and the upper 95% confidence limit is  $61 \mu J$ , so the standard deviation of the normal distribution at the 1<sup>st</sup> percentile is

$$\pm 1.96\sigma = UCL/LCL - \bar{y} = 61/17 - 39 = +/- 22 \mu J \quad (\text{A.17})$$

$$\implies \sigma \approx 11.2 . \quad (\text{A.18})$$

Using  $n = 18$ , since 18 ignition tests were performed to derive the logistic distribution, the test statistic  $z$  can now be calculated:

$$z = \frac{\bar{y} - \mu}{\sigma/\sqrt{n}} = \frac{39 - 100}{11.2/\sqrt{18}} \approx -23.1 . \quad (\text{A.19})$$

To determine whether or not to reject  $H_0$ ,  $z_\alpha$  must be defined. For 99% confidence,  $\alpha = 0.01$  is used and from tables for the standard normal distribution it is found that  $z_{0.01} \approx 2.33$ . The null hypothesis  $H_0$  can be rejected with significance  $\alpha = 0.01$  if  $z \leq z_\alpha$ , and for this case

$$z = -23.1 \leq -2.33 \quad (\text{A.20})$$

so  $H_0 : \mu = 100 \mu\text{J}$  is easily rejected for the 1<sup>st</sup> percentile. In fact,  $H_0$  is rejected in this case for any nonzero  $\alpha$ , i.e., practically with a confidence of 100%. Therefore, this analysis has shown with greater than 99% confidence that based on the current ignition tests, the energy with a probability of ignition of 0.01 is less than 100  $\mu\text{J}$ .

(A.21)

### A.3.2 Probability = 0.50 (50<sup>th</sup> Percentile)

The same statistical procedure was followed to test the null hypothesis that the energy corresponding to  $p = 0.50$  (50% probability of ignition) is 100  $\mu\text{J}$  versus the alternative hypothesis that the energy is less than 100  $\mu\text{J}$ . Therefore,

$$H_0 : \mu = 100\mu\text{J} \quad (\text{A.22})$$

$$H_1 : \mu < 100\mu\text{J} . \quad (\text{A.23})$$

From the logistic distribution,  $\bar{y}$  (the observed energy at  $p = 0.50$ ) is 56  $\mu\text{J}$  with lower and upper 95% confidence limits of 48 and 64  $\mu\text{J}$ , respectively. Therefore the standard deviation of a normal distribution at the 50<sup>th</sup> percentile is estimated as,

$$\pm 1.96\sigma = UCL/LCL - \bar{y} = 64/48 - 56 = +/- 8 \mu\text{J} \quad (\text{A.24})$$

$$\implies \sigma \approx 4.1 . \quad (\text{A.25})$$

The test statistic  $z$  can now be calculated:

$$z = \frac{\bar{y} - \mu}{\sigma/\sqrt{n}} = \frac{56 - 100}{4.1/\sqrt{18}} \approx -45.5 \ll z_{0.01} . \quad (\text{A.26})$$

Once again  $H_0 : \mu = 100 \mu\text{J}$  is easily rejected for the 50<sup>th</sup> percentile, showing with greater than 99% confidence that based on the current tests, the energy with a 50% probability of ignition is less than 100  $\mu\text{J}$ . Therefore, using statistical hypothesis testing based on current ignition test results, it is shown not only that the energy with a probability of 0.01 is less than 100  $\mu\text{J}$ , but that the energy with 99% probability of ignition is greater than 100  $\mu\text{J}$ .

(A.27)

### A.3.3 Probability = 0.99 (99<sup>th</sup> Percentile)

Finally, the null hypothesis that the energy corresponding to  $p = 0.99$  (99% probability of ignition) is 100  $\mu\text{J}$  was tested versus the alternative hypothesis that the energy is less than 100  $\mu\text{J}$ . From the logistic distribution,  $\bar{y}$  (the observed energy at  $p = 0.99$ ) is 73  $\mu\text{J}$  with lower and upper 95% confidence limits of 48 and 98  $\mu\text{J}$ , respectively. Therefore standard deviation of a normal distribution at the 50<sup>th</sup> percentile is estimated as,

$$\pm 1.96\sigma = UCL/LCL - \bar{y} = 98/48 - 73 = +/ - 25 \mu\text{J} \quad (\text{A.28})$$

$$\implies \sigma \approx 12.8 . \quad (\text{A.29})$$

The test statistic  $z$  can be calculated:

$$z = \frac{\bar{y} - \mu}{\sigma/\sqrt{n}} = \frac{73 - 100}{12.8/\sqrt{18}} \approx -8.9 < z_{0.01} . \quad (\text{A.30})$$

As with the 1<sup>st</sup> and 50<sup>th</sup> percentiles, the hypothesis that the energy corresponding to the 99<sup>th</sup> percentile is 100  $\mu\text{J}$  is rejected with greater than 99% confidence.

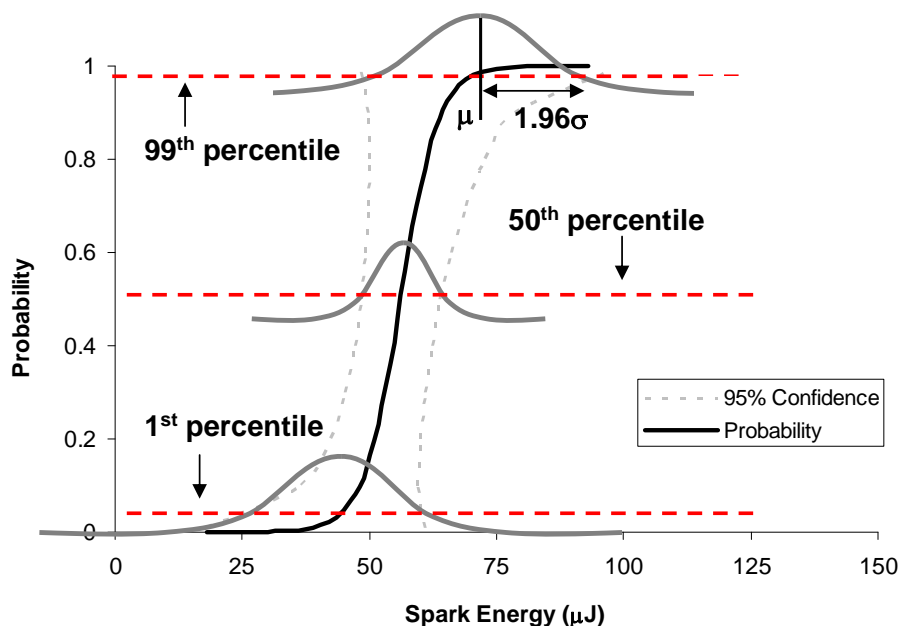


Figure A.3: Illustration of using normal distributions at the 1<sup>st</sup>, 50<sup>th</sup>, and 99<sup>th</sup> percentiles to test hypotheses for the mean energy

## A.4 Summary

In summary, in Moorhouse et al. (1974) the authors claim that minimum ignition energies obtained by Lewis and von Elbe (1951), Metzler (1952a,b), and Calcote et al. (1952) correspond to an ignition probability of 0.01. The cited references have been thoroughly examined as well as several additional reports and papers that document the work of Lewis and von Elbe on spark ignition. The concept of ignition probability was not discussed in any of the documents, and the 1% probability criterion is never mentioned. Unless Moorhouse et al. had access to unpublished information documenting the raw data or statistical analysis of these tests, there does not appear to be any basis for the 0.01 probability claim.

Finally, current measured ignition probability results for a 7% H<sub>2</sub> mixture were compared with the minimum ignition energy value for a similar mixture obtained by Lewis and von Elbe (1951). The probability distribution obtained from the current tests is centered (50% ignition probability) at 56 μJ, while the value given by Lewis and von Elbe is nearly twice as large, 100 μJ. In fact, it was found that the probability

of ignition is nearly 100% for an energy of 100  $\mu\text{J}$ . Therefore it is unreasonable to assume that Lewis and von Elbe only obtained one ignition out of 100 tests using a spark energy of 100  $\mu\text{J}$ . Our statistical analysis predicts that the ignition probability is 0.01 for a spark energy of only 39  $\mu\text{J}$ , but the confidence interval is so large that a 1% probability of ignition is not reasonable for defining a minimum ignition criterion.

## Appendix B

# Spark Ignition Test Checklist

Shot : \_\_\_\_\_ Date: \_\_\_\_\_ Time: \_\_\_\_\_

Mixture: 5.00% H<sub>2</sub>, 12.00% O<sub>2</sub>, 83.00% Ar      P<sub>final</sub>: \_\_\_\_\_ kPa

T<sub>final</sub>: \_\_\_\_\_ °C      P<sub>post-shot</sub>: \_\_\_\_\_ kPa      P<sub>max</sub>: \_\_\_\_\_ kPa

C: \_\_\_\_\_ pF      Voltage: \_\_\_\_\_ kV      Stored Energy: \_\_\_\_\_ μJ

Spark Energy: \_\_\_\_\_ μJ      Binary Result: \_\_\_\_\_

### Experiment Preparation

1. \_\_\_ Turn on:
  - \_\_\_ vacuum pump    \_\_\_ gas bottles    \_\_\_ hand valves    \_\_\_ amplifiers
  - \_\_\_ light source for schlieren    \_\_\_ Phantom camera
  - \_\_\_ oscilloscope    \_\_\_ spark ignition system
2. \_\_\_ Load software for the Phantom camera and LabVIEW
3. \_\_\_ Check parameters in the computer programs and on the oscilloscope

### Experiment

4. \_\_\_ Open V1, V3, V4 and evacuate to  $< 100$  mTorr, then zero Heise gauge, amplifier
5. \_\_\_ Close V1 and V4 and turn on warning lights

Gas	Target Fraction	Target Partial Pressure	Target Final Pressure	Final Pressure
Ar	0.8300	83.00 kPa	83.00 kPa	kPa
O2	0.1200	12.00 kPa	95.00 kPa	kPa
H2	0.0500	5.00 kPa	100.00 kPa	kPa

6. \_\_\_ Fill with appropriate gases (fill order: diluent, oxidizer, fuel), closing V1 and evacuating the line between gases
7. \_\_\_ Close V1, V3 and turn on mixer for at least 3 minutes, transferring key to ignition panel, then wait 3 minutes
8. \_\_\_ Open V3 and record the final pressure and temperature, then close V3 and check that interlock light is on
9. \_\_\_ Set all triggers:  
 \_\_\_ Phantom software to capture mode \_\_\_ oscilloscope \_\_\_ vacuum pump VI
10. \_\_\_ Turn fireset key, verify triggers are on
11. \_\_\_ Hold up the "AR" switch and press the "FIRE" button, release "AR" switch
12. \_\_\_ Save the schlieren video and waveforms; verify pressure trace
13. \_\_\_ Record post-shot pressure
14. \_\_\_ Record maximum pressure from pressure trace
15. \_\_\_ Open V4 to evacuate the chamber

### Experiment Shut-Down

16.  Check that all information has been entered in the test matrix, save
17.  Turn off:
  - vacuum pump  gas bottles  hand valves  amplifiers
  - light source for schlieren  Phantom camera
  - oscilloscope  spark ignition system  control panel
18.  Cover all lens/mirrors and put lens cap on Phantom camera lens

**Comments:**

# Appendix C

## Test Matrix: Spark Ignition Tests in 3 to 13% Hydrogen, Oxygen, Argon Mixtures

Table [C.1](#) gives information on the spark ignition tests performed in mixtures with 3 to 13% hydrogen discussed in Section [3.2](#). The test matrix includes the following details of each test: shot number, date the experiment was performed, target concentrations, argon-to-oxygen ratio, actual concentrations achieved, initial and post-shot pressures, and comments on test result.

Table C.1: Test matrix of spark ignition tests performed in mixtures with 3 to 12% hydrogen in oxygen and argon

		Target Concentration				Actual Concentration					
Shot Number	Date	% H <sub>2</sub>	% Ar	% O <sub>2</sub>	Ar/O <sub>2</sub>	% H <sub>2</sub>	% Ar	% O <sub>2</sub>	$p_i$ kPa	$p_{max}$ kPa	Combustion?
14	05/11/07	3.00	84.75	12.25	6.9167	3.00	84.75	12.25	99.89	100.31	NO
15	05/11/07	3.50	84.31	12.19	6.9167	3.51	84.31	12.18	99.92	105.03	YES - small, buoyant
25	05/31/07	3.50	84.31	12.19	6.9167	3.52	84.30	12.18	99.94	105.03	YES - tiny buoyant flame
30	05/31/07	3.50	84.31	12.19	6.9167	3.50	84.31	12.19	99.90	105.03	YES - flame on 3rd spark
13	05/11/07	4.00	83.87	12.13	6.9167	4.00	83.87	12.13	99.90	108.89	YES - small, buoyant
26	05/31/07	4.00	83.87	12.13	6.9167	4.03	83.84	12.13	100.00	108.03	YES - tiny buoyant flame!
27	05/31/07	4.50	83.44	12.06	6.9167	4.51	83.45	12.04	99.90	112.32	YES - buoyant flame
33	06/05/07	4.50	83.44	12.06	6.9167	4.50	83.45	12.05	99.91	113.17	YES - buoyant flame
7	05/10/07	5.00	83.00	12.00	6.9167	5.00	83.00	12.00	100.00	122.18	YES - buoyant flame
34	06/05/07	5.00	83.00	12.00	6.9167	5.00	83.00	12.00	99.91	120.89	YES - buoyant flame
37	06/08/07	5.25	82.78	11.97	6.9167	5.27	82.76	11.97	99.96	124.32	YES - buoyant w/ small "fingers"
35	06/05/07	5.50	82.56	11.94	6.9167	5.52	82.55	11.93	99.90	132.89	YES - between 5, 6% style
38	06/08/07	5.75	82.34	11.91	6.9167	5.76	82.33	11.91	99.94	141.47	YES - very similar to 6%
5	05/09/07	6.00	82.13	11.87	6.9167	6.00	82.15	11.85	99.93	274.36	YES - Good shot!
39	06/08/07	6.25	81.91	11.84	6.9167	6.24	81.91	11.85	99.96	292.37	YES - close to 7%, still buoyant
36	06/08/07	6.50	81.69	11.81	6.9167	6.52	81.68	11.80	99.98	331.38	YES - between 6, 7% style
40	06/08/07	6.75	81.47	11.78	6.9167	6.74	81.47	11.79	99.90	365.68	YES - very close to 7%

6	05/09/07	7.00	81.25	11.75	6.9167	7.01	81.26	11.73	99.85	389.68	YES
22	05/30/07	7.50	80.82	11.68	6.9167	7.49	80.82	11.69	99.90	429.55	YES - just like 7%
8	05/11/07	8.00	80.38	11.62	6.9167	7.98	80.39	11.63	99.94	458.27	YES
23	05/30/07	8.50	79.94	11.56	6.9167	8.53	79.92	11.55	99.94	486.14	YES - just like 7%
11	05/11/07	9.00	79.51	11.49	6.9167	9.03	79.49	11.49	100.03	514.00	YES
24	05/30/07	9.50	79.07	11.43	6.9167	9.52	79.07	11.41	99.89	532.01	YES
12	05/11/07	10.00	78.63	11.37	6.9167	10.01	78.63	11.36	99.86	551.30	YES - fast!
41	06/08/07	10.50	78.19	11.31	6.9167	10.50	78.19	11.31	99.90	569.73	YES
42	06/11/07	11.00	77.76	11.24	6.9167	11.00	77.78	11.22	99.84	586.02	YES
43	06/11/07	11.50	77.32	11.18	6.9167	11.51	77.32	11.17	99.95	611.32	YES
44	06/11/07	12.00	76.88	11.12	6.9167	12.00	76.88	11.12	99.93	628.89	YES
45	06/11/07	12.50	76.45	11.05	6.9167	12.50	76.45	11.05	99.95	646.04	YES
46	06/11/07	13.00	76.01	10.99	6.9167	13.00	76.01	10.99	99.94	662.76	YES

## Appendix D

# Short, Fixed-Length Spark Ignition Tests: Spark Energies

Tables [D.1](#), [D.2](#), and [D.3](#) give the spark data and the calculated spark energy for the short, fixed-length spark ignition tests in the 5, 6, and 7% hydrogen test mixtures, respectively. The measured quantities included in the tables are the capacitance and breakdown voltage. The calculated quantities in the table include stored energy and charge, residual charge in the capacitor, residual energy in the capacitor, and the estimated spark energy. The equations used to calculate these quantities are discussed in Section [2.4](#).

### D.1 5% Hydrogen Test Mixture

Table D.1: Spark energy data for the short, fixed-length  
spark ignition tests in the 5% hydrogen test mixture

Spark Number	C (pF)	$V_{breakdown}$ (kV)	$E_{stored}$ ( $\mu$ J)	$Q_{stored}$ (nC)	$Q_{spark}$ (nC)	$Q_{residual}$ (nC)	$E_{residual}$ ( $\mu$ J)	$E_{spark}$ ( $\mu$ J)	Result	% Energy in Spark
1	27.2	7.8	827	212	167	44.9	37.1	790	1	96
2	27.2	8.2	924	224	209	15.3	4.3	920	1	100
3	27.2	10.0	1351	271	217	54.3	54.1	1297	1	96
4	27.2	7.0	659	189	155	34.1	21.4	638	0	97
5	27.2	6.4	558	174	142	32.2	19.1	539	0	97
6	27.2	8.9	1076	242	189	53.1	51.9	1024	1	95
7	27.2	9.7	1276	263	242	21.3	8.3	1268	1	99
8	27.2	6.3	532	170	149	20.7	7.9	524	0	99
9	27.2	8.3	933	225	196	29.1	15.5	917	0	98
10	27.2	9.8	1311	267	257	10.0	1.9	1309	1	100
11	27.2	8.3	941	226	217	9.3	1.6	939	1	100
12	27.2	6.6	600	181	149	31.3	18.0	582	0	97
13	27.2	6.5	574	177	154	22.5	9.3	564	0	98
14	27.2	6.3	533	170	130	40.3	29.9	503	0	94
15	27.2	9.0	1101	245	225	20.2	7.5	1094	1	99
16	27.2	10.3	1443	280	206	73.8	100.2	1343	1	93
17	27.2	9.1	1116	246	183	63.5	74.0	1042	1	93
18	27.2	5.2	366	141	119	22.4	9.2	356	0	97

19	27.2	7.5	764	204	197	6.8	0.8	763	0	100
20	27.2	5.0	344	137	114	22.8	9.6	335	0	97
21	27.2	5.1	356	139	113	25.8	12.2	344	0	97
22	27.2	10.4	1471	283	227	56.0	57.6	1413	1	96
23	27.2	5.0	338	136	103	32.6	19.5	319	0	94
24	27.2	9.1	1137	249	229	19.8	7.2	1130	1	99
25	27.2	6.9	641	187	139	48.0	42.4	599	0	93
26	27.2	6.0	482	162	120	42.0	32.4	449	0	93
27	27.2	8.9	1067	241	191	49.6	45.2	1021	1	96
28	27.2	8.6	1000	233	216	17.6	5.7	994	0	99
29	27.2	5.9	473	160	136	24.3	10.9	462	0	98
30	27.2	8.9	1080	242	222	20.6	7.8	1073	1	99
31	27.2	5.4	392	146	110	35.9	23.7	369	0	94
32	27.2	8.6	1009	234	204	30.4	17.0	992	0	98
33	27.2	7.1	679	192	188	3.7	0.3	679	0	100
34	27.2	9.8	1301	266	232	33.8	21.0	1280	1	98
35	27.2	6.7	615	183	144	38.9	27.9	587	0	95
36	27.2	8.7	1024	236	227	8.8	1.4	1022	0	100
37	27.2	8.7	1034	237	199	38.3	27.0	1007	1	97
38	27.2	9.6	1264	262	219	43.3	34.5	1229	1	97
39	27.2	7.5	769	205	168	36.7	24.8	744	0	97
40	27.2	7.0	662	190	146	43.5	34.8	627	0	95

## D.2 6% Hydrogen Test Mixture

41	27.2	8.7	1018	235	193	42.4	33.0	985	0	97
42	27.2	7.1	677	192	164	27.8	14.2	663	0	98
43	27.2	6.5	580	178	129	48.3	42.9	537	0	93
44	27.2	6.9	649	188	161	26.8	13.2	636	0	98
45	27.2	8.2	917	223	203	20.4	7.6	909	0	99
46	27.2	7.2	710	196	160	36.3	24.3	685	0	97
47	27.2	10.2	1408	277	234	43.1	34.1	1373	1	98

Table D.2: Spark energy data for the short, fixed-length spark ignition tests in the 6% hydrogen test mixture

Spark Number	C (pF)	$V_{breakdown}$ (kV)	$E_{stored}$ ( $\mu$ J)	$Q_{stored}$ (nC)	$Q_{spark}$ (nC)	$Q_{residual}$ (nC)	$E_{residual}$ ( $\mu$ J)	$E_{spark}$ ( $\mu$ J)	Result	% Energy in Spark
1	16.5	5.4	243	90	72	17.6	9.4	234	0	96
2	21.3	7.4	589	158	151	7.6	1.3	588	1	100
3	21.3	7.6	607	161	150	11.4	3.0	604	1	100
4	16.5	7.7	490	127	118	9.1	2.5	488	1	99
5	9.7	6.8	225	66	59	7.6	2.9	222	0	99

6	11.7	6.9	281	81	73	7.7	2.5	279	0	99
7	14.9	6.9	351	102	95	6.9	1.6	350	1	100
8	15.7	7.8	476	122	114	8.0	2.0	474	1	100
9	15.7	6.8	361	106	95	11.2	4.0	357	0	99
10	26.6	6.3	527	167	127	40.4	30.6	496	1	94
11	18.9	5.1	246	96	76	20.6	11.2	235	0	95
12	18.9	6.9	453	131	110	20.9	11.5	442	1	97
13	18.9	6.1	357	116	92	24.2	15.5	341	1	96
14	16.5	4.6	172	75	61	13.9	5.9	166	0	97
15	16.3	6.6	351	107	96	10.9	3.7	348	0	99
15.5	16.3	6.4	334	104	93	11.0	3.7	330	0	99
16	17.9	5.1	231	91	79	11.8	3.9	227	0	98
17	22.1	7.1	559	157	137	19.7	8.8	550	1	98
18	19.3	5.5	293	106	88	18.7	9.0	284	0	97
18.5	19.3	6.6	424	128	109	19.4	9.7	414	1	98
19	19.3	6.8	445	131	122	8.7	2.0	443	1	100
20	16.7	7.2	434	120	109	11.1	3.7	430	1	99
21	15.3	7.2	402	111	90	20.6	13.8	388	1	97
22	15.3	6.4	315	98	86	12.7	5.2	310	0	98
22.5	15.3	6.7	345	103	88	14.7	7.1	338	1	98
23	15.3	6.7	345	103	80	22.6	16.7	328	1	95
24	15.3	6.9	361	105	88	17.2	9.7	352	0	97

24.5	15.3	6.4	316	98	89	9.0	2.6	313	0	99
25	15.3	6.2	290	94	81	13.7	6.2	284	0	98
25.5	15.3	4.6	161	70	66	3.7	0.4	160	0	100
26	19.4	6.3	381	122	107	14.1	5.1	376	0	99
26.5	19.4	5.8	325	112	86	26.7	18.4	306	0	94
27	21.4	6.4	445	138	120	18.0	7.5	437	1	98
28	19.5	6.6	423	128	98	30.0	23.1	400	1	95
29	19.5	6.3	390	123	107	16.3	6.9	383	1	98
30	14.9	7.8	456	117	101	15.5	8.0	448	1	98
31	16.4	6.6	361	109	99	9.9	3.0	358	1	99
32	14.1	6.7	319	95	86	8.7	2.7	316	0	99
33	14.1	6.1	267	87	73	13.5	6.5	260	0	98
33.5	14.1	6.5	295	91	75	16.3	9.4	286	0	97
34	14.1	5.1	186	72	65	7.7	2.1	184	0	99
34.5	14.1	5.7	232	81	70	11.4	4.6	228	0	98
35	16.4	7.2	426	118	94	24.6	18.4	407	1	96
36	14	6.6	303	92	79	13.1	6.1	297	0	98
36.5	14	5.7	229	80	81	-0.8	0.0	229	0	100
37	14.9	5.6	236	84	75	9.0	2.7	233	0	99
37.5	14.9	6.8	348	102	86	15.9	8.5	340	0	98

## D.3 7% Hydrogen Test Mixture

Table D.3: Spark energy data for the short, fixed-length spark ignition tests in the 7% hydrogen test mixture

Spark Number	C (pF)	$V_{breakdown}$ (kV)	$E_{stored}$ ( $\mu$ J)	$Q_{stored}$ (nC)	$Q_{spark}$ (nC)	$Q_{residual}$ (nC)	$E_{residual}$ ( $\mu$ J)	$E_{spark}$ ( $\mu$ J)	Result	% Energy in Spark
1	14.9	6.1	279	91	72	19.3	12.5	267	1	96
2	6	6.0	109	36	31	5.2	2.2	106	0	98
3	6	7.7	177	46	41	4.8	1.9	175	1	99
4	6	7.9	186	47	26	20.8	36.0	150	0	81
5	6	7.5	168	45	41	3.6	1.1	167	0	99
6	6	6.9	142	41	37	4.7	1.9	141	0	99
7	6	7.3	159	44	22	21.6	39.0	120	1	75
8	6	5.8	99	35	22	12.4	12.8	87	0	87
9	6	5.2	81	31	28	3.6	1.1	80	0	99
10	6	6.2	117	37	32	5.3	2.4	114	0	98
11	6	8.6	223	52	42	10.0	8.3	215	1	96
12	6	7.5	167	45	35	10.0	8.3	159	1	95
13	6	7.7	180	46	38	8.6	6.2	173	0	97
14	6	7.8	183	47	39	8.3	5.8	177	1	97
15	6	7.5	170	45	41	4.0	1.3	168	1	99
16	6	7.9	186	47	40	7.7	4.9	181	1	97

17	8.2	9.2	350	76	58	17.6	19.0	331	1	95
18	5.7	6.8	131	39	31	8.1	5.8	125	1	96
19	5.7	7.3	153	42	35	6.6	3.8	149	1	98
20	5.7	6.4	115	36	19	17.4	26.6	88	1	77
21	5.7	5.1	73	29	23	6.3	3.5	69	0	95
22	5.7	6.3	114	36	39	-2.9	0.7	114	1	99
23	5.8	5.2	78	30	23	7.2	4.5	74	0	94
24	5.8	6.2	111	36	27	9.0	7.0	104	0	94
25	5.8	5.9	102	34	25	9.1	7.1	95	0	93
26	5.8	5.7	95	33	30	3.6	1.1	94	0	99
27	5.8	6.5	123	38	30	7.5	4.9	118	0	96
28	6.1	5.4	88	33	25	7.8	5.0	83	0	94
29	6.1	7.0	148	43	35	7.1	4.1	144	1	97
30	6.1	8.1	202	50	43	6.1	3.1	199	1	98
31	6.1	5.9	107	36	27	8.7	6.2	101	0	94
32	6.1	5.8	103	35	27	8.0	5.2	97	0	95
33	6.1	5.9	105	36	25	10.5	9.0	96	0	91
34	6.1	6.4	124	39	36	3.4	0.9	123	1	99
35	9	5.4	129	48	38	9.8	5.4	124	0	96
36	9	5.6	142	51	44	7.0	2.7	139	0	98
37	9	7.1	225	64	55	9.0	4.5	220	1	98
38	9.9	7.5	282	75	61	14.1	10.0	272	1	96

39	9.9	7.7	296	77	66	10.2	5.2	291	1	98
40	5.8	5.3	81	31	28	3.1	0.8	80	0	99
41	5.8	6.2	110	36	28	8.2	5.7	104	0	95

# Appendix E

## Variable-Length Spark Ignition Tests: Spark Energy Densities

Tables [E.1](#), [E.2](#), and [E.3](#) give the spark data and the calculated spark energy and spark energy density (energy divided by the spark length) for the variable-length spark ignition tests in the 6% hydrogen,  $\phi = 1.0$  hexane-air, and  $\phi = 1.72$  hexane-air mixtures, respectively. The measured quantities included in the tables are the capacitance, breakdown voltage, and spark length (from schlieren images). The calculated quantities in the table include stored energy and charge, residual charge in the capacitor, residual energy in the capacitor, and the estimated spark energy and energy density. The equations used to calculate these quantities are discussed in Section [2.4](#).

### E.1 6% Hydrogen, 12% Oxygen, 82% Argon Test Mixture

Table E.1: Spark length and energy data for the variable-length spark ignition tests in the 6% hydrogen test mixture

Spark Number	C (pF)	$V_{breakdown}$ (kV)	$E_{stored}$ ( $\mu$ J)	$Q_{stored}$ (nC)	$Q_{spark}$ (nC)	$Q_{residual}$ (nC)	$E_{residual}$ ( $\mu$ J)	$E_{spark}$ ( $\mu$ J)	% Energy in Spark	Gap (mm)	E/d ( $\mu$ J/mm)	Result
2	14.0	15.1	1596	211	135	76	206	1390	87	5.6	248	1
3	14.0	16.7	1957	234	139	95	321	1636	84	5.4	301	1
4	14.0	15.1	1596	211	132	80	226	1370	86	5.3	261	1
5	14.0	11.2	875	157	93	63	143	732	84	2.9	253	1
6	14.0	11.2	884	157	94	63	143	741	84	3.0	247	1
7	14.0	11.3	886	158	90	68	163	722	82	6.0	121	0
8	14.0	11.3	894	158	94	64	148	746	83	3.2	235	1
9	14.0	11.3	886	158	91	66	157	729	82	6.9	105	0
10	14.0	11.3	886	158	89	69	169	717	81	5.8	124	1
11	14.0	11.2	880	157	91	66	157	723	82	3.6	203	1
13	14.0	11.3	900	159	94	65	150	750	83	3.0	250	1
14	14.0	11.3	891	158	95	63	143	748	84	5.4	139	0
15	14.0	11.3	891	158	96	62	137	754	85	5.8	130	1
21	14.0	20.2	2845	282	168	114	466	2379	84	11.4	209	1
22	10.0	15.0	1131	150	77	74	272	859	76	4.9	177	1
23	10.0	15.0	1131	150	73	77	300	831	73	6.7	123	0
26	10.0	15.1	1133	151	79	71	254	878	78	6.0	147	0
27	10.0	15.1	1134	151	61	89	400	734	65	4.5	164	0
28	10.0	15.2	1148	152	79	73	264	884	77	3.4	264	1

29	10.0	6.4	202	64	30	33	56	146	72	3.0	49	0
31	10.0	6.4	202	64	34	29	43	159	79	2.0	79	0
32	10.0	7.5	281	75	38	37	69	212	76	1.8	118	0
33	10.0	18.2	1656	182	86	96	460	1196	72	8.8	136	0
34	10.0	5.4	143	54	28	25	31	112	78	1.3	86	0
35	10.0	5.4	143	54	28	25	32	111	78	1.3	86	0
38	10.0	16.6	1383	166	92	75	279	1104	80	7.5	148	1
39	10.0	20.5	2101	205	102	103	533	1568	75	11.2	140	1
40	10.0	9.9	494	99	59	41	83	411	83	4.5	90	0
41	10.0	10.0	495	100	59	41	83	412	83	8.2	51	0
42	10.0	10.0	495	100	59	41	82	413	83	4.7	87	0
43	10.0	9.9	494	99	59	41	83	411	83	2.4	169	0
44	10.0	10.0	495	100	45	54	147	348	70	3.1	113	0
45	10.0	13.0	842	130	76	53	143	699	83	5.8	121	1
46	10.0	13.0	846	130	68	62	193	653	77	7.8	84	0
47	10.0	13.1	858	131	83	48	113	745	87	4.9	154	1
48	10.0	13.0	842	130	76	54	145	697	83	4.1	169	1
49	10.0	13.0	842	130	79	50	127	715	85	3.6	201	1
50	10.0	13.1	854	131	73	58	167	687	80	6.0	115	0
51	10.0	13.1	852	131	73	57	165	686	81	3.4	205	0
52	10.0	13.1	852	131	79	51	130	721	85	3.1	235	1
53	10.0	16.2	1307	162	76	86	370	937	72	4.0	235	0

54	10.0	16.2	1311	162	49	113	642	669	51	6.2	108	0
55	10.0	16.2	1312	162	46	116	669	643	49	5.4	118	0
56	10.0	16.2	1312	162	98	64	206	1106	84	10.9	101	1
57	10.0	16.1	1298	161	64	97	474	824	64	2.9	285	1
58	10.0	14.5	1050	145	88	57	162	888	85	5.1	175	1
59	10.0	14.4	1030	144	59	85	360	669	65	3.7	179	0
60	10.0	14.4	1032	144	84	60	180	852	83	7.6	111	0
61	10.0	14.4	1032	144	56	87	383	650	63	7.3	89	0
62	14.0	14.4	1445	201	82	119	510	935	65	2.9	323	1
63	14.0	14.4	1460	202	78	124	553	907	62	5.6	162	0
64	14.0	14.4	1454	202	72	130	605	848	58	5.2	162	0
65	14.0	14.4	1456	202	82	120	517	939	64	4.1	228	1
66	14.0	16.6	1934	233	71	162	938	995	51	9.1	110	0
67	14.0	11.5	926	161	105	56	110	816	88	2.9	282	1
68	14.0	11.4	911	160	109	50	91	821	90	4.5	180	1
69	14.0	11.4	916	160	111	49	86	831	91	6.1	136	1
70	14.0	8.1	459	113	76	38	51	408	89	2.9	141	1
71	14.0	10.1	714	141	94	48	82	632	89	7.3	87	0
72	14.0	10.1	715	142	96	45	72	643	90	3.6	181	1
73	14.0	11.4	902	159	106	53	98	803	89	5.4	148	1

## E.2 Stoichiometric Hexane-Air Test Mixture

Table E.2: Spark length and energy data for the variable-length spark ignition tests in the stoichiometric (2.16% C<sub>6</sub>H<sub>14</sub>) hexane-air mixture

Spark Number	C (pF)	$V_{breakdown}$ (kV)	$E_{stored}$ ( $\mu$ J)	$Q_{stored}$ (nC)	$Q_{spark}$ (nC)	$Q_{residual}$ (nC)	$E_{residual}$ ( $\mu$ J)	$E_{spark}$ ( $\mu$ J)	% Energy in Spark	Gap (mm)	E/d ( $\mu$ J/mm)	Result
1	28.8	9.1	1192	262	211	51	45	1147	96	2.9	396	0
2	28.8	9.1	1192	262	185	77	104	1088	91	2.3	471	0
3	28.8	11.2	1806	323	137	185	595	1212	67	2.8	434	0
4	28.8	12.7	2326	366	259	107	198	2128	91	3.3	654	0
5	28.8	14.4	2986	415	313	102	181	2805	94	3.1	891	1
6	28.8	14.3	2953	412	284	128	285	2668	90	9.7	274	0
7	28.8	14.3	2957	413	245	168	491	2466	83	3.6	679	1
8	28.8	14.4	2978	414	271	143	357	2621	88	10.0	261	0
9	28.8	12.6	2286	363	277	85	127	2159	94	10.0	217	0
10	28.8	12.6	2286	363	243	120	249	2037	89	7.0	290	0
11	28.8	12.6	2275	362	239	123	263	2012	88	6.0	334	0
12	28.8	12.6	2275	362	229	133	307	1968	87	6.7	295	0
13	28.8	10.7	1646	308	253	55	52	1594	97	8.6	186	0
15	28.8	11.8	2019	341	236	105	192	1826	90	2.6	705	0
16	28.8	12.8	2341	367	315	52	47	2294	98	2.3	1015	0
19	28.8	14.5	3015	417	286	131	296	2719	90	3.5	781	1

20	28.8	15.4	3397	442	326	116	234	3163	93	3.2	996	1
21	28.8	16.8	4064	484	362	122	258	3806	94	12.1	315	1
22	39.9	11.8	2773	470	373	98	120	2653	96	6.5	408	1
23	39.9	10.3	2100	409	212	198	490	1610	77	2.6	621	1
24	39.9	9.3	1729	371	218	153	293	1436	83	2.4	595	1
25	39.9	10.2	2055	405	270	135	230	1826	89	2.4	749	1
26	39.9	11.5	2634	458	293	165	341	2293	87	3.0	771	1
27	39.9	12.9	3310	514	377	137	236	3074	93	8.7	354	0
30	39.9	14.8	4388	592	364	227	648	3740	85	6.0	627	1
31	39.9	8.8	1527	349	239	110	152	1376	90	2.3	608	0
34	50.4	9.9	2480	500	325	175	302	2177	88	2.4	902	0
35	50.4	10.7	2901	541	342	199	392	2509	86	2.6	959	1
37	74.7	12.4	5780	929	585	345	795	4985	86	2.0	2549	1
38	74.7	13.6	6949	1019	642	377	949	6000	86	4.1	1449	1
39	74.7	11.0	4544	824	578	246	405	4139	91	3.3	1244	1
40	74.7	10.5	4079	781	527	253	430	3649	89	2.6	1422	1
41	74.7	11.2	4660	834	667	167	187	4473	96	2.0	2202	1
42	74.7	10.8	4365	808	458	349	816	3548	81	2.3	1518	1
43	74.7	12.0	5387	897	481	416	1159	4228	78	2.4	1734	1
44	69.3	11.9	4890	823	544	279	563	4328	88	2.3	1893	1
45	69.3	13.3	6092	919	584	335	808	5284	87	5.5	963	1
46	69.3	12.6	5457	870	688	182	239	5219	96	2.5	2089	1

47	69.3	13.5	6296	934	548	387	1078	5218	83	2.5	2089	1
48	45.2	9.4	1988	424	243	181	363	1625	82	3.1	526	0
52	59.1	10.3	3141	609	470	139	163	2978	95	3.0	989	1
53	59.1	10.3	3117	607	437	170	243	2873	92	2.6	1109	1
54	59.1	10.7	3402	634	322	312	826	2576	76	3.1	838	1
55	59.1	10.8	3428	637	331	306	791	2637	77	2.5	1059	0
56	59.1	10.8	3415	635	314	321	872	2543	74	3.5	731	1
57	59.1	10.8	3428	637	388	248	522	2906	85	3.6	811	1
58	59.1	9.6	2735	569	401	168	238	2496	91	2.2	1117	1

### E.3 Rich ( $\phi = 1.72$ Hexane-Air Test Mixture)

Table E.3: Spark length and energy data for the variable-length spark ignition tests in the rich (3.67% C<sub>6</sub>H<sub>14</sub>) hexane-air mixture with  $\phi = 1.72$

Spark Number	C (pF)	$V_{breakdown}$ (kV)	$E_{stored}$ ( $\mu$ J)	$Q_{stored}$ (nC)	$Q_{spark}$ (nC)	$Q_{residual}$ (nC)	$E_{residual}$ ( $\mu$ J)	$E_{spark}$ ( $\mu$ J)	% Energy in Spark	Gap (mm)	E/d ( $\mu$ J/mm)	Result
1	23.9	13.1	2051	313	210	103	222	1828	89	4.0	457	1
2	23.9	11.9	1687	284	197	87	157	1530	91	3.0	510	1
3	23.9	10.8	1381	257	163	94	184	1197	87	2.8	427	1

4	23.9	9.1	990	217	157	61	78	912	92	2.1	434	1
5	12.4	9.9	611	123	86	37	55	556	91	2.5	223	0
6	12.4	9.9	603	122	83	39	62	540	90	2.1	257	0
7	12.4	10.7	712	133	103	30	36	677	95	2.0	338	0
8	12.4	10.7	705	132	96	36	52	653	93	2.9	225	0
9	12.4	12.6	981	156	114	42	71	911	93	3.1	294	0
10	12.4	14.4	1282	178	138	40	65	1217	95	3.4	358	0
11	12.4	9.5	560	118	88	30	36	524	94	2.3	228	0
12	16.3	10.7	940	175	144	31	30	910	97	2.5	364	1
13	16.3	13.0	1371	211	99	112	386	985	72	4.8	205	1
14	16.3	11.1	1008	181	153	28	25	983	98	1.8	546	0
15	16.3	11.1	1008	181	136	45	62	946	94	2.6	364	0
16	16.3	11.1	1008	181	145	37	41	967	96	3.3	293	0
17	16.3	15.8	2027	257	126	131	527	1499	74	3.1	484	1
18	16.3	10.8	949	176	150	26	21	928	98	2.2	422	1
19	16.3	9.4	717	153	120	33	34	683	95	2.3	297	0
20	16.3	12.0	1166	195	145	50	76	1089	93	3.2	340	1
21	16.3	11.9	1160	194	54	141	607	553	48	4.2	132	1
22	16.3	13.2	1429	216	173	43	56	1373	96	8.4	163	1
23	16.3	9.3	702	151	103	49	73	629	90	1.9	331	1
24	16.3	10.3	861	168	99	68	144	718	83	2.7	266	1
25	16.3	12.5	1265	203	178	25	19	1247	99	2.3	542	1

26	8.5	9.9	419	84	52	32	61	358	85	5.8	62	0
27	8.5	10.7	486	91	55	36	75	411	85	5.8	71	0
28	8.5	9.5	385	81	37	44	115	270	70	3.4	79	0
29	8.5	9.5	385	81	45	36	77	308	80	3.8	81	0
30	8.5	9.3	364	79	26	53	163	201	55	3.1	65	0
31	8.5	9.4	372	80	43	36	77	296	79	3.6	82	0
32	8.5	11.9	604	101	75	26	40	564	93	7.6	74	0
33	8.5	10.7	487	91	73	18	18	469	96	7.6	62	0
34	8.5	9.6	388	81	38	43	109	278	72	3.5	80	0
35	8.5	8.5	309	73	60	13	9	300	97	1.6	187	0
36	8.5	8.5	306	72	49	23	31	275	90	2.2	125	0
37	8.5	9.9	412	84	68	15	14	399	97	2.4	166	0
38	8.5	10.7	485	91	58	33	62	423	87	5.8	73	0
39	8.5	10.7	484	91	36	55	178	306	63	3.7	83	0
40	8.5	12.2	627	103	71	32	60	567	90	8.4	68	0
41	8.5	12.2	627	103	46	57	191	436	70	4.1	106	0
42	11.2	10.0	564	112	58	54	132	433	77	6.3	69	0
43	11.2	10.1	571	113	41	72	232	339	59	3.2	106	0
44	11.2	11.1	695	125	41	84	315	380	55	3.8	100	0
45	11.2	12.3	844	138	55	83	306	539	64	4.5	120	0
46	11.2	10.7	642	120	62	58	148	494	77	5.6	88	0
47	11.2	8.6	415	96	51	45	92	324	78	3.1	104	0

48	11.2	8.1	368	91	29	61	169	200	54	3.7	54	0
49	11.2	8.2	373	91	35	57	144	229	61	2.8	82	0
50	11.2	9.5	504	106	50	56	140	364	72	4.8	76	0
51	11.2	7.9	347	88	30	58	150	197	57	1.9	104	0
52	11.2	7.4	303	82	37	45	91	212	70	2.4	88	0
53	11.2	7.4	303	82	36	46	95	208	69	2.9	72	0
54	11.2	6.8	257	76	34	42	78	179	70	1.8	99	0
55	11.2	10.7	641	120	52	68	204	437	68	4.5	97	0

# Appendix F

## MATLAB Scripts for Performing Statistical Analysis on Ignition Test Data

```
%%%%%%%%%%%%%%%%%%%%%%%%%%%%%%%%%%%%%%%%%%%%%%%%%%%%%%%%%%%%%%%%%%%%%%%%%%  
%                                                                    %  
% IGNITION_TESTS_STATISTICS.m                                       %  
%   A script for performing statistical analysis on ignition test data. %  
%                                                                    %  
%%%%%%%%%%%%%%%%%%%%%%%%%%%%%%%%%%%%%%%%%%%%%%%%%%%%%%%%%%%%%%%%%%%%%%%%%%  
% Written by:  Sally Bane           Date:  June 9, 2008           %  
%%%%%%%%%%%%%%%%%%%%%%%%%%%%%%%%%%%%%%%%%%%%%%%%%%%%%%%%%%%%%%%%%%%%%%%%%%  
% This script performs the following calculations:                   %  
%   1. Fits a logistic probability distribution to the binary        %  
%      test results.                                               %  
%   2. Calculates percentiles from the 10th percentile to the     %  
%      90th in increments of 10%.                                  %  
%   3. Estimates the 95% confidence interval for each percentile.  %  
% The parameters for the probability distribution, percentiles, and %  
% confidence intervals are then written to an Excel file.         %  
%%%%%%%%%%%%%%%%%%%%%%%%%%%%%%%%%%%%%%%%%%%%%%%%%%%%%%%%%%%%%%%%%%%%%%%%%%
```

```

clear

%%%%%%%%%%%%%%%%%%%%%%%%%%%%%%%%%%%%%%%%%%%%%%%%%%%%%%%%%%%%%%%%%%%%%%%%
% INPUT REST RESULTS                                             %
%%%%%%%%%%%%%%%%%%%%%%%%%%%%%%%%%%%%%%%%%%%%%%%%%%%%%%%%%%%%%%%%%%%%%%%%
%      N:  number of tests                                       %
%      X:  vector of length N containing the stimulus level     %
%           (e.g. spark energy, energy density, charge, etc.)  %
%      Y:  vector of length N containing the test results (1 or 0) %
%%%%%%%%%%%%%%%%%%%%%%%%%%%%%%%%%%%%%%%%%%%%%%%%%%%%%%%%%%%%%%%%%%%%%%%%

X = []; % vector of N stimulus levels

Y = []; % vector of N test results

% verify that the two vectors are the same size
N1 = size(X);
N2 = size(Y);
N = N1(2);

N1
N2

%%%%%%%%%%%%%%%%%%%%%%%%%%%%%%%%%%%%%%%%%%%%%%%%%%%%%%%%%%%%%%%%%%%%%%%%
% MAXIMIZE THE LIKELIHOOD FUNCTION TO FIND PARAMETERS BETA0 & BETA1
%%%%%%%%%%%%%%%%%%%%%%%%%%%%%%%%%%%%%%%%%%%%%%%%%%%%%%%%%%%%%%%%%%%%%%%%
%      The function "max_likelihood" uses the test results (X and Y
%      vectors) to calculate the likelihood function, which has two
%      initially undetermined parameters beta0 and beta1.  The MATLAB

```

```

%      built-in function "fminsearch" then finds the values of beta0      %
%      and beta1 which minimize the negative of the likelihood function  %
%      (i.e. maximizes the actual likelihood function). The results      %
%      for the two parameters are then stored in the vector "Beta."      %
%%%%%%%%%%%%%%%%%%%%%%%%%%%%%%%%%%%%%%%%%%%%%%%%%%%%%%%%%%%%%%%%%%%%%%%%

```

```

max_likelihood;

```

```

%%%%%%%%%%%%%%%%%%%%%%%%%%%%%%%%%%%%%%%%%%%%%%%%%%%%%%%%%%%%%%%%%%%%%%%%
% CALCULATE THE PROBABILITY DISTRIBUTION                                  %
%%%%%%%%%%%%%%%%%%%%%%%%%%%%%%%%%%%%%%%%%%%%%%%%%%%%%%%%%%%%%%%%%%%%%%%%
%      Calculate the logistic probability distribution using the values    %
%      found for beta0 and beta1.                                         %
%%%%%%%%%%%%%%%%%%%%%%%%%%%%%%%%%%%%%%%%%%%%%%%%%%%%%%%%%%%%%%%%%%%%%%%%

```

```

i1 = 1;
upper_lim = max(X)+50; % define energy limits
lower_lim = min(X)-50; % for plotting

```

```

% calculate the probability at energy levels between the limits
for en=lower_lim:5:upper_lim
    energy(i1) = en;
    probability(i1) = 1./(1+exp(-Beta(1)-Beta(2).*en));
    i1 = i1+1;
end

```

```

%%%%%%%%%%%%%%%%%%%%%%%%%%%%%%%%%%%%%%%%%%%%%%%%%%%%%%%%%%%%%%%%%%%%%%%%
% CALCULATE PERCENTILES OF THE PROBABILITY DISTRIBUTION                  %
%%%%%%%%%%%%%%%%%%%%%%%%%%%%%%%%%%%%%%%%%%%%%%%%%%%%%%%%%%%%%%%%%%%%%%%%

```

```

%%%%%%%%%%%%%%%%%%%%%%%%%%%%%%%%%%%%%%%%%%%%%%%%%%%%%%%%%%%%%%%%%%%%%%%%
%       Here we are calculating the 10th through 90th percentiles in       %
%       increments of 10%.                                                %
%%%%%%%%%%%%%%%%%%%%%%%%%%%%%%%%%%%%%%%%%%%%%%%%%%%%%%%%%%%%%%%%%%%%%%%%

```

```

Q = [0.1 0.2 0.3 0.4 0.5 0.6 0.7 0.8 0.9];
num1 = size(Q);
num2 = num1(2);
i2 = 1;
for i2=1:1:num2
    Xq(i2) = (log(Q(i2)/(1-Q(i2)))-Beta(1))/Beta(2);
end

```

```

%%%%%%%%%%%%%%%%%%%%%%%%%%%%%%%%%%%%%%%%%%%%%%%%%%%%%%%%%%%%%%%%%%%%%%%%
% CALCULATE THE 95% CONFIDENCE LIMITS ON THE PERCENTILES                %
%%%%%%%%%%%%%%%%%%%%%%%%%%%%%%%%%%%%%%%%%%%%%%%%%%%%%%%%%%%%%%%%%%%%%%%%

```

```

% First calculate the second derivatives of the likelihood function
% with respect to beta0 and beta1 and the cross derivative

```

```

% second derivative with respect to beta0
i3=0;
derivative_b0=0;

```

```

for i3=1:1:N
    prob1(i3)=1./(1+exp(-Beta(1)-Beta(2).*X(i3)));
    D1(i3)=-prob1(i3)*(1-prob1(i3));
    derivative_b0 = derivative_b0 + D1(i3);
end

```

```

% second derivative with respect to beta1
i4=0;
derivative_b1=0;

for i4=1:1:N
    prob2(i4)=1./(1+exp(-Beta(1)-Beta(2).*X(i4)));
    D2(i4)=-X(i4)^2*prob2(i4)*(1-prob2(i4));
    derivative_b1 = derivative_b1 + D2(i4);
end

% second derivative with respect to beta0 and beta1
i5=0;
derivative_b0b1=0;

for i5=1:1:N
    prob3(i5)=1./(1+exp(-Beta(1)-Beta(2).*X(i5)));
    D3(i5)=-X(i5)*prob3(i5)*(1-prob3(i5));
    derivative_b0b1 = derivative_b0b1 + D3(i5);
end

% store values of the second derviatives of the likelihood
% in the information matrix and take the inverse to find
% the variances of beta0, beta1 and the covariance

infomatrix =
[-derivative_b0 -derivative_b0b1; -derivative_b0b1 -derivative_b1];

varmatrix = infomatrix^(-1);

```

```

var_b0 = varmatrix(1,1);
var_b1 = varmatrix(2,2);
covar = varmatrix(1,2);

% need the value of the (100 - alpha/2)^th percentile
% (alpha = 1-confidence = 0.05 for 95% confidence) from a standard
% (mu = 0, sigma = 1) cumulative Gaussian distribution
% NOTE: this value was calculated using Mathematica and is constant
% for a given confidence (i.e. 95% in this case); if using a different
% confidence, must recalculate using the correct alpha value
Z_95 = 1.95996;

% Calculate the lower and upper 95% confidence limits for each percentile

i6 = 0;
for i6=1:1:num2
    LCL(i6)=Xq(i6)-Z_95*
    sqrt((var_b0 + 2*Xq(i6)*covar + Xq(i6)^2*var_b1)/(Beta(2)^2));

    UCL(i6)=Xq(i6)+Z_95*
    sqrt((var_b0 + 2*Xq(i6)*covar + Xq(i6)^2*var_b1)/(Beta(2)^2));
end

%%%%%%%%%%%%%%%%%%%%%%%%%%%%%%%%%%%%%%%%%%%%%%%%%%%%%%%%%%%%%%%%%%%%%%%%
% PLOT THE PROBABILITY DISTRIBUTION AND 95% CONFIDENCE INTERVAL      %
%%%%%%%%%%%%%%%%%%%%%%%%%%%%%%%%%%%%%%%%%%%%%%%%%%%%%%%%%%%%%%%%%%%%%%%%

% using calculations of probability vs. energy done previously
plot(energy,probability,'k',LCL,Q,'r',UCL,Q,'r')

```

```

%%%%%%%%%%%%%%%%%%%%%%%%%%%%%%%%%%%%%%%%%%%%%%%%%%%%%%%%%%%%%%%%%%%%%%%%
% WRITE IMPORTANT PARAMETERS TO AN EXCEL FILE %
%%%%%%%%%%%%%%%%%%%%%%%%%%%%%%%%%%%%%%%%%%%%%%%%%%%%%%%%%%%%%%%%%%%%%%%%
%       Write the values for beta0 and beta1, the 10th-90th percentiles, %
%       the 95% confidence bounds, and the interval widths to a CSV file %
%       for use in Excel. %
%%%%%%%%%%%%%%%%%%%%%%%%%%%%%%%%%%%%%%%%%%%%%%%%%%%%%%%%%%%%%%%%%%%%%%%%

```

```

data1 = {'Beta0', 'Beta1'; Beta(1) Beta(2)}; % write beta0, beta1
s1 = xlswrite('statistics.xls', data1, 'Sheet1', 'A1');
data2 = {'Percentile', 'Energy', 'LCL', 'UCL'; Q(1) Xq(1) LCL(1) UCL(1);...
        Q(2) Xq(2) LCL(2) UCL(2); Q(3) Xq(3) LCL(3) UCL(3); Q(4) Xq(4)...
        LCL(4) UCL(4); Q(5) Xq(5) LCL(5) UCL(5); Q(6) Xq(6) LCL(6) UCL(6);...
        Q(7) Xq(7) LCL(7) UCL(7); Q(8) Xq(8) LCL(8) UCL(8);...
        Q(9) Xq(9) LCL(9) UCL(9)};
s2 = xlswrite('statistics.xls', data2, 'Sheet1', 'D1');
data3 = {'Interval Width'; UCL(1)-LCL(1); UCL(2)-LCL(2); UCL(3)-LCL(3);...
        UCL(4)-LCL(4); UCL(5)-LCL(5); UCL(6)-LCL(6); UCL(7)-LCL(7);...
        UCL(8)-LCL(8); UCL(9)-LCL(9)};
s3 = xlswrite('statistics.xls', data3, 'Sheet1', 'I1');

```

```

%%%%%%%%%%%%%%%%%%%%%%%%%%%%%%%%%%%%%%%%%%%%%%%%%%%%%%%%%%%%%%%%%%%%%%%%
% %
% LIKELIHOOD.m %
%       A script to define the likelihood function as a function of beta0 %
%       and beta1 (vector B) and the input test results from the main %
%%%%%%%%%%%%%%%%%%%%%%%%%%%%%%%%%%%%%%%%%%%%%%%%%%%%%%%%%%%%%%%%%%%%%%%%

```

```

%      script "ignition_tests_statistics.m."                                     %
%%%%%%%%%%%%%%%%%%%%%%%%%%%%%%%%%%%%%%%%%%%%%%%%%%%%%%%%%%%%%%%%%%%%%%%%%%

function L = likelihood(B,X,Y);
P = 1./(1+exp(-B(1)-B(2).*X));
L = -prod(P.^Y.*(1-P).^(1-Y));

%%%%%%%%%%%%%%%%%%%%%%%%%%%%%%%%%%%%%%%%%%%%%%%%%%%%%%%%%%%%%%%%%%%%%%%%%%
%                                                                 %
% MAX_LIKELIHOOD.m                                             %
%      A script to call the MATLAB function "fminsearch" to maximize the %
%      likelihood function calculated in the script "likelihood.m." %
%                                                                 %
%%%%%%%%%%%%%%%%%%%%%%%%%%%%%%%%%%%%%%%%%%%%%%%%%%%%%%%%%%%%%%%%%%%%%%%%%%

[Beta,maxL] = fminsearch(@(b) likelihood(b,X,Y),[-1 .01]);

```

# Appendix G

## Statistical Analysis Results

### G.1 Short, Fixed-Length Spark Tests: Probability Versus Energy

Table G.1: Percentiles and 95% upper confidence limit (UCL) and lower confidence limit (LCL) for the short, fixed-length spark ignition tests

Percentile	5% H <sub>2</sub> , 12% O <sub>2</sub> , 83% Ar			6% H <sub>2</sub> , 12% O <sub>2</sub> , 82% Ar			7% H <sub>2</sub> , 12% O <sub>2</sub> , 81% Ar		
	Energy ( $\mu$ J)	LCL ( $\mu$ J)	UCL ( $\mu$ J)	Energy ( $\mu$ J)	LCL ( $\mu$ J)	UCL ( $\mu$ J)	Energy ( $\mu$ J)	LCL ( $\mu$ J)	UCL ( $\mu$ J)
0.1	780	633	927	312	281	343	97	67	127
0.2	843	729	958	326	303	350	114	91	136
0.3	885	789	982	336	315	357	125	106	144
0.4	920	833	1006	344	325	363	134	116	153
0.5	952	870	1033	351	332	371	143	123	162
0.6	983	901	1066	359	338	380	151	130	172
0.7	1018	929	1107	366	343	390	160	136	185
0.8	1060	957	1163	376	348	404	171	142	201
0.9	1123	990	1257	391	354	427	188	150	226

Table G.2: Logistic probability distribution parameters  $\beta_0$  and  $\beta_1$  for the short, fixed-length spark ignition tests

Mixture	$\beta_0$	$\beta_1$
5% H <sub>2</sub> , 12% O <sub>2</sub> , 83% Ar	-12.171	0.0128
6% H <sub>2</sub> , 12% O <sub>2</sub> , 82% Ar	-19.631	0.056
7% H <sub>2</sub> , 12% O <sub>2</sub> , 81% Ar	-6.860	0.0481

## G.2 Variable-Length Spark Tests: Probability Versus Energy Density

Table G.3: Percentiles and 95% upper confidence limit (UCL) and lower confidence limit (LCL) for the variable-length spark ignition tests

Percentile	6% H <sub>2</sub> , 12% O <sub>2</sub> , 82% Ar			Stoichiometric Hexane-Air			Rich ( $\phi = 1.72$ ) Hexane-Air		
	E/d ( $\mu\text{J}/\text{mm}$ )	LCL ( $\mu\text{J}/\text{mm}$ )	UCL ( $\mu\text{J}/\text{mm}$ )	E/d ( $\mu\text{J}/\text{mm}$ )	LCL ( $\mu\text{J}/\text{mm}$ )	UCL ( $\mu\text{J}/\text{mm}$ )	E/d ( $\mu\text{J}/\text{mm}$ )	LCL ( $\mu\text{J}/\text{mm}$ )	UCL ( $\mu\text{J}/\text{mm}$ )
0.1	81	41	122	255	-37	548	163	81	245
0.2	108	79	138	403	184	622	219	154	285
0.3	126	102	150	502	323	680	257	197	317
0.4	141	119	163	582	427	738	288	228	349
0.5	154	132	176	656	510	802	316	252	381
0.6	168	144	191	730	580	880	345	274	416
0.7	182	155	210	811	642	979	376	295	456
0.8	200	166	234	909	704	1115	414	319	508
0.9	227	182	272	1057	780	1334	470	351	589

Table G.4: Logistic probability distribution parameters  $\beta_0$  and  $\beta_1$  for the variable-length spark ignition tests

Mixture	$\beta_0$	$\beta_1$
6% H <sub>2</sub> , 12% O <sub>2</sub> , 82% Ar	4.652	0.030
Stoichiometric Hexane-Air	-3.596	0.005
Rich ( $\phi = 1.72$ ) Hexane-Air	-4.520	0.014

### G.3 Probability Versus Charge

Table G.5: Spark charge percentiles and 95% upper confidence limit (UCL) and lower confidence limit (LCL) for the short, fixed-length spark ignition tests

Percentile	5% H <sub>2</sub> , 12% O <sub>2</sub> , 83% Ar			6% H <sub>2</sub> , 12% O <sub>2</sub> , 82% Ar			7% H <sub>2</sub> , 12% O <sub>2</sub> , 81% Ar		
	Charge (nC)	LCL (nC)	UCL (nC)	Charge (nC)	LCL (nC)	UCL (nC)	Charge (nC)	LCL (nC)	UCL (nC)
0.1	162	138	186	80	72	89	21	10	31
0.2	175	156	193	85	79	92	26	19	34
0.3	184	168	199	88	83	94	30	24	36
0.4	191	177	205	91	86	96	33	28	38
0.5	197	184	211	94	88	99	36	30	41
0.6	204	190	218	96	90	102	39	32	45
0.7	211	195	226	99	92	105	42	34	49
0.8	219	201	238	102	94	110	45	36	55
0.9	233	209	257	107	96	117	51	38	64

Table G.6: Spark charge percentiles and 95% upper confidence limit (UCL) and lower confidence limit (LCL) for the variable-length spark ignition tests

Percentile	6% H <sub>2</sub> , 12% O <sub>2</sub> , 82% Ar			Stoichiometric Hexane-Air			Rich ( $\phi = 1.72$ ) Hexane-Air		
	Charge (nC)	LCL (nC)	UCL (nC)	Charge (nC)	LCL (nC)	UCL (nC)	Charge (nC)	LCL (nC)	UCL (nC)
0.1	60	47	72	179	96	262	75	47	103
0.2	67	57	77	221	160	281	95	72	117
0.3	72	64	80	248	200	296	108	87	128
0.4	76	69	83	270	229	312	118	98	139
0.5	80	73	86	291	252	330	128	106	150
0.6	83	77	90	312	271	353	138	114	162
0.7	87	80	95	334	286	382	148	121	176
0.8	92	83	101	362	302	422	161	129	194
0.9	100	88	112	403	320	486	181	140	221

# Appendix H

## Constant Pressure Explosion Method MATLAB Code

```
%%%%%%%%%%%%%%%%%%%%%%%%%%%%%%%%%%%%%%%%%%%%%%%%%%%%%%%%%%%%%%%%%%%%%%%%%  
% ESTIMATE_Ea_n_FROM_CP_METHOD.m %  
% A script that estimates effective activation energies and %  
% reaction orders for hydrogen-air mixtures using constant %  
% pressure explosion computations. %  
% %  
% Written by: Sally Bane %  
% Last Updated: 04/25/10 %  
%%%%%%%%%%%%%%%%%%%%%%%%%%%%%%%%%%%%%%%%%%%%%%%%%%%%%%%%%%%%%%%%%%%%%%%%%  
  
clear all; clc;  
  
results = zeros(85,13);  
  
j = 1; % counter for overall loop  
i = 1; % counter for imbedded loop
```

```

% vector of equivalence ratios
phi = [5.55; 4.42; 3.57; 2.91; 2.38; 1.95; 1.59; 1.28; 1.02; ...
       0.79; 0.59; 0.42; 0.39; 0.36; 0.32];

% values of n found using rho = 1.10*rho_0
% rxn_order = [1.846; 1.9322; 1.9612; 1.8801; 1.8203; 1.7724; ...
%             1.7957; 1.8492; 1.8109; 1.9542; 1.886; 1.8616; 1.9275; ...
%             1.9106; 1.8201];

% values of n found using rho = 1.20*rho_0
rxn_order = [1.7812; 1.8256; 1.8327; 1.8299 ;1.7848; 1.7931; ...
            1.7338; 1.7785; 1.7666; 1.8657; 1.8362; 1.8182; 1.8398; ...
            1.8005; 1.7368];

% calculate percent H2 and set gas to initial conditions
for j=1:1:length(phi)

    percentH2(j) = phi(j)/(phi(j)+0.5+1.88)*100;

    gas = importPhase('Lietal_mech_2003.cti');
    set(gas,'T',300,'P',100000,'X', ...
        strcat('H2:',num2str(phi(j))),' ,O2:0.5,N2:1.88'));
    equilibrate(gas,'HP');
    T_equil = temperature(gas);

    frac_T = [0.5; 0.6; 0.7; 0.8; 0.9; 1.0];

    for i=1:1:size(frac_T)

```

```

%%%%%%%%%%%%%%%%%%%%%%%%%%%%%%%%%%%%%%%%%%%%%%%%%%%%%%%%%%%%%%%%%%%%%%%%
% STEP 1: Calculate a constant pressure explosion for initial
% temperature T0 (some fraction of the burned gas temperature
% from a constant HP equilibration). Estimate the induction
% time for this initial temperature T0.
%%%%%%%%%%%%%%%%%%%%%%%%%%%%%%%%%%%%%%%%%%%%%%%%%%%%%%%%%%%%%%%%%%%%%%%%

% Perform a constant pressure explosion using initial
% temperature T0
% Plot temperature vs. time to verify explosion and
% store the time and temperature vectors.

    T0 = frac_T(i)*T_equil;
    set(gas,'T',T0,'P',100000,'X', ...
        strcat('H2:',num2str(phi(j)),' ,O2:0.5,N2:1.88'));
    [time, T_trace] = ignite_hp2(gas);
    Tf(i) = max(T_trace);

    figure
    plot(time(1,:),T_trace(1,:)); xlabel('time (s)');
    ylabel('T (K)');
    title(strcat('Temperature vs. Time ...
        for T0 = ',num2str(T0),' K'));
    axis([0 0.0003 1200 3200]);

    t = transpose(time); Temp = transpose(T_trace);
    s1 = size(t); t_end = s1(1);
    s2 = size(Temp); temp_end = s2(1);

% Find the maximum temperature gradient and the

```

```

% time where it occurs - this will be used as
% the INDUCTION TIME for temperature T0.

    m = 1;
    for m=1:1:temp_end-2
        gradT(m)=(((Temp(m+2)-Temp(m+1))/(t(m+2)-t(m+1)))+ ...
            ((Temp(m+1)-Temp(m))/(t(m+1)-t(m))))/2;
        t_gradT(m) = t(m+1);
    end

    maxgradT = max(gradT); % max temperature gradient
    gradTmax(i) = maxgradT;
    imax = find(gradT==maxgradT);
    ti(i) = t_gradT(imax); % induction time

%%%%%%%%%%%%%%%%%%%%%%%%%%%%%%%%%%%%%%%%%%%%%%%%%%%%%%%%%%%%%%%%%%%%%%%%
% STEP 2: Calculate a constant pressure explosion for initial
% temperature T0 + T' where T' << T0 (see below for chosen
% value). Estimate the induction time at this slightly
% elevated temperature.
%%%%%%%%%%%%%%%%%%%%%%%%%%%%%%%%%%%%%%%%%%%%%%%%%%%%%%%%%%%%%%%%%%%%%%%%

    T0_p = T0 + 30; % slightly elevated temperature
    set(gas,'T',T0_p,'P',100000,'X', ...
        strcat('H2:',num2str(phi(j)),'.02:0.5,N2:1.88'));
    [time, T_trace] = ignite_hp2(gas);
    Tf_p(i) = max(T_trace);
    %plot(time(1,:),T_trace(1,:));
    xlabel('time (s)'); ylabel('T (K)');

```

```

t = transpose(time); Temp = transpose(T_trace);
s1 = size(t); t_end = s1(1);
s2 = size(Temp); temp_end = s2(1);

% Find the maximum temperature gradient and the time
% where it occurs - this will be used as
% the INDUCTION TIME for temperature T0.

k = 1;
for k=1:1:temp_end-2
    gradT(k)=(((Temp(k+2)-Temp(k+1))/(t(k+2)-t(k+1)))+ ...
              ((Temp(k+1)-Temp(k))/(t(k+1)-t(k))))/2;
    t_gradT(k) = t(k+1);
end

maxgradT = max(gradT); % find max temperature gradient
gradTmax_p(i) = maxgradT;
imax = find(gradT==maxgradT);
ti_p(i) = t_gradT(imax); % induction time

%%%%%%%%%%%%%%%%%%%%%%%%%%%%%%%%%%%%%%%%%%%%%%%%%%%%%%%%%%%%%%%%%%%%%%%%
% STEP 3: Use the two calculations at slightly different
% initial temperatures to approximate the derivative of the
% induction time with respect to initial temperature
%  $D(t_i)/D(T_0) = (t_{i_p} - t_i) / (T_{0_P} - T_0)$ .
% Then estimate activation energy using
%  $T_0/t_i * D(t_i)/D(T_0) \sim -E_a/RT_0$ 
%%%%%%%%%%%%%%%%%%%%%%%%%%%%%%%%%%%%%%%%%%%%%%%%%%%%%%%%%%%%%%%%%%%%%%%%

```

```

Dti_DT0(i) = (ti_p(i) - ti(i))/(T0_p - T0);
Ea_1(i) = -1.986*T0*(T0/ti(i))*Dti_DT0(i);
Ea_2(i) = -1.986*T0*((T0/ti(i))*Dti_DT0(i)-1-rxn_order(j));
Ti(i) = T0;
Zeldovich1(i) = (Ea_1(i)/1.987)*(T_equil-300)/((T_equil)^2);
Zeldovich2(i) = (Ea_2(i)/1.987)*(T_equil-300)/((T_equil)^2);

% store calculation parameters and results in a matrix
results(j+(i-1)*16,1) = phi(j);
results(j+(i-1)*16,2) = percentH2(j);
results(j+(i-1)*16,3) = Ti(i);
results(j+(i-1)*16,4) = Tf(i);
results(j+(i-1)*16,5) = gradTmax(i);
results(j+(i-1)*16,6) = ti(i);
results(j+(i-1)*16,7) = Tf_p(i);
results(j+(i-1)*16,8) = gradTmax_p(i);
results(j+(i-1)*16,9) = ti_p(i);
results(j+(i-1)*16,10) = Ea_1(i);
results(j+(i-1)*16,11) = Zeldovich1(i);
results(j+(i-1)*16,12) = Ea_2(i);
results(j+(i-1)*16,13) = Zeldovich2(i);

end

end

% write the results to a CSV file
csvwrite('results_Ea.csv',results)

```

# Appendix I

## Effective Reaction Orders and Activation Energies for Hydrogen-Air Systems

Table I.1 lists the values of effective reaction order  $n$  and activation energy  $E_a$  calculated for a range of hydrogen-air compositions using the constant pressure explosion method with reaction order dependence (Equations 6.18 and 6.23). The pressure is 1 bar, and the initial temperature used in the explosion calculations was  $T_0 = 0.9T_b$  where  $T_b$  is the adiabatic flame temperature found by equilibrating the mixture at constant pressure and enthalpy. The temperature and density intervals used for the derivatives were  $T' = 30$  K and  $\rho' = 1.1\rho_0$ , respectively. The unburned temperature is 300 K and the adiabatic flame temperature  $T_b$  was used for the burned gas temperature in calculating the Zeldovich number.

Table I.2 lists the values of effective activation energy  $E_a$  calculated for a range of hydrogen-air compositions using the constant pressure explosion method with constant volume initial conditions (Equation 6.28). The initial pressure is 1 bar, and the initial temperature used in the explosion calculations was  $T_0 = 0.9T_b$  where  $T_b$  is the adiabatic flame temperature found by equilibrating the mixture at constant pressure and enthalpy. The temperature interval used for the derivative was  $T' = 30$  K. The unburned temperature is 300 K and the adiabatic flame temperature  $T_b$  was used for the burned gas temperature in calculating the Zeldovich number.

Table I.3 lists the values of effective activation energy  $E_a$  calculated for a range

of hydrogen-air compositions using the constant volume explosion method (Equation 6.34). The initial pressure is 1 bar, and the initial temperature used in the explosion calculations was  $T_0 = 0.9T_b$  where  $T_b$  is the adiabatic flame temperature found by equilibrating the mixture at constant pressure and enthalpy. The temperature interval used for the derivative was  $T' = 30$  K. The unburned temperature was 300 K and the constant volume explosion temperature, found by equilibrating the mixture at constant volume and energy, was used in this case for the burned gas temperature for calculating the Zeldovich number.

Table I.1: Effective reaction orders and activation energies calculated using the constant pressure explosion method with reaction order dependence (Equations 6.18 and 6.23)

%H <sub>2</sub>	$n$	$\beta$	$E_a$ (kcal/mol)
70	1.8	6.3	21.602
65	1.9	6.0	22.173
60	2.0	5.7	22.862
55	1.9	5.5	23.358
50	1.8	5.3	24.131
45	1.8	5.0	24.305
40	1.8	5.1	26.061
35	1.8	4.9	26.181
30	1.8	5.1	27.856
25	2.0	4.3	21.425
20	1.9	5.0	21.806
15	1.9	5.5	20.263
14	1.9	5.7	20.176
13	1.9	5.8	20.017
12	1.8	6.3	20.308

Table I.2: Effective activation energies calculated using the constant pressure explosion method with constant volume initial conditions (Equation 6.28)

%H <sub>2</sub>	$\beta$	$E_a$ (kcal/mol)
70	6.3	21.435
65	5.9	21.961
60	5.7	22.968
55	5.3	22.863
50	5.4	24.841
45	5.0	24.084
40	5.2	26.702
35	5.1	27.422
30	5.2	28.359
25	4.2	20.765
20	5.0	21.759
15	5.5	20.250
14	5.7	20.259
13	5.8	20.009
12	6.2	20.211

Table I.3: Effective activation energies calculated using the constant volume explosion method (Equation 6.34)

%H <sub>2</sub>	$\beta$	$E_a$ (kcal/mol)
70	5.3	21.174
65	4.9	21.285
60	4.7	22.071
55	4.7	23.717
50	4.7	25.253
45	4.4	24.934
40	4.7	27.566
35	4.6	28.277
30	4.9	30.460
25	3.5	20.373
20	4.2	21.313
15	4.7	20.058
14	4.8	19.938
13	5.0	19.777
12	5.4	20.079

## Appendix J

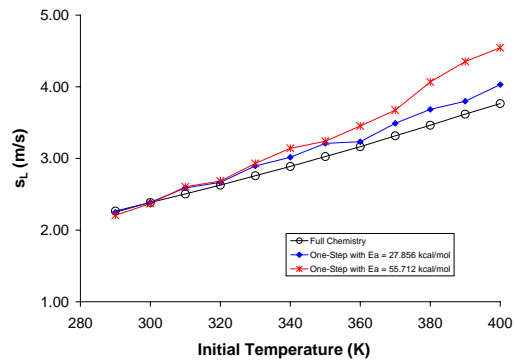
# Sensitivity of Effective Activation Energy to Flamespeed

The basic theory of the flame speed method for calculating the effective activation energy as presented by FM Global (Bauwens, 2007) and discussed in Shepherd et al. (2008) is that the activation energy can be estimated using the sensitivity of the flame speed to small changes in the initial temperature and pressure. To assess the validity of this approach, the dependence of the flame speed on initial temperature and pressure was investigated using two different values for the activation energy. If the activation energy is in fact dependent on the flame speed sensitivity to temperature and pressure, one would expect to see a change in the slopes of the flame speed versus temperature and pressure curves for the two different activation energies.

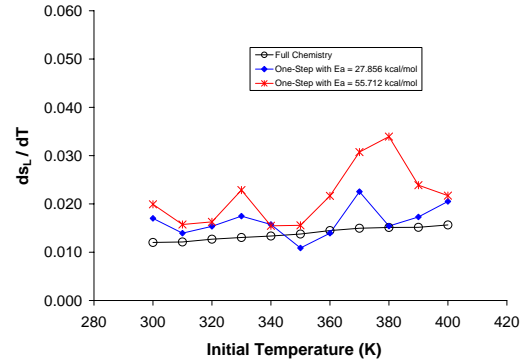
Previous calculations were performed to examine the flame speed versus small changes in the initial temperature and pressure using a second-order one-step model for a 30% hydrogen mixture, as discussed in Section 6.6.2. The effective activation energy used was the value calculated from the constant pressure explosion method,  $E_a = 27.856$  kcal/mol and the pre-exponential factor  $A$  was  $5.80 \times 10^{14}$ . The activation energy was then doubled to  $E_a = 55.712$  kcal/mol and a new value of the pre-exponential factor was found to match the one-step flamespeed to the full chemistry at 300 K and 1 bar,  $A = 1.35 \times 10^{18}$ . The flamespeed with initial temperatures increasing from 290 K to 400 K by 10 K with pressure fixed at 1 bar was then calculated, and with initial pressures increasing from 0.85 bar to 1.5 bar by 0.05 bar with

temperature fixed at 300 K.

The flame speed versus initial temperature calculated using full chemistry, the second-order one-step model with  $E_a = 27.856$  kcal/mol, and the second-order one-step model with  $E_a = 55.712$  kcal/mol is shown in Figure J.1(a). For initial temperatures of 280 K to 350 K the flame speed results from the two one-step models with different activation energies match to within 4%, and for initial temperatures from 360 K to 400 K the two results match to within 6 to 16%. The slopes of the flame-speed curves, estimated using the average of the forward and backward differences, are plotted in Figure J.1(b). The slopes of the flamespeed versus initial temperature curves calculated using the two different activation energies are very close (within 2 to 15% of each other) for several initial temperatures, i.e., 300, 310, 320, 340, and 400 K, and differ by more than 30% for other initial temperatures. However, there is no consistent significant difference in the slopes of the flamespeed versus temperature curves for the two different activation energies. The flamespeed versus small changes in initial pressure is shown in Figure J.2(a) with values calculated using full chemistry and the second-order one-step models with  $E_a = 27.856$  kcal/mol and with  $E_a = 55.712$  kcal/mol. For all three cases the flamespeed is approximately constant for small changes in initial pressure (0.85 to 1.50 bar) and there is no apparent difference in the slopes of the curves calculated using the one-step models with two different activation energies. The slopes of the flamespeed versus initial pressure curves, estimated once again using the average of forward and backward differences, are plotted in Figure J.2(b). The slopes from the two one-step model calculations both oscillate around zero, as expected for a one-step model with  $n = 2$ . While the sensitivities of the flamespeed to small changes in the initial temperature and pressure are not numerically identical for the two different activation energies, in this example there is no consistent difference in the flamespeed dependence that can be identified and attributed to the differing values of  $E_a$ . Therefore, it does not appear that the activation energy is sensitive enough to the flamespeed dependence on small changes in the initial conditions to use the flamespeed to extract an effective value of  $E_a$ .

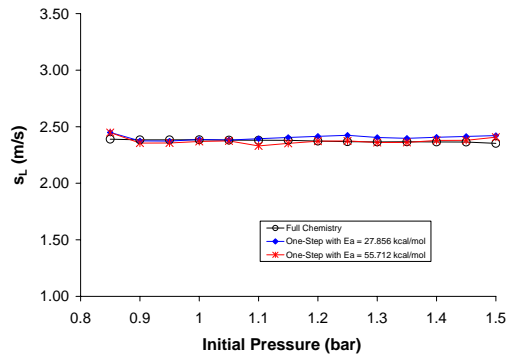


(a)

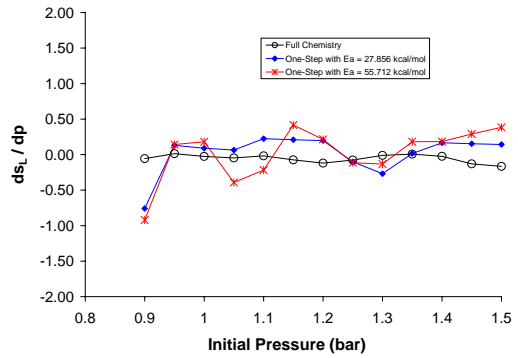


(b)

Figure J.1: (a) Flamespeed versus small changes in initial temperature calculated using full chemistry and one-step models with two different activation energies and (b) the slopes of the flame speed curves



(a)



(b)

Figure J.2: (a) Flamespeed versus small changes in initial pressure calculated using full chemistry and one-step models with two different activation energies and (b) the slopes of the flame speed curves

# Appendix K

## Python 1D Adiabatic Flame Code

```
#
# ONESTEP_FLAME - A freely-propagating, adiabatic, premixed
#           flat (1D) flame using a one step chemistry model.
#
from Cantera import *
from Cantera.OneD import *
from Cantera.OneD.FreeFlame import FreeFlame

#####
#
# parameter values
#
p          = 100000          # pressure
tin        = 300            # unburned gas temperature

comp = 'R:1, P:0' # premixed gas composition
           # R = reactant, P = product

initial_grid = [0.0, 0.001, 0.01, 0.02, 0.029, 0.03] # meters

tol_ss     = [1.0e-5, 1.0e-9] # [rtol atol] for steady-state
```

```

# problem
tol_ts      = [1.0e-5, 1.0e-9]      # [rtol atol] for time stepping

loglevel    = 1                      # amount of diagnostic output (0
                                     # to 5)

refine_grid = 1                      # 1 to enable refinement, 0 to
                                     # disable

# use one step model input (.cti) file
gas = importPhase('onestep.cti')

# set the gas state to the unburned state
gas.setState_TPX(tin, p, comp)

# initialize the flame object
f = FreeFlame(gas=gas, grid=initial_grid, tfix=600.0)

# set the upstream properties
f.inlet.set(mole_fractions=comp, temperature=tin)

f.set(tol = tol_ss, tol_time = tol_ts)
f.showSolution()

# solve without the energy equation
f.set(energy = 'off')
f.setRefineCriteria(ratio=10.0, slope=1, curve=1)
f.setMaxJacAge(50, 50)
f.setTimeStep(1.0e-5, [1, 2, 5, 10, 20])

```

```

f.solve(loglevel, refine_grid)
f.save('ch4_adiabatic.xml', 'no_energy',
      'solution with the energy equation disabled')

# solve with the energy equation
f.set(energy = 'on')
f.setRefineCriteria(ratio=3.0, slope=0.1, curve=0.2)
f.solve(loglevel, refine_grid)
f.save('ch4_adiabatic.xml', 'energy',
      'solution with the energy equation enabled')
print 'mixture-averaged flamespeed = ', f.u()[0]

# write the velocity, temperature, density, and mole
# fractions to a CSV file
z = f.flame.grid()
T = f.T()
u = f.u()
V = f.V()
fcsv = open('onestep_flame.csv', 'w')
writeCSV(fcsv, ['z (m)', 'u (m/s)', 'V (1/s)', 'T (K)', 'rho (kg/m3)']
          + list(gas.speciesNames()))
for n in range(f.flame.nPoints()):
    f.setGasState(n)
    writeCSV(fcsv, [z[n], u[n], V[n], T[n], gas.density()]
              +list(gas.moleFractions()))
fcsv.close()

# print the laminar flame speed and flame temperature to the output
# screen

```

```
print 'solution saved to onestep_flame.csv'  
print 'multicomponent flamespeed = ',u[0]  
print 'flame temperature = ', T[n-1]  
f.showStats()
```

# Appendix L

## One-Step Model Parameters for Hydrogen-Air Systems

Table L.1 lists first-order ( $n = 1$ ) one-step model values for activation energy  $E_a$ , pre-exponential factor  $A$ , heat release  $q$ , and corresponding constant  $(a_5)_P$  used in the Cantera input (.cti) file for a range of hydrogen-air compositions. The activation energies were found using the constant pressure explosion method (Equation 6.23) with effective reaction orders also found from the constant pressure explosion method (Equation 6.18); the heat release values were found directly from the flame temperature, and the pre-exponential factors were obtained through iteration.

Table L.2 lists second-order ( $n = 2$ ) one-step model values for activation energy  $E_a$ , pre-exponential factor  $A$ , heat release  $q$ , and corresponding constant  $(a_5)_P$  used in the Cantera input (.cti) file for a range of hydrogen-air compositions. The activation energies were found using the constant pressure explosion method (Equation 6.23) with effective reaction orders also found from the constant pressure explosion method (Equation 6.18); the heat release values were found directly from the flame temperature, and the pre-exponential factors were obtained through iteration.

Table L.1: First-order ( $n = 1$ ) one-step model parameters for hydrogen-air systems

$\%H_2$	$E_a$ (kcal/mol)	$A$ (1/s)	$(a_5)_P$	$q$ (kJ/mol)
70	21.602	4.080E+09	-3338	21.56
65	22.173	4.790E+09	-3712	24.66
60	22.862	5.150E+09	-4084	27.76
55	23.358	4.860E+09	-4448	30.78
50	24.131	4.740E+09	-4812	33.81
45	24.305	3.550E+09	-5170	36.79
40	26.061	4.040E+09	-5522	39.71
35	26.181	2.330E+09	-5847	42.41
30	27.856	2.260E+09	-5972	43.46
25	21.425	3.580E+08	-5355	38.33
20	21.806	3.450E+08	-4493	31.16
15	20.263	8.200E+07	-3579	23.56
14	20.176	5.510E+07	-3398	22.06
13	20.017	3.110E+07	-3216	20.54
12	20.308	1.185E+07	-2984	18.61

Table L.2: Second-order ( $n = 2$ ) one-step model parameters for hydrogen-air systems

%H <sub>2</sub>	$E_a$ (kcal/mol)	$A$ (m <sup>3</sup> /mol·s)	$(a_5)_P$	$q$ (kJ/mol)
70	21.602	7.000E+14	-3338	21.56
65	22.173	8.800E+14	-3712	24.66
60	22.862	9.960E+14	-4084	27.76
55	23.358	1.010E+15	-4448	30.78
50	24.131	1.027E+15	-4812	33.81
45	24.305	7.940E+14	-5170	36.79
40	26.061	9.970E+14	-5522	39.71
35	26.181	5.690E+14	-5847	42.41
30	27.856	5.870E+14	-5972	43.46
25	21.425	7.110E+13	-5355	38.33
20	21.806	6.580E+13	-4493	31.16
15	20.263	1.350E+13	-3579	23.56
14	20.176	8.750E+12	-3398	22.06
13	20.017	4.610E+12	-3216	20.54
12	20.308	1.820E+12	-2984	18.61

# Appendix M

## Cantera Python Code *STFLAME1.py* for Simulating a Flat Flame in a Strained Flow Field

This is the Cantera code used in examining the flame response to straining, applied to a mixture of 15% hydrogen in air ( $\phi = 0.42$ ).

```
#  
# STFLAME1 - A detached flat flame stabilized at a stagnation point  
#  
  
# This script simulates a lean hydrogen-oxygen flame stabilized in  
# a strained flow field at an axisymmetric stagnation point on a  
# non-reacting surface. The solution begins with a flame attached  
# to the inlet (burner), and the mass flow rate is progressively  
# increased, causing the flame to detach and move closer to the  
# surface. This example illustrates use of the new 'prune' grid  
# refinement parameter, which allows grid points to be removed if  
# they are no longer required to resolve the solution. This is  
# important here, since the flame front moves as the mass flowrate  
# is increased. Without using 'prune', a large number of grid
```

```

# points would be concentrated upstream of the flame, where the
# flamefront had been previously. (To see this, try setting prune
# to zero.)

from Cantera import *
from Cantera.OneD import *
from Cantera.OneD.StagnationFlow import StagnationFlow

#####
#
# parameter values
#
p          = OneAtm          # pressure
tburner    = 301             # burner temperature
tsurf      = 302

# each mdot value will be solved to convergence, with grid refinement,
# and then that solution will be used for the next mdot

mdot       = [0.1, 0.5, 1.0, 1.5, 2, 2.5, 2.6, 2.7, 2.8, 2.9, 3,
3.1, 3.2, 3.3, 3.4, 3.5]    # kg/m^2/s

comp       = 'H2:0.42, O2:0.5, N2:1.88' # premixed gas composition

# The solution domain is chosen to be 50 cm, and a point very near the
# downstream boundary is added to help with the zero-gradient boundary
# condition at this boundary.

initial_grid = [0.0, 0.0001, 0.001, 0.002, 0.003, 0.005,
0.0059, 0.006];

```

```

tol_ss    = [1.0e-4, 1.0e-12]      # [rtol atol] for steady-state
                                         # problem
tol_ts    = [1.0e-3, 1.0e-8]      # [rtol atol] for time stepping

loglevel  = 1                       # amount of diagnostic output (0
                                         # to 5)

refine_grid = 1                     # 1 to enable refinement, 0 to
                                         # disable

ratio = 5.0
slope = 0.1
curve = 0.2
prune = 0.05

##### create the gas object #####
#
# This object will be used to evaluate all thermodynamic, kinetic,
# and transport properties
#

#gas = IdealGasMix(rxnmech)
gas = importPhase('Lieta1_mech_2003.cti','gas')
# set its state to that of the unburned gas at the burner
gas.setState_TPX(tburner, p, comp)

# Create the stagnation flow object with a non-reactive surface. (To
# make the surface reactive, supply a surface reaction mechanism. see

```

```

# example catcomb.py for how to do this.)
f = StagnationFlow(gas = gas, grid = initial_grid)

# set the properties at the inlet
f.inlet.set(massflux = mdot[0], mole_fractions=comp,
temperature=tburner)

# set the surface state
f.surface.setTemperature(tsurf)

f.set(tol = tol_ss, tol_time = tol_ts)
f.setMaxJacAge(5, 10)
f.set(energy = 'off')
f.init(products = 'equil') # assume adiabatic equilibrium products
f.showSolution()

f.solve(loglevel, refine_grid)

f.setRefineCriteria(ratio = ratio, slope = slope,
                    curve = curve, prune = prune)
f.set(energy = 'on')

m = 0
for md in mdot:
    f.inlet.set(mdot = md)
    f.solve(loglevel,refine_grid)
    m = m + 1
    f.save('stflame1.xml', 'mdot'+m, 'mdot = '+md+' kg/m2/s')

```

```

# write the velocity, temperature, and mole fractions
# to a CSV file
z = f.flow.grid()
T = f.T()
u = f.u()
V = f.V()
fcsv = open('stflame1_'+m+'.csv','w')
writeCSV(fcsv, ['z (m)', 'u (m/s)', 'V (1/s)',
'T (K)'] + list(gas.speciesNames()))
for n in range(f.flow.nPoints()):
    f.setGasState(n)
    writeCSV(fcsv, [z[n], u[n], V[n], T[n]]+
list(gas.moleFractions()))
fcsv.close()

print 'solution saved to flame1.csv'

f.showStats()

```

# Appendix N

## Second-Order One-Step Model Cantera Input (.cti) File

Below is an example Cantera input (.cti) file using second-order one-step model parameters for 30% hydrogen-air.

```
# ONE-STEP MODEL FOR HYDROGEN-AIR WITH PHI=1.02
# 2nd ORDER REACTION WITH ARGON ATOMS
#
# Generated from file argon.inp
# by ck2cti on Mon Aug 25 09:52:59 2003
#
# Transport data from file ../transport/gri30_tran.dat.

units(length = "cm", time = "s", quantity = "mol", act_energy = "cal/mol")

ideal_gas(name = "gas",
           elements = " Ar ",
           species = "" R P """,
           reactions = "all",
           transport = "Mix",
```

```

initial_state = state(temperature = 300,
                      pressure = OneAtm) )

#-----
# Species data
#-----

species(name = "R",
        atoms = " Ar:1 ",
        thermo = (
            NASA( [ 300.00, 1000.00], [ 2.5000000000E+00, 0.000000000E+00,
                0.000000000E+00, 0.000000000E+00, 0.000000000E+00,
                -7.453750000E+02, 4.379674910E+00] ),
            NASA( [ 1000.00, 5000.00], [ 2.5000000000E+00, 0.000000000E+00,
                0.000000000E+00, 0.000000000E+00, 0.000000000E+00,
                -7.453750000E+02, 4.379674910E+00] )
        ),
        transport = gas_transport(
            geom = "atom",
            diam = 3.33,
            well_depth = 136.50),
        note = "120186"
    )

species(name = "P",
        atoms = " Ar:1 ",
        thermo = (
            NASA( [ 300.00, 1000.00], [ 2.5000000000E+00, 0.000000000E+00,

```

```

        0.000000000E+00,  0.000000000E+00,  0.000000000E+00,
        -5.972000000E+03,  4.379674910E+00] ),
NASA( [ 1000.00,  5000.00], [ 2.500000000E+00,  0.000000000E+00,
        0.000000000E+00,  0.000000000E+00,  0.000000000E+00,
        -5.972000000E+03,  4.379674910E+00] )
    ),
transport = gas_transport(
        geom = "atom",
        diam =      3.33,
        well_depth = 136.50),
note = "5"
)

```

```

#-----
# Reaction data
#-----

```

```

# Reaction 1
reaction( "R + R => P + P", [5.870E+14, 0, 27856])

```

# Appendix O

## Four-Species One-Step Model Cantera Input (.cti) File

This is the Cantera input (.cti) file for the four-species one-step model for a mixture of 15% hydrogen-air with  $Le = 0.42$ .

```
# ONE-STEP MODEL FOR 15% HYDROGEN-AIR
# 2nd ORDER REACTION WITH 4 SPECIES
# AND ACCURATE TRANSPORT PARAMETERS

units(length = "cm", time = "s", quantity = "mol", act_energy = "cal/mol")

ideal_gas(name = "gas",
           elements = " H O N ",
           species = "" H2 H2O O2 N2 """,
           reactions = "all",
           transport = "Mix",
           initial_state = state(temperature = 300,
                                pressure = OneAtm) )

#-----
```

```

# Species data
#-----

species(name = "H2",
  atoms = " H:2 ",
  thermo = (
    NASA( [ 300.00, 1000.00], [ 1.5000000000E+01, 0.0000000000E+00,
      0.0000000000E+00, 0.0000000000E+00, 0.0000000000E+00,
      -7.453750000E+02, 4.379674910E+00] ),
    NASA( [ 1000.00, 5000.00], [ 1.5000000000E+01, 0.0000000000E+00,
      0.0000000000E+00, 0.0000000000E+00, 0.0000000000E+00,
      -7.453750000E+02, 4.379674910E+00] )
  ),
  transport = gas_transport(
    geom = "linear",
    diam = 2.92,
    well_depth = 38.00,
    polar = 0.79,
    rot_relax = 280.00),
  note = "121286"
)

species(name = "O2",
  atoms = " O:2 ",
  thermo = (
    NASA( [ 300.00, 1000.00], [ 1.5000000000E+01, 0.0000000000E+00,
      0.0000000000E+00, 0.0000000000E+00, 0.0000000000E+00,
      -7.453750000E+02, 4.379674910E+00] ),
    NASA( [ 1000.00, 5000.00], [ 1.5000000000E+01, 0.0000000000E+00,
      0.0000000000E+00, 0.0000000000E+00, 0.0000000000E+00,
      -7.453750000E+02, 4.379674910E+00] )
  ),
  transport = gas_transport(
    geom = "linear",
    diam = 2.92,
    well_depth = 38.00,
    polar = 0.79,
    rot_relax = 280.00),
  note = "121286"
)

```

```

        -7.453750000E+02, 4.379674910E+00] )
    ),
transport = gas_transport(
    geom = "linear",
    diam = 3.46,
    well_depth = 107.40,
    polar = 1.60,
    rot_relax = 3.80),
note = "121386"
)

species(name = "H2O",
atoms = " H:1 O:1 ",
thermo = (
    NASA( [ 300.00, 1000.00], [ 1.5000000000E+01, 0.000000000E+00,
        0.000000000E+00, 0.000000000E+00, 0.000000000E+00,
        -3.087000000E+04, 4.379674910E+00] ),
    NASA( [ 1000.00, 5000.00], [ 1.5000000000E+01, 0.000000000E+00,
        0.000000000E+00, 0.000000000E+00, 0.000000000E+00,
        -3.087000000E+04, 4.379674910E+00] )
    ),
transport = gas_transport(
    geom = "nonlinear",
    diam = 2.61,
    well_depth = 572.40,
    dipole = 1.84,
    rot_relax = 4.00),
note = "20387"
)

```

```

species(name = "N2",
  atoms = " N:2 ",
  thermo = (
    NASA( [ 300.00, 1000.00], [ 3.298677000E+000, 1.408240000E-003,
      -3.963222000E-006, 5.641515000E-009, -2.444855000E-012,
      -1.020900000E+003, 3.950372000E+000] ),
    NASA( [ 1000.00, 5000.00], [ 2.926640000E+000, 1.487977000E-003,
      -5.684761000E-007, 1.009704000E-010, -6.753351000E-015,
      -9.227977000E+002, 5.980528000E+000] )
  ),
  transport = gas_transport(
    geom = "linear",
    diam = 3.62,
    well_depth = 97.53,
    polar = 1.76,
    rot_relax = 4.00),
  note = "121286"
)

#-----
# Reaction data
#-----

# Reaction 1
reaction( "H2 + O2 => H2O + H2O", [2.85E+14, 0, 20263])

```